EXPERIMENTAL INVESTIGATION OF THE TURBULENT NEAR WAKE
FLOW FIELD OF MULTISCALE/FRACTAL GRIDS

A THESIS SUBMITTED TO
THE GRADUATE SCHOOL OF NATURAL AND APPLIED SCIENCES
OF
MIDDLE EAST TECHNICAL UNIVERSITY

BY

HOOMAN AMIRI HAZAVEH

IN PARTIAL FULFILLMENT OF THE REQUIREMENTS
FOR
THE DEGREE OF DOCTOR OF PHILOSOPHY
IN
AEROSPACE ENGINEERING

SEPTEMBER 2018

Approval of the thesis:

EXPERIMENTAL INVESTIGATION OF THE TURBULENT NEAR WAKE FLOW FIELD OF MULTISCALE/FRACTAL GRIDS

submitted by **HOOMAN AMIRI HAZAVEH** in partial fulfillment of the requirements for the degree of **Doctor of Philosophy in Aerospace Engineering Department, Middle East Technical University** by,

Prof. Dr. Halil Kalıpçılar   _____
Dean, Graduate School of **Natural and Applied Sciences**

Prof. Dr. Ozan Tekinalp   _____
Head of Department, **Aerospace Engineering**

Assoc. Prof. Dr. Oğuz Uzol   _____
Supervisor, **Aerospace Engineering Dept., METU**

Examining Committee Members:

Prof. Dr. İsmail H. TUNCER   _____
Aerospace Engineering Dept., METU

Assoc. Prof. Dr. Oğuz Uzol   _____
Aerospace Engineering Dept., METU

Assoc. Prof. Dr. M. Metin Yavuz   _____
Mechanical Engineering Dept., METU

Asst. Prof. Dr. Sıtkı Uslu   _____
Mechanical Eng. Dept., TOBB ETU

Asst. Prof. Dr. Mustafa Kaya   _____
Aerospace Eng. Dept., Ankara Yıldırım Beyazıt University

Date: 05.09.2018

I hereby declare that all information in this document has been obtained and presented in accordance with academic rules and ethical conduct. I also declare that, as required by these rules and conduct, I have fully cited and referenced all material and results that are not original to this work.

Name, Last Name : Hooman, Amiri Hazaveh

Signature   :

ABSTRACT

EXPERIMENTAL INVESTIGATION OF THE TURBULENT NEAR WAKE FLOW FIELD OF MULTISCALE/FRACTAL GRIDS

Amiri Hazaveh, Hooman
Ph.D., Department of Aerospace Engineering
Supervisor: Assoc. Prof. Dr. Oğuz Uzol

September 2018, 176 pages

Turbulent near-field flow of three different fractal grids, as well as conventional square grid, is investigated using two-dimensional particle image velocimetry. All grids are designed to maintain similar solidity, effective mesh size, and the smallest thickness for comparison. Experiments are conducted at a Reynolds number of 1.2×10^4 based on effective mesh size. The instantaneous velocity field is realized on four sets of 35 equally spaced horizontal planes downstream of turbulence-generating-grids. Three-dimensional mean flow is reconstructed by stitching aforementioned horizontal planes, extending to 22 effective mesh size downstream of each grid. Additional mean flow variables are then obtained by rotating horizontal planes to the corresponding vertical ones in grids comprising geometrical symmetry. Turbulent mixing characteristics in the near-wake region are assessed and turbulent kinetic energy production, decay, and dissipation rate as well as estimation of length scales downstream of turbulence-generating-grids are carried out. It has been shown that grids with different fractal patterns can be used as a passive devices to custom tailor turbulence even in the non-homogeneous anisotropic near grid region. Dissipation rate coefficient is also shown to be not constant in the near-wake region.

Keywords: Turbulence, Fractal grids, Multi-scale grids, Turbulence-generating-grids, Particle Image Velocimetry

ÖZ

ÇOK ÖLÇEKLİ/FRAKTAL IZGARA KAYNAKLI AKIŞIN YAKIN İZ BÖLGESİNİN DENEYSEL İNCELENMESİ

Amiri Hazaveh, Hooman
Doktora, Havacılık ve Uzay Mühendisliği Bölümü
Tez Yöneticisi: Doç.Dr. Oğuz Uzol

Eylul 2018, 176 Sayfa

Bu tezde geleneksel kare ağın yanında üç farklı fraktal ağların yakın akış bölgesini 2-boyutlu parçacık görüntülemeli hız ölçümleri yapılmıştır. Karşılaştırma amacıyla bütün gridler benzer katılıkta, etkin ağ boyutunda ve en küçük kalınlıkta tasarlanmıştır. Deneyler, 1.2×10^4 etkin ağ boyutu Reynolds sayısında yapılmıştır. Anlık hız alanı ölçümleri türbülans üretici ağların arkasında 35 eşit boşluklu yatay düzlemde dört set olarak yapılmıştır. Üç-boyutlu ortalama akış alanı bu yatay düzlemler birleştirilerek gridlerin arkasında 22 etkin ağ boyutu mesafesine kadar oluşturulmuştur. Diğer ortalama akış değişkenleri simertrik gridlerde yatay düzlemlerin karşılık geldiği şekilde dikey hale döndürülmesiyle elde edilmiştir. Yakın iz bölgeindeki türbülanslı karışım karakteristikleri hesaplanmış ve türbülansli kinetik enerji üretimi, türbülans bozuşması, ve yayılım oranı ile birlikte türbülans üretici gridlerin arkasında uzunluk ölçekleri değerlendirilmiştir. Farklı fraktal yapıların, ağa yakın bölgede homejen olmayan akışta bile pasif araçlar olarak kullanarak isteğe uyarlanmış türbülans oluşturulabileceği gösterilmiştir. Yakın iz bölgesinde yayılım oranı katsayısının sabit olmadığı da gösterilmiştir.

Anahtar kelimeler: Türbülans, Fraktal ağlar, Çok ölçekli ağlar, Türbülans üretici ağlar, Parçacık Görüntülemeli Hız Ölçer

To my dearest parents, Saeed and Soroor,
my beloved wife and son, Pegah and Radin

ACKNOWLEDGMENTS

TABLES OF CONTENTS

LIST OF TABLES

LIST OF FIGURES

xvi

LIST OF SYMBOLS

Acronyms

2-D 2-C PIV	Two-dimensional two-component PIV
2-D PIV	Two-dimensional particle image velocimetry
CMOS	Complementary metal–oxide–semiconductor
Conv	Conventional grid
CSG	Conventional square grid
DNS	Direct numerical simulation
FCG	Fractal circular grid
FIG	Fractal I grid
FOV	Field of view
FSG	Fractal square grid
GGT	Grid-generated turbulence
HIT	Homogeneous and isotropic turbulence
HWA	Hotwire anemometry
IA	Interrogation area
ILS	Integral length scale
LBM	Lattice-Boltzmann method
LDA	Laser Doppler anemometry
LILS	Longitudinal integral length scale
Nd:YAG	Neodymium-doped yttrium aluminum garnet (Nd:$Y_3Al_5O_{12}$)
NRSS	Normalized Reynolds shear stress
PIV	Particle image velocimetry
PLIF	Planar Laser-induced fluorescence
POD	Proper orthogonal decomposition
RG	Regular grid
RNS	Reynolds normal stress
RSS	Reynolds shear stress

RST	Reynolds stress tensor
SFG	Square fractal grid
SRG	Square regular grid
SSU	Space scale unfolding
TGG	Turbulence generating grid
TKE	Turbulent kinetic energy
Tomo-PIV	Tomographic particle image velocimetry

Dimensionless numbers

$Ħ_D$	Uncertainty in measurement/calculation of variable D
$C_{\Delta P_S}$	Static pressure drop coefficient
$C_{\Delta P_T}$	Total pressure drop coefficient
$F(u)$	Flatness of streamwise velocity component
$K_1, K_3, \boldsymbol{K}$	Small scale isotropy factors
Re_D	Reynolds number based on length D, $Re_D = \dfrac{U_0 D}{\nu_{air}}$
Re_λ	Reynolds number based on Taylor microscale, $Re_\lambda = \dfrac{\sqrt{\langle u^2 \rangle}.\lambda}{\nu_{air}}$
Re_η	Reynolds number based on Kolmogorov scale
$S(u)$	Skewness of streamwise velocity component

Roman Symbols

P_{S_u}	Static pressure upstream of the grid
$\langle S_i S_j \rangle\, i,j = 1,2,3$	Components of mean velocity strain rate tensor
$\langle k \rangle_{ISO}$	Turbulent kinetic energy based on isotropic turbulence assumption
$\langle k \rangle_{RS}$	Turbulent kinetic energy based on symmetric flow
$\langle s_i s_j \rangle\, i,j = 1,2,3$	Components of fluctuating rate of strain tensor
$\langle u_i u_j \rangle\, i,j = 1,2,3$	Reynolds stress tensor components
D_0	Diameter of the largest circle in FCG
D_f	Fractal dimension
E_{11}	1-D Energy spectra

L_0	Length of the largest fractal element (bar)
L_{TS}	Test section length
$L_i\ (i = 0,1,2,3)$	Element length of zeroth, first, second, and third iterations
L_{min}	Length of the smallest element
R^2	Goodness of fit
R_D	Diameter ratio of each circle at one successive iteration
R_L	Length ratio of each element (bar) at one successive iteration
R_t	Ratio of bar thickness in one iteration
T_e	Eddy turnover time
U_∞, U_0	Wind tunnel test section inlet speed
U_u	Incoming velocity upstream of the grid
$\tilde{f}(r)$	Two-point correlation of velocity fluctuation
q^2	Twice the total turbulent kinetic energy of the flow
$t_i\ (i = 0,1,2,3)$	Thickness of zeroth, first, second, and third iterations
t_{min}	thickness of the smallest element
t_r	Thickness ratio
x_*	Wake-interaction length scale
x_0	Virtual origin
x_{peak}	Streamwise distance where turbulence intensity is maximum
y_{wake}	Wake width
$A\ (A')$	Power (exponential) function coefficient
B	number of patterns at each iteration of fractal grids
$L\ (L_u = L_{pq})$	integral length scale (Longitudinal integral length scale)
M, M_{eff}	Mesh size, Effective Mesh size
N	Number of fractal iterations
P	Pressure
S	Number of rectangular bars in fractal pattern
T	Test section side length
TI_u	Streamwise turbulence intensity
U, V, W	Instantaneous velocity components in streamwise, spanwise, and lateral directions

b	Bar width in conventional grid
c_1	Coefficient of equality in C_ε scaling
c_2	Coefficient of equality in C_ε scaling
$f\#$	Aperture in camera lens
$f(r) = R_{uu}$	Autocorrelation coefficient
k	turbulent kinetic energy
$n\ (n')$	Power (exponential) function slope
r	Space separation
u, v, w	Fluctuating velocity components in streamwise, spanwise, and lateral directions
u'	Root mean square (rms) streamwise velocity fluctuation
v'	Root mean square (rms) spanwise velocity fluctuation
x, X	Streamwise direction
y, Y	Spanwise direction
z, Z	vertical direction
$\boldsymbol{A}$	Wet area of fractal grid
$\boldsymbol{P}$	Fractal perimeter's length
$\boldsymbol{V}$	Velocity
$\boldsymbol{n}$	Number of samples

Greek Symbols

$\overline{\Omega_i}$	Mean vorticity component in i direction
$\langle \varepsilon \rangle_d$	Mean dissipation rate calculated from kinetic energy decay
$\langle \varepsilon \rangle_{iso}\ (\langle \varepsilon \rangle_{ISO})$	Mean dissipation rate based on small scale (large scale) isotropy
C_ε	Coefficient of dissipation rate
C_μ	Semi-empirical constant in $k - \varepsilon$ modeling
$\langle D \rangle$	Ensemble averaged of variable D
κ_1	Wavenumber
σ_U	Standard deviation of streamwise velocity component
ν_{air}	kinematic viscosity of air
ΔP_S	Static pressure difference

ΔP_T	Total pressure difference
Δt	Time between two pulses of laser
Δx	Streamwise interval
$\mathcal{L}$	Normalizing length scale
$\mathbb{P}$	Rate of production
α, β	constants
δ	Boundary layer thickness
ε	Turbulent kinetic energy mean dissipation rate
η	Kolmogorov microscale
λ	Taylor microscale
ρ	Density
σ	Solidity (blockage ratio)
τ	Time separation

CHAPTER 1

INTRODUCTION

1.1   Motivation

Turbulent flow generated by grids and screens has been the most common experimental configuration used to achieve nearly homogeneous and isotropic turbulence (HIT) where the theoretical study concentrates [1–4]. In fact, until more recent progress wherein turbulent flow is generated experimentally [5] or numerically [6], the only way to study on the isotropic flow is grid turbulence. It was shown that flow characteristics such as turbulence decay [7,8], Reynolds shear stress [9], self-preservation and similarity [10], spectra and rms vorticity distribution [11] are highly influenced by the grid geometry (i.e., initial conditions). Since then, the study on the near-field of the turbulence grids has received considerable attention [12–19]; Near-field flow is highly inhomogeneous due to the presence of simultaneous wakes and jets [3,13,20]. It was found that, close to the grid, the turbulence is in a "*non-equilibrium*" condition where the mean flow inhomogeneity causes severe turbulent kinetic energy (TKE) transport and production in transverse direction [21].

The study on the turbulence generated in the near-field and produced by conventional grids was accompanied by the introduction of a new generation of turbulence grids, called fractal/multi-scale grids [22]. It was discovered that specifically downstream of a "*space-filling fractal square grid*", turbulence intensities, as well as Reynolds number, are unusually high. There is also an '*exponential like*' fast decay of TKE which was in broad contrast to the classical power law decay [23]. It was shown later that the range where this exponential decay applies is rather short and a classical power law fit to the data is also possible [13]. However, still, there are some unanswered questions about the multi-scale/fractal-generated turbulence. For example, the ratio of the integral length scale to the Taylor microscale during the decay was found to be

constant while local Reynolds number is decreasing which contradicts the assumption of a constant 'coefficient of dissipation rate' in an isotropic turbulent flow. Numerical studies and experiments ensure that the near-field of the grid-generated turbulence (GGT) is undeniably worth studying.

It has been almost a century since the first measurement of velocity fluctuations by Simmons and Salter [1] utilizing hotwire anemometry (HWA). Since then, a vast amount of the grid experiments was focused on the far-field region using HWA as a measurement technique [7,12,22,24,25]. Unlike the far-field of turbulence generator grids, the flow is highly three-dimensional in the near-field; specifically near the grid, turbulence properties such as the temporal and spatial development of coherent structures are very complex. Typically, there exists a large recirculation zone behind solid bars, where the flow is strongly reversed. This recirculation zone (the distance between the grid and the possible apparent stagnation point) is reported to be extended from $\frac{x}{M} \approx 1$ to 1.75 [13,15] where x is the downstream distance from the grid and M is the grid mesh size[1]. The existence of regions with mean flow reversal and high turbulent intensities in the vicinity of the grid solid bars, make HWA useless to measure the flow correctly [18]. In this respect, Particle Image Velocimetry (PIV) and Laser Doppler Anemometry (LDA) are more suitable candidates to investigate the near-field region. PIV itself gives spatial information at an acceptable spatial resolution that can be used to obtain velocity gradients and derive correlation functions. This is the benefit on the point measurement techniques such as LDA. On the other hand, PIV techniques are still in a lack of spatial filtering effects and the ability of PIV to effectively resolve all turbulent scales has yet to be established [26].

1.2   Literature Survey on Fractal Grid-Generated-Turbulence

Line, square and cube are simple geometries defined in Euclidean space with integer dimensions of 1, 2, and 3, respectively. Fractals are special geometries with non-integer (fractional number) dimensions. The concept of non-integer dimension was generalized by Hausdorff [27] in the early-1900s. Although it was just a mathematical object to the 1980s, in the late-1970s, Mandelbrot turned this purely mathematical

---

[1] Mesh size for regular grids is defined as the spacing between two nearby rods.

concept into a realizable sense. He could convince scientists that shapes with "*non-integer dimensions*" are not exceptional but very common. Fractals are everywhere. In nature, they appear in clouds, trees, rivers, leaves, water drops, pinecone seeds, ice crystals, and air bubbles. Geological sites, coastlines, fluid turbulence, polymers, and fractures are all made of fractal shapes. The word "fractal" was originated since then from a Latina word "Fractus" meaning "Broken" or "Fractured" to describe such shapes. By that time, it was figured out that fractal shapes could fit an effectively infinite length within a limited surface, or at a higher order an infinite surface within a finite volume. In other words, a fractal shape can maximize contact within a finite boundary. Human lungs as a part of the respiratory system rely on their fractal character maximizing the delivery of oxygen to the blood, as well as trees where the photosynthesis is maximized through their fractal shape [28].

Fractals are '*scale-similar*'; i.e., by zooming to a fractal body and proceeding to the infinite level, only repeating patterns are seen. As an example, we can point to Koch curves [29] – also known as Koch snowflakes – which is depicted in Figure 1-1. Mathematically, fractals could be generated by "*self-iterative process*".

It has been nearly two decades since the pioneering studies on fractal – tree-like – objects obstructing a steady laminar flow. Queiros-Conde and Vassilicos [30] designed the first fractal object for wind tunnel experiments. Staicu et al. [31] measured the statistics of turbulence in the wake of fractal tree-like generators. Although the results were not conclusive to individuate the effects of the fractal elements and their self-similar structure, an elongated production region was reported downstream of the fractal bodies compared with regular grids. This led to some early attempts on computer simulation of fractal/multi-scale-forced turbulence [32–34] and after a while to the first extensive experimental study of turbulent flow generated by mono-plane fractal grids by Hurst and Vassilicos [22] who introduced three different patterns to generate fractal grids. Schematic of these turbulence-generating-grids are shown in Figure 1-2. The three fractal-generating patterns and corresponding fractal grids, from left to right, cross, I, and square, from Hurst and Vassilicos [22]. Hurst and Vassilicos reported remarkable features in turbulent flow generated by fractal square grids – i.e., an exponential fit to turbulent kinetic energy decay instead of well-known

power law fit – have inspired a chain of discussion and debate both on experimental [13,14,17–19,35–55] and numerical [28,56–62] point of view.
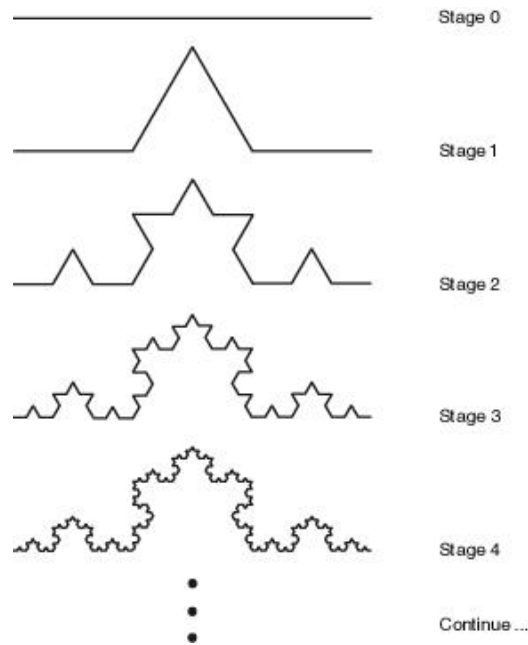
Figure 1-1 Koch curve as an example of fractal geometry [29].

There is no agreement on the actual extension of the near-field even in the case of regular grids. Batchelor [63] proposed that the near-field of conventional grid extends to $x \leq 20M$, while it is reported to be extended down to $40M$ by Corrsin [64].
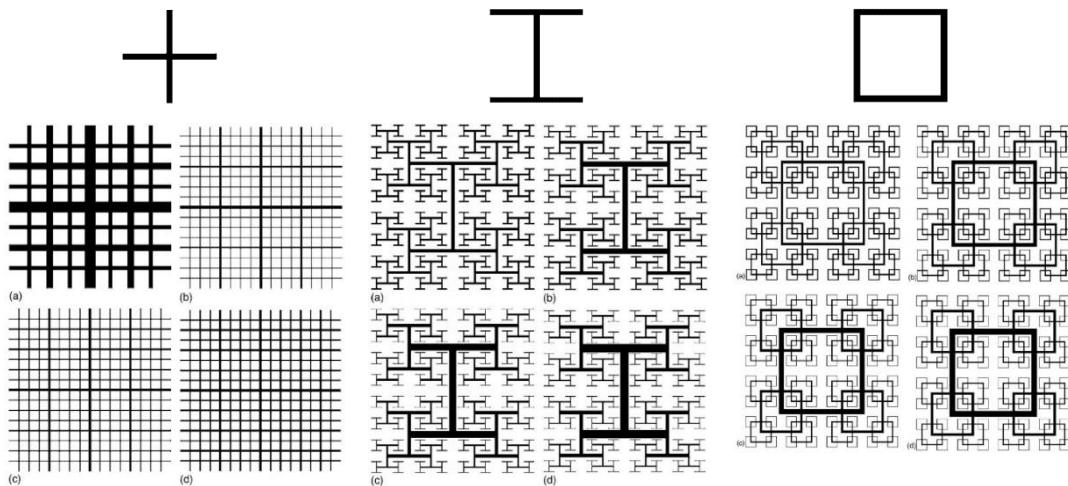
Figure 1-2. The three fractal-generating patterns and corresponding fractal grids, from left to right, cross, I, and square, from Hurst and Vassilicos [22].

4

To the best of the authors' knowledge, the literature on PIV measurements in the near-field region can be summarized in a few following attempts.

Bai et al. [65] studied the structure of turbulent flow and mixing length in the near wake of a fractal tree-like model. They demonstrated the significance of the multi-scale structure of trees for the actual modeling of the flow.

Cardesa et al. measured turbulence statistics immediately downstream of a two different biplane regular grids made of circular and square rods [66]. They reported spanwise homogenization in Reynolds shear stresses for $\frac{x}{M} \geq 7$. To check for the isotropy, they used an isotropic relation between longitudinal and lateral correlation functions of velocity fluctuations and conclude that the flow has yet far from being isotropic at the furthermost downstream measurement location ($\frac{x}{M} = 14$). In another study [15] by the same group, the rate of dissipation of turbulent kinetic energy (TKE) was assessed and its value was examined by changing the number of derivatives involved in the dissipation relation. They believed that the assumptions of isotropy or axisymmetric condition do not influence the dissipation estimation.

Gomes-Fernandes et al. performed 2-D PIV on fractal square grids inside a water tunnel with non-negligible free-stream turbulence intensity. Succeeded in characterizing the effects of background turbulence fluctuations on the grid-generated flow, they proposed a '*generalized wake-interaction length scale*' [14]. This was an improvement to the '*wake-interaction length scale*' which was first suggested by Mazellier and Vassilicos [52]. This scale characterizes the longitudinal extent of the production region and is shown by x_*. The generalized wake-interaction length scale made it possible to compare the results for regular and fractal square grids as well as being a good estimator of the location of peak turbulence intensity. Gomes-Fernandes et al. assessed the local global and local isotropy of the flow using the velocity gradients.

Earl et al. performed tomographic PIV (Tomo-PIV) on the regular grids in an open water channel [67]. They were able to visualize the instantaneous structure in the flow passing through different grids. They analyzed the turbulent kinetic energy decay and measured dissipation from the three-dimensional velocity field data.

Among the fractal patterns introduced by Hurst and Vassilicos [22], fractal square grid got more attention because of their unusual flow characteristics. Gomes-Fernandes et al. [50] studied on a space-filling fractal square grid with low solidity using stereoscopic PIV in a water channel. They obtained all components of the fluctuating velocity gradient in three downstream stations, on planes parallel to the grid. The planes are located in the production region, at the peak turbulence intensity and in the "*non-equilibrium*" decay region, respectively. They discussed on the flow structure using the $Q - R$ diagram and the strain-rate-tensor eigenvalues. Later on, they used 2-D PIV to study on different terms of the "*non-homogeneous Kármán-Howarth-Monin equation*" in the production region of a fractal square grid [17]. They found out that in the centerline of the grid and around the center of the production zone, the two-point advection term, the transport term, as well as the production are very high and the interscale energy transfer is highly anisotropic both in forward and inverse directions. However, the resultant flux of interscale energy is negative which shows the forward cascade. In addition, the -5/3 power law is detected in the energy spectrum of the streamwise component of fluctuating velocity.

Uijttewaal and Jirka [68] studied the near-field of grid turbulence in the shallow water. The grids were square and round cross-section vertical columns put in a row inside a basin with shallow water depth. Using PIV, they could capture the large-scale phenomena, and with the help of LDA, flow statistics were accurately determined.

In comparison to the results of enhanced heat transfer by fractal grids [69], Cafiero et al. [16] studied the near-wake flow of a round-jet with a fractal grid insert using 2-D 2-C PIV. They analyzed the effect of the fractal grid on the distribution of turbulence intensity as well as the planar component of the Reynolds stress tensor. They also applied proper orthogonal decomposition (POD) to show the high contribution of intermittent wakes shed from the largest bars to the modal energy.

In a recent study by Gan and Krogstad [18] which was inspired by the works of Cardesa et al. [15] and is built on the works of Krogstad and Davidson [13], a detailed 2-D PIV was performed on three monoplane square grids two of which are multiscale and the third one is of a conventional type. They found out that the multiple length scales forced to the flow by the different bar sizes in the grids lose their impact on the

flow much earlier than the turbulence turns into homogeneous at about $6M$. Because of the simplicity in the grid geometries, they were able to select a few generic characteristic lines which were representative of many of the grid sections. They showed that there was no significant difference among the three grids in terms of the mean and integral quantities, whereas the rate of decay of peak vorticity magnitude and sectional vortex circulation show a clear difference specifically after the initial development region ($x < 4M$). They linked the difference between decay rates to the multiple length scales introduced to the flow.

It is worth mentioning some PIV studies on fractal-generated flows, in the far-field region. Geipel et al. [70] carried out a parametric study on the turbulent flow generated by opposing jets with fractal cross grids. Grids are located at the outlet section of nozzles. They reported an increase of up to 100% of the turbulence intensity compared to conventional perforated plates.

Suzuki et al. [54] used planar laser-induced fluorescence (PLIF) in addition to PIV to look at the mixing of a passive scalar with a high-Schmidt-number in the flow generated by regular and fractal square grids. An appreciable stirring and scalar transfer improvement are reported by the use of the fractal square grid.

The capability of stereoscopic PIV to measure moderately low turbulence intensity flows –where the noise can take over the signal– was evaluated by Discetti et al. [55]. They used fractal square grid to generate turbulence and discovered a problem of noise far downstream of the grid where the turbulence intensity has reduced too much. However, they concluded that "*PIV is capable of detecting many of the flow features*" reported by [22], [51] and [52]. The result is that PIV is well appropriate to the near-field of grid-generated turbulence.

It is necessary to remark some of the studies in the near-field region of turbulence generator grids, in which measurements tools other than PIV is used. Hotwire anemometry (HWA) has been used as the major experimental apparatus to investigate the flow. The studies cover the field from the very near neighborhood of the grid to the far downstream. As mentioned before, flow reversal and high turbulence intensity regions are big trouble to hotwire measurements in the near-field of any bluff body.

Not only in the near-field but everywhere inside the flow, only single point statistics can be acquired by HWA which is not enough to assess the global structure of the flow – or spatial information [15].

Krogstad & Davidson [13] performed Laser Doppler Anemometry (LDA) and HWA measurements in the near-field region of cross-grids. They found that the flow is analogous to that produced by a square fractal grid.

Hearst and Lavoie [43] designed a novel fractal square grid in which several fractal square patterns are mounted to a conventional grid with a large mesh size of L_0. Because of the reduction in L_0 comparing to older studies where used only one space filling fractal inside the tunnel, the downstream measurement range relative to the largest element of the grid has increased. They reported a very inhomogeneous and anisotropic turbulence in the near grid region ($\frac{x}{L_0} < 20$) with a large power law decay exponent of -2.79 and growing dissipation coefficient C_ε. Their results reconcile with classical grid turbulence measurements.

Thormann and Meneveau [8] proposed an active grid which is made up of fractal winglets to generate turbulence with the multi-scale forcing of kinetic energy at more elevated Reynolds numbers. They verified the rate of power-law decay in the near and far-field and reported a dependency of decay exponent and dissipation coefficient on the initial condition.

In a very recent study by Nagata et al. [19], turbulence development and decay characteristics has been investigated in different types of turbulence generator grids including regular, fractal, combined regular, and a newly proposed '*quasi-fractal*' grids; the latter has been obtained by replacing the region of fractal iterations with regular grids. It was shown that the presence of fractal pattern is not obligatory to create an elongated non-equilibrium region, which is the specific nature of fractal grid turbulence.

Despite the extensive experimental studies on fractal-generated turbulent flow, there are remarkable computational efforts as well. Some near-field studies using direct numerical simulation (DNS) are as follows. It is worth to note that because of

computational limitations, the Reynolds number in DNS is typically one order of magnitude smaller than that in experiments.

To compare the experimental and numerical results of isotropic turbulence approximation, Djenidi [71] used the lattice-Boltzmann method (LBM) to perform DNS of grid-generated turbulence. The grid was similar to the conventional square grids in a four by four array. The results were in agreement with existing experimental data, and they showed the importance of the mesh resolution and computational domain size in the turbulence decay.

Nagata et al. [57] simulated the turbulent mixing of heat in grid-generated turbulence (GGT) using DNS. They used different types of grids and investigated the effect of Prandtl number on the turbulent mixing and heat transfer.

Ertunc et al. [72] investigated the homogeneity of turbulence generated by static grids using hot-wire measurements and direct numerical simulations based on the LBM. Their experimental grid solidity was lower than that suggested in the literature to establish homogeneous turbulent flow. However, they could perform DNS over a wide range of solidities to explain the possible reasons for inhomogeneity. DNS results showed that the homogeneity is only found in the mean velocity behind the symmetric grids. In the case of slightly non-uniform grid, the flow is neither homogeneous in the mean quantities nor the turbulence quantities.

1.2.1   <u>Applications</u>

In addition to the interesting physical properties, multi-scale/fractal grids have also been examined in a wide range of engineering applications including

- Enhance mixing by energy-efficient turbulent mixers in which it is required to have high turbulence intensities with low-pressure drops (i.e., less power loss) [37], and its usage in inline static mixers [54,73];
- Fractal fluid-mixers used in high-precision epoxies, sugar manufacturing, and chromatography, developed by Amalgamated Research Inc. [74];
- Fractal blades to be used instead of solid paddles in stirring mixers [75];
- Enhancing pressure drop while maintaining turbulence intensities as low as possible in airbrakes [28];

- Enhance heat transfer from impinging jets passing through grids [69];

- Flow metering and flow conditioning using fractal shape orifices [76,77];

- Acoustic noise reduction from wings by modifying the geometry of spoilers [78];

- Reducing the vortex shedding intensity of flows past normal plates [79];

- Turbulence generators for combustion process [80–82];

- Applications in wind energy as in wind fences comprising fractal geometries [83][84];

- Enhancing convective and radiative heat transfer in fins or heat sinks [85];

- Microscale heat sinks used in electronic microchips [86,87];

- Fractal Antennas produced for applications such as cell phones and Wi-Fi systems [88,89].

1.2.2   <u>The Interest on the study of fractal grid generated turbulence</u>

The existence of unusual turbulence properties (high TI and Reynolds number compared to conventional square grids) downstream of relatively low blockage ratio fractal square grids (FSG) ($\sigma \approx 0{,}25$) was previously shown in different experiments [51][52][35][14][39]. This is the main idea behind introducing CSG and FSG with more or less the same blockage ratio to produce a similar value of drag, so the near wake flow of these two can be compared. In addition, DNS of FSG [90] reveals much longer production and non-equilibrium decay region downstream of the fractal grids. Also from the point of view of industrial applicability, the most attractive feature of square fractals is the possibility to tune the position of the turbulent energy peak intensity with a simple geometrical scaling [16].

The planar fractal I-grid introduced by Hurst & Vassilicos [22] is, in fact, the analogus 2-D type of the 3-D fractal structures used by Queiros-Conde & Vassilicos [30] and Staicu et al. [31] resembling trees. There exist very limited study of turbulence generated by fractal I-grids after Hurst and Vassilicos [22]. Chester et al. [91] and Chester and Meneveau [92] numerically studied fractal trees similar to fractal I trees of [30]. The focus of these studies was on the calculation of drag using renormalized numerical simulation to understand the interaction of turbulent flows with boundaries characterized by multiple length scales and model the drag of unresolved branches of

a fractal tree. Mazellier & Vassilicos [93] used fractal I-grid and fractal cross grid data from Hurst & Vassilicos [22] to demonstrate the dependency of turbulence dissipation constant to inlet conditions. More recently, Bai et al. carried out PIV measurements in the near-field of a fractal-like tree to demonstrate the significance of the multi-scale structures of trees for the actual modeling of the flow in sparse vegetation canopies [65].

1.3 Objectives and Scope

In this study, we perform two-dimensional particle image velocimetry (2-D PIV) on three different pattern fractal grids as well as a conventional (regular) square grid. The main objectives and contributions of this thesis to the turbulence and its applications are as follows:

- To characterize fractal-generated-turbulent-flow in more details. These include statistical quantities (e.g., turbulence intensity, homogeneity and isotropy, skewness and flatness of the streamwise velocity, correlation functions, and length scales, etc.)

- Propose a new generation of fractal turbulence generating grids with circular elements (FCG) to compare with the well-known fractal square grid (FSG).

- To examine a method to reproduce mean three-dimensional flow using two-dimensional data for axisymmetric flows. This will provide an opportunity to investigate the evolution of fractal-generated turbulence flow in more detail since the spatial development of cross-sectional profiles, at least for mean values are available.

- To investigate the flow development in the near wake of different grids to come up with the most effective design in mixing performance (i.e., homogeneity and turbulence intensities), etc.

- Trends of longitudinal integral length scales as well as Taylor microscale in the near-field region of the turbulence-generating grids. Previously, Hurst and Vassilicos [22] showed that these values are almost constant along the centerline of the space filling, low-blockage fractal square grids in the decay region.

- Investigation on turbulent kinetic energy budget, concerning two-dimensional production rate and estimated mean dissipation rates.

1.4 Thesis outline

The present thesis is structured as follows. In chapter 2 general details and technical properties of the experimental facility and measurement methods are described. These include a wind tunnel, details of the turbulence-generating grids and 2-D PIV components. In chapter 3, results are given and discussed. Final discussions and conclusions are presented in the closing chapter four.

CHAPTER 2

EXPERIMENTAL SETUP AND MEASUREMENT DETAILS

In this chapter, we first explain the wind tunnel in which the measurements are done. Fractal grids design, geometric parameters, and manufacturing process, as well as PIV equipment such as Laser, optics, and camera, are reviewed, and experimental procedure and data processing are described. In the end, some notes on the uncertainty of PIV experiments are included.

2.1 Wind Tunnel

Measurements are conducted in an open-circuit suction type wind tunnel. Schematics of the tunnel is shown in Figure 2-1. Incoming air flow passes through a honeycomb, a screen, and a 1.0 meter long settling chamber, then enters into a 9:1 contraction before reaching the test section. The test section is made of 10mm thick transparent Plexiglas with dimensions of $340 \times 340 \times 1000$ mm^3, specifically designed to mount the turbulence-generator-grids at its front section. The flow is then diffused through a 2.0m long diffuser. The divergence angle is 2.43° to prevent adverse pressure gradient. A 1.7m long adapter is turning the square cross section into circular one to attach to the fan casing. A 4.0 KW electric motor drives the fan.

The inlet speed (U_∞) is adjusted according to the frequency-velocity diagram shown in Figure 2-2. In this figure TI_u refers to the streamwise turbulence intensity. The velocity is obtained at the center of the test section entrance using hotwire anemometry (HWA). Maximum velocity of about 20 m/s can be achieved inside the test section. The free stream background turbulence intensity approaching the grid is estimated to be about 0.5% of the mean flow velocity of 10 m/s.
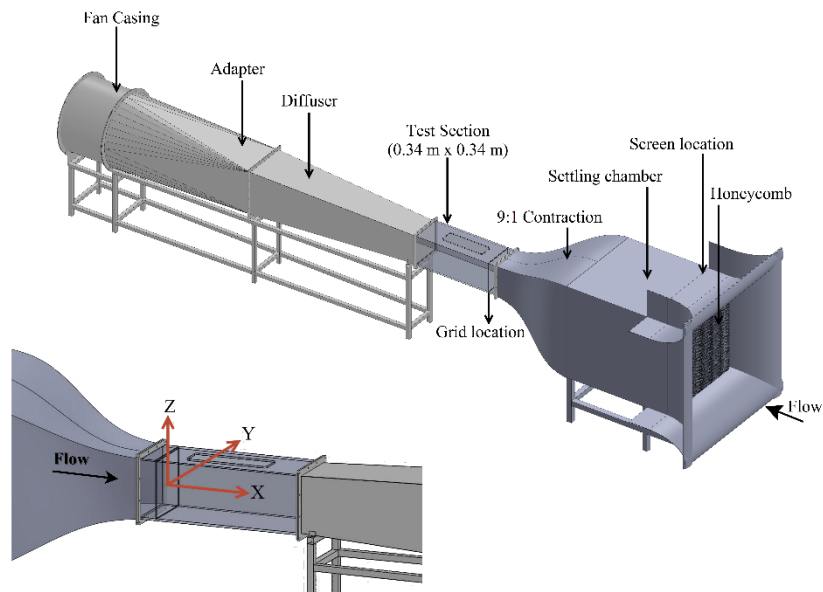
Figure 2-1 Schematics of the open loop wind tunnel and the coordinate system.

2-D PIV Measurements were carried out from February, 8th to March, 4th 2017. The ambient air properties were monitored during the experiments with the help of a barometric pressure/humidity/temperature data logger. Distribution of these variables is briefly expressed in Figure 2-2. Global Reynolds number variation is therefore considered to be negligible.
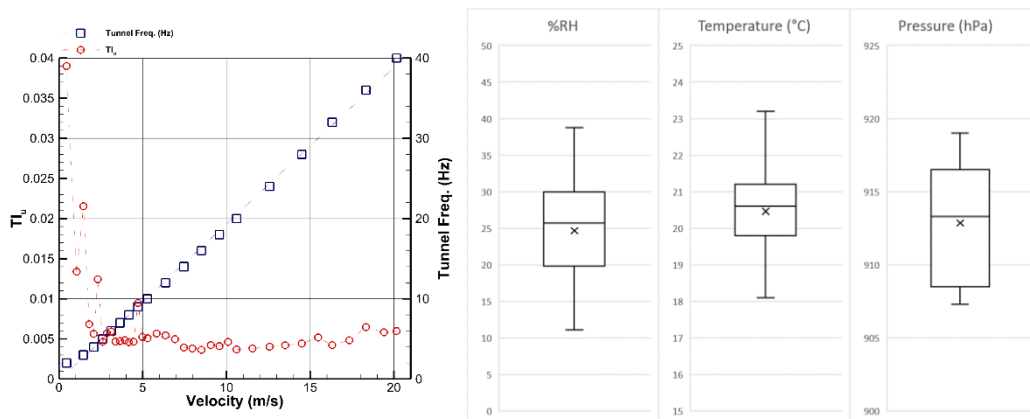
Figure 2-2 (Left) Streamwise velocity and turbulence intensity in the centerline of the test section entry, as a function of driver motor frequency, (Right) Variation of relative humidity, temperature, and atmospheric pressure throughout the experiments.

Uniformity of the flow entering the test section is investigated twice both for streamwise velocity and turbulence intensity. The coordinate system is fixed at the centerline of the tunnel where the grids are mounted. The streamwise direction (x) is

14

along the tunnel, the spanwise direction (y) is from the center to the test section vertical walls, and the vertical direction (z) is governed by the right-hand rule. The coordinate system is shown in Figure 2-1. HWA is carried out along y=0 line at the entrance of the test section. The results are illustrated in Figure 2-3. Characterization is carried out at three different frequencies corresponding to three inlet speeds (5, 10, and 15 m/s).
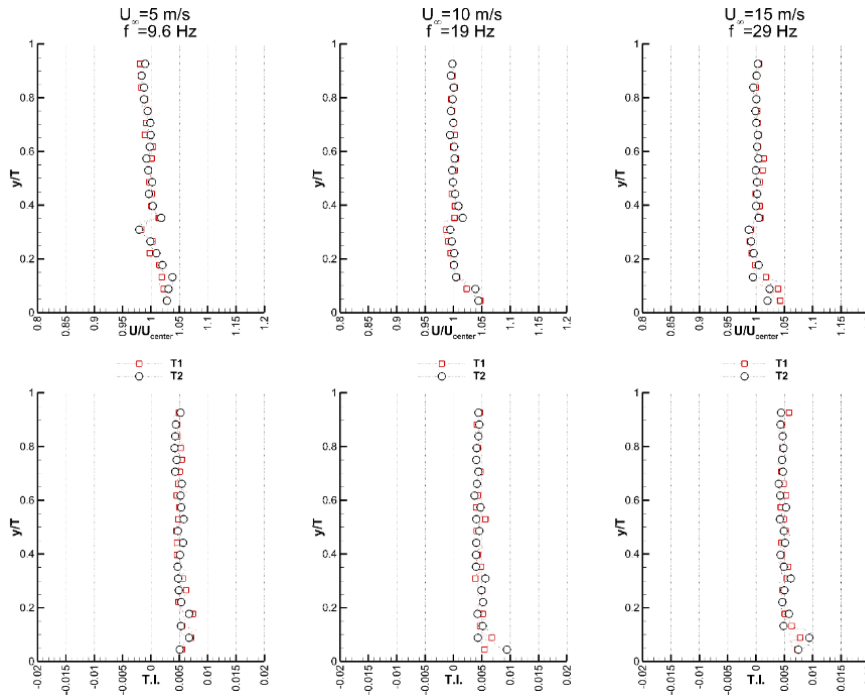
Figure 2-3 Test section characterization at three different inlet velocities.

A picture of the tunnel and traversing unit for HWA is shown in Figure 2-4. For the rest of the measurements, the frequency of the electric motor is kept at 19.3 Hz.

Figure 2-4 Open loop suction type wind tunnel and traversing unit at the top of the test section to measure the incoming flow using HWA.

2.2 Turbulence-generating Grids

Four mono-plane turbulence-generating grids (TGG's) made of 4 mm thick Plexiglas, are installed 100 mm downstream of the entrance of the test section. Grids are cut in a CO_2 glass tube type Laser cutting machine with a resolution of 0.5 mm. The Laser cutting machine is shown in Figure 2-5.

Figure 2-5 Laser cutting machine.

Grids are covered with black spray paint to avoid laser light reflections. The first grid is of a conventional type with regular repeating square holes (denoted as CSG standing for the classical square grid). Other grids are of three different fractal patterns; I-type, Square, and Circular (denoted as FIG, FSG, and FCG respectively). These grids are shown in Figure 2-6. Various parameters required to define grid geometry are summarized in Table 2-1.

Table 2-1 Parameters defining conventional and fractal grids geometry.

GRID	S	N	D_f	t_{min} (mm)	t_r	R_t	$\dfrac{L_0}{T}$	R_L	M_{eff} (mm)	σ (%)
CSG	2	1	2	2.10	1.0	1.00	≈ 0.06	0.5	20.0	20.0
FIG	3	4	2	2.00	8.5	0.49	≈ 0.53	0.5	25.34	29.4
FSG	4	4	2	1.20	8.5	0.49	≈ 0.53	0.5	19.76	23.7
FCG	N/A	4	2	1.20	8.5	0.49	≈ 0.73	0.5	20.43	24.6

The pattern type is embedded in the parameter (S) which is the number of rectangular bars in each pattern. Since there is no rectangular element in FCG, the value of S

cannot be defined for this grid. (N) is the number of fractal iterations, and (D_f) – the fractal dimension – is defined as in [22],

$$D_f = \frac{\log B}{\log \frac{1}{R_L}} \tag{2.1}$$

where (B) is the number of patterns at each iteration and (R_L) is the length ratio of each element (bar) at each successive iteration. Fractal dimension is the scaling exponent that characterizes the fractal perimeter. For FCG, this length is considered to be the mean diameter of each circle.

All grids are designed to have the largest possible value for D_f to maximize flow homogeneity [22]. For this purpose, R_L and B in equation (2.1), are fixed to 0.5 and 4.0 respectively. Grids with a maximum value of D_f (i.e. 2.0) are called *'space-filling'* grids [22]. Other parameters listed in the table are as follows:

- Minimum thickness (t_{min}) which is the "spanwise" thickness of the smallest element and is shown in Figure 2-6;
- Thickness ratio (t_r) which is the ratio between the thickness of the thickest bar and of the thinnest bar. Note that minimum thickness is adjusted to maintain the same value of t_r for all fractal grids. The thickness ratio for the fractal grids was fixed at 8.5. In [22], different values of t_r were investigated for different grid types involving 2.5, 5.0, 8.5, 13.0, and 17.0. Although the value of 8.5 for t_r, was not very high compared to previous studies, there are evidences that this value is also acceptable (see for example [52], [14], [50]).
- Maximum bar length (diameter for FCG) is denoted as L_0 (displayed in Figure 2-6) and its ratio to the test section width ($\frac{L_0}{T}$) is given in Table 2-1. For CSG, L_0 is considered equal to its mesh size.
- Parameter R_L refers to the ratio of bar lengths in one iteration which is kept constant for all the grids as 0.5 (i.e., in one iteration the length of bars – or the diameter of a circle in FCG – becomes half).

It is worth to note that conventional grids can be considered as a special case of fractal grids where S=2, $R_L = 0.5$, $D_f = 2$ and $t_r = 1$. [22]. According to [22], minimum

17

four parameters are required to define a complete fractal grid geometry, provided that (S) – i.e. Fractal pattern – is known. In this study T, N, t_{min}, t_r, and D_f are chosen as the geometry defining parameters.
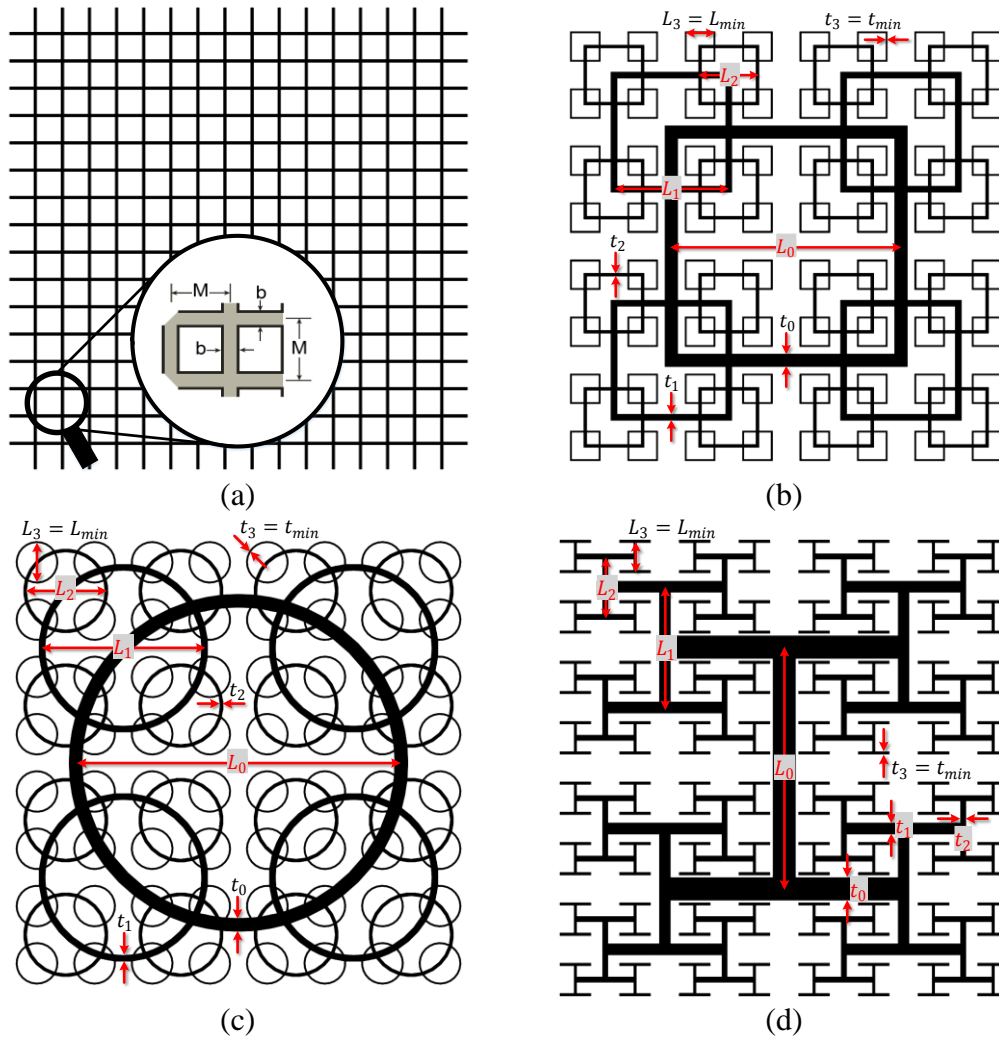
Figure 2-6 Bar lengths and thicknesses in (a) CSG, (b) FSG, (c) FCG, and (d) FIG.

- The mesh size for a conventional grid is the repeating pattern size (center-to-center bar spacing) as illustrated in Figure 2-6.

It is obvious that common definition of mesh size cannot be applied to fractal grids as they have multiple bars with different sizes placed at different distances. Instead, the "*effective mesh size*" is defined as,

$$M_{eff} = \frac{4T^2}{P}\sqrt{1-\sigma} \tag{2.2}$$

18

where P is the fractal perimeter's length, i.e., the total length of the grid when it is stripped of its thickness [22]. The highest value of M_{eff} – for FIG – is still smaller than 10% of the test section height (or width) which is a common practice in turbulence generating grids [94].

- Solidity – or blockage ratio – (σ) is the ratio of solid area to the total area covered by the grid (T^2). It was tried to keep σ similar for all grids to maintain the same drag coefficient. In the case of the conventional grid, it is easy to derive the solidity as a function of bar width (b) and mesh size (M),

$$\sigma = \frac{b}{M}\left(2 - \frac{b}{M}\right) \tag{2.3}$$

For fractal I and square grids this formula is more complex,

$$\sigma = \frac{L_0 t_0 \sum_{j=0}^{N-1} 4^{j+1} R_L^j R_t^j - t_0^2 \sum_{j=1}^{N-1} 2^{2j+1} R_t^{2j-1}}{T^2} \tag{2.4}$$

where $t_0 = t_r.t_{min}$ is the bar thickness of the largest iteration and $R_t = \sqrt[1-N]{t_r}$ refers to the ratio of bar thickness in one iteration (i.e. $t_j = R_t^j.t_0$). The same holds for the length of the bars (i.e. $L_j = R_L^j.L_0$) [22]. Another representation for (2.4) which is taken from [22] is,

$$\sigma = \frac{SL_0 t_0}{T^2} \sum_{j=0}^{N-1} (BR_L R_t)^j = \frac{SL_0 t_0}{T^2} \frac{1 - (BR_L R_t)^N}{1 - BR_L R_t} \tag{2.5}$$

For the fractal circular grid, a straightforward formula like (2.4) could not be obtained. Instead, areas of each iteration are calculated separately and summed up to calculate the solidity. This was also performed for the perimeter of all four iterations to be included in the effective mesh size calculation. The perimeter and area of a 4-iteration circular grid can be estimated by,

$$P_{FCG} = 2\pi D_0 \left(1 - 2.844 R_D^3 + \sum_{j=1}^{N-1} 4^j R_D^j \right)$$
$$- 4t_0 (79 R_t^3 + 72 R_t^2 + 45 R_t + 20) \tag{2.6}$$
$$= 2\pi D_0 \left(1 - 2.844 R_D^3 + \frac{(4R_D)[1 - (4R_D)^{N-1}]}{1 - 4R_D} \right)$$
$$- 4t_0 (79 R_t^3 + 72 R_t^2 + 45 R_t + 20)$$

$$A_{FCG} = \left[\pi D_0 t_0 \sum_{j=0}^{N-1} (N R_L R_t)^j \right]$$
$$- 2^{N-1} t_0^2 R_t \left[1 + R_t + \left(1.117 \frac{D_0}{t_0} R_L^3 + 6 \right) R_t^2 \right.$$
$$\left. + 8 R_t^3 + 15 R_t^4 \right]$$
$$= \left[\pi D_0 t_0 \frac{1 - (N R_L R_t)^N}{1 - N R_L R_t} \right] \tag{2.7}$$
$$- 2^{N-1} t_0^2 R_t \left[1 + R_t + \left(1.117 \frac{D_0}{t_0} R_L^3 + 6 \right) R_t^2 \right.$$
$$\left. + 8 R_t^3 + 15 R_t^4 \right]$$

where $R_D = R_L$ to be consistent with circular pattern notation. The estimated error in perimeter and area was $\leq 3.0\%$ and $\leq 0.6\%$, respectively. The blockage ratio for CSG, FSG, and FCG is below than 25% while for I grid, due to cutting restrictions, this value is about 29%. Nevertheless, the solidity ratio is kept well below the critical solidity above which the homogeneity cannot be satisfied. This will be discussed in more details in chapter 3. In addition to that, the value of solidities for the grids used in previous experiments is in the same order; see for example [17,22,51–53,72].

In addition to what is defined above, it is required to use more parameters to compare the results with the literature. One important parameter which is defined by Mazellier and Vassilicos [52] is the wake-interaction length scale, and the distance turbulence intensity reaches its peak denoted by x_* and x_{peak}, respectively.

$$x_* = \frac{L_0^2}{t_0} \tag{2.8}$$

$$x_{peak} \approx 0.45 x_* \tag{2.9}$$

A regular square grid is made of equally spaced bars with equal thicknesses (width). Therefore, the wakes from the neighboring bars meet at the same distance from the grid which scales as,

$$x_* = \frac{M^2}{b} \tag{2.10}$$

where M and b are the mesh size and bar width for the regular grid, respectively as defined in Equation (2.3). Equation (2.10) is obtained using the wake growth relation, i.e., the wakes grow with downstream distance (x) as [52],

$$y_{wake} \sim \sqrt{bx} \tag{2.11}$$

and two neighboring wakes meet where $x = x_*$ and $y_{wake} = M$.

For the fractal grids, there is no unique distance since there are different bar widths as well as bar lengths. However, the distance obtained from the largest bar length and width using Equation (2.8) includes the other interaction distances due to smaller iterations. So one can expect increased turbulence where the largest interaction happens [37]. A schematic for wake interactions from a four iteration fractal square grid is shown in Figure 2-7. Since these values are determined by the geometric characteristics of the grids and test section, an estimation of those for our grids are presented in Table 2-2. From the values of x_{peak} in this table, one can understand that this study is carried out in the *"very near wake"* region of fractal grids.

Another estimation of turbulence intensity peak point is from Hurst and Vassilicos [22], and we call this as $x_{peak_{HV}}$:

$$x_{peak_{HV}} \approx 75 \frac{t_{min}}{L_{min}} T \tag{2.12}$$

However, the peak of turbulence intensity along the centerline of CSG should be captured since it is still inside the current measurement region.

21
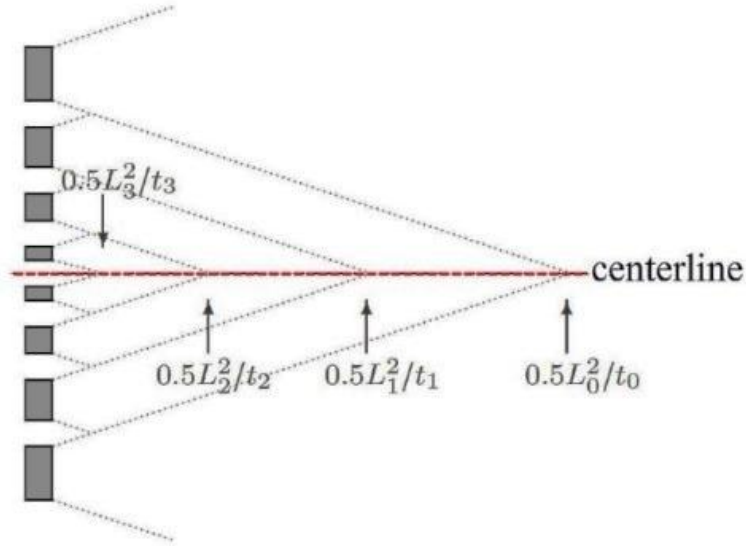
Figure 2-7 Schematic of wake interactions in a four-iteration fractal grid [52].

A set of space-filling ($D_f = 2.0$) fractal square grids with different thickness ratios and a conventional grid were studied by Mazellier and Vassilicos [52] (hereafter denoted by MV(2010)), among which SFG8 grid is very similar to FSG in the current study. SRG grid in [52] is also comparable to our CSG grid. Details of these grids are given in Table 2-3.

Table 2-2 Wake interaction length scale and the peak of turbulence intensity for various grids; x_{peak} values are obtained according to [17] and [32].

Grid	Symbol	t_{min} (mm)	L_{min} (mm)	t_0 (mm)	L_0 (mm)	M_{eff} (mm)	x_* (mm)	$x_{peak_{HV}}$ (mm) [22]	x_{peak} (mm) [52]
CSG	+	2.11	2.11	2.11	20.0	20.0	$\cong 189$	-	$\cong 85$
FIG	I	2.0	22.5	17.0	180.2	25.34	$\cong 1910$	N/A	N/A
FSG	◻	1.2	22.58	10.2	180.7	19.76	$\cong 3201$	$\cong 1355$	$\cong 1440$
FCG	O	1.2	31.1	10.2	249	20.43	$\cong 6078$	$\cong 984$	$\cong 2735$

22

Table 2-3 Comparison between similar previous studies and the current study.

	Ref. [52] MV(2010)		Ref. [18] GK(2016)	Ref. [35] V(2011)		Ref. [40] Disc(2013)		Current study	
Grid	SFG8	Conv (SRG)	CONV	SFG	Conv (RG)	FSG (t_r=13)	FSG (t_r=17)	FSG	CSG
T (mm)	460		900×500	460		154		340	
L_{TS} (mm)	9100		8000	9100		1500		1000	
N	4	1	1	4	1	4	4	4	1
D_f	2	2	2	2	2	2	2	2	2
σ	0.25	0.34	0.44	0.25	0.32	0.34	0.32	0.237	0.2
R_L	0.5		1	0.5	1			0.5	1
R_t	≅ 0.49	1	1	0.39	1			≅ 0.49	1
t_r	≅ 8.5	1	1	17	1	13	17	8.5	1
M_{eff} (mm)	26.4	32	37.5	26.2	60	15.3	15.7	19.76	20.00
x_* (mm)	≅ 3972	≅ 171	≅ 150	2945	360	804	748	≅ 3201	≅ 189
L_0(mm)	237.5	32	37.5	237.8	60	80.8	80.3	180.69	20.0
L_1(mm)	118.8	-	-	118.9	-			90.34	-
L_2(mm)	59.4	-	-	59.45	-			45.17	-
L_3(mm)	29.7	-	-	29.72	-	10.1	10.0	22.58	-
t_0(mm)	14.2	6	9.4	19.2	10	8.12	8.62	10.2	2.11
t_1(mm)	6.9	-	-	7.46	-			4.99	-
t_2(mm)	3.4	-	-	2.9	-			2.45	-
t_3(mm)	1.7	-	-	1.129	-	0.62	0.5	1.2	-
U_0 (ms^{-1})	5.2, 10, 15		0.5 ± 0.02	10, 15	10, 15, 20	3.5, 11.5		10.2376	
Re_{Meff}	≅ 9080 ≅ 17470 ≅ 26200	≅ 11000 ≅ 21170 ≅ 31760	18750 ± 750					11885	12064
Re_{L_0}	81680-235700	11000-31760						108680	12064
Re_{t_0}	4880-14090	2060-5950						6153	1273
Re_λ	[140-370]		840[1]					[90-260]	[50-200]
$\Delta x/x_*$	[0.06-17300]	[53-560]				[0.45-0.75]		[0.0025-0.139]	[0.1-2.38]
$\Delta x/M_{eff}$	[10-115]	[10-105]				[21.4-35.7]		[0.4-22.5]	[1-22.5]

2.3 Particle Image Velocimetry Measurements

Two-dimensional particle image velocimetry (2-D PIV) is carried out in the near-field of four types of turbulence-generating-grids. DynamicStudio® commercial software is used to record the data and analyzing afterward. Details of 2-D PIV components, as

---

[1] Measured at $x \approx 1M$ where Turbulence intensity is maximum.

well as the analysis method, are listed in Table 2-4. The components of the 2-D PIV experiment are discussed in the next section.

2.3.1   Measurement procedure

Shown in Figure 2-8, is emitted a 532 nm (green light) beam from the Laser head. Using Mirror 1, this beam is reflected upwards (+Z direction) to the desired height. The beam is then directed in +Y direction into a set of spherical and cylindrical lenses, using Mirror 2. The first lens makes the beam focused on the measurement region while the second one turns it into a laser sheet. The first illuminated plane, which is shown in Figure 2-8, is at the center of the test section, i.e., the XY plane (Z=0), just behind the grid. The calibration image is taken at this position so that a PIV field of $128 \times 204 \ mm^2$ (in X and Y directions, respectively) is obtained. The whole optical system (mirrors and lenses) and the camera stays on a 3-axis ISEL heavy-duty traverse system and all but the Mirror 1 are fixed onto the Z arm as shown in Figure 2-8.
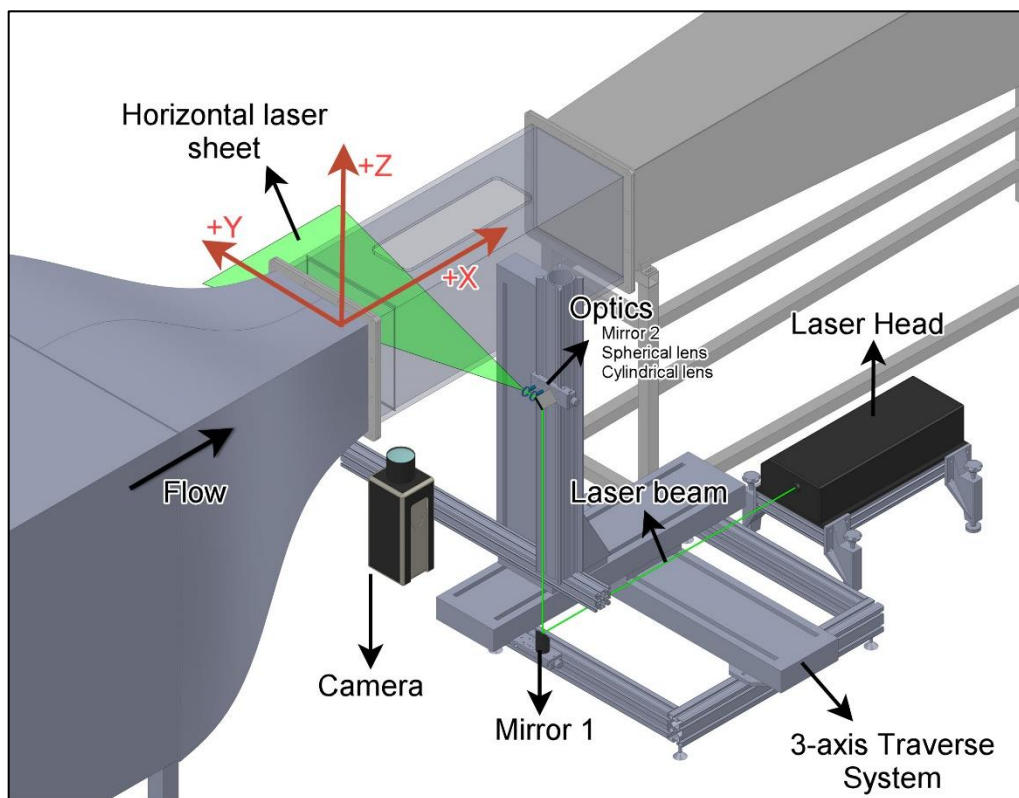
Figure 2-8 . 2-D PIV horizontal configuration.

Table 2-4 2-D PIV experimental parameters.

Seeding	Type	Olive oil
	Nominal diameter	$\approx 1\mu m$
	Specific gravity (at 15°C)	0.91
	Refractive index [95]	1.5
	Seeding generator	six-jet oil droplet generator utilizing Laskin nozzle
Laser Sheet	Laser type	Nd: YAG
	Manufacturer	New Wave research
	Model	Solo 120XT
	Maximum Energy	120 mJ/pulse
	Wavelength	532 nm
	Thickness	$\approx 2mm$
	Repetition rate	21 Hz
Optics	Mirrors	Dielectric Mirror, 532 nm
	Spherical Lens	Plano-convex, 500mm FL
	Cylindrical Lens	Plano-concave, -6.4mm FL
Camera	Sensor type	CMOS
	Sensor resolution	2560×1600 pixel^2
	Sensor size	25.6×16.0 mm^2
	Pixel pitch (size)	$10~\mu m$
	Depth	12 bit
	Repetition rate	1400 fps @ Full resolution 2500 fps @ 1920×1080
	Internal memory buffer	16 GB
Camera Lens	Manufacturer	Nikon
	focal length	60 mm
	f#	2.8
Imaging	Image magnification	0.125
	Field of view (FOV)	$128 \times 204~mm^2$
	Camera-object distance	540 mm
	Time between pulses (Δt)	$50~\mu s$
PIV analysis	Correlation method	Cross-correlation
	Interrogation area (IA)	32×32 pixel^2
	Overlap between IAs	50%
	Post-processing	Moving average validation 3×3 neighborhood
	Vector spacing	$\approx 1.28~mm$

Therefore, the distance from the camera to the object (Laser light sheet) is not changing while traversing along the vertical direction and is always equal to 540mm. Thus, the magnification factor of the image is always fixed and equal to 0.125.

Olive oil particles are uniformly seeded into the flow from the tunnel inlet. Oil particles with $1\mu m$ diameter are generated using a six-jet oil droplet generator which utilizes a Laskin nozzle. Pressurized air atomizes oil in the generator reservoir to produce the droplets. The Reynolds number based on the effective mesh size, $Re_{M_{eff}} = \frac{U_0 M_{eff}}{\nu_{air}}$, for CSG, FSG, and FCG is about 12000 while it is about 15000 for FIG. U_0 is the free stream mean velocity at the grid position when the test section is empty. U_0 was measured using a single hot-wire probe, prior to the PIV experiments. The wire has a $5\,\mu m$ diameter and $1.25\,mm$ sensor length. ν_{air} is the kinematic viscosity of the air at the time of the experiments. 1003 image pairs are recorded with the time delay of $50\,\mu s$ between each two pulses. This provides a good convergence of turbulence statistics. The images are transferred to PC, and the traverse is moved to the next vertical position (+5mm in the Z direction). 35 horizontal planes are recorded this way to cover the upper half of the test section. The streamwise location is marked as window 1 (see Figure 2-9).
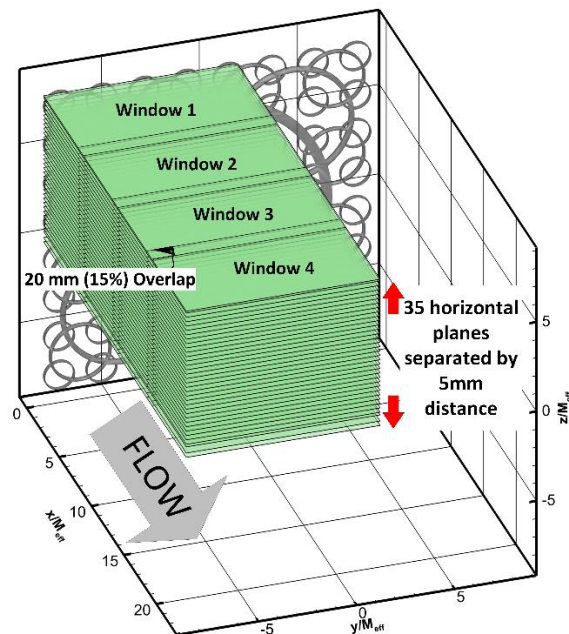
Figure 2-9 Horizontal planes captured by 2-D PIV.

The traverse is then moved to the second streamwise position – marked as window 2 – which is 108mm downstream of the first one. Two more stations in the x-direction are captured, and the overlap between neighboring windows is 20mm corresponding to 14 to 15 processed vectors. These Four window positions are schematically shown in Figure 2-9. At the end of the measurements, there exist 140 PIV windows, each having 1003 image pairs, for each grid.

Measurements are carried out in the region $0 < x < 445\ mm$, $-168 < y < 34\ mm$, and $0 < z < 168\ mm$, corresponding to $0 < \frac{x}{T} < 1.308$, $-0.495 < \frac{y}{T} < 0.1$, and $0 < \frac{z}{T} < 0.495$, respectively. Since the effective mesh size for each grid is different than the other, these values are normalized by the corresponding mesh size and listed in Table 2-5. The cross section of the measurement volume for each grid is shown in Figure 2-10.
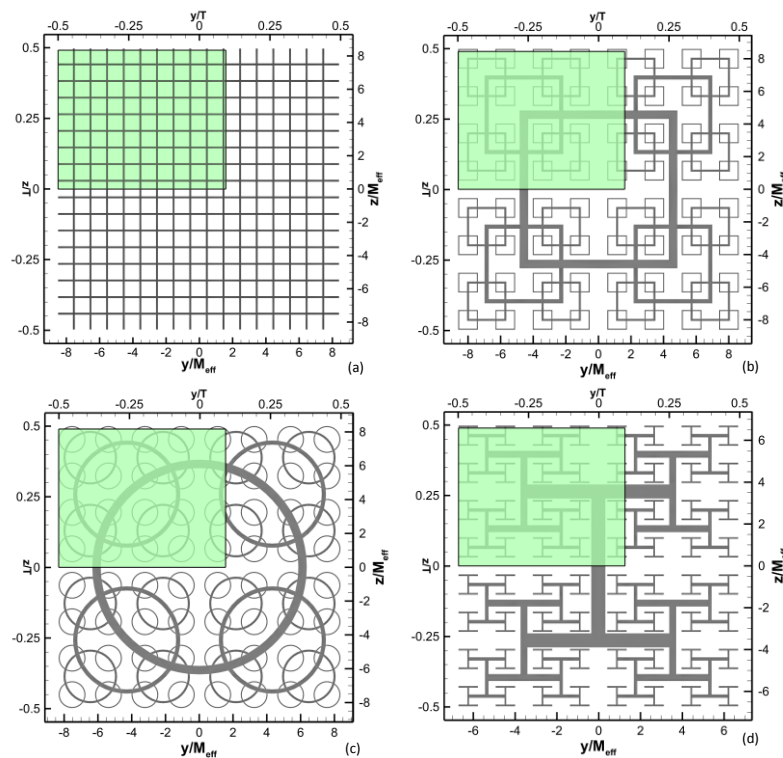
Figure 2-10 The cross-section of the whole measurement volume in CSG (a), FSG (b), FCG (c), and FIG (d).

Table 2-5 Measurement volume normalized by effective mesh size for each grid.

Grid	$\dfrac{x}{M_{eff}}$	$\dfrac{y}{M_{eff}}$	$\dfrac{z}{M_{eff}}$
CSG	[0,22.25]	[−8.40,1.70]	[0,8.40]
FSG	[0,22.52]	[−8.50,1.72]	[0,8.50]
FCG	[0,21.78]	[−8.22,1.66]	[0,8.22]
FIG	[0,17.56]	[−6.63,1.34]	[0,6.63]

2.3.2 Data analysis

PIV Image analysis is carried out in DynamicStudio software. A pre-processing is applied to raw images in order to enhance the contrast and reduce the background noise. It is followed by cross-correlation between each two image pair with interrogation window size of $32 \times 32 \, \text{pixel}^2$. Using a 50% overlap for the interrogation windows results in a resolved field of view of about $128 \times 204 \, mm^2$ with a vector resolution of about 1.28 mm, i.e., 99×159 vectors. The vector spacing is comparable to the smallest bar thickness according to Table 2-3, however, it is not enough to resolve the wakes of the small iterations. As for post-processing, moving average validation on the resultant vector maps in a 3x3 neighborhood is applied. The instantaneous flow fields (x, y, U, and V) were exported as data files for further analysis using MATLAB and Tecplot.

2.4 Uncertainties

A typical PIV algorithm has its particular uncertainty in obtaining the instantaneous velocity field, and this uncertainty propagates into statistical quantities which are derived from the instantaneous velocity field [96]. As stated in [97], roughly 90% of the total uncertainty in 2-D-PIV comes from the determination of the displacement in pixels from raw images and the remainder 10% is due to camera calibration. There is a minor and negligible uncertainty on the time interval between the two laser pulses. Since the current measurements were carried out using 2-D PIV technique, the out-of-plane velocity is not accessible, and thus, the contribution of that to bias errors cannot be quantified.

However, with a light sheet thickness of 2mm, no significant errors were expected from the out-of-plane motion. Since the camera pixel size ($10\ \mu m$) is larger than the averaged particle diameter ($\sim 1\ \mu m$) the present data set is not affected by peak locking which is a major source of systematic (bias) errors in PIV [95].

A typical PIV algorithm finds peaks and evaluates the displacement shift. In many experimental studies, a displacement uncertainty of 0.05-0.1 pixel is reported [97]. The uncertainty on the instantaneous velocity field is obtained based on the particle disparity method [98] and peak height ratio method [99]. Both methods were carried out on one randomly chosen instantaneous vector map in each measured window of each grid. The maximum uncertainty in the instantaneous velocity is calculated about 0.1 pixel which is in agreement with typical values in the literature [18]. As the measurement of velocity in the presence of large velocity gradient is affected by larger uncertainty [100], the values are calculated specifically in regions with large velocity gradients (e.g., a shear layer in the jet-wake combination) rather than to be averaged on the whole window.

The uncertainty in turbulent statistics depends on the quantity of interest. Using a 95% confidence level, the uncertainty in averaged velocity $\langle U \rangle$ is estimated to be,

$$\mathrm{U}_{\langle U \rangle} = \pm 1.96 \frac{\sigma_U}{\sqrt{n}} \tag{2.13}$$

where σ_U is the standard deviation of U and n is the number of finite samples [18]. The uncertainty in mean velocities $\langle U \rangle$ and $\langle V \rangle$ is estimated where the fluctuations are the highest levels.

For the normal components of the Reynolds stress tensor, the uncertainty is computed with [96],

$$\mathrm{U}_{\langle u^2 \rangle} = \langle u^2 \rangle \sqrt{\frac{2}{n}} = \sigma_U^2 \sqrt{\frac{2}{n}} \tag{2.14}$$

Uncertainty in turbulent kinetic energy can be determined by [96],

$$\mathrm{U}_{\langle TKE \rangle} = \sqrt{\langle u^2 \rangle^2 + \langle v^2 \rangle^2 + \langle w^2 \rangle^2} \sqrt{\frac{1}{2n}} \tag{2.15}$$

29

with the assumption of diagonal symmetry ($\langle ww \rangle = \langle vv \rangle$),

$$\text{Ʊ}_{\langle TKE \rangle} = \sqrt{\sigma_U{}^4 + 2\sigma_v{}^4}\sqrt{\frac{1}{2\boldsymbol{n}}} \tag{2.16}$$

The values are listed in Table 2-6 for selected high fluctuating regions in the flow field of each grid.

Table 2-6 Uncertainty in statistical quantities. Points are sampled at a high fluctuating region inside the wake of bars.

Grid	Window	Elevation $(\frac{z}{M_{eff}})$	Selected point [x,y] (mm) {x,y} (grid)	TI_u	Uncertainty (%)			
					$\langle U \rangle$	$\langle V \rangle$	$\langle u^2 \rangle$	$\langle v^2 \rangle$
CSG	1	0	[19,-30] - {10,107}	22%	8.7%	10%	8.8%	11%
FSG	1	0	[25,-92] - {15,61}	46%	7%	4%	7%	2%
FCG	1	0	[89,-125] - {70,35}	52%	11%	17%	15%	34%
FIG	1	0	[100,0] - {79,133}	60%	9%	10%	11%	12%

CHAPTER 3

RESULTS AND DISCUSSION

This chapter consists of four sections. In the first section, the process of reconstruction of the three-dimensional mean flow field through symmetry is explained. In the second section, the mean flow characteristics of TGG's in the near-field region are analyzed, and turbulent mixing is quantified. Third section concerns mean turbulent kinetic energy (TKE) and estimation of its dissipation and production rates. In the last section length scales in the near-field of TGG's being investigated.

3.1   General aspects

3.1.1   Instantaneous velocity field

An example of instantaneous velocity map for CSG is shown in Figure 3-1. This image belongs to the centerline ($z/M_{eff} = 0$) data in the vicinity of the grid (Window 1 in Figure 2-9). Square region on the instantaneous velocity field is zoomed in at the right of Figure 3-1 involving streamwise velocity vectors while the mean velocity is subtracted. The wakes of two individual bars at the top and bottom are clearly seen and Coherent structures can be distinguished. Instantaneous velocity fields are employed to calculate some flow properties like Reynolds stress tensor, dissipation and production rates, length scales, etc. while the combination of ensemble averaged of these instantaneous fields would result in a three-dimensional like mean data in the near-field of TGG's.
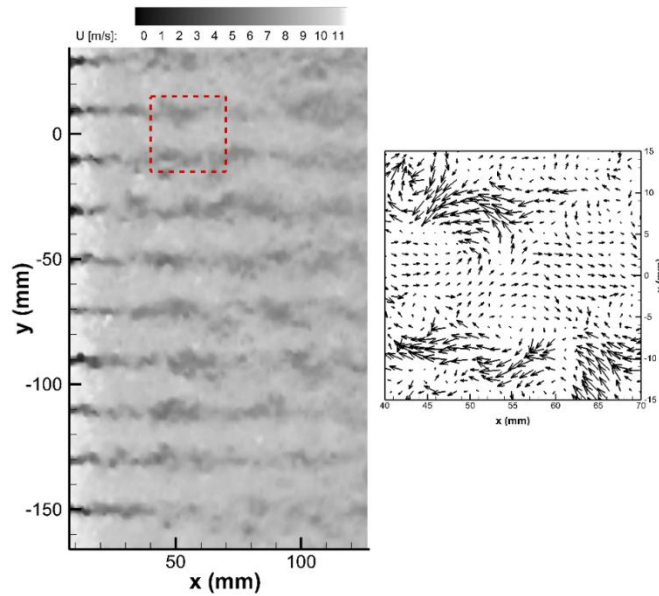
Figure 3-1 Sample map of instantaneous streamwise velocity U as obtained from 2-D PIV for CSG at Z=0 (left). Y=0 represents the test section and grid centerline. Zoomed-in region of a jet-wake interaction (right) with vectors of the magnitude of "$U - \langle U \rangle$".

3.1.2   Diagonal Symmetry

Looking at the geometry of CSG, FSG, and FCG (Figure 2-6) one can notice a diagonal symmetry. In other words, the ensemble-averaged airflow is expected to hold a 90-degree rotational symmetry about the test section centerline (X-axis), keeping in mind that this is not valid for the fractal I-grid. It is also important to note that this assumption is only valid if the incoming flow is inherently uniform. Effects of non-uniformities existing in the test section inlet – shown in the characterization plot of Figure 2-3 – on the symmetry of the downstream mean flow are inevitable. The assumption of conventional grid generated turbulent averaged-flow to be diagonally symmetric is fair according to the literature [3]. This has been validated for the fractal cross and square grids ([39][46]). However, the diagonal symmetry feature of the flow is validated by comparing mean and rms velocities and Reynolds stress components on some horizontal planes to those on corresponding vertical planes. A vertical laser sheet is configured as shown in Figure 3-2. All specifications for 2-D vertical planes are kept the same as in horizontal configuration. Only downstream windows next to the grids are captured.

32
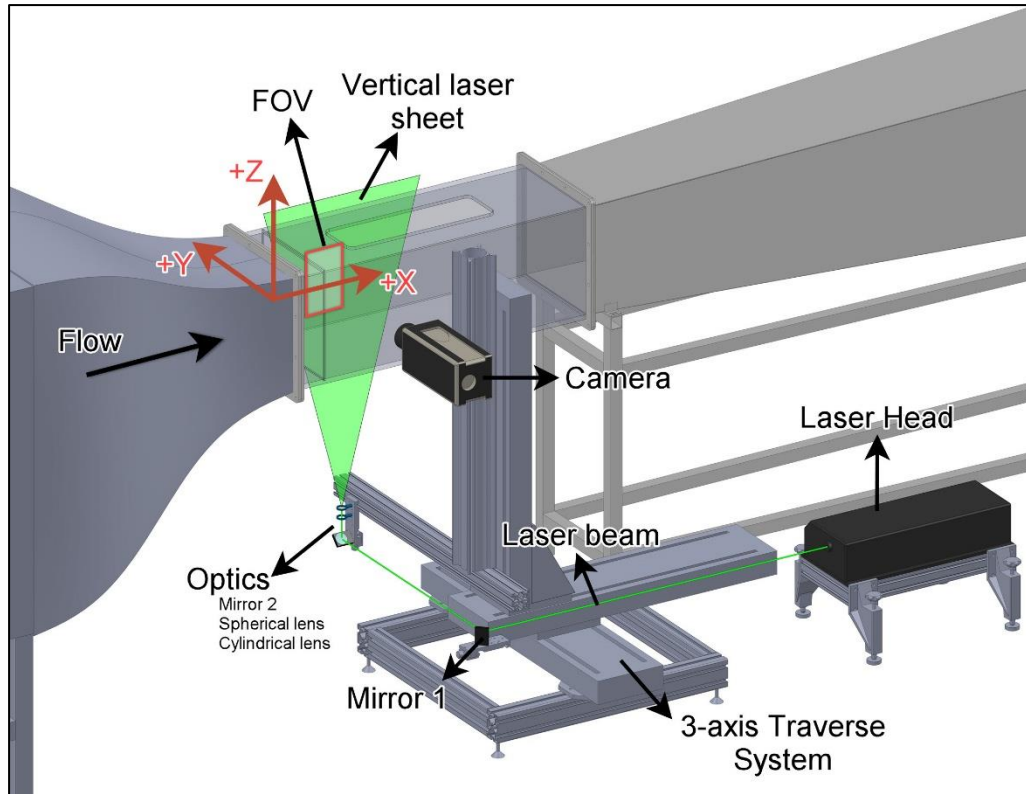
Figure 3-2 Vertical Laser sheet configuration.

Sample vertical windows and corresponding horizontal ones are shown in Figure 3-3 with contours of the mean streamwise velocity $\langle U \rangle$. Here, $\langle \ \rangle$ denotes the ensemble average and is used interchangeably with ($\overline{\ \ }$). FIG vertical planes are also shown in order to compare the available mean velocity components ($\langle U \rangle$ and $\langle V \rangle$) to those in the volumetric data later in this section. Exact position of the planes are listed in Table 3-1.

According to the literature [39] and based on our analysis, the diagonal symmetry in the flow can be shown by comparing mean velocities, mean vorticity, and components of the Reynolds stress tensor. To understand the diagonal symmetry in the flow and check the validity of our hypothesis in the case of symmetrical grids, directly measured vertical planes (a' to e' in Figure 3-3) were compared to the corresponding rotated planes, i.e., those planes resulted from rotating horizontal ones (a to e in Figure 3-3). Furthermore, after generating volumetric data, profiles of transverse rms velocities can be examined to check whether they are in line with literature or not [39]. As an example of this comparison, a contour plot of the mean vorticity component in the

33

spanwise direction ($\overline{\Omega_y}$) for FSG is shown in Figure 3-4. The window is the middle vertical one (a' in Figure 3-3-C). Data is extracted along a vertical line at $x = 3\ M_{eff}$.

Table 3-1 Position of the horizontal and vertical planes for CSG, FSG, FCG, and FIG.

Grid	Horizontal plane		Corresponding vertical plane		Grid	Horizontal plane		vertical plane	
	Label	Position (z/M_{eff})	Label	Position (y/M_{eff})		Label	Position (z/M_{eff})	Label	Position (y/M_{eff})
CSG	a	0	a'	0	FIG	a	0	f	0
	b	2	b'	-2		b	1.578	g	-1.578
	c	4	c'	-4		c	3.157	h	-3.157
	d	6	d'	-6		d	4.735	i	-4.735
	e	8	e'	-8		e	6.314	j	-6.314
FSG	a	0	a'	0					
	b	2.024	b'	-2.024					
	c	4.048	c'	-4.048					
	d	6.072	d'	-6.072					
	e	8.097	e'	-8.097					
FCG	a	0	a'	0					
	b	1.958	b'	-1.958					
	c	3.915	c'	-3.915					
	d	5.873	d'	-5.873					
	e	7.831	e'	-7.831					

This is somewhere within the wake of the largest horizontal bar (upper horizontal bar in Figure 3-3-C at around $z = 5\ M_{eff}$) and the mean streamwise velocity profile along this line is plotted on the contours. In Figure 3-4, (a) represents the vertical window that was originally measured while in (b) the result of 90 degree rotation of the original horizontal window at Z=0 is shown. The former is marked as "Measured" in the plots to the right while the latter is marked as "Rotated" there. The mean vorticity fields on (a) and (b) are in a good agreement as it is shown in Figure 3-4, and the profiles of mean streamwise velocity are almost identical (c), while there is a small difference in the upper half of the wake for the vertical mean velocity component (d). This similarity is still visible in available Reynolds stress components (e and f).

As another example, the diagonal symmetry is investigated in CSG. The mean transverse vorticity field $\overline{\Omega_y}$, in the vertical plane marked by (a') in Figure 3-3-a is represented in Figure 3-5-a. The corresponding vertical window obtained by rotating the Z=0 plane (plane a in Figure 3-3-a) is also shown in Figure 3-5-b.
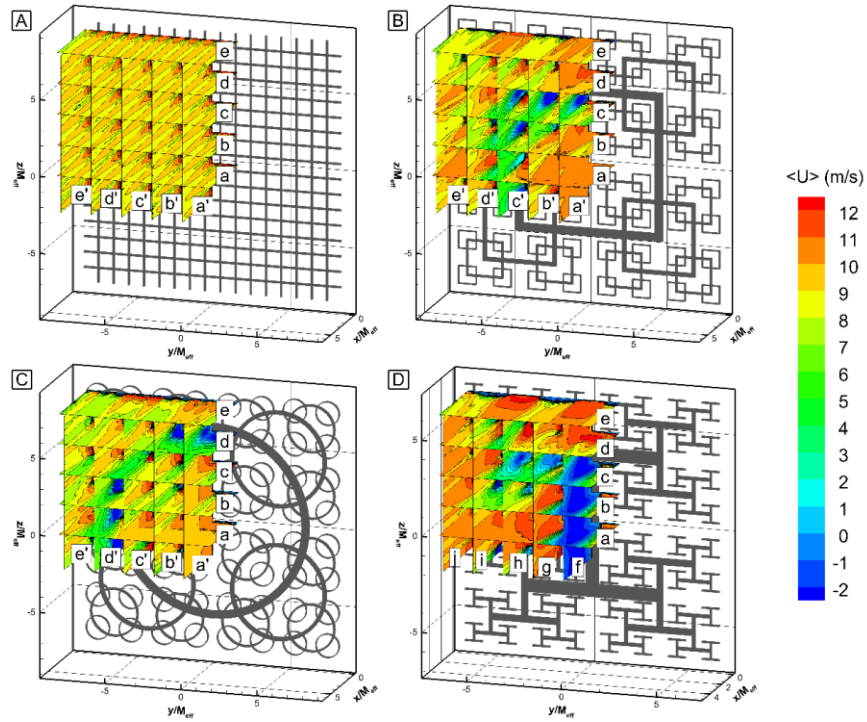
Figure 3-3 Measured horizontal and corresponding vertical planes of 2-D PIV for (A) CSG, (B) FSG, and (C) FCG; Measured horizontal and vertical planes for FIG (D).
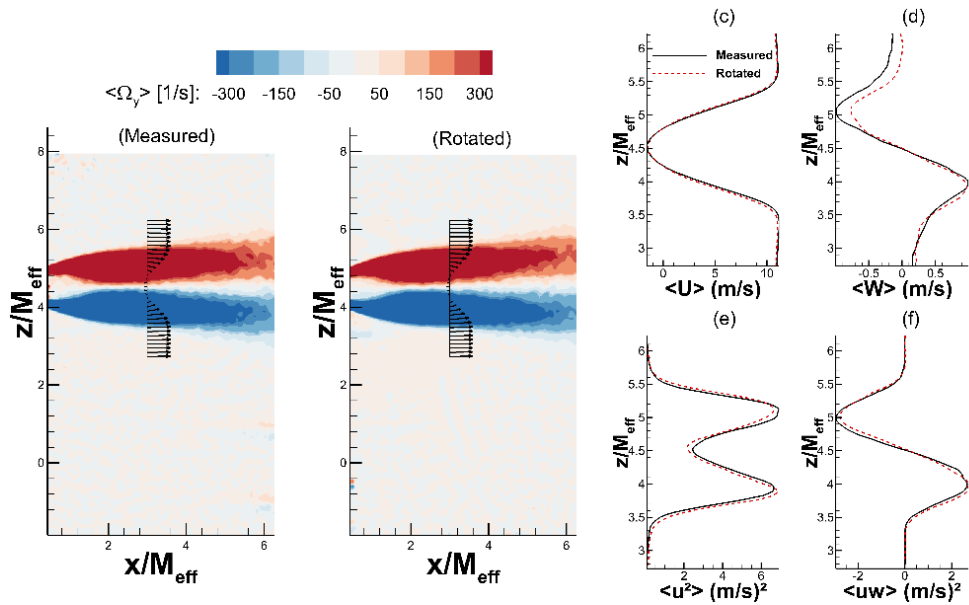
Figure 3-4 Plots of mean transverse vorticity on (a) measured vertical window(Y=0), (b) corresponding vertical window obtained by rotating the (Z=0) window in FSG, (c) to (f) represent profiles of mean streamwise and vertical velocities and Reynolds stress components extracted along a line cutting the wake of a bar. The solid line is the originally measured data, and the dashed line is the rotated data. The vertical extracted line is shown in both (a) and (b).
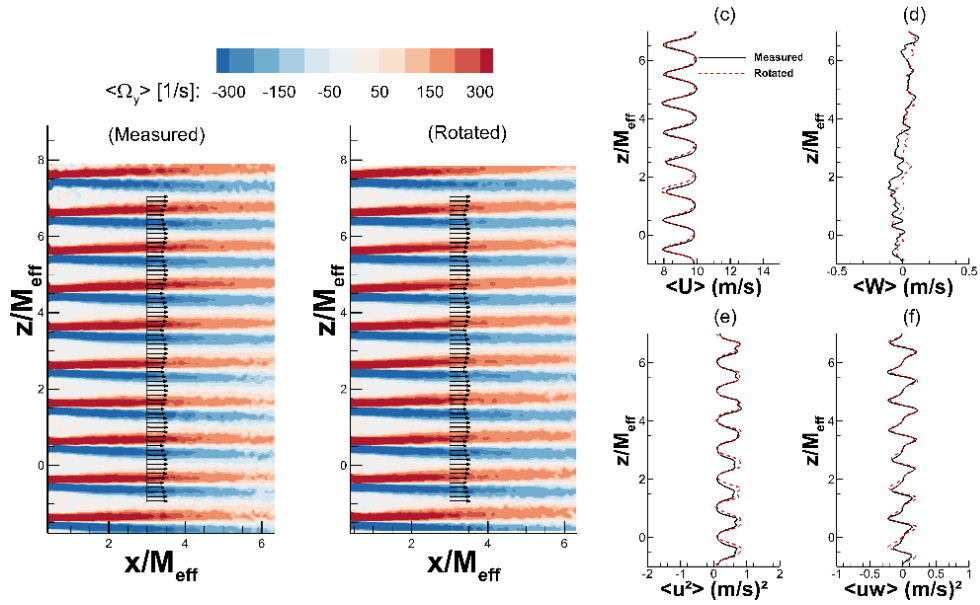
Figure 3-5 Plots of mean transverse vorticity on (a) measured vertical window(Y=0), (b) corresponding vertical window obtained by rotating the (Z=0) window in CSG, (c) to (f) represent profiles of mean streamwise and vertical velocities and Reynolds stress components extracted along a line passing consecutive wakes and jets formed by bars and holes. The solid line is the originally measured data, and the dashed line is the rotated data. The vertical extracted line is shown in both (a) and (b).

Again the whole vorticity fields seem to show similar behavior, and the profiles of mean velocities and Reynolds stresses on the right of Figure 3-5 prove this claim. The profiles are extracted along a vertical line at $x/M_{eff} = 3.0$ for both cases.

3.1.3 Reconstruction of the three-dimensional mean flow field

Using 2-D PIV data, one can obtain some information about the 2-D flow field which is listed in the first column of Table 3-2. As it is mentioned before, there exist 140 windows captured for each grid in an array of 35×4 (Figure 2-9). Each set of 4 streamwise windows at the same height are patched together. Thus a region with 35 long horizontal planes distributed in typically 5mm distance in Z-direction is formed. Considering the diagonal symmetry in the flow, the third component of the mean velocity $\langle W \rangle$ can be obtained by rotating these horizontal planes to the corresponding vertical ones. An example of a corresponding vertical plane to that of horizontal ones is shown in Figure 3-6-left for FCG. In this example, the horizontal plane is the center plane (Z=0) which was rotated 90 degrees clockwise to yield the corresponding vertical plane (Y=0). The mean transverse velocity component $\langle V \rangle$ in the horizontal

36

window would be the mean vertical velocity component in the vertical one with a negative sign $\langle -W \rangle$. Subsequently, the components of the Reynolds stress tensor and mean velocity strain rate are changed to the rotated components in the vertical planes as listed in Table 3-2.
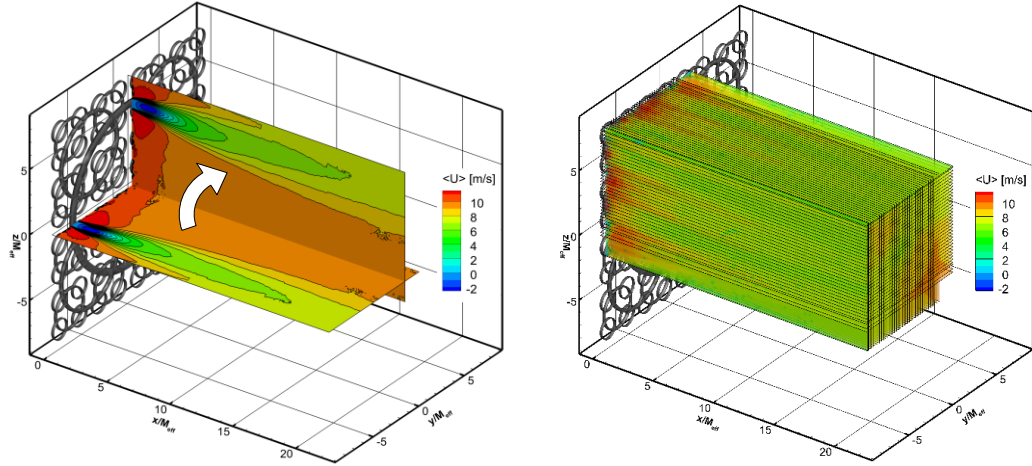
Figure 3-6 Sample rotation of horizontal planes to corresponding vertical ones in FCG; Z=0 plane is rotated 90 degrees clockwise to result in Y=0 plane; Overlay is the mean streamwise velocity (Left) 35 horizontal and 35 corresponding vertical planes in FCG creating a volume-like region. The overlay is the mean streamwise velocity (Right).

Rotating all 35 planes to corresponding vertical ones creates a volume-like region, as shown in Figure 3-6-right. Additional variables on the vertical planes (Table 3-2) are then interpolated to the horizontal planes. This is done by selecting all vertical planes as a source of interpolation and each horizontal plane as a destination. This results in 35 horizontal planes with complementary data on mean variables as it is seen in Table 3-3. Two other mean vorticity components ($\overline{\Omega_x}$ and $\overline{\Omega_y}$) are calculated knowing all the three mean velocities. Two components of the Reynolds stress tensor ($\overline{uw} = \overline{wu}, \overline{ww}$) as well as other components of the mean velocity gradient tensor ($\overline{S_{13}} = \overline{S_{31}}, \overline{S_{23}} = \overline{S_{32}}, \overline{S_{33}}$) are also obtained. The only variable which remains unknown is the shear stress on the planes parallel to the grid, i.e. $\overline{vw} = \overline{wv}$. As a result, a set of 35 horizontal planes with more information on the mean flow variables are produced. These planes are sufficiently close to each other (distance is 5mm) to allow smooth interpolation of the statistical fields, to show the development of the mean flow using parallel planes to the grid. The inverse-distance interpolation is applied in the Z direction to create a

3-D volumetric dataset. This volume is extended only in a quarter of the whole grid. It is also possible to mirror the volume data along XZ and XY planes to create a full volumetric data. A detailed discussion of velocity fields and statistics are presented in the results section.

Table 3-2 Data obtained by 2-D PIV on horizontal planes (original) and corresponding data on vertical planes (rotated).

	Horizontal plane (original)	Vertical plane (rotated)
	X	X
Coordinate vector	Y	$-Z$
	Z	$-Y$
Mean velocity vector	$\langle U \rangle$	$\langle U \rangle$
	$\langle V \rangle$	$\langle -W \rangle$
Reynolds stress tensor	$\langle uu \rangle$	$\langle uu \rangle$
	$\langle uv \rangle = \langle vu \rangle$	$\langle -uw \rangle = \langle -wu \rangle$
	$\langle vv \rangle$	$\langle ww \rangle$
Mean velocity strain rate Tensor	$\langle S_{11} \rangle$	$\langle S_{11} \rangle$
	$\langle S_{12} \rangle = \langle S_{21} \rangle$	$\langle -S_{13} \rangle = \langle -S_{31} \rangle$
	$\langle S_{22} \rangle$	$\langle S_{33} \rangle$

Table 3-3 Mean flow data obtained by 2-D PIV and complementary data after interpolating the vertical planes variables.

	2-D PIV data (original)	Rotated data
Mean velocity field	$\langle U \rangle \ \langle V \rangle$	$\langle U \rangle \ \langle V \rangle \ \langle W \rangle$
Mean vorticity field	$\overline{\Omega_z}$	$[\overline{\Omega_x} \ \overline{\Omega_y} \ \overline{\Omega_z}]$
Mean velocity strain rate tensor	$\begin{bmatrix} \overline{S_{11}} & \overline{S_{12}} & \square \\ \overline{S_{21}} & \overline{S_{22}} & \square \\ \square & \square & \color{red}{\overline{S_{33}}} \end{bmatrix}$	$\begin{bmatrix} \overline{S_{11}} & \overline{S_{12}} & \overline{S_{13}} \\ \overline{S_{21}} & \overline{S_{22}} & \overline{S_{23}} \\ \overline{S_{31}} & \overline{S_{32}} & \overline{S_{33}} \end{bmatrix}$
Reynolds stress tensor	$\begin{bmatrix} \overline{uu} & \overline{uv} & \square \\ \overline{vu} & \overline{vv} & \square \\ \square & \square & \square \end{bmatrix}$	$\begin{bmatrix} \overline{uu} & \overline{uv} & \overline{uw} \\ \overline{vu} & \overline{vv} & \square \\ \overline{wu} & \square & \overline{ww} \end{bmatrix}$

3.1.4 Characteristic lines

To investigate the mean flow evolution in the near-field, in addition to the general patterns which are obtained by the area averaged values in $x = cte$ planes, one could extract variables along some generic lines.
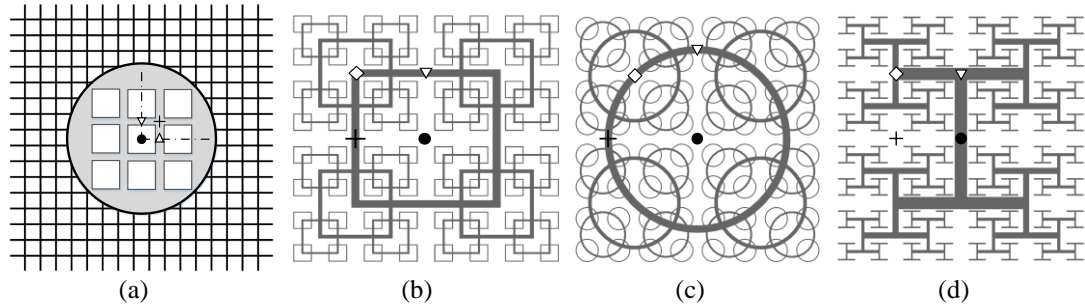
Figure 3-7 Starting point of characteristic lines in grids under investigation. (a) CSG, ● centerline (C1), ▽ middle of the horizontal bar (C2), △ middle of the vertical bar (C3), and ✚ cross of horizontal and vertical bars (C4). (b) FSG, ● centerline (FS1), ▽ middle of the horizontal bar in the largest square (FS2), ◇ top left corner of the largest square (FS3), and ✚ middle of the vertical bar in the largest square (FS4). (c) FCG, ● centerline (FC1), ▽ middle of the largest circle at the top (FC2), ◇ middle of the largest circle on the diagonal of the grid at the top left (FC3), and ✚ middle of the largest circle at left (FC4). (d) FIG, ● centerline (FI1), ▽ middle of the largest I at the top (FI2), ◇ top left corner of the largest I (FI3), and ✚ diagonally reflected point of FI2.

Table 3-4 Characteristic lines for grids under investigation, their symbol and location.

Grid	Starting point of the line	Symbol	Location
CSG	C1	●	Centerline (opening)
	C2	▽	Middle of horizontal bars
	C3	△	Middle of vertical bars
	C4	✚	Cross of horizontal and vertical bars
FSG	FS1	●	Centerline
	FS2	▽	Middle of the 1st iteration bar at the top of the grid
	FS3	◇	Top left corner of the 1st iteration bar
	FS4	✚	Middle of the vertical bar in the largest square
FCG	FC1	●	Centerline
	FC2	▽	Middle of the 1st iteration circle at the top of the grid
	FC3	◇	Top left corner of the 1st iteration circle
	FC4	✚	Middle of the largest circle at the left side of the grid
FIG	FI1	●	Centerline
	FI2	▽	Middle of the 1st iteration bar at the top of the grid
	FI3	◇	Top left corner of the 1st iteration bar
	FI4	✚	Diagonally reflected point of FI2

These lines are called characteristic lines as they represent a distinct location on each grid. The starting point is chosen very near to the grid, and each line extends through the whole domain under investigation. The starting point of the lines are schematically shown in Figure 3-7 and listed in Table 3-4. Variation of many statistics of the turbulent flow along these lines are presented in following sections.

3.2 Mean flow characteristics

Effects of the growth of test section boundary layer can be investigated while there was no grid installed inside the test section. Some planes at different heights (Z) were captured with the help of PIV. Boundary layer thickness defined by the height with $\langle U \rangle = 0.95 U_0$ was started from $\delta|_{\frac{x}{T}=0.15} = 0.0247T$ at the test section entrance and grows to $\delta|_{\frac{x}{T}=1.32} = 0.0536T$ at the rear part of the measurement region. The free stream flow uniformity outside the boundary layer was confirmed by extracting some spanwise lines from the PIV planes.

3.2.1 <u>Center plane</u>

Distribution of the mean streamwise velocity $\langle U \rangle$, on the horizontal center plane $(\frac{Z}{M_{eff}} = 0)$ is shown in Figure 3-8. $\langle U \rangle$ is normalized by the free stream velocity U_0. For conventional grid (Figure 3-8-a), the streamwise velocity is recovered to about $0.85 U_0$ after almost 10 mesh sizes downstream and the field seems to get uniform afterwards. This is not the case for all other fractal grids and the flow field is still under the influence of the wakes of the largest iterations (elements) even at the endpoint of the measurement region. It is clear that for fractal square (Figure 3-8-b) and fractal circular (Figure 3-8-c) grids the wakes still require more space to get fully merged. This shows the importance of the central plane flow field which was at the focus of study in most of the earlier works [22]. Normalized mean velocities $\left(\frac{\langle U \rangle}{U_0}, \frac{\langle V \rangle}{U_0} \right)$ and streamwise turbulence intensity $TI_u = \frac{u'}{\langle U \rangle}$ across the test section, are extracted at three downstream locations, $x = 1, 17, 22\ M_{eff}$ – start, the endpoint of the FIG measurement region, and the endpoint of the measurement region of the rest of grids – and profiles are accordingly shown in Figure 3-9, Figure 3-10, and Figure 3-11,

respectively. It is clear from Figure 3-9 that close to the grid, particularly downstream of the grid's bars, deficits of mean velocity is very high. These deficits are surrounded by high mean flow gradients with local maximum turbulence intensity as one compares Figure 3-9 and Figure 3-11.
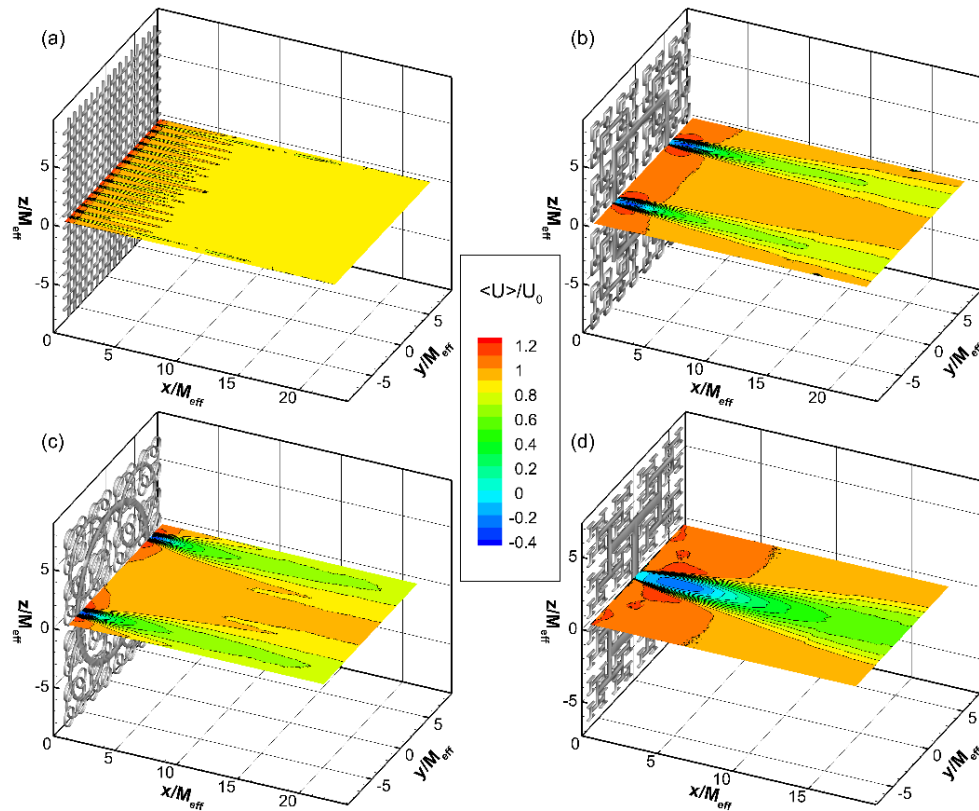
Figure 3-8 Normalized mean streamwise velocity $\frac{\langle U \rangle}{U_0}$ distribution on $z/M_{eff} = 0$ plane for CSG (a), FSG (b), FCG (c), and FIG (d).

Unlike the symmetric grids (CSG, FSG, and FCG), FIG does not possess diagonal symmetry and the mean streamwise velocity on $y/M_{eff} = 0$ plane is not the same as in $z/M_{eff} = 0$ plane. Normalized mean streamwise velocity at $y/M_{eff} = 0$ is shown in Figure 3-12. Minor differences in the plots of mean streamwise velocity in horizontal and vertical planes are due to the fact that the vertical planes are produced from the reconstructed 3-D volume where the actual data belongs to the horizontal planes.
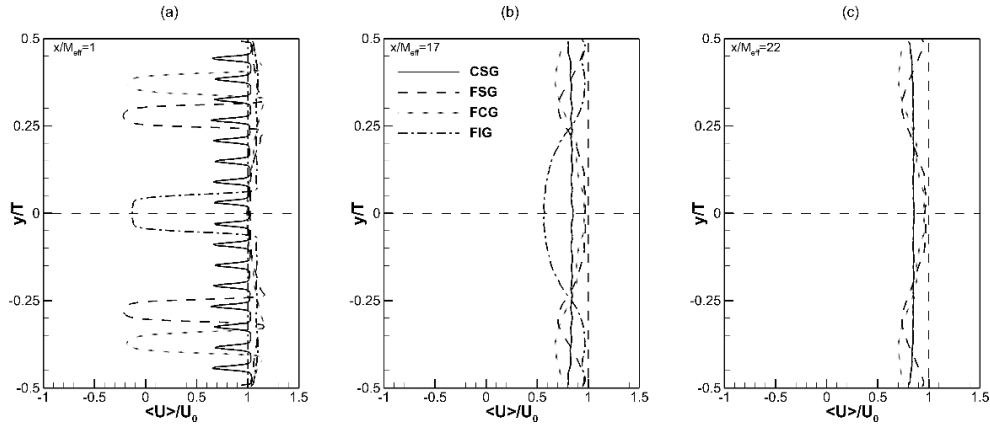
Figure 3-9 Spanwise distribution of mean streamwise velocity $\langle U \rangle$ normalized by free stream velocity U_0, at $x = 1M_{eff}$ (a), $x = 17M_{eff}$ (b), and $x = 22M_{eff}$ (c) on the center plane. $\frac{y}{T} = 0$ is the centerline of the test section. $\langle U \rangle = U_0$ is shown by vertical dashed line.
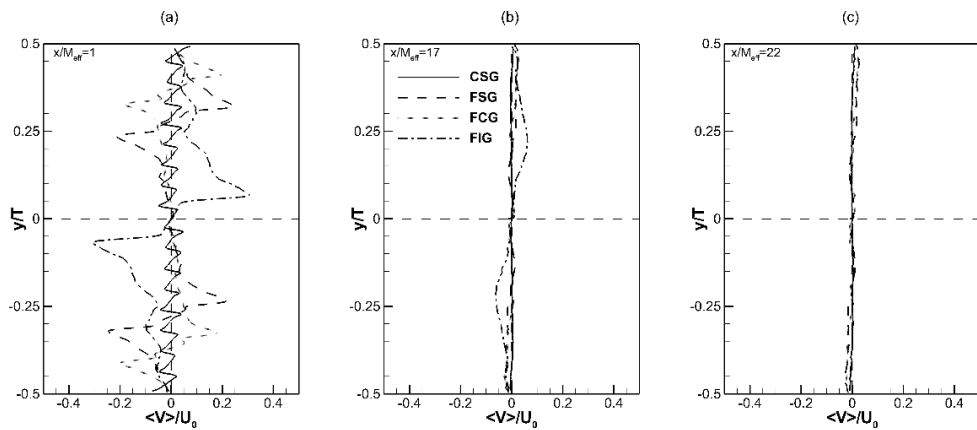
Figure 3-10 Spanwise distribution of mean spanwise velocity $\langle V \rangle$ normalized by free stream velocity U_0, at $x = 1M_{eff}$ (a), $x = 17M_{eff}$ (b), and $x = 22M_{eff}$ (c) one the center plane. $\frac{y}{T} = 0$ is the centerline of the test section. $\langle V \rangle = 0$ is shown by a vertical dashed line.

42
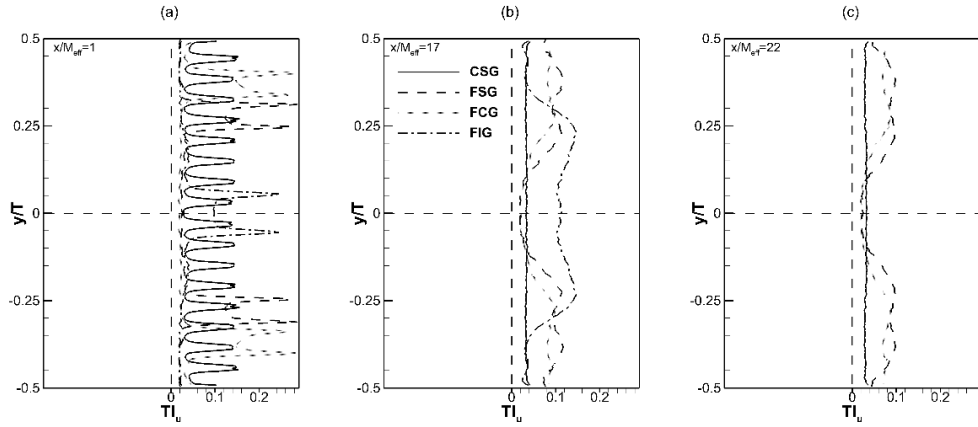
Figure 3-11 Spanwise distribution of streamwise turbulence intensity $TI_u = \frac{u'}{\langle U \rangle}$, at $x = 1M_{eff}$ (a), $x = 17M_{eff}$ (b), and $x = 22M_{eff}$ (c) on the center plane. $\frac{y}{T} = 0$ is the centerline of the test section. Vertical dashed line is zero turbulence intensity.
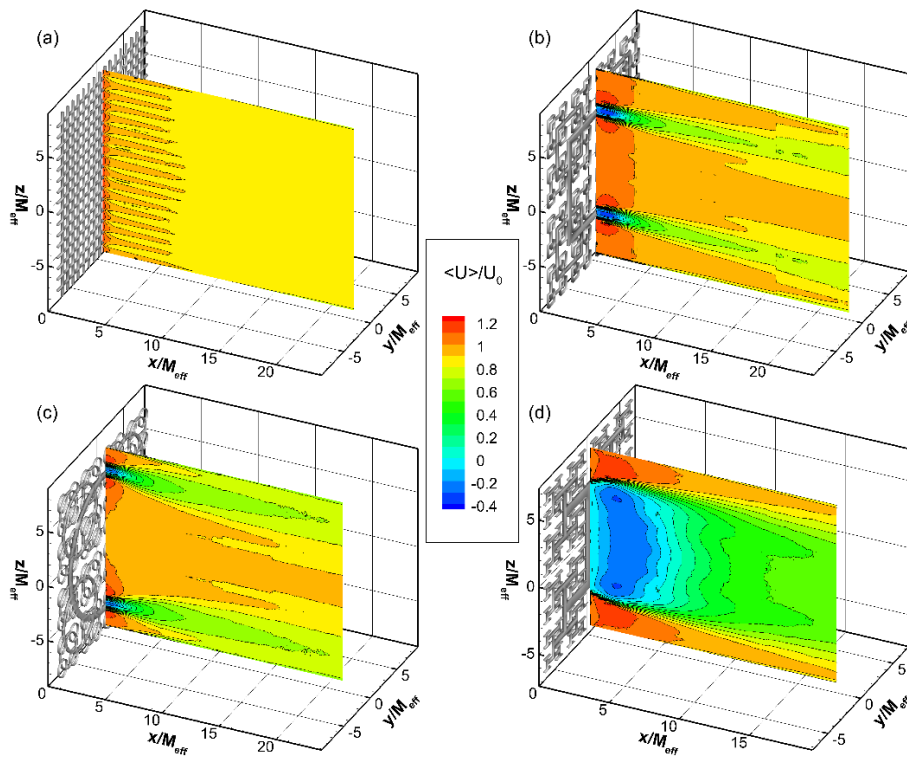
Figure 3-12 Normalized mean streamwise velocity $\frac{\langle U \rangle}{U_0}$ distribution on the plane $^y/_{M_{eff}} = 0$ for CSG (a), FSG (b), FCG (c), and FIG (d).

43

Normalized mean out-of-plane vorticity $\langle\Omega_z\rangle\frac{M_{eff}}{U_0}$, is shown in Figure 3-13. Vortices shed by the thickest vertical bar are appropriately resolved. These dominant vortices are better shown in Figure 3-14, which is an instantaneous data for normalized in-plane vorticity at $\frac{z}{M_{eff}} = 0$ plane in the vicinity of FSG. According to Table 2-1, the width of the thinnest element among these grids is 1.2mm which is even smaller than the spatial resolution of the measurements. Thus, the vortices shed by the small bars could not be properly resolved.
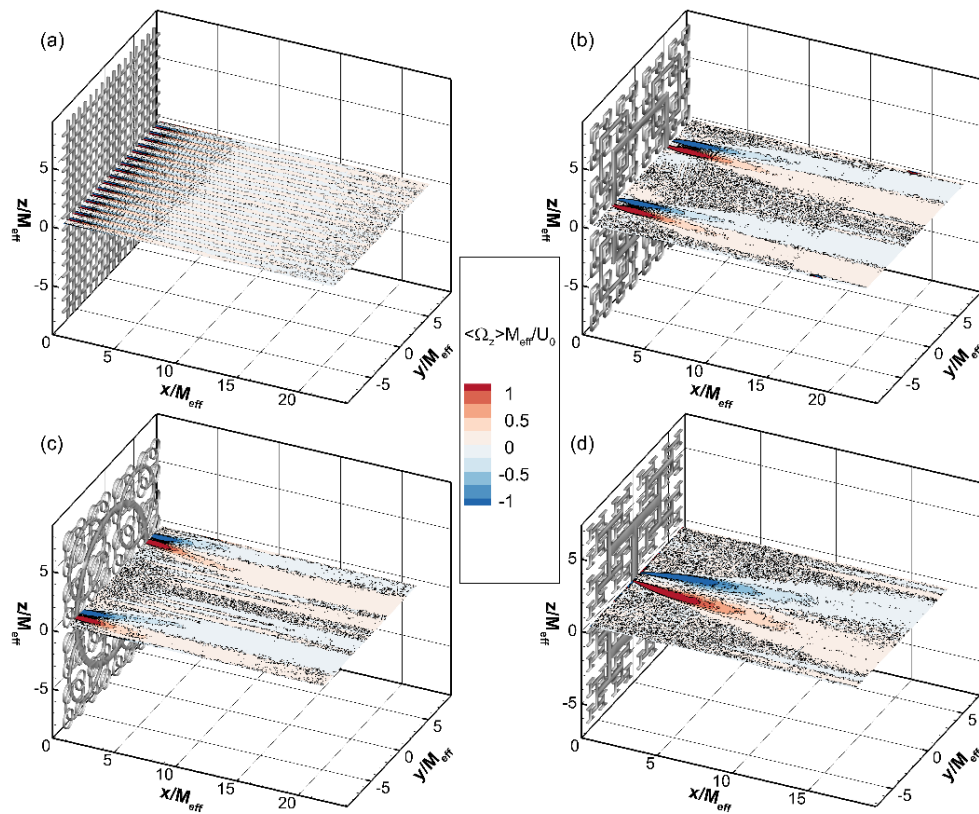
Figure 3-13 Normalized mean out-of-plane vorticity $\langle\Omega_z\rangle\frac{M_{eff}}{U_0}$ on $^z/M_{eff} = 0$ plane for (a) CSG, (b) FSG, (c) FCG, and (d) FIG.
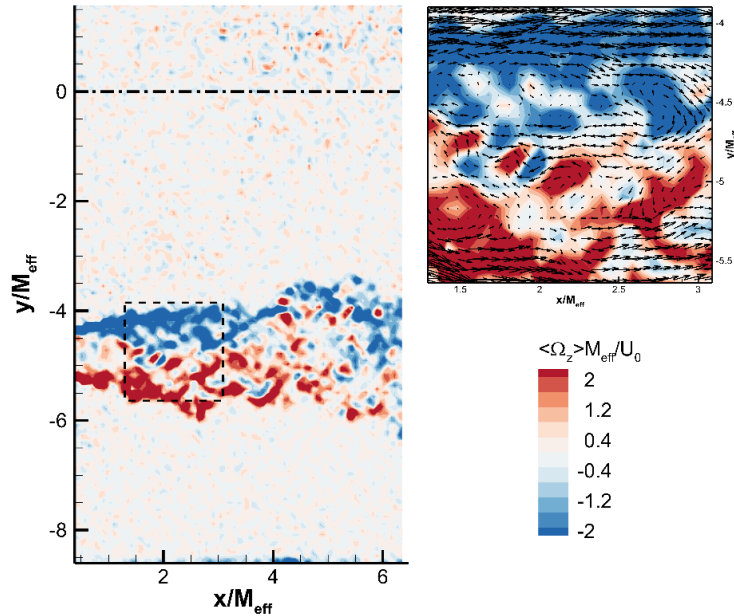
Figure 3-14 Instantaneous map of normalized Z-vorticity, belonging to FSG, window 1, $z/M_{eff} = 0$ where the wake of the biggest bar is dominant and completely resolved. The velocity vector map of the rectangular region is shown in a zoomed view at right. Grid centerline is shown by the dashed line at $y/M_{eff} = 0$.

3.2.2 Off-center planes

The resolution of the current PIV images, make it possible to capture all flow characteristics behind two largest (zeroth and first) iterations of fractal grids. We here exclude FIG since it creates a very different turbulent flow field. Therefore, additional horizontal planes rather than the central one are extracted from the mean flow data. These planes typically cut sections from two largest iterations of fractal square and circular grids, hence can be thought as some generic planes available to investigate flow properties. Vertical position (z/M_{eff}) of these planes are listed in Table 3-5. Plane 2 corresponds to a cut from the middle of a horizontal bar in CSG and a cut form the middle of the largest horizontal iteration in FSG and FCG. Plane 3 cuts the second iteration of FSG (FCG) from the corner of square (circle).
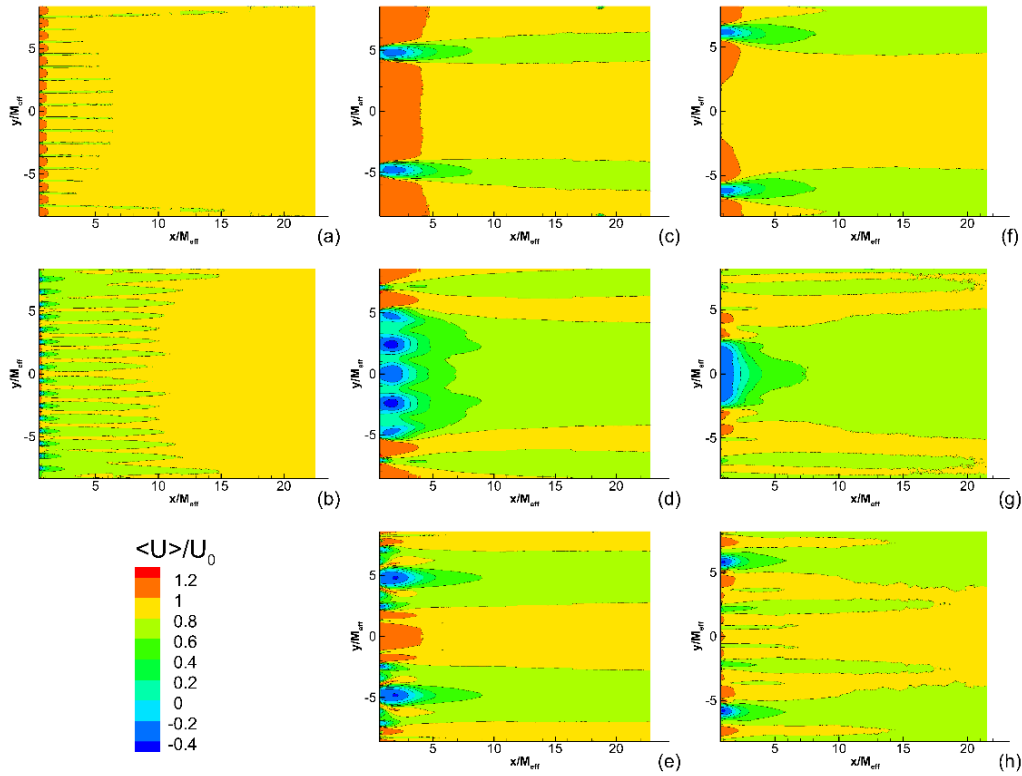
Figure 3-15 Normalized streamwise velocity $\frac{\langle U \rangle}{U_0}$ distribution over selected horizontal planes of CSG (a-b), FSG (c-e), and FCG (f-h). Vertical position of planes is listed in Table 3-5.

Table 3-5 Vertical positions of extracted planes from the reconstructed 3-D mean flow field. Letters refer to the contour plots in Figure 3-15.

Grid	Center plane		Plane 2		Plane 3	
	Z/M_{eff}	Letter	Z/M_{eff}	Letter	Z/M_{eff}	Letter
CSG	0	a	0.50	b	-	-
FSG	0	c	4.57	d	2.43	e
FCG	0	f	6.10	g	2.20	h

Complex wake-jet interactions between different blockage-opening pairs create very different flow pattern in the near-wake of fractal grids. Even the range of advancement of jet-like flow on the central plane (Figure 3-15-c,f) is different. An example where 3-D flow field shows itself can be found in the wake of the largest bar of FSG in Figure 3-15-d. Although this plane is cut from the middle of the bar, an alternating wake pattern with peaks of slightly positive and valleys of recirculating zones indicates the

46

effects of neighbor bars along the vertical direction. Starting from the left corner of the largest horizontal bar, a small recirculating zone is captured at $\frac{y}{M_{eff}} \cong -5.0$. Moving along the +y axis, the horizontal bar is surrounded by another two horizontal bars belonging to the smallest (3rd) iteration ($-4 < \frac{y}{M_{eff}} < -2.75$). The interaction of two different shear layers from these two different thicknesses within this distance, shrinks the recirculation zone along the largest bar and results in a positive streamwise velocity. At the intersection of the two largest iterations ($-2.5 < \frac{y}{M_{eff}} < -1.9$), a relatively big recirculating zone does exist. The pattern of two surrounding 3rd iteration bars is repeated in the range of $-1.8 < \frac{y}{M_{eff}} < -0.4$, and around the centerline $-0.35 < \frac{y}{M_{eff}} < +0.35$, flow recirculates without the effects of any surrounding bars. To get more quantitative results, it is better to extract data at different downstream stations and compare them. First, we will focus on the center plane flow.

The important point to note about the FCG is the collision of the wake of the 0th iteration to the test section walls during its evolution (Figure 3-15-f,h). This could leave some effects in the flow which are not directly related to fractal grid-generated-turbulence and has to be kept in mind.

In the following, we used upstream air velocity corresponding to each grid (U_∞) for normalization. The velocity of air approaching each grid is measured with the help of HWA and is equal to 8.117, 8.321, and 8.171 m/s for CSG, FSG, and FCG, respectively. As it has been mentioned FIG is excluded in these comparisons as it produces a completely different turbulent flow. Minor differences in the mean flow field are found between the center plane and plane 2 of CSG (Figure 3-15-a,b). These initial, geometry-dependent variances are shown in Figure 3-16 for normalized streamwise velocity distribution. These differences all vanish after about $x = 10M_{eff}$ downstream of the grid. Only in the very near wake region of CSG, one can find recirculation regions. A sample is shown in Figure 3-16-c which is extracted at a downstream distance of $x = 0.51M_{eff}$ within the wake of three consecutive vertical bars in the spanwise direction.
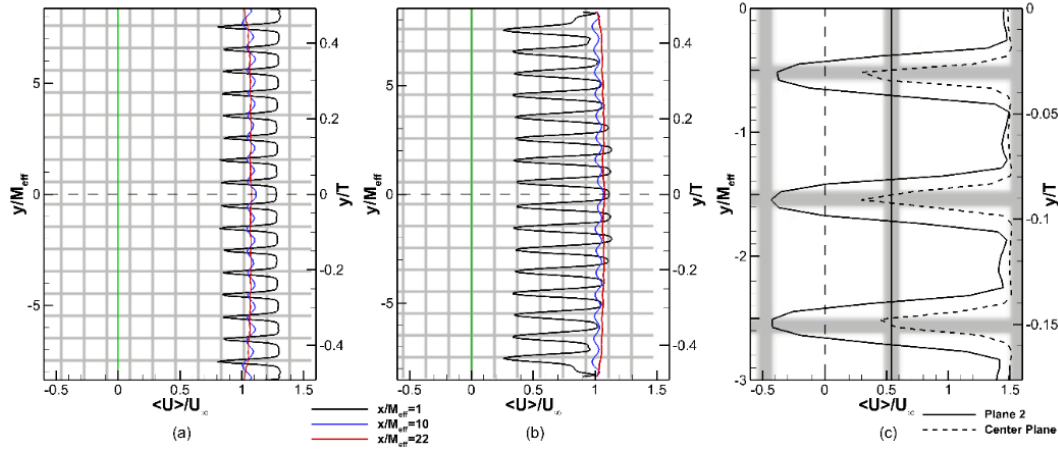
Figure 3-16. Normalized mean streamwise velocity distribution on the center plane (a) and plane 2 (b) of CSG, at three downstream locations ($x/M_{eff} = 1,10,22$). Vertical green line shows the PIV laser sheet and the horizontal dashed line at $y/M_{eff} = y/T = 0$ is the grid centerline. Zoomed view of mean streamwise velocity very near to the grid (at $x/M_{eff} = 0.51$) (c), showing recirculation region with negative velocity magnitudes behind horizontal bars and off-jet-center maximum velocities on plane 2 (solid black line). Center plane data is shown by the dashed black line. Schematics of CSG geometry is shown at the background.

At $x = 1M_{eff}$, streamwise velocity fluctuates within 0.04 and 0.18 of U_∞ in the center plane (Figure 3-17-a), while its fluctuations behind the horizontal bar (plane 2) is within 0.15 and 0.25 of U_∞. However, after $x = 10M_{eff}$, there is no significant difference between streamwise velocity fluctuations on both planes, such that it decays to about 6% and 4% of U_∞ at $10M_{eff}$ and $22M_{eff}$, respectively. Mean velocities and rms values are in a good agreement with similar studies previously done using PIV technique [15].

Spanwise distribution of the normalized streamwise velocity component $\frac{\langle U \rangle}{U_\infty}$ in FSG is shown in Figure 3-18, at three different downstream distances over the center plane as well as two off-center planes as listed in Table 3-5. Over the center plane ($z/M_{eff} = 0$), just behind the grid (Figure 3-18-a), mean flow is highly inhomogeneous and both wake-like and jet-like flows are observed. Maximum velocity is not in the centerline but in the shear layer of the largest vertical bars where the streamwise velocity overshoots from $1.258U_\infty$ (at centerline) to about $1.435U_\infty$. At the farthest point from the grid ($\frac{x}{M_{eff}} = 22$) centerline velocity is slightly decreased to about $1.19U_\infty$. At this

48

location, effects of the wake of the largest vertical bars still exist with maximum deficit of 23% in the streamwise velocity. Another point to note is by examining the minimum spanwise location of the wake which suggests a diverging mean flow from the centerline which was numerically shown before [61].
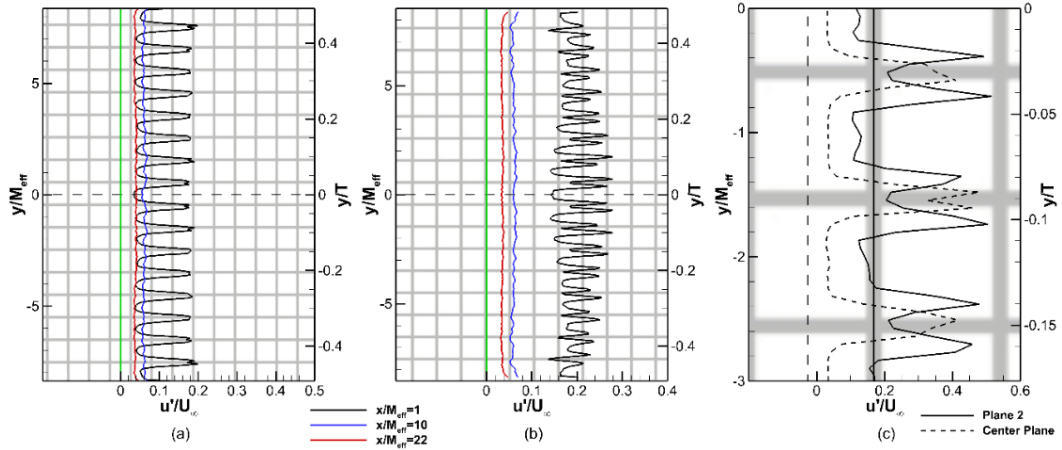
Figure 3-17. Normalized rms streamwise velocity distribution on the center plane (a) and the plane cutting the horizontal bars, i.e., plane 2 (b) of CSG, at three downstream locations ($x/M_{eff} = 1,10,22$). Vertical green line shows the PIV laser sheet and the horizontal dashed line at $y/M_{eff} = $ y/T $ = 0$ is the grid centerline. Zoomed view of rms streamwise velocity very near to the grid (at $x/M_{eff} = 0.51$) (c), on plane 2 (solid black line). Center plane data is shown by the dashed black line. Schematics of CSG geometry is shown at the background.

On the second plane ($z = 4.57M_{eff}$), so called effects of the smallest iterations on the wake of the largest iteration's horizontal bar, is obvious with alternating velocity profile (Figure 3-18-b). On this plane, however, the maximum streamwise velocity at the farthest measurement point reaches to about $1.06U_\infty$. One of the most complex distributions can be found on the third plane ($z = 2.43M_{eff}$) where the interactions of three iterations and the effects of the smallest ones exist such that wherever there are two smallest iterations surrounding a larger element, a recirculating zone fades away and turns into the jet-like flow. This is obvious in Figure 3-18-c, e.g., in the ranges of $-6.5 < \dfrac{y}{M_{eff}} < -5.3, -4.2 < \dfrac{y}{M_{eff}} < -3.0$, and $-1.8 < \dfrac{y}{M_{eff}} < -0.6$.
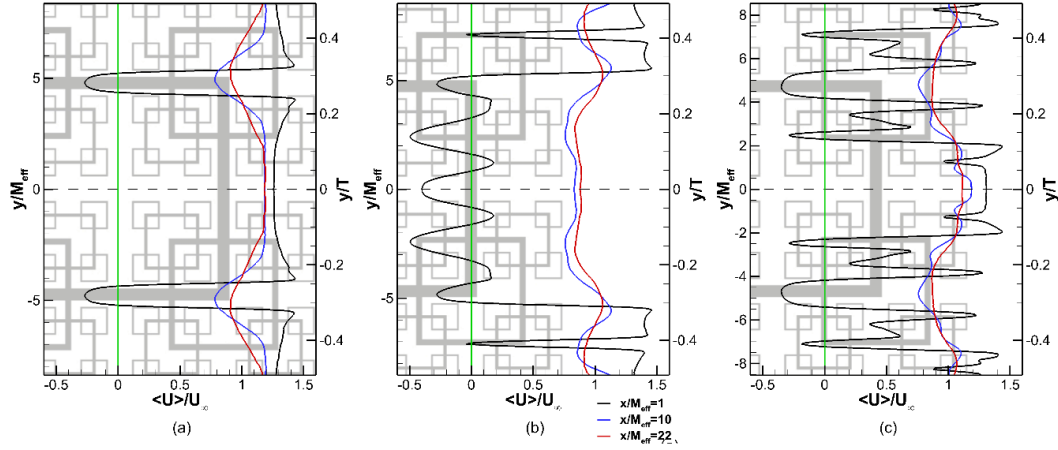
Figure 3-18. Normalized mean streamwise velocity distribution on the center plane ($z = 0$) (a), $z = 4.57 M_{eff}$ plane (b), and $z = 2.43 M_{eff}$ plane (c) of FSG, at three downstream locations ($x/M_{eff} = 1, 10, 22$). Vertical green line shows the PIV laser sheet and the horizontal dashed line at $y/M_{eff} = $ y/T $= 0$ is the grid centerline. Schematics of the grid is shown at the background.

For FSG, fluctuations of streamwise velocity are normalized by U_∞, and shown in Figure 3-19. Very near to the grid, high shear ($\approx 34\%$ of U_∞) exists at both sides of the grid's largest bar (Figure 3-19-a), and everywhere else there is a constant level of fluctuations in the order of 2.5% of free stream velocity. This value remains preserved only about the centerline of FSG until the endpoint of the measurement region. On the second plane ($\frac{z}{M_{eff}} = 4.57$), vertical bar belonging to the first iteration square (at $y \approx \pm 7.2 M_{eff}$) creates levels of turbulence ($\approx 37\%$ of U_∞) even higher than that of the 0th iteration, and the cross of 0th and 1st iterations, comparing Figure 3-19-b with Figure 3-19-a and Figure 3-19-c at $x = 1 M_{eff}$, respectively. The values of turbulence intensity are also in a good agreement with previous DNS results [61].

Distributions of mean streamwise velocity and turbulence intensity for FCG, are shown in Figure 3-20 and Figure 3-21, respectively. Over the center plane ($z/M_{eff} = 0$), again there is an overshoot of streamwise velocity from $1.23 U_\infty$ (at centerline) to about $1.46 U_\infty$ (at the shear layer of the largest circular element) (Figure 3-20-a). Maximum deficit in the streamwise velocity is about 26% at the endpoint of the measurement region over the center plane.

50
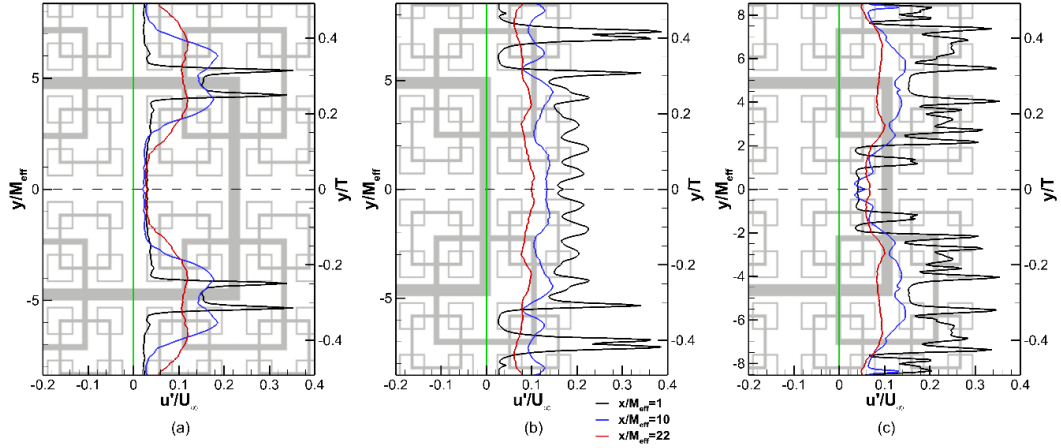
Figure 3-19. Normalized rms streamwise velocity distribution on the center plane ($z = 0$) (a), $z = 4.57M_{eff}$ plane (b), and $z = 2.43M_{eff}$ plane (c) of FSG, at three downstream locations ($x/M_{eff} = 1,10,22$). Vertical green line shows the PIV laser sheet and the horizontal dashed line at $y/M_{eff} = y/T = 0$ is the grid centerline. Schematics of the grid is shown at the background.
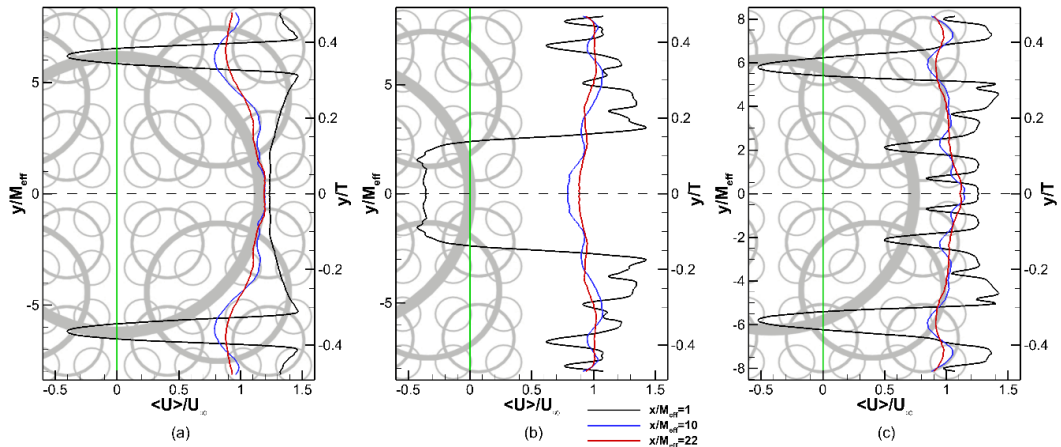
Figure 3-20. Normalized mean streamwise velocity distribution on the center plane ($z = 0$) (a), $z = 6.1M_{eff}$ plane (b), and $z = 2.2M_{eff}$ plane (c) of FCG, in three downstream locations ($x/M_{eff} = 1,10,22$). Vertical green line shows the PIV laser sheet and the horizontal dashed line at $y/M_{eff} = y/T = 0$ is the grid centerline. Schematics of the grid is shown at the background.

The second plane in FCG cuts from the middle of the largest circular element. However, the smallest iterations are ordered asymmetrically on either side of this plane, whereas in the FSG, the smallest squares are symmetrically arranged (compare Figure 3-18-b with Figure 3-20-b). Because of this, one cannot find the alternating velocity distribution in the vicinity of the FCG, just like that is found in FSG case. On

51

this plane, however, velocity distribution seems to be more uniform (within $\pm 0.07 U_\infty$) at the farthest measurement point, compared to FSG case. On the third plane of FCG at $z = 2.2 M_{eff}$, interactions between the wakes of the first three iterations are detected near to the grid (Figure 3-20-c). Due to the presence of the smallest circular elements on either sides of the plane 3, reverse flow only occurs at the largest iteration, and everywhere else the mean streamwise velocity is larger than the free stream velocity. Maximum turbulence intensity (($\approx 37\%$ of U_∞) induced by the largest element of FCG is higher than that of FSG (Figure 3-21-a). At the intersection of 0th and 1st iterations, the level of fluctuations reaches to almost $0.4 U_\infty$ (Figure 3-21-b).
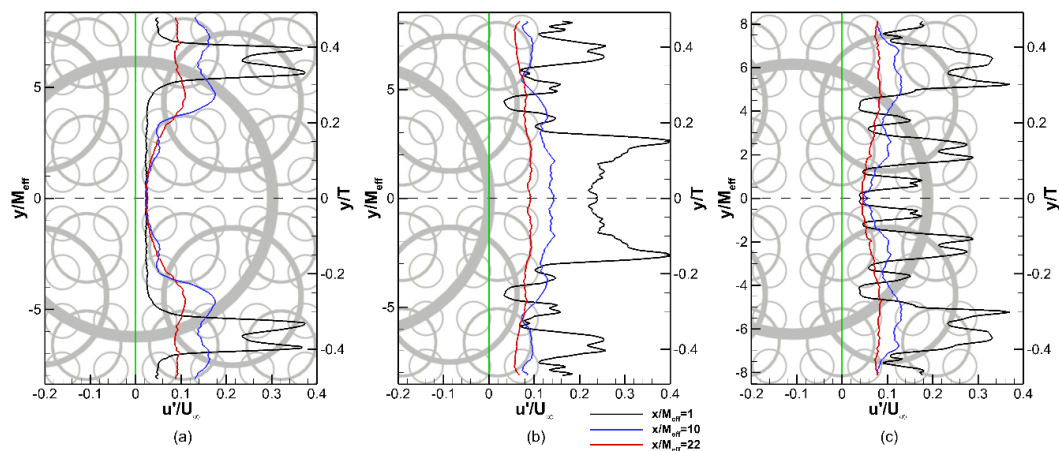
Figure 3-21. Normalized rms streamwise velocity distribution on the center plane ($z = 0$) (a), $z = 6.1 M_{eff}$ plane (b), and $z = 2.2 M_{eff}$ plane (c) of FCG, at three downstream locations ($x/M_{eff} = 1, 10, 22$). Vertical green line shows the PIV laser sheet and the horizontal dashed line at $y/M_{eff} = $ y/T $= 0$ is the grid centerline. Schematics of the grid is shown at the background.

3.2.3 Cross-sectional planes

To further investigate the near flow field, it is valuable to extract some planes parallel to the grid ($\frac{x}{M_{eff}} = cte$) to show the flow development. As an example, cross sectional profiles of the mean streamwise velocity are shown in Figure 3-22 to qualitatively understand the mean flow development in the near grid region of conventional and fractal grids. Nagata et. al. [39] divided the flow into 'upstream' and 'downstream' sections where $\frac{x}{x_*} = 0.3 - 0.4$ discriminates these two, since the decay of turbulence occurs after $0.45 x_*$. Based on their classification, measurement region for fractal grids in the current study falls inside the 'upstream' section where the turbulence is being

produced. However, for CSG the measurement region extends to more than twice of x_* value according to Table 2-3.

The regular wake-jet pattern in conventional grid continuously merges into a nearly homogeneous flow, and at the end of the measurement region, streamwise flow is almost homogeneous (Figure 3-22-a). This is also clear from the spanwise distribution of $\langle U \rangle$ in Figure 3-16-b. In that figure, the boundary layer velocity profile is clearly seen near the test section walls.
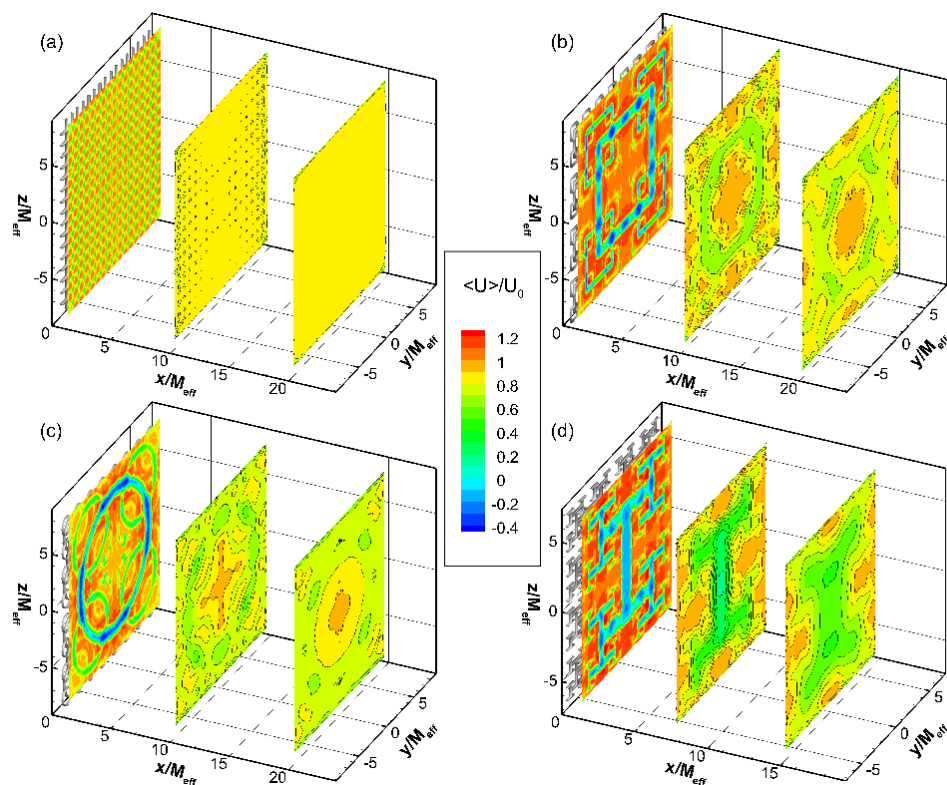
Figure 3-22 Normalized mean streamwise velocity $\frac{\langle U \rangle}{U_0}$ distribution on the planes $x/M_{eff} = 1, 10, and\ 20$ for CSG (a), FSG (b), FCG (c), and planes $x/M_{eff} = 1, 7.5, and\ 15$ for FIG (d).

Wakes of the 0th and 1st iterations of fractal grids are persistently dominant in the flow, and unlike the conventional grid, streamwise flow is still buckling with some degree of inhomogeneity at the end of the measurement region (Figure 3-22). Also, the distribution and magnitudes of $\langle U \rangle$ at similar downstream distances are different. For example, the jet region formed around the centerline ($\frac{y}{M_{eff}} = \frac{z}{M_{eff}} = 0$) seems to be

stronger in FSG. Interestingly the cross sectional shape of this jet seems to have a circular pattern in FSG while in FCG it is in the shape of a cross sign.

Results of cross-sectional planes are in good agreement with previously hotwire measurements [39] at similar locations ($\frac{x}{x_*}$ =0.05, 0.1, and 0.2 corresponding to about 6, 12, and 24 M_{eff}). Supplementary analysis on the mean flow evolution is carried out in the following section to assess mixing characteristics.

3.2.4   Near-field mixing quantification

Flow becomes turbulent as it moves through the grids. This turbulence determines the random stirring which causes transfers and turbulent diffusion [37]. The diffusivity of turbulence increases rates of momentum, heat, and mass transfer. Since the scalar transfer represents the degree of mixing inside the flow, the higher the turbulence, the more efficient the mixing. In general, there are two mechanisms responsible for scalar transfer: a) advection by velocity field and b) diffusion by molecular processes. It has been shown that the transfer of a scalar is mainly due to the turbulent field in the transverse direction; see Figure 2(c) in [37]. Laizet and Vassilicos reported a new mechanism to increase the scalar transfer and turbulent diffusion in fractal grids. They called it '*space scale unfolding*' (SSU) mechanism [37]. From the Lagrangian viewpoint, when a particle enters the wake of a regular grid bar, it will probably remain at the similar transverse location inside that wake, since these wakes are almost equal and ordered. However, the particle passing the smallest iteration of a fractal grid has a chance to get involved with a larger neighboring wake, and when traveling downstream with even larger and larger wakes with larger and larger eddy turnover length-scales [37]. This increases the probability of finding the particle in a very different transverse location when compared to the regular grid.

Maximizing the degree of mixing is important in some applications; e.g., to enhance combustion process in scramjet engines where air with supersonic speeds enters the combustor. This requires rapid fuel-air mixing in a relatively short distance [101,102]. There are evidences of high turbulence levels in the near-field region of fractal square grids, concluding a better mixing performance than the single square grid so that they can be considered as an "*efficient additional turbulence generators*" in the near-field

[54,61,103]. DNS was carried out in the near-field of a fractal grid and a single square grid [61]. Streamwise velocity contours, as well as transverse distributions of the velocity and turbulence intensity, suggest better characteristics of mixing for fractal grids. They also conclude the small fractal iterations provide a high mixing rate in the near-field region. These results were in qualitative agreement with the experimental data of fractal cross grids [13]. Krogstad and Davidson showed that for the fractal cross grids, the distribution of mean streamwise velocity is considerably more uniform than that in the regular grids [13].

3.2.4.1 Homogeneity

Studies above suggest that to evaluate the mixing performance, homogeneity in velocity and turbulence intensity are two important criteria. Higher turbulence intensities increase the spread of the embedded wakes and lead to a higher mixing speed [61] while the homogeneity of the mean flow variables shows the equal distribution of those variables. It is clear from Figure 3-22 that the flow passing the conventional grid (CSG) gets the most homogeneity in velocity distribution among the grids under investigation. However, by the act of turbulent diffusion, it is seen that the non-uniformities in mean streamwise velocity are smoothed out further downstream as well in fractal grids. Evolution of the normalized mean streamwise velocity is illustrated in Figure 3-23 toFigure 3-26 for CSG, FSG, FCG, and FIG. Similar cross sectional ($x = cte$) planes are illustrated as contours for streamwise turbulence intensity in Figure 3-28 to Figure 3-31. As one can notice in the plots of velocity and turbulence intensity, there exist local differences at each downstream location ($\frac{x}{M_{eff}}$) between FSG and FCG grids. This implies the fact that turbulence can be custom tailored. In other words depending on the application, one can adjust the peak of turbulence in the center of any flow domain, while there might be high levels of fluctuations needed in the corners. Contour plots are useful for qualitative representations; however to compare the effects of different grids on turbulence properties quantitatively, a single value for each $x = cte$ plane can be considered; that is the average of any desired flow property. Here, we call it *"area-averaged"* value.

This is useful when interpreting turbulence properties for engineering applications where average values are more comprehensible.
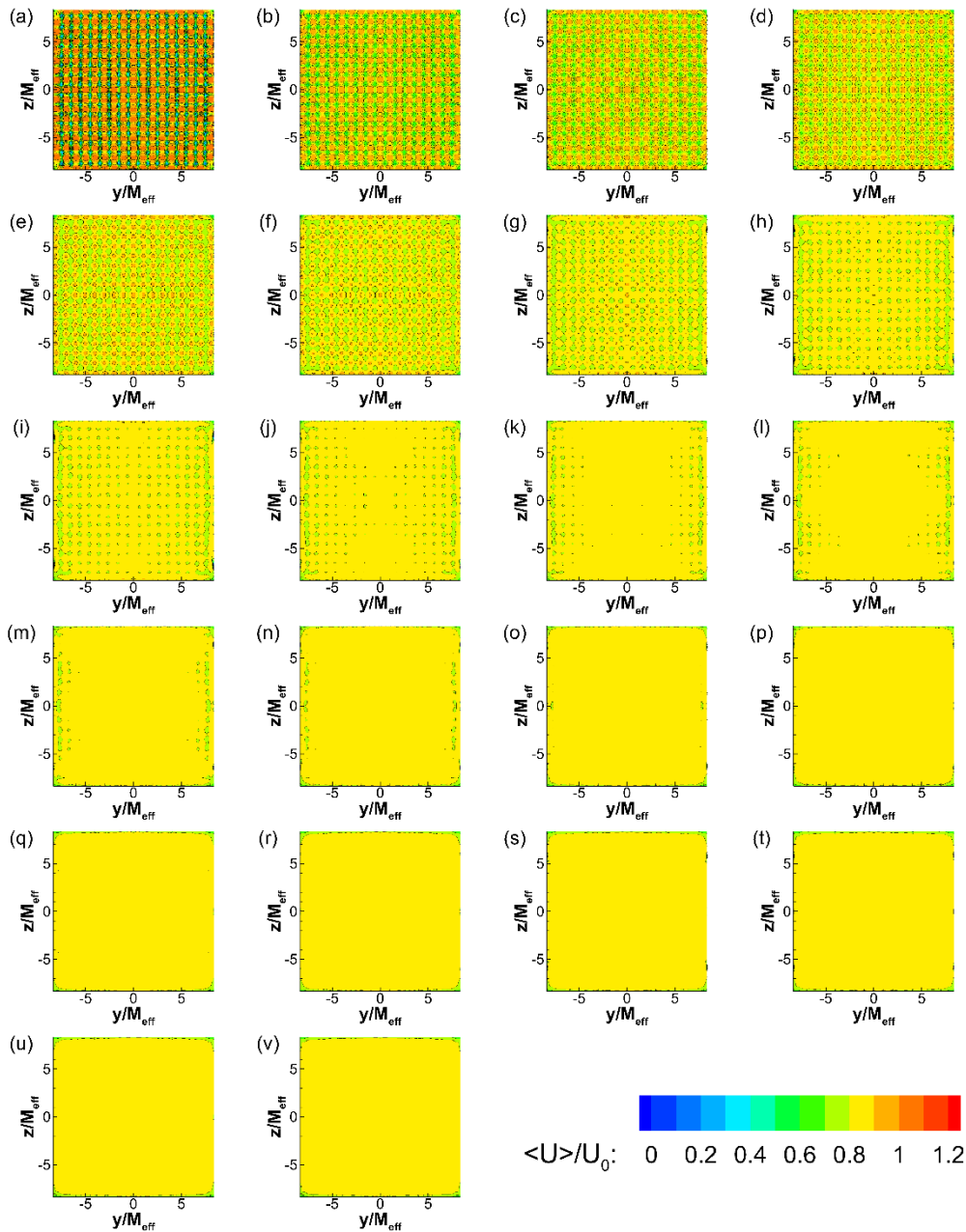
Figure 3-23 Development of normalized mean streamwise velocity $\frac{\langle U \rangle}{U_0}$ in the near grid region of CSG. Distributions are given in $1\,M_{eff}$ increment from $1\,M_{eff}$ (a) to $22\,M_{eff}$ (v).
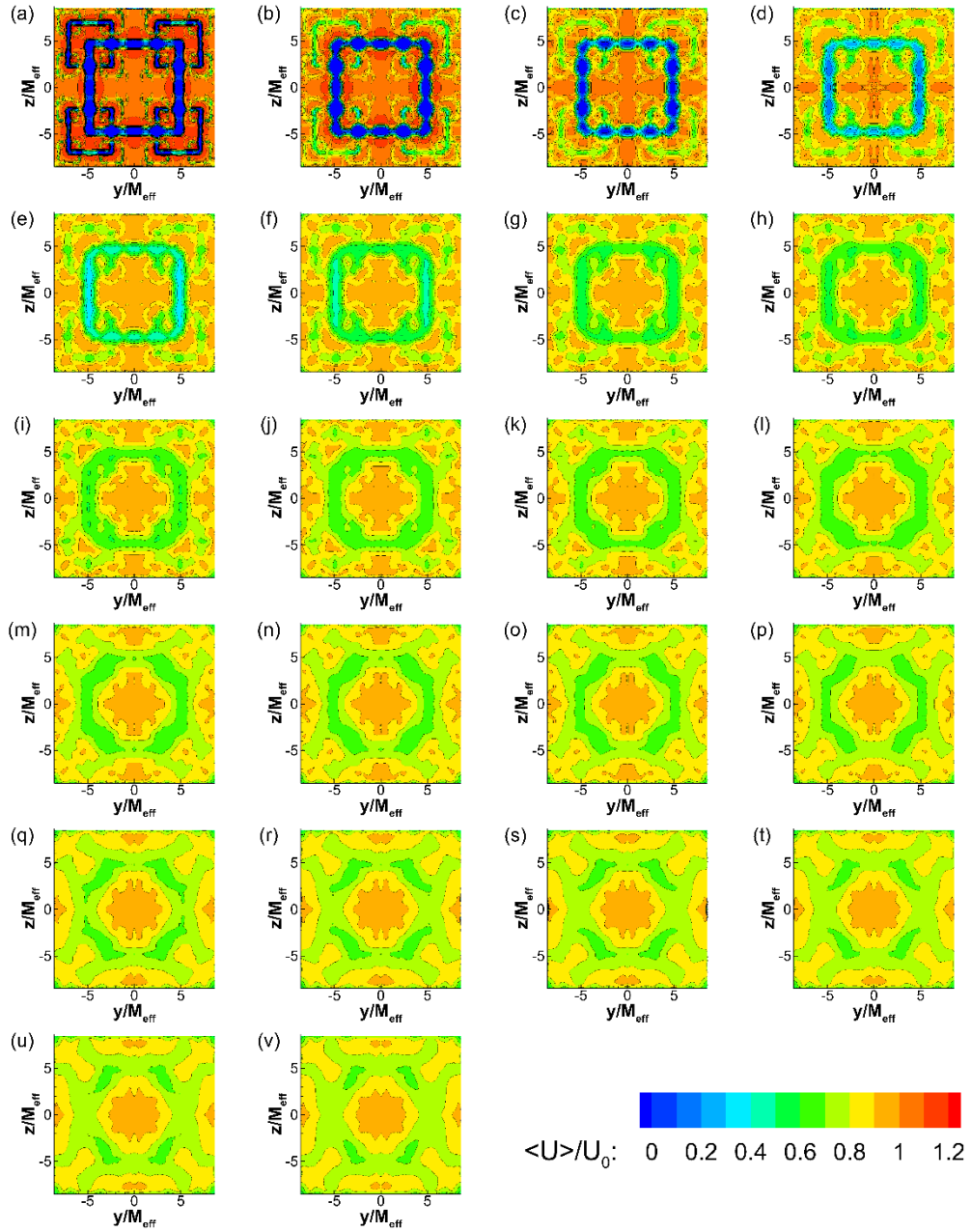
Figure 3-24 Development of normalized mean streamwise velocity $\frac{\langle U \rangle}{U_0}$ in the near grid region of FSG. Distributions are given in 1 M_{eff} increment from 1 M_{eff} (a) to 22 M_{eff} (v).
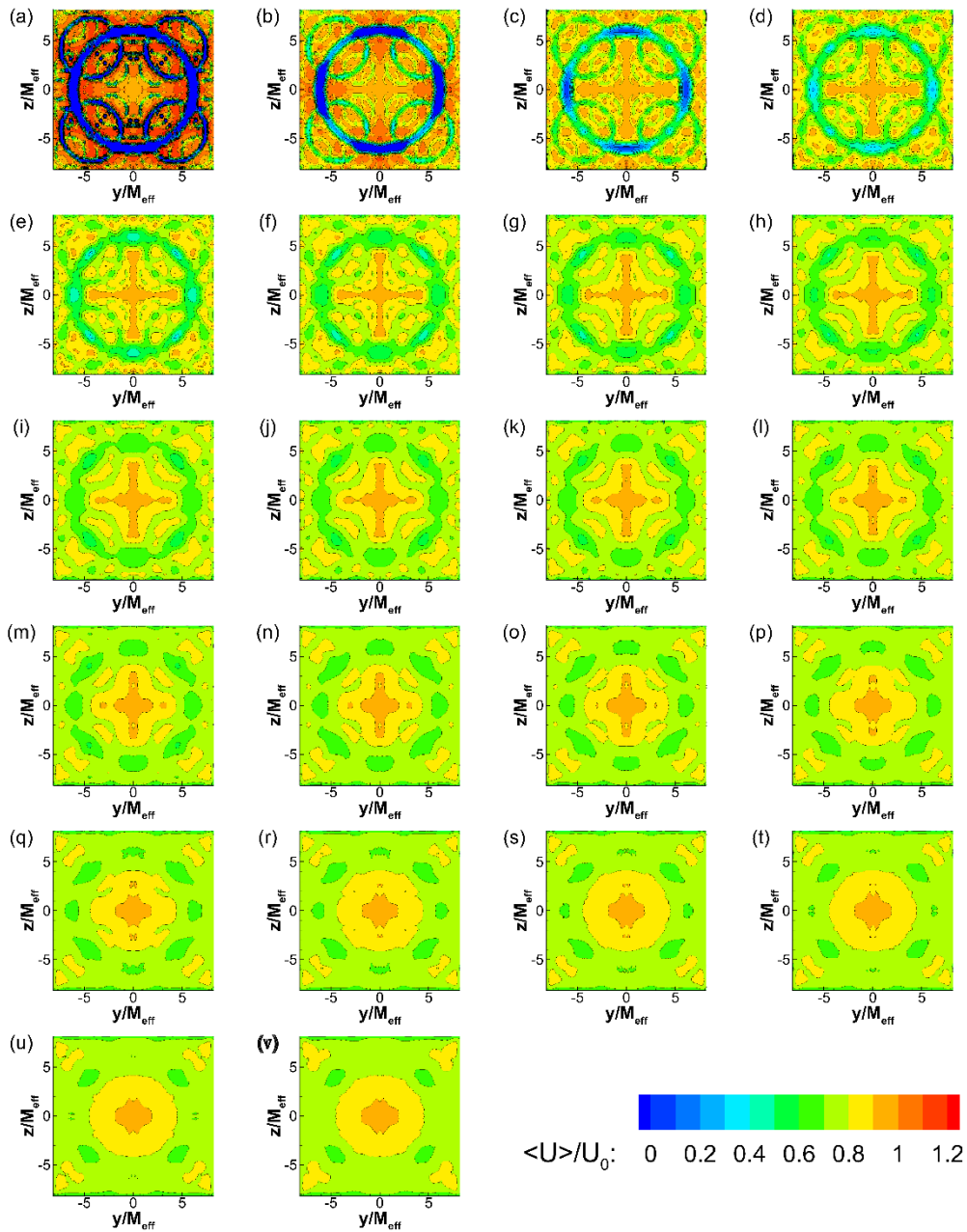
Figure 3-25 Development of normalized mean streamwise velocity $\frac{\langle U \rangle}{U_0}$ in the near grid region of FCG. Distributions are given in $1\,M_{eff}$ increment from $1\,M_{eff}$ (a) to $22\,M_{eff}$ (v).
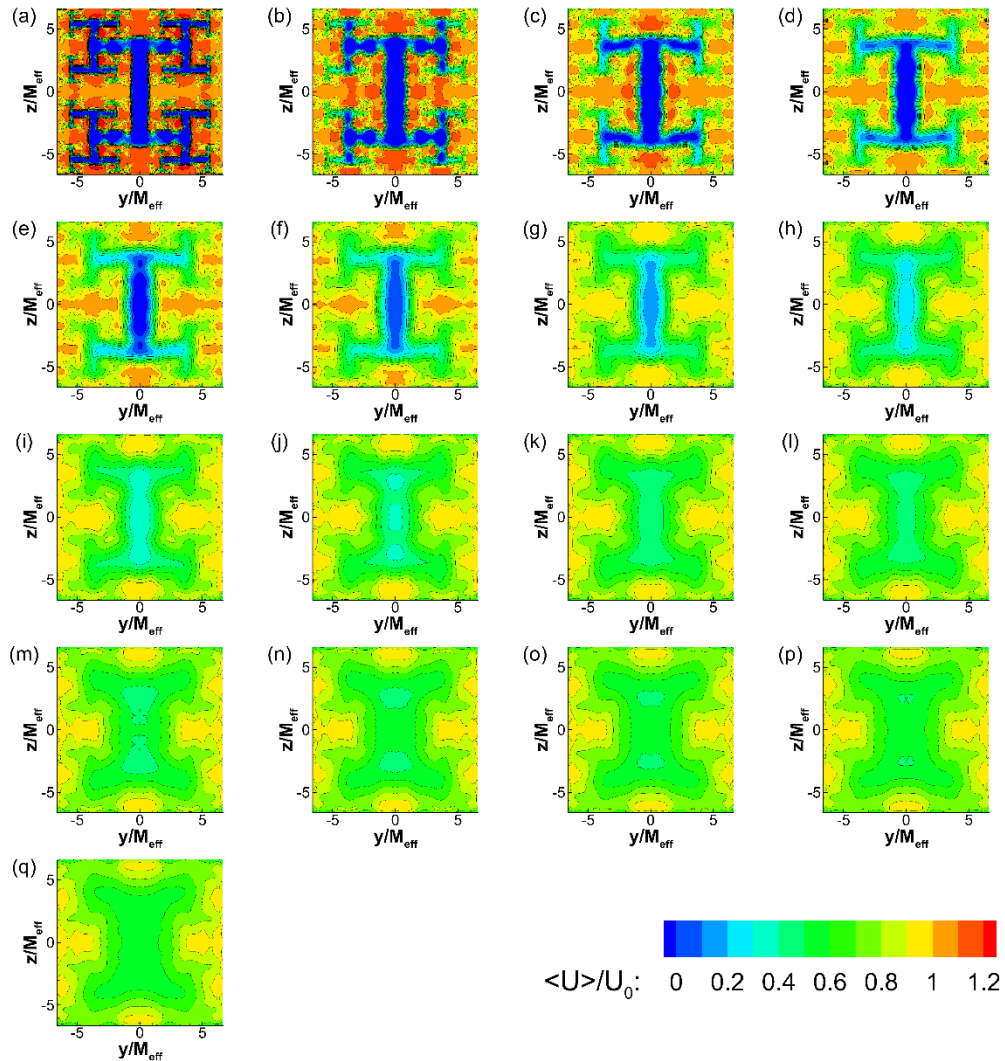
Figure 3-26 Development of normalized mean streamwise velocity $\frac{\langle U \rangle}{U_0}$ in the near grid region of FIG. Distributions are given in 1 M_{eff} increment from 1 M_{eff} (a) to 17 M_{eff} (q).

Variation of streamwise velocity along characteristic lines of TGG's as well as area averaged of those is shown in Figure 3-27. Interestingly the area averaged value is not changing very much in the near grid region of all TGG's. In Figure 3-27-a, a jet flow along C1 and wake along C4 show almost mirrored behavior regarding streamwise velocity variation, while velocity distribution along C2 and C3 from horizontal and vertical bars wake are almost the same. All streamwise velocities converge to about $0.85 U_0$ after $x/M_{eff} \approx 19$. The jet region of FSG and FCG (FS1 and FC1 in Figure

3-27-b and c, respectively), always possess higher streamwise velocity than the area averaged flow. The opposite behavior can be found in the wake of I grid (FI1 in Figure 3-27-d).
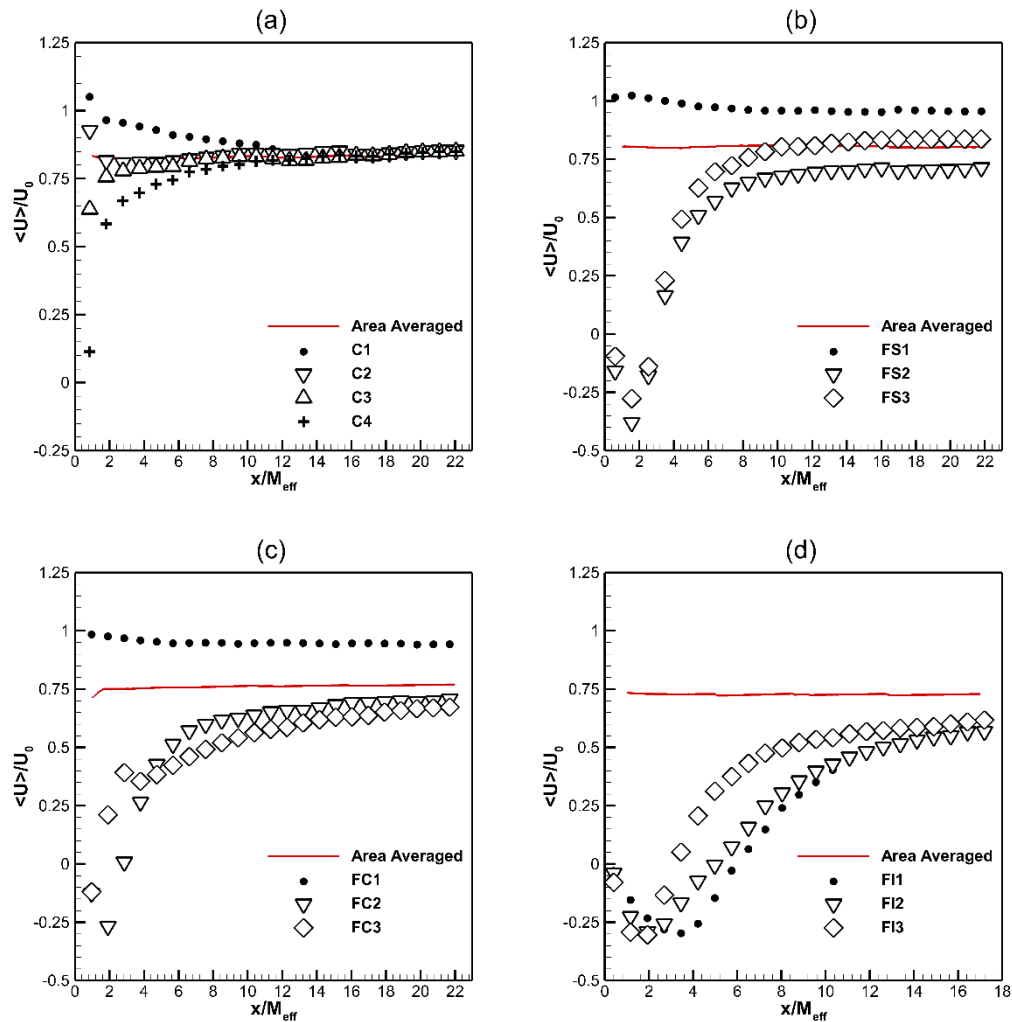
Figure 3-27 Normalized mean streamwise velocity averaged on $x = cte$ planes (red line) and along characteristic lines of TGG's. (a) CSG, (b) FSG, (c) FCG, and (d) FIG. characteristic lines are specified in section 3.1.4.
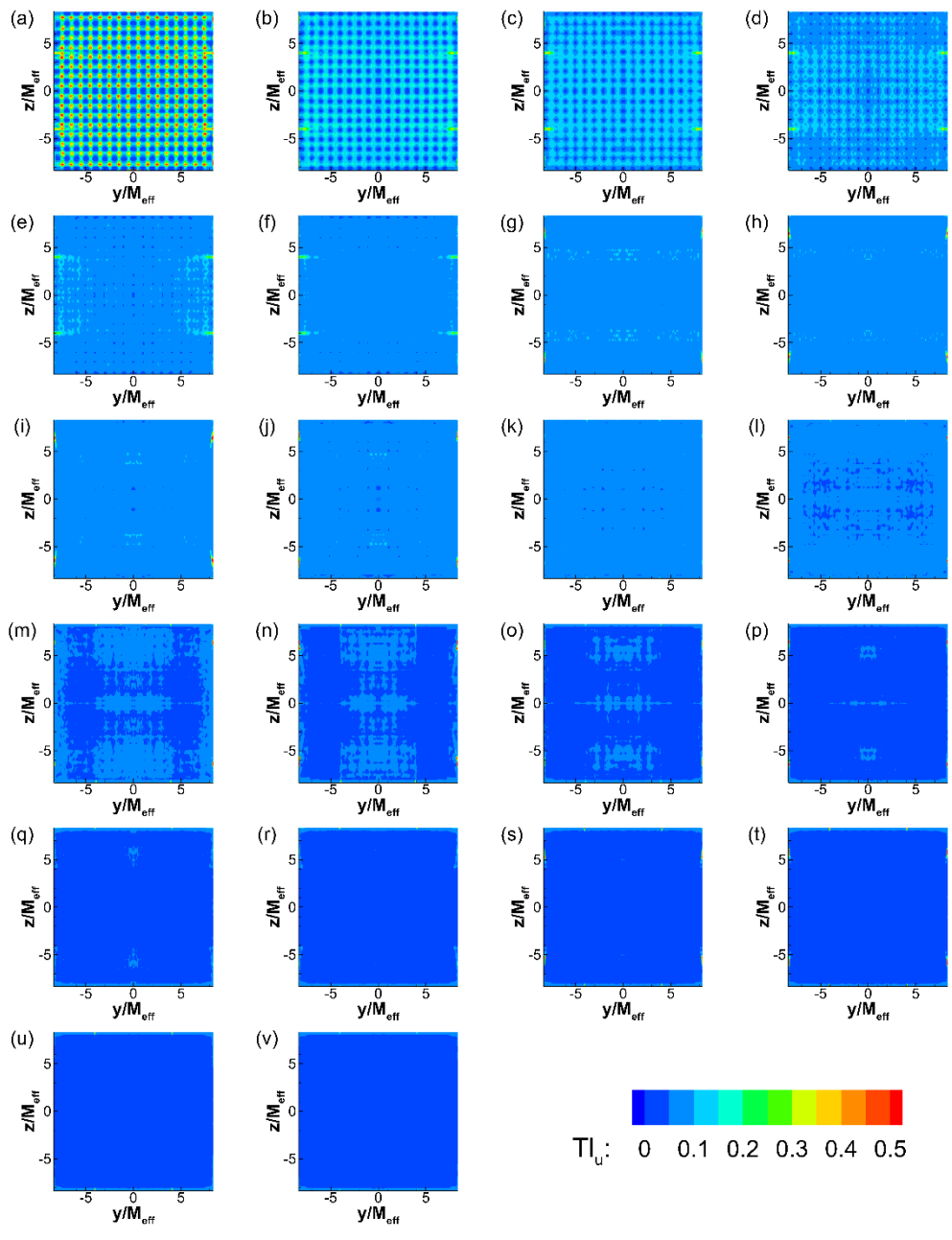
Figure 3-28 Development of the streamwise turbulence intensity TI_u in the near grid region of CSG. Distributions are given in $1\,M_{eff}$ increment from $1\,M_{eff}$ (a) to $22\,M_{eff}$ (v).

61
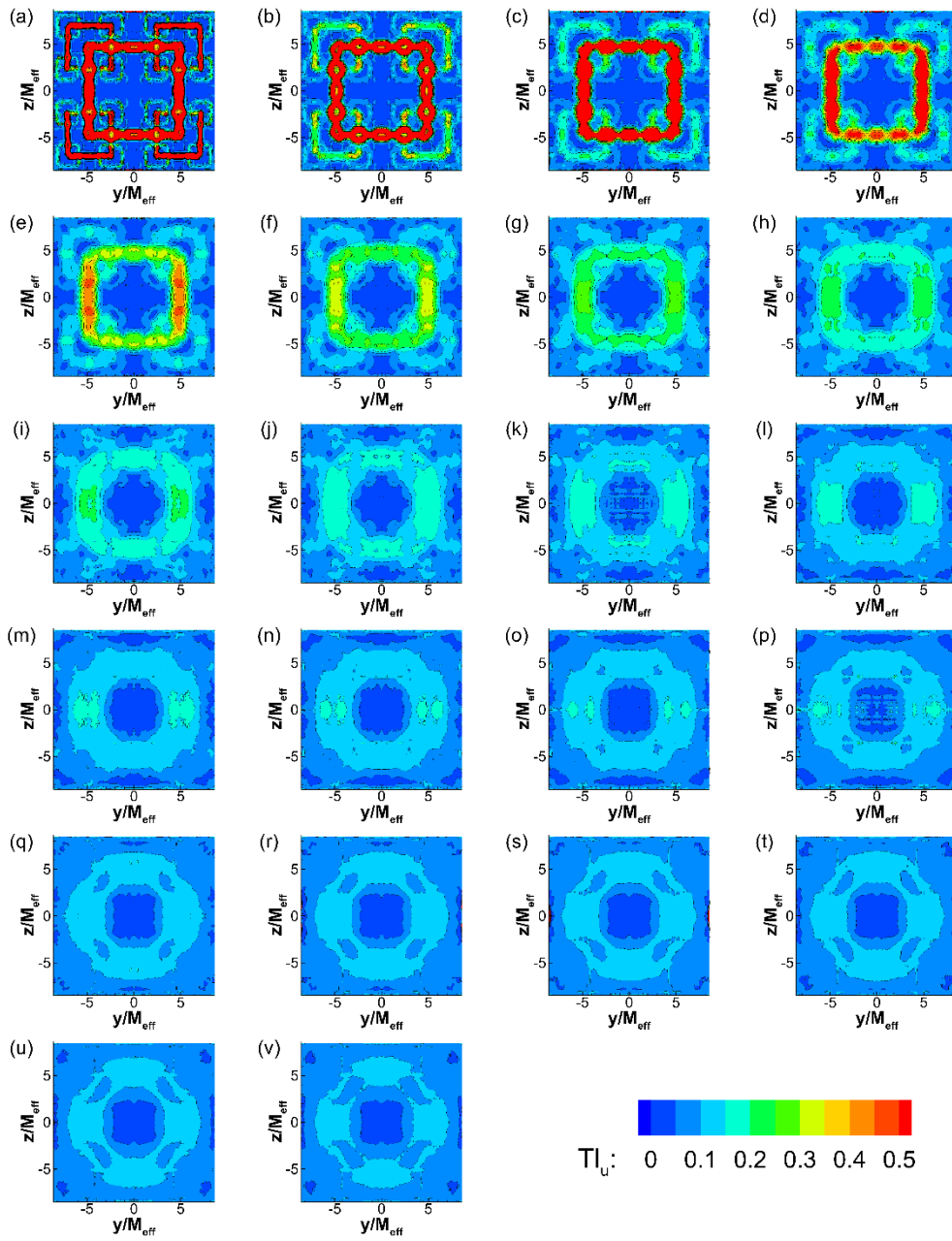
Figure 3-29 Development of the streamwise turbulence intensity TI_u in the near grid region of FSG. Distributions are given in 1 M_{eff} increment from 1 M_{eff} (a) to 22 M_{eff} (v).

62
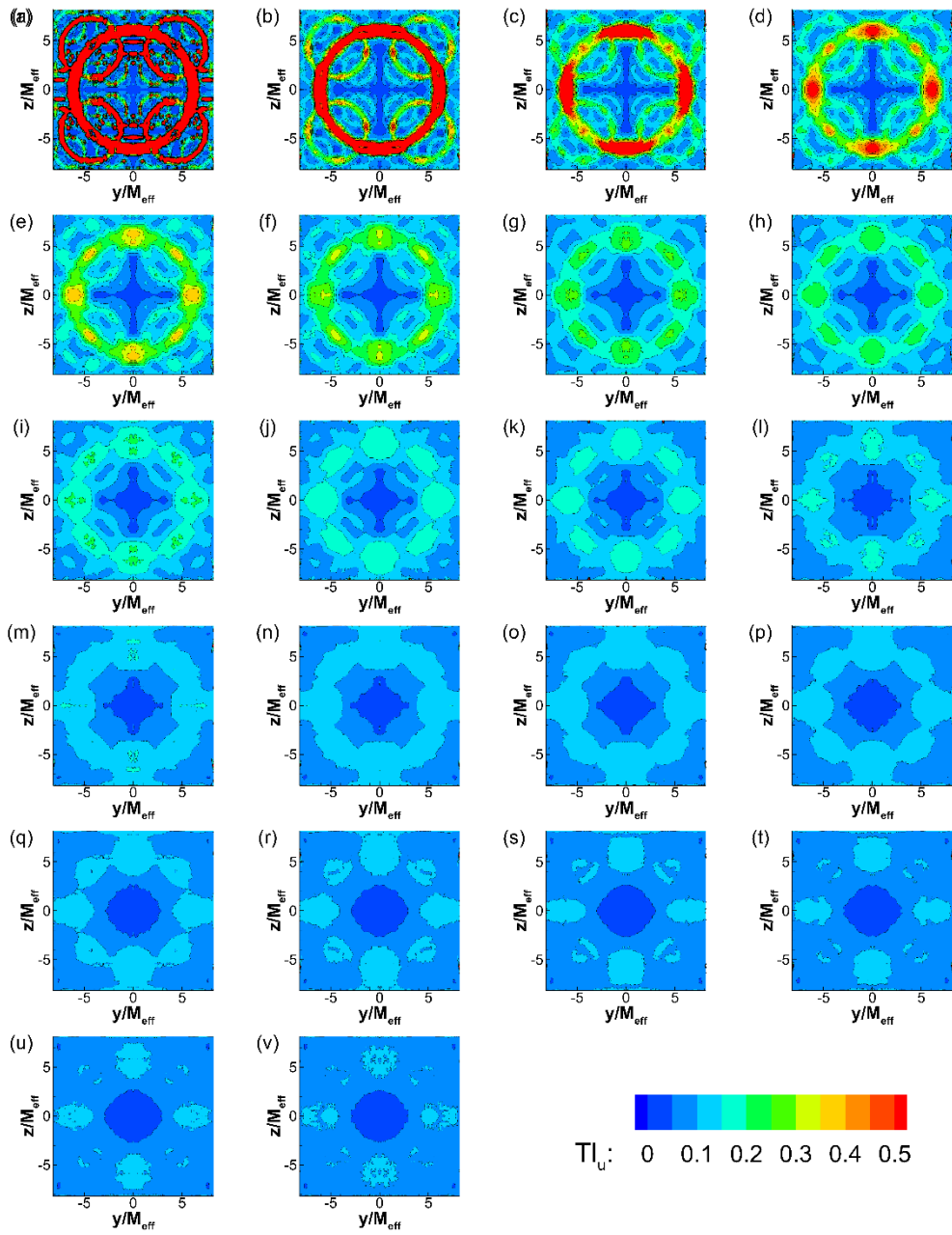
Figure 3-30 Development of the streamwise turbulence intensity TI_u in the near grid region of FCG. Distributions are given in $1\,M_{eff}$ increment from $1\,M_{eff}$ (a) to $22\,M_{eff}$ (v).
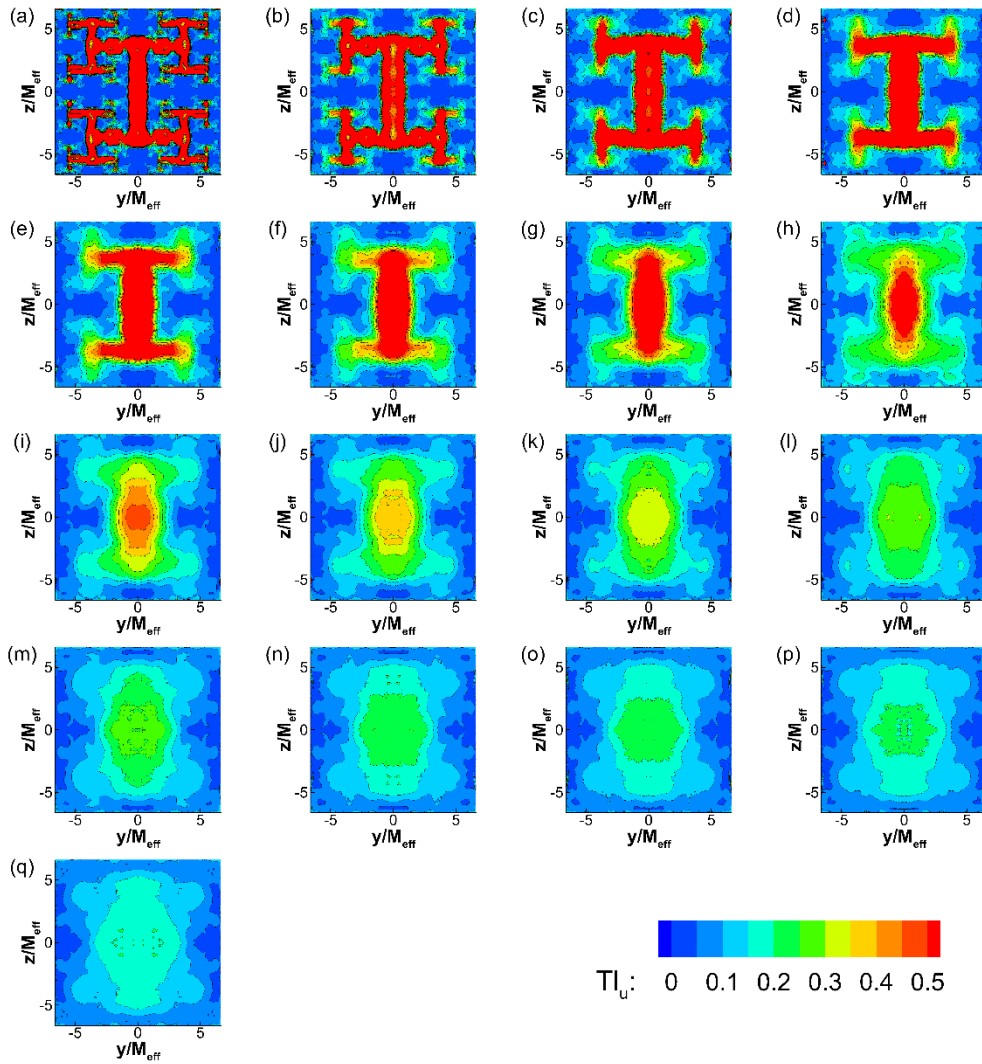
Figure 3-31 Development of the streamwise turbulence intensity TI_u in the near grid region of FIG. Distributions are given in 1 M_{eff} increment from 1 M_{eff} (a) to 17 M_{eff} (q).

Streamwise turbulence intensity along characteristic lines are shown in Figure 3-32 along with area-averaged values depicted in red. Along centerline of CSG, the peak of turbulence intensity (x_{peak}) is estimated to be at about 4.25 M_{eff} using Equation (2.9). However, our result (Figure 3-32-a) shows a peak starting at about $\frac{x}{Meff} = 6.0$ which lasts until $\frac{x}{M_{eff}} = 15.0$ and then decays. Turbulence intensity along centerline will remain at about 2-3% for FSG and FCG while it always preserves higher values in CSG case. Although FIG geometry is too different from other TGG's to declare any

explicit comparison, very high area averaged turbulence intensity in the region $0 < \frac{x}{M_{eff}} < 6$ (Figure 3-32-d) is found.
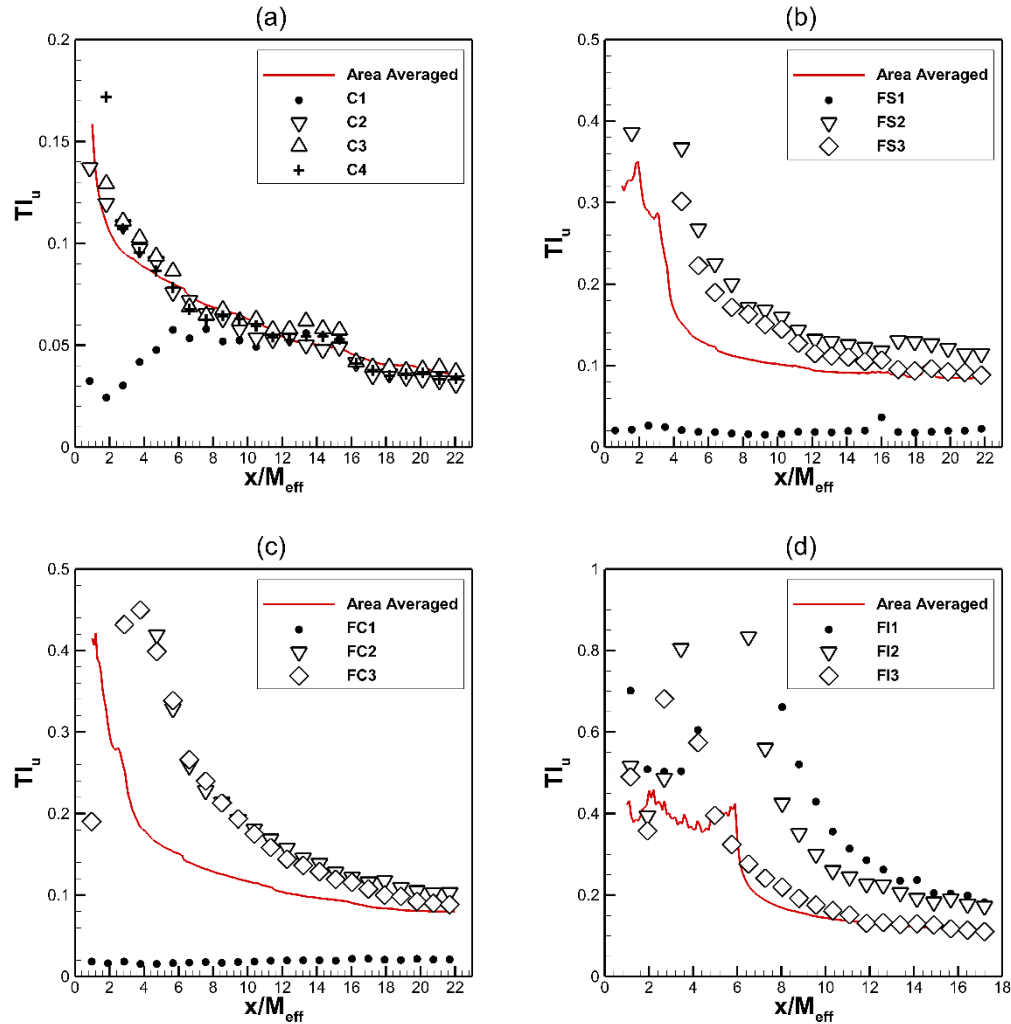
Figure 3-32 Streamwise turbulence intensity (TI_u) averaged on $x = cte$ planes (red line) and along characteristic lines of TGG's. (a) CSG, (b) FSG, (c) FCG, and (d) FIG. characteristic lines are specified in section 3.1.4.

3.2.4.2 Isotropy

In addition to homogeneity in the mean velocity and turbulence intensity, isotropy of scales inside the flow is also important, since the calculation of mean dissipation rate will be simplified in homogeneous isotropic turbulence (HIT). To assess the isotropy, skewness, and flatness of streamwise flow as well as large-scale and small-scale isotropy factors are considered.

65

The Gaussian distribution has been found to be a good approximation for each component of the velocity fluctuation in the turbulent motion behind a grid [104]. The confidence of this fitting can be examined regarding the third and fourth normalized central moments, skewness and flatness, respectively,

$$S(u) = \frac{\langle u^3 \rangle}{\langle u^2 \rangle^{\frac{3}{2}}}$$ (3.1)

$$F(u) = \frac{\langle u^4 \rangle}{\langle u^2 \rangle^2}$$ (3.2)

where u is the fluctuating streamwise velocity. In isotropic flow (i.e., Gaussian distribution) these factors should have the values of zero and three, respectively. Skewness and flatness for velocity derivative $\frac{\partial u}{\partial x}$, which was first presented by Isaza et al. [105] for regular biplane turbulence grids is used as a characteristic for the transition from near-field to far-field regions. This was validated by Hearst and Lavoie [44] for the case of FSG. Though, in this study, we do not present moments of velocity gradients. Evolution of $S(u)$ and $F(u)$ for all 4 types of TGG's are presented in appendix (B). In the following, the main focus is on the area averaged values of $S(u)$ and $F(u)$.

Generally, at large Reynolds numbers, small scales of turbulence are isotropic [106], i.e., the velocity gradient statistics are invariant to rotations and reflections about all axes [14]. This is also known as local isotropy [107]. The velocity derivative and vorticity statistics are more representative of the small-scale motions than the global isotropy parameter $\left(\frac{\langle u^2 \rangle}{\langle v^2 \rangle}\right)$. For locally isotropic turbulence [7],

$$\left\langle \left(\frac{\partial u}{\partial z}\right)^2 \right\rangle = 2 \left\langle \left(\frac{\partial u}{\partial x}\right)^2 \right\rangle$$

$$\left\langle \left(\frac{\partial w}{\partial x}\right)^2 \right\rangle = 2 \left\langle \left(\frac{\partial u}{\partial x}\right)^2 \right\rangle$$

$$\left\langle \left(\frac{\partial u}{\partial z}\right)\left(\frac{\partial w}{\partial x}\right) \right\rangle = -\frac{1}{2} \left\langle \left(\frac{\partial u}{\partial x}\right)^2 \right\rangle$$ (3.3)

$$\langle \omega_y^2 \rangle = 5 \left\langle \left(\frac{\partial u}{\partial x}\right)^2 \right\rangle$$

66

In the case of 2-D PIV results where only two components of fluctuating velocities and two gradients are available, according to derivations by Taylor [2], one can find the ratios,

$$K_1 = 2\frac{\left\langle\left(\frac{\partial u}{\partial x}\right)^2\right\rangle}{\left\langle\left(\frac{\partial v}{\partial x}\right)^2\right\rangle}, \quad K_3 = 2\frac{\left\langle\left(\frac{\partial u}{\partial x}\right)^2\right\rangle}{\left\langle\left(\frac{\partial u}{\partial y}\right)^2\right\rangle} \tag{3.4}$$

equal to 1.0 where the small scales are isotropic. It explains the responsibility of the small scales for the behavior of the velocity derivatives [14]. It is shown that local isotropy parameters do not converge to unity even far downstream of the grids ($\frac{x}{x_*^{peak}} >$ 35) and this applies to both regular and fractal grids, however values K_1 and K_3 are shown not to be very different in the case of fractal grids. On the other hand, in many studies the ratio,

$$K = \frac{\overline{\left(\frac{\partial v}{\partial x}\right)^2}}{\overline{\left(\frac{\partial u}{\partial x}\right)^2}} \tag{3.5}$$

is considered to be a criterion for small-scale isotropy [7,35,43,61,105,108,109] such that at large Reynolds numbers it is equal to 2. The evolution of area-averaged streamwise velocity, turbulence intensity, skewness, flatness, and large and small scale isotropy factors are presented in Figure 3-33.

The so-called isotropy factor is the ratio of longitudinal to transverse (span-wise) root-mean-square velocity fluctuation, i.e.

$$\frac{u'}{v'} = \frac{\sqrt{\overline{(U-\langle U\rangle)^2}}}{\sqrt{\overline{(V-\langle V\rangle)^2}}}) \tag{3.6}$$

Isotropy factor was found to be 1.15 in the far-field region of regular grids [110]. While some studies are showing the dependency of u'/v' to the Reynolds number [111], it is still being used as an indicator of large scale anisotropy [14] and the criteria of homogeneity in the spanwise direction [22].
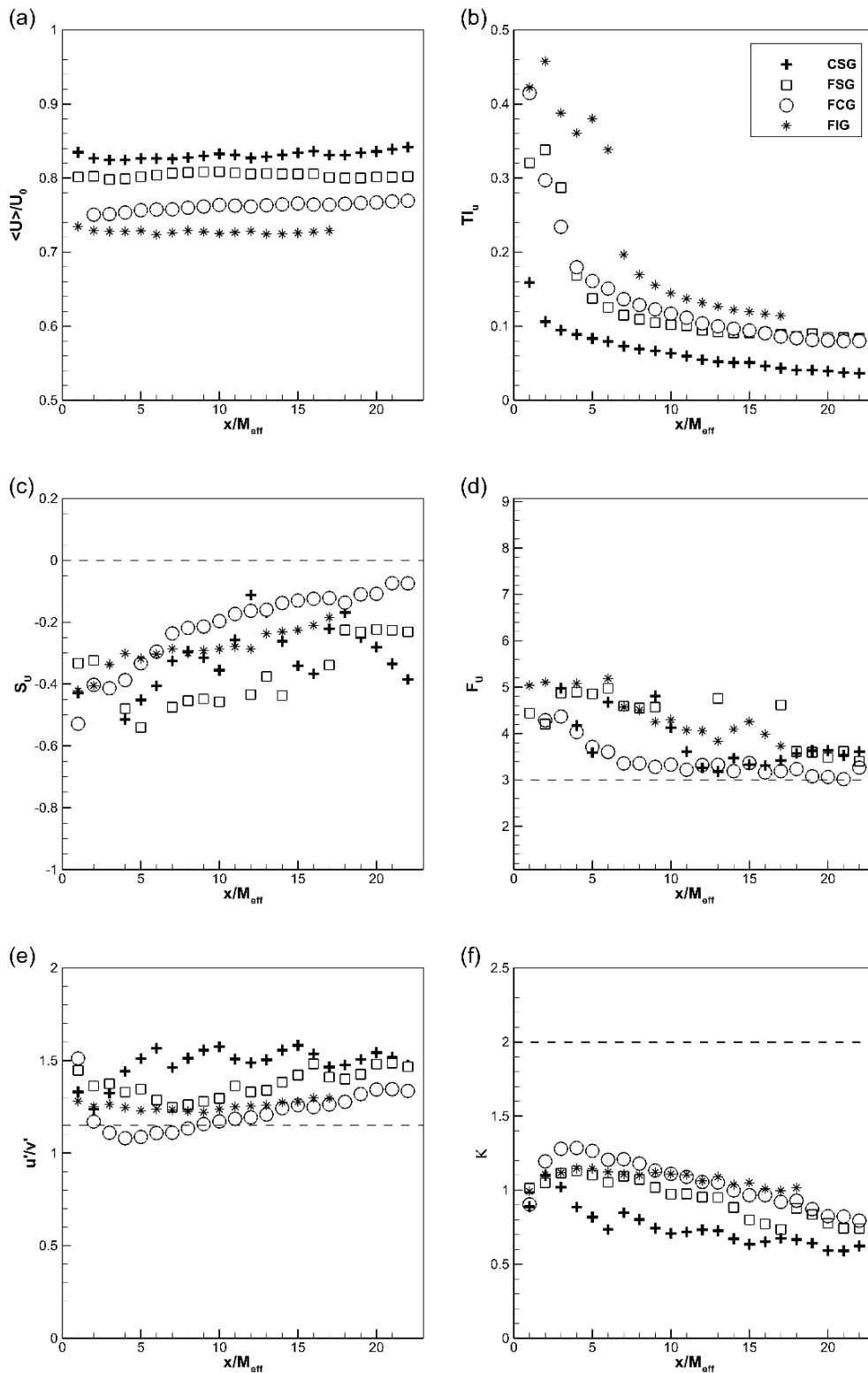
Figure 3-33 Area averaged values for normalized mean streamwise velocity (a), streamwise turbulence intensity (b), streamwise velocity skewness (c), streamwise velocity flatness (d), large-scale isotropy factor (e), and small-scale isotropy factor (f), in the near wake region of conventional and fractal grids.

Distribution of large-scale isotropy factor along the test section span, at the beginning of measurement region ($x = 1M_{eff}$) and the last point ($x = 22M_{eff}$ for CSG, FSG, and FCG) and ($x = 17M_{eff}$) for FIG, is presented in Figure 3-34.
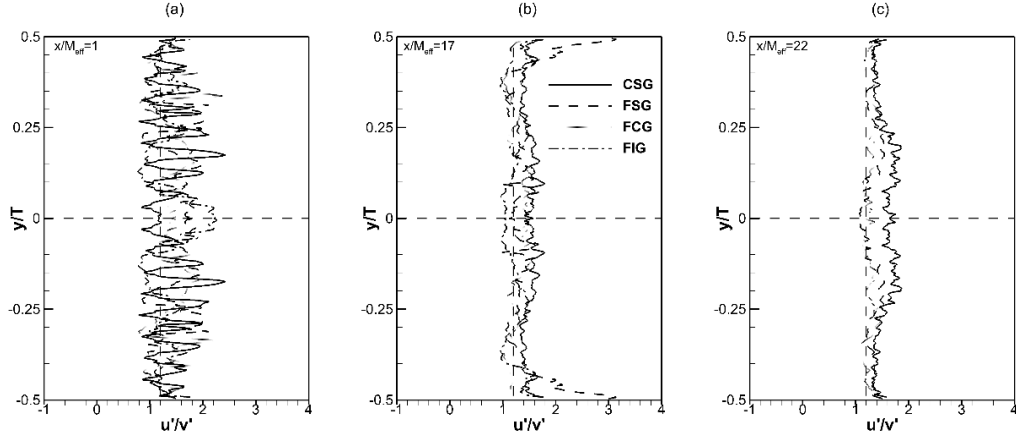
Figure 3-34 Spanwise distribution of large-scale isotropy factor (u'/v') at $x = 1, 17, 22\ M_{eff}$.

In Figure 3-35 to Figure 3-38, u'/v' distribution on cross sectional planes is shown in the near grid region of TGG's. The aim here is not to assess the local isotropy of the flow, but to find to how much extent one can rely on the simplifications based on this criteria to obtain/estimate length scales of grid-generated turbulence. In other words, if one assumes isotropy in small scales, many turbulence properties such as Taylor and Kolmogorov scales and coefficient of dissipation can be easily calculated [45],

$$\lambda^2 = \frac{15\nu u'^2}{\varepsilon} \qquad \eta = \left(\frac{\nu^3}{\varepsilon}\right)^{\frac{1}{4}} \qquad C_\varepsilon = \frac{\varepsilon}{\left(\frac{u'^3}{L_u}\right)} = \frac{\left(\frac{L_u}{\lambda}\right)}{Re_\lambda} \tag{3.7}$$

where u' is the rms of streamwise fluctuating velocity (i.e. $\sqrt{\langle (U - \langle U \rangle)^2 \rangle}$). The aim here, is to show how much deviation does exist between actual values and simplified ones. Local Taylor length-scale Reynolds number (Re_λ) is by definition,

$$Re_\lambda \equiv \frac{\sqrt{\langle u^2 \rangle}.\lambda}{\nu} \tag{3.8}$$
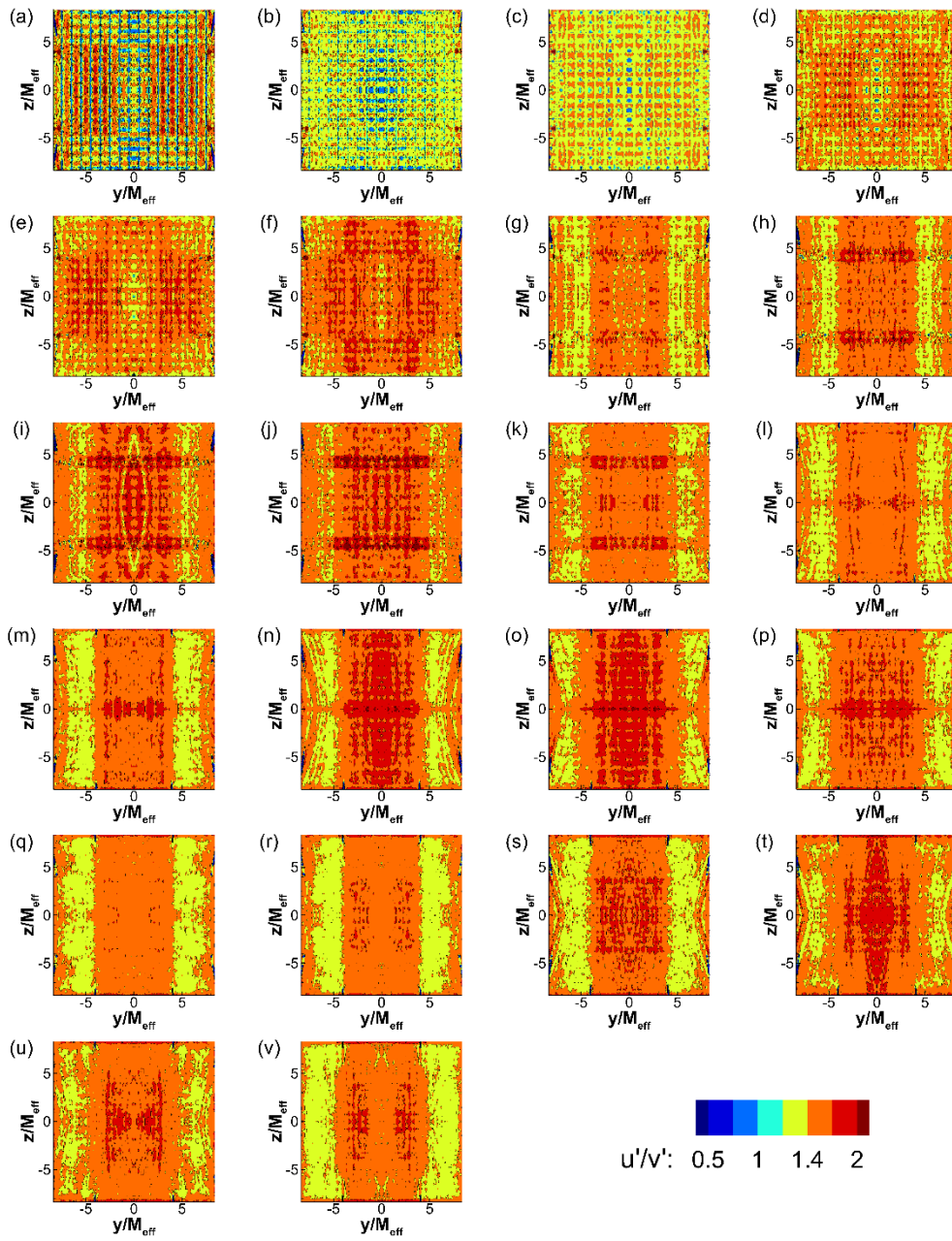
Figure 3-35 Development of large-scale isotropy factor $\frac{u'}{v'}$ in the near grid region of CSG. Distributions are given in 1 M_{eff} increment from 1 M_{eff} (a) to 22 M_{eff} (v).
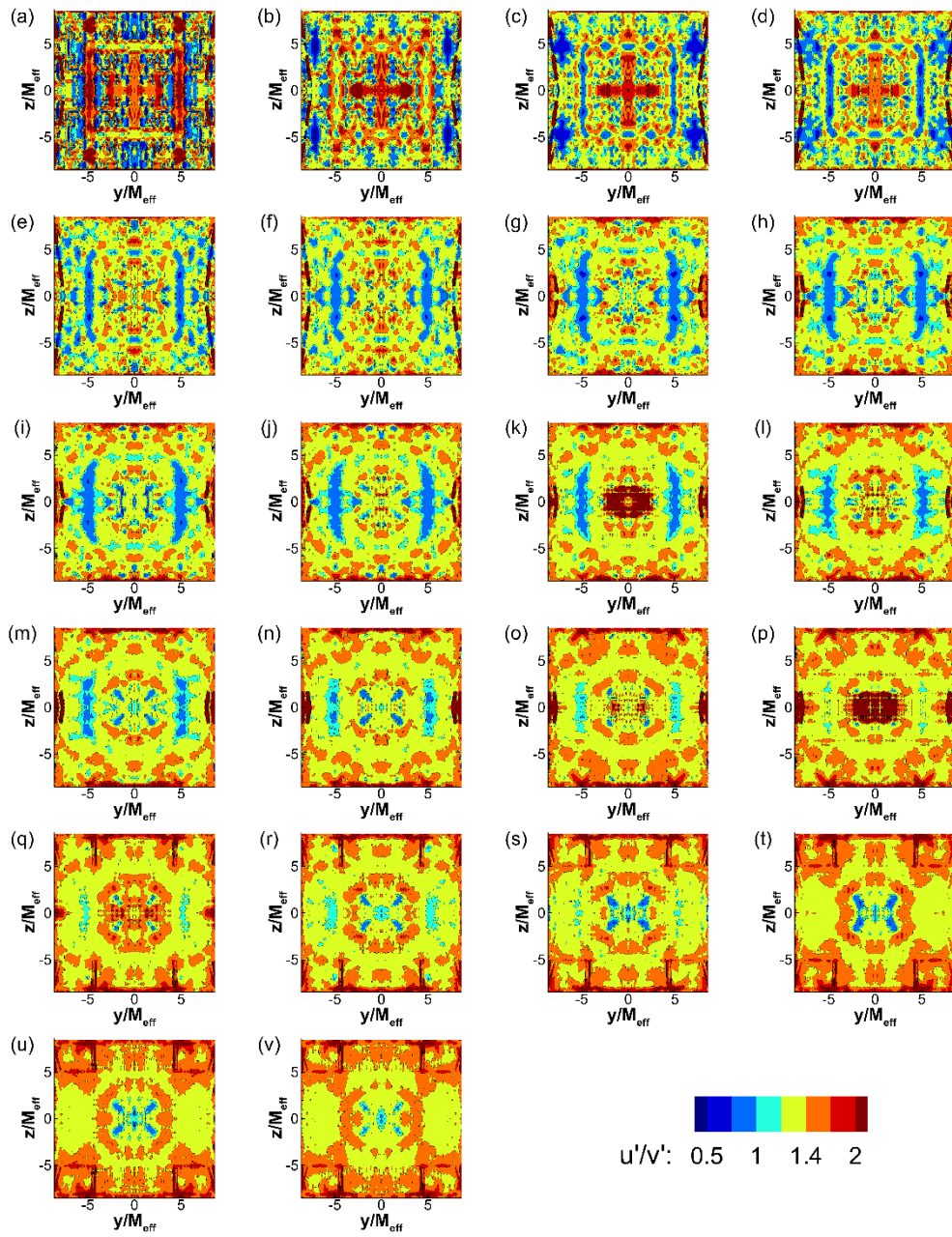
Figure 3-36 Development of large-scale isotropy factor $\frac{u'}{v'}$ in the near grid region of FSG. Distributions are given in 1 M_{eff} increment from 1 M_{eff} (a) to 22 M_{eff} (v).
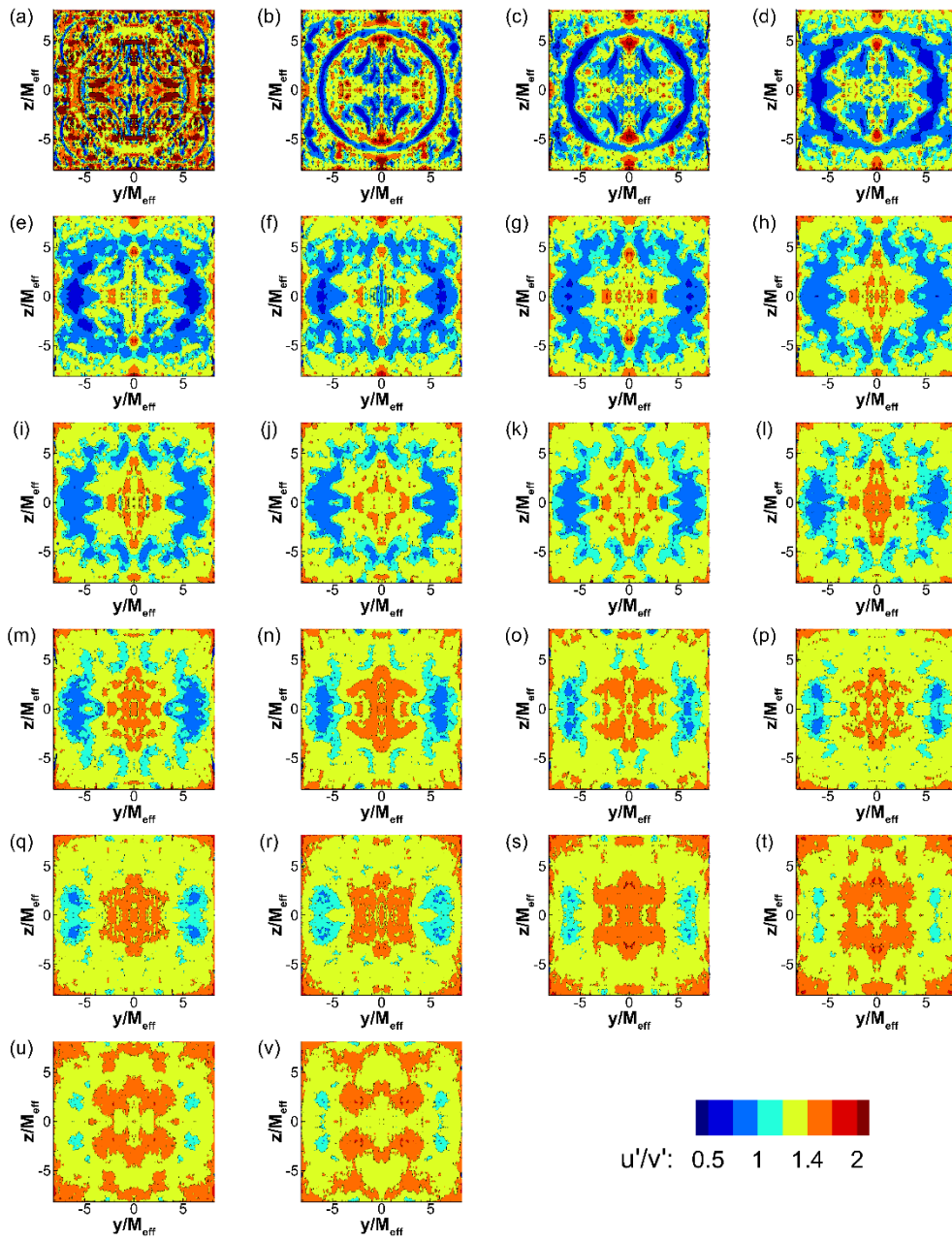
Figure 3-37 Development of large-scale isotropy factor $\frac{u'}{v'}$ in the near grid region of FCG. Distributions are given in 1 M_{eff} increment from 1 M_{eff} (a) to 22 M_{eff} (v).
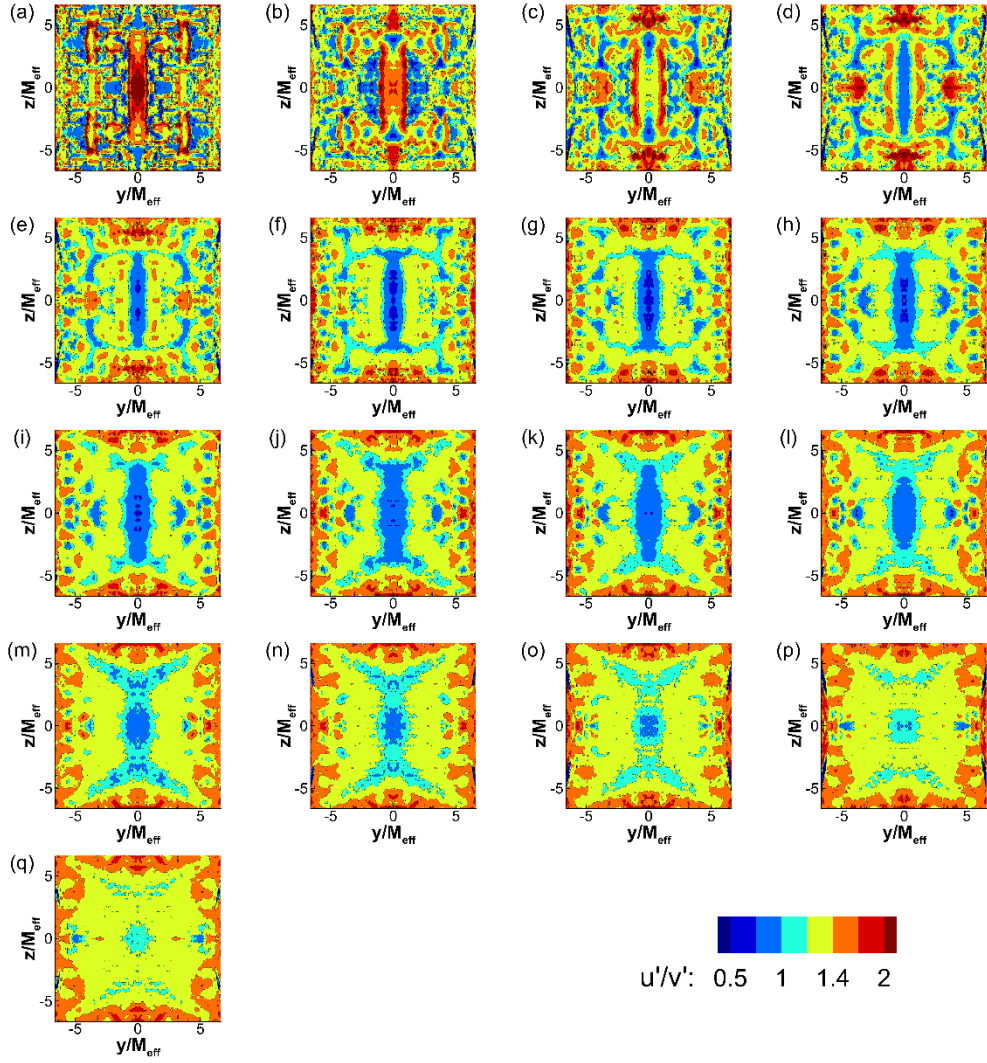
Figure 3-38 Development of large-scale isotropy factor $\frac{u'}{v'}$ in the near grid region of FIG. Distributions are given in 1 M_{eff} increment from 1 M_{eff} (a) to 17 M_{eff} (q).

3.2.4.3 Grid efficiency (Pressure drop)

The total pressure drop across the grid is due to static pressure drop and change in the kinetic energy of the flow,

$$\Delta P_T = \Delta P_S + \frac{1}{2}\rho\Delta(V^2) \tag{3.9}$$

where ΔP_T (ΔP_S) is the difference between total (static) pressures upstream and downstream of the grid and $\Delta(V^2)$ is the difference in squared mean velocity between

73

downstream and upstream locations. Measurements of static pressure drop across conventional grids show that $\Delta P_s \propto U_u^2$ [22]. Thus, one can express (3.9) in the form of pressure coefficients as,

$$C_{\Delta P_T} = C_{\Delta P_S} + \frac{\Delta(\boldsymbol{V^2})}{U_u^2} \qquad (3.10)$$

where U_u is the upstream velocity and,

$$C_{\Delta P_S} = \frac{P_S - P_{S_u}}{\frac{1}{2}\rho U_u^2} \qquad (3.11)$$

where, P_{S_u} is the static pressure measured upstream of the grid. To estimate the total pressure drop ($C_{\Delta P_T}$) across turbulence-generating grids, one needs data for static pressure. It has been already shown that the drop in static pressure coefficient ($C_{\Delta P_S}$) is minimum when the grids are space-filling, i.e. $D_f = 2.0$ [22]. It is also known that for conventional type screens in an incompressible flow, $C_{\Delta P_S}$ is particularly a function of the solidity and the Reynolds number based on the thickness of the bars [112,113]. In other words, the static pressure loss is literally the drag of the grid. Since the solidity and the minimum thickness of FSG and FCG are kept similar, one could conclude that the total pressure drop in these two grids can be determined by the kinetic energy drop. This is not the case for CSG and FIG, since the solidity and minimum thicknesses are not comparable.

Static pressure is measured upstream and downstream of TGG's with the help of a 16 channel digital pressure scanner manufactured by DSA Scanivalve, and a Pitot-static tube which is placed along the test section centerline. Data is taken at two upstream and 13 locations downstream of grids. 4000 samples are taken at each channel with a sampling frequency of 31Hz. In Figure 3-39, centerline streamwise velocity data extracted from PIV measurements is compared to that obtained from Pitot-static measurements. The pitot-static probe is aligned with x-direction, and the vertical line at x=0 represents the place where grids are mounted. Note that, here, velocities are normalized by U_0 which is the velocity at the inlet when no grid is placed inside the test section. Deviation of results in FIG (within $0 \leq x/M_{eff} \leq 5.5$) is due to error

74

arising in Pitot-static measurement within the large wake region of the largest I-element wherein majority of the flow is reversed and Pitot-tube cannot measure negative velocities, while PIV result shows complete negative velocity in this region, where the flow is very much turbulent and local flow is not aligned with the Pitot tube.
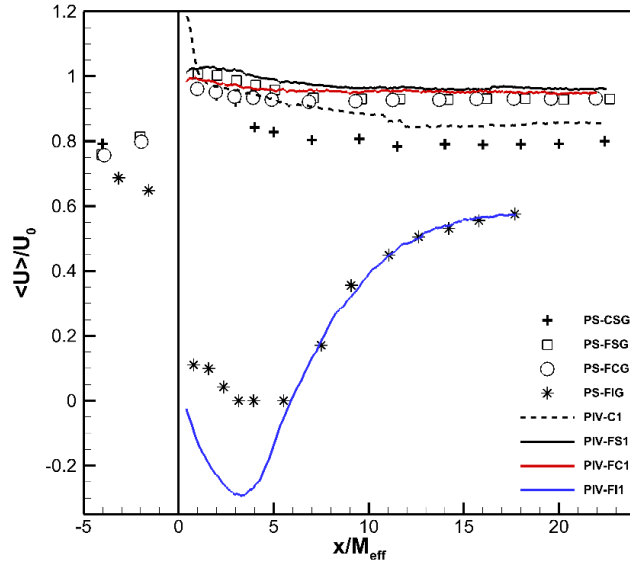
Figure 3-39 Normalized mean velocity along the centerline of TGGs. PIV data (curves) is compared to pitot-static (symbols) measurement. Vertical line at $\frac{x}{M_{eff}} = 0$ shows the grid place.

Development of $C_{\Delta P_S}$ and $C_{\Delta P_T}$ along centerline for each TGG are illustrated in Figure 3-40. Variation of $\Delta(V^2)/U_u^2$ is also depicted in Figure 3-41. For FIG, additional point (FIG-Jet) is also considered where it starts from $(x = 0, y = 0, z = 5.5M_{eff})$, (see Figure 2-10) i.e., where there is no blockage to the flow. Static pressure drop for CSG ($C_{\Delta P_S} \cong -0.4$ in Figure 3-40-left) is in agreement with that reported for a classic grid of the same solidity (σ) [22]. It is also clear that due to the higher solidity of FIG (about 29%) compared to other grids, drop in static pressure is higher even though it is measured whether along wake (blockage) or jet (opening) region. Solidity magnitude (See Table 2-1) supports the existing difference between static pressures of CSG and two fractal grids, FSG and FCG. On the other hand, initial changes in $C_{\Delta P_S}$ ($0 < \frac{x}{M_{eff}} \leq 7$) for FSG and FCG cannot be explained by blockage ratio. In fact, different geometry (bar positions) in FSG and FCG will create local differences which shows itself in the very near wake flow pressure distribution. However, since the solidity

75

values of FSG and FCG are very close, static pressure drop converges to a single value $(C_{\Delta P_S} \cong -0.52)$ after about $\frac{x}{M_{eff}} = 7$.
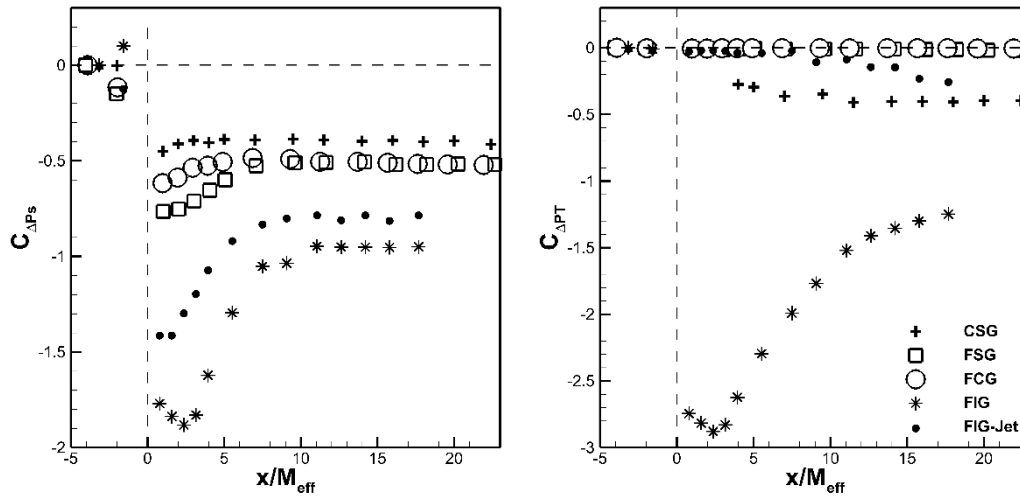
Figure 3-40 Coefficient of static pressure (left), and total pressure (right) difference across TGGs. Values are obtained along the centerline. The vertical dashed line represents the location of the grid. The horizontal dashed line represents zero pressure difference.

According to Figure 3-40, drop in total pressure $(C_{\Delta P_T})$ is very low (less than 2%) along the centerline of FSG and FCG compared to CSG and FIG. This implies that to evaluate the efficiency of these grids, one either should capture the whole cross sectional distribution of total pressure (traversing a Kiel probe is suggested) or should rely on static pressure values which seems to be more promising.

In Figure 3-41, dynamic pressure $(0.5\rho U^2)$ is normalized by its upstream value $(0.5\rho U_u^2)$. $\Delta(U^2)/U_u^2$ is the difference between downstream and upstream points. Values presented by symbols are directly obtained from the readings of the Pitot-static tube. Hence, the existence of incompatible results within the wake of FIG ($1 \leq \frac{x}{M_{eff}} \leq$ 5.5) where the readings of Pitot-tube are not correct, is explicable. Coefficient of dynamic pressure difference along centerline as well as the jet region of FIG obtained by PIV are shown in Figure 3-41 by dashed and solid lines. It is clear that along any line in the jet (opening) regions, the coefficient of dynamic pressure difference is

positive, unlike the region behind the wake of I bar which shows whole negative values.
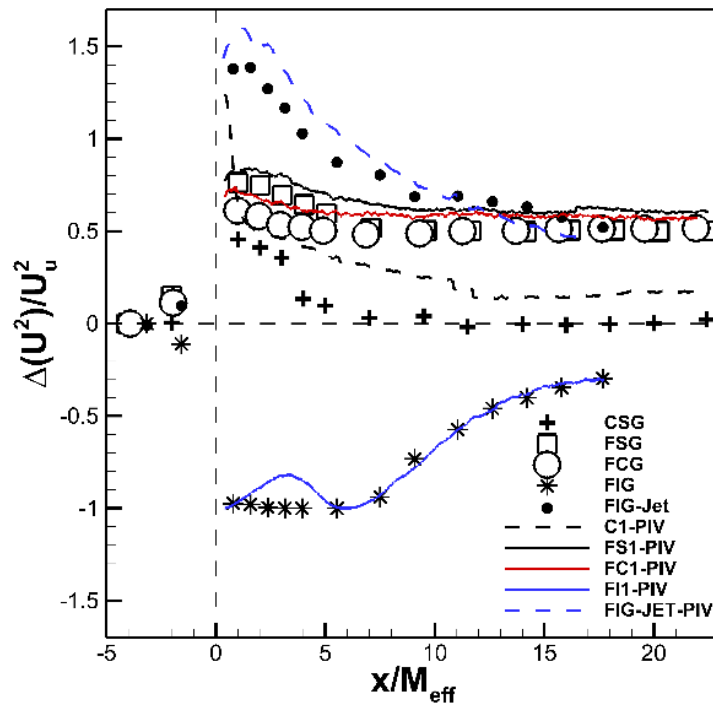
Figure 3-41 Coefficient of dynamic pressure difference across TGGs. Values are obtained along the centerline. The vertical dashed line represents the location of the grid. The horizontal dotted line represents zero velocity difference.

For grids to be used as a mixing device, the aim is to obtain the highest turbulence intensity, with the lowest pressure loss, while maintaining the geometry of grid as simple as possible so the production cost will be minimum. Therefore, it is valuable to compare turbulence intensity to static pressure drop as representatives for gain and loss, respectively, in the system. Turbulence intensity averaged on $x = cte$ planes is introduced before. Values of the static pressure drop coefficient ($C_{\Delta P_s}$) are available at 13 downstream locations. Data for TI_u is extracted at the same locations and compared to the loss. This tells us how much turbulence intensity (on average) is obtained in return of static pressure loss. Since the geometry of FIG is irrelevant to other three grids, only the results of CSG, FSG, and FCG are shown in the *"performance-chart"* in Figure 3-42.
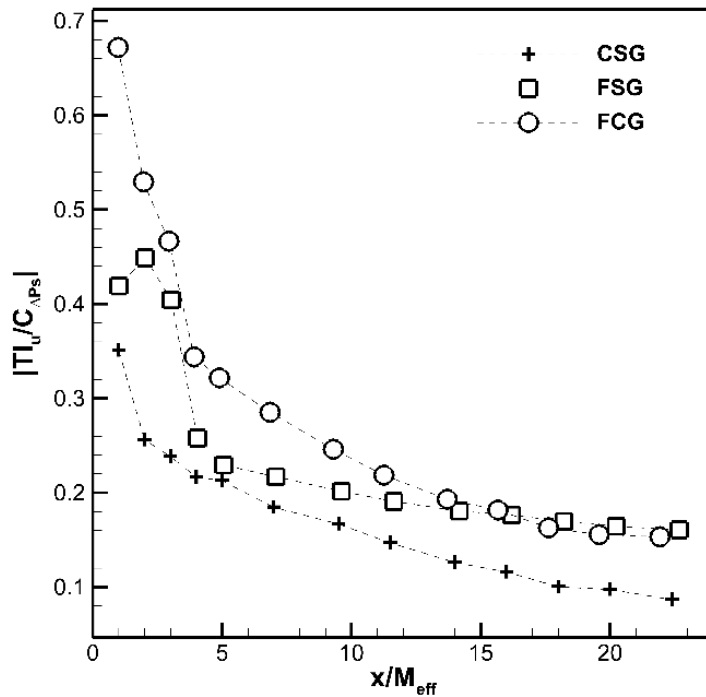
Figure 3-42 Ratio of streamwise turbulence intensity to static pressure drop coefficient along the centerline of TGG's. Downstream distance x is normalized by effective mesh size (M_{eff}).

It is clear that fractal grids with square and circular patterns would be advantageous over conventional grid if a limited distance is required for turbulence enhancement. However, after about $\frac{x}{M_{eff}} = 14.0$ square and circular grids show almost the same performance but still almost 100% higher than the conventional grid. In the very near wake region ($1 < \frac{x}{M_{eff}} < 5$) the performance of FCG is twice that of CSG and 20% higher than that of FSG.

As solidities of all grids are different, one can normalize the performance, i.e., $TI_u/C_{\Delta P_S}$ with respect to grid solidity. Variation of $\left(TI_u / C_{\Delta P_S} \right) / \sigma$ is shown in Figure 3-43, including FIG. According to this figure, normalization introduces minor changes only in the case of CSG. In fact, this chart indicates more or less the same performance of conventional and fractal grids, again excluding FIG from this evaluation.

78
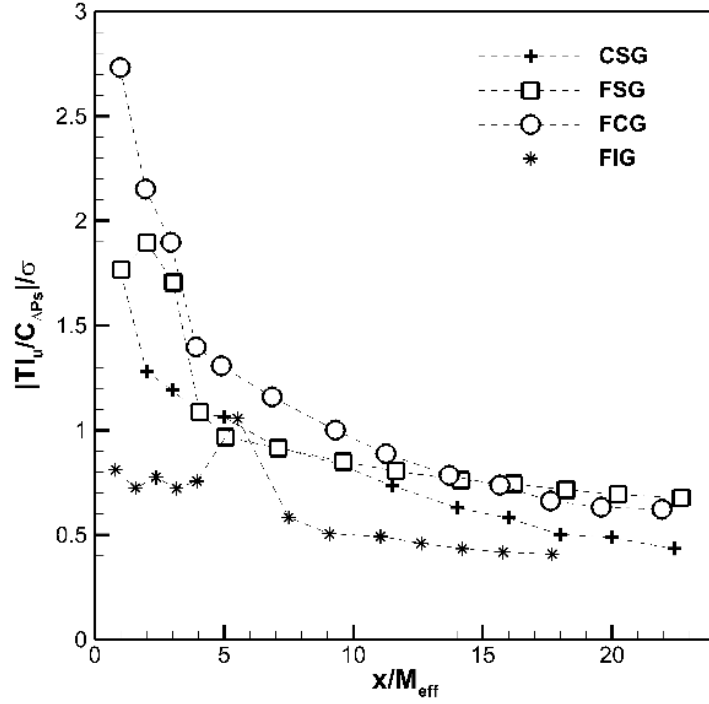
Figure 3-43 Performance of conventional and fractal grids normalized by grid solidity $(^{TI_u}\!/_{C_{\Delta P_S}}\,/\sigma)$. Downstream distance x is normalized by effective mesh size (M_{eff}).

3.2.4.4 Reynolds Stresses

Reynolds stress tensor (RST) plays an important role in momentum transport and mixing efficiency in turbulent flows because it represents the rate of mean momentum transfer by turbulent fluctuations [96]. Fractal grids were shown to produce larger turbulent stress values resulting from different length scale interactions [114]. Reynolds stress tensor is defined as,

$$\begin{bmatrix} \langle u^2 \rangle & \langle uv \rangle & \langle uw \rangle \\ \langle vu \rangle & \langle v^2 \rangle & \langle vw \rangle \\ \langle wu \rangle & \langle wv \rangle & \langle w^2 \rangle \end{bmatrix} \tag{3.12}$$

where the velocity fluctuations are the difference between instantaneous and ensemble averaged quantities.

79
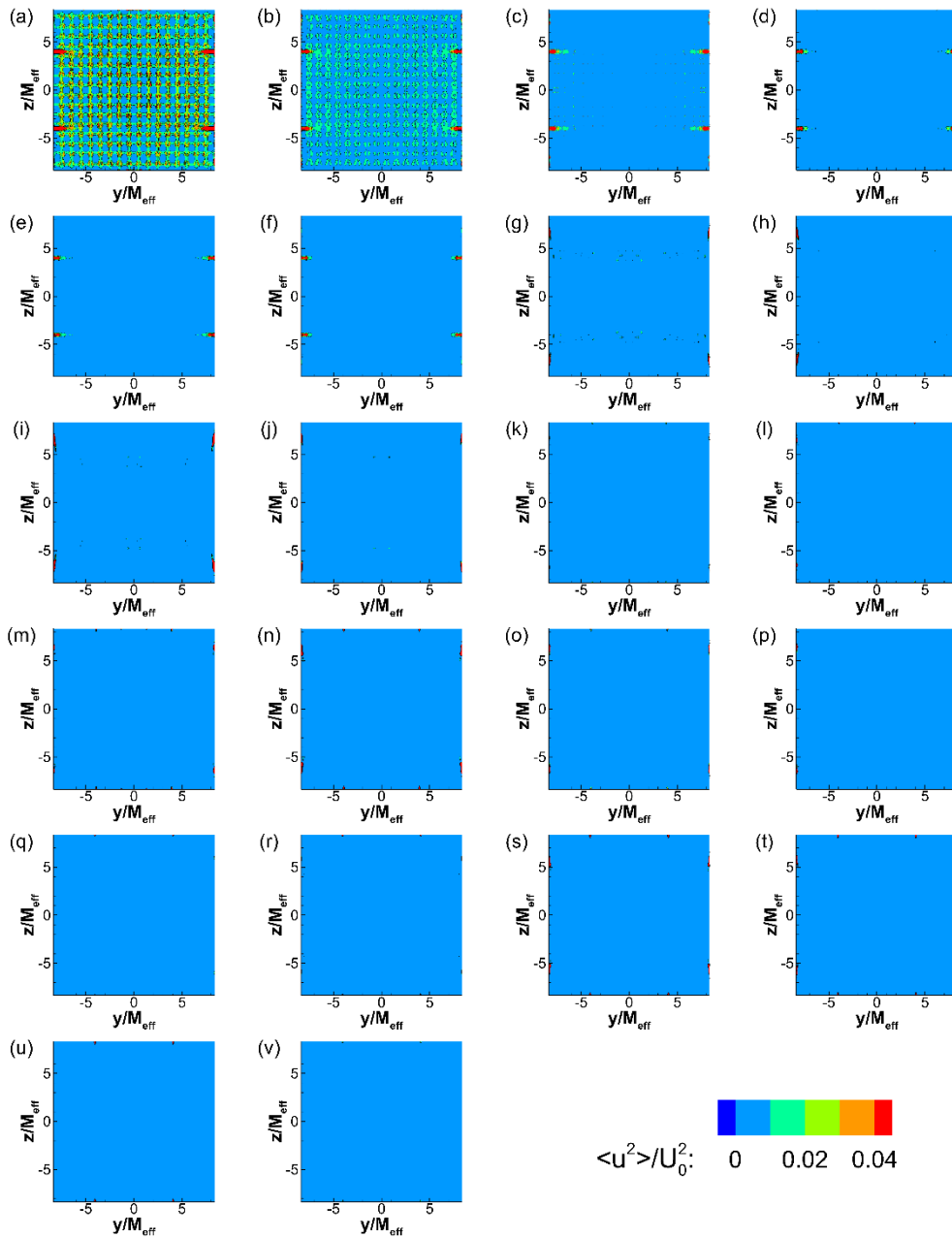
Figure 3-44 Development of the Reynolds normal stress $\langle u^2 \rangle$ in the near grid region of CSG. Distributions are given in 1 M_{eff} increment from 1 M_{eff} (a) to 22 M_{eff} (v).
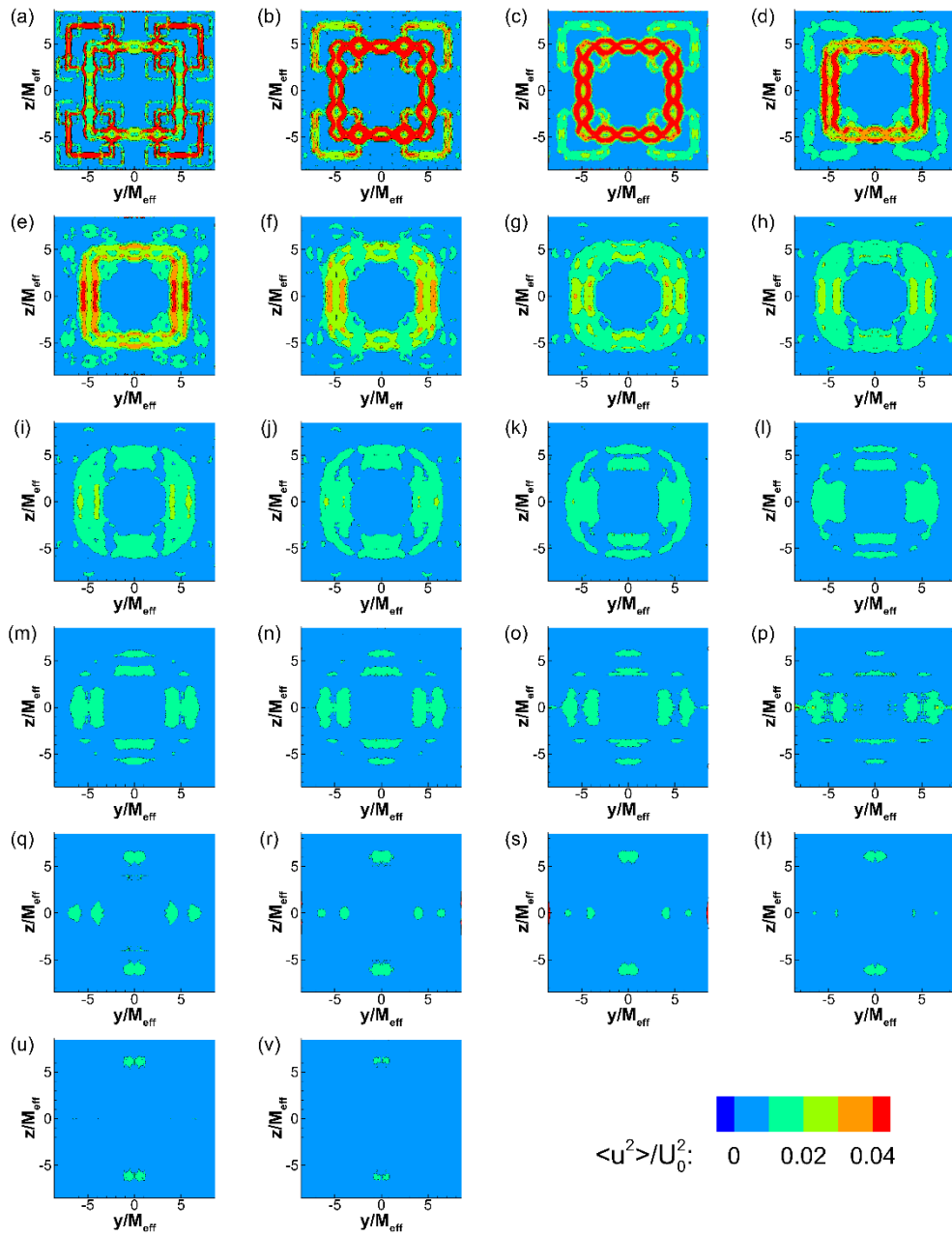
Figure 3-45 Development of the Reynolds normal stress $\langle u^2 \rangle$ in the near grid region of FSG. Distributions are given in 1 M_{eff} increment from 1 M_{eff} (a) to 22 M_{eff} (v).
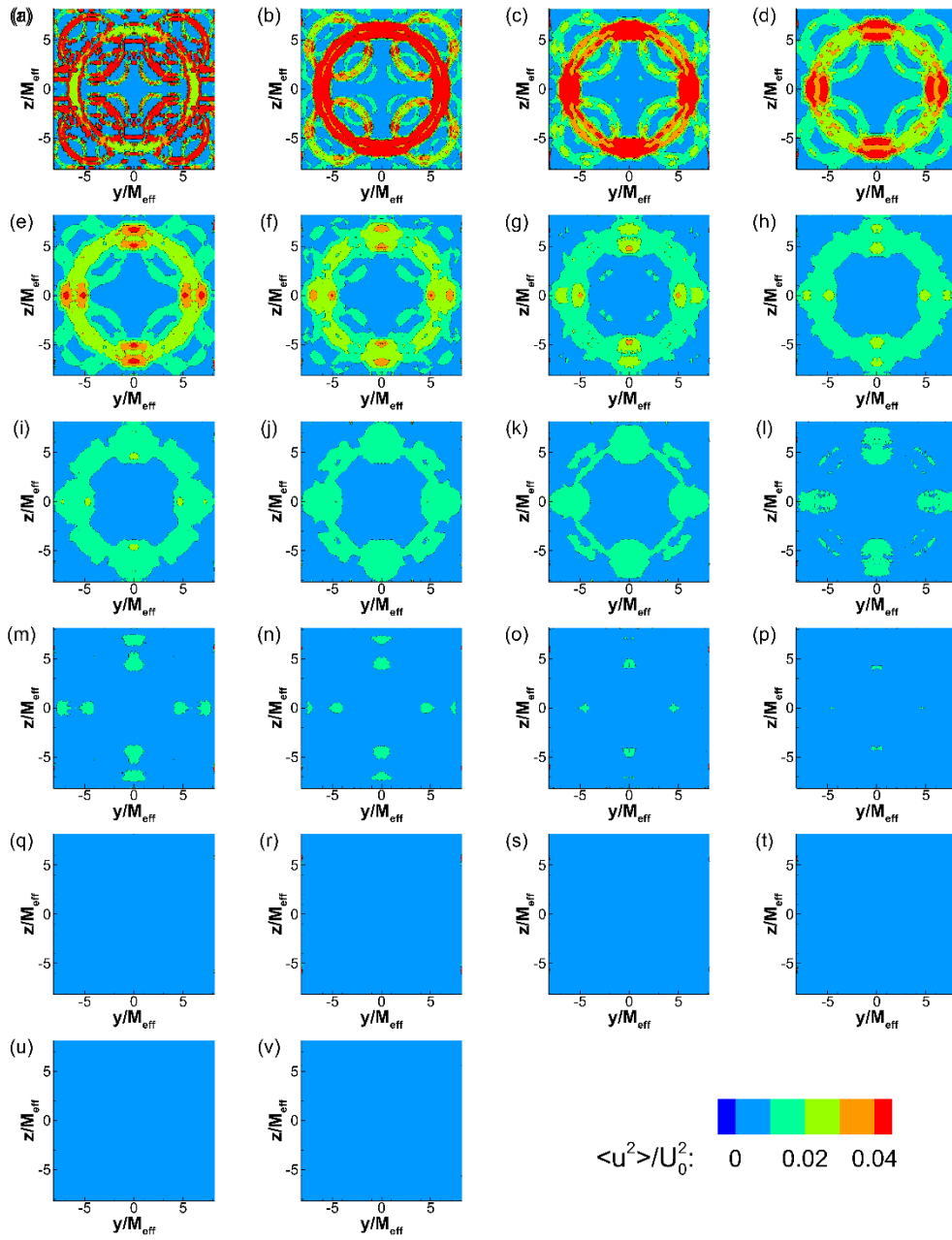
Figure 3-46 Development of the Reynolds normal stress $\langle u^2 \rangle$ in the near grid region of FCG. Distributions are given in 1 M_{eff} increment from 1 M_{eff} (a) to 22 M_{eff} (v).
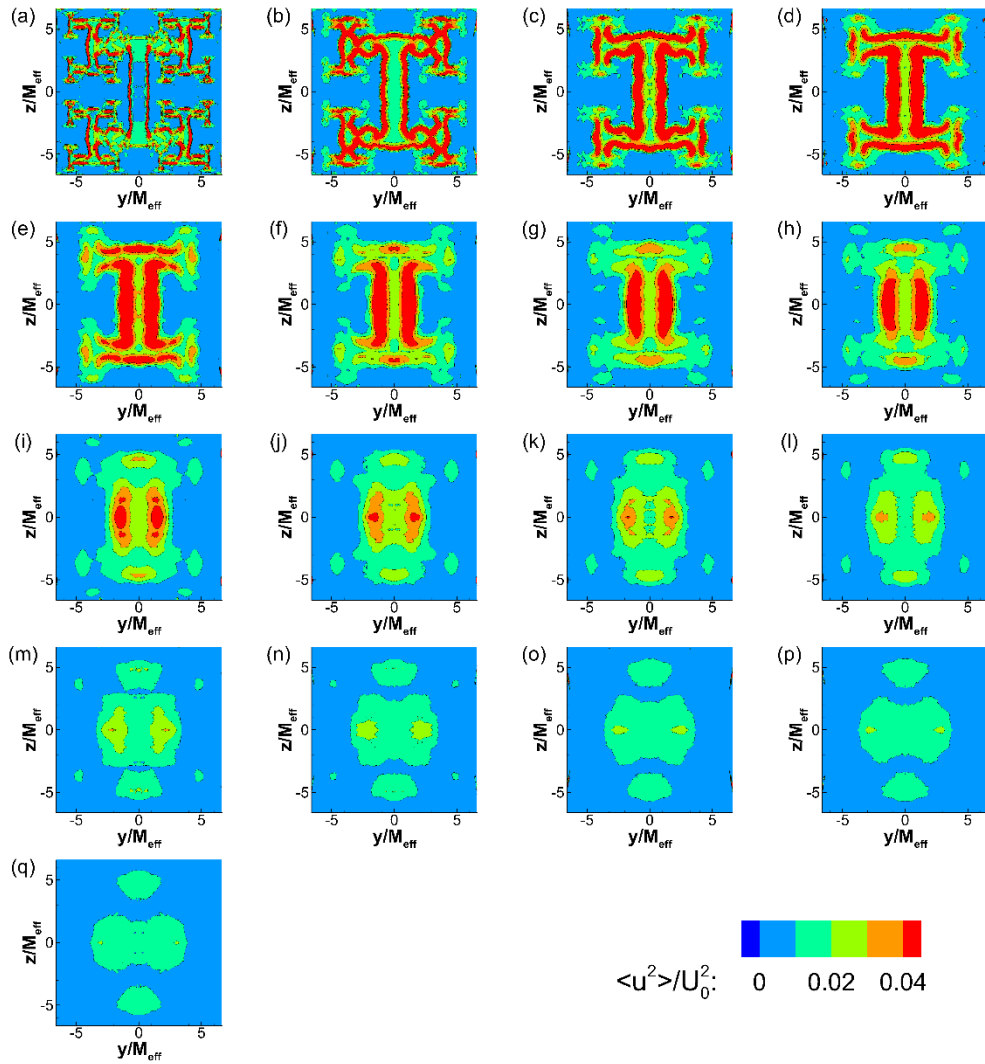
Figure 3-47 Development of the Reynolds normal stress $\langle u^2 \rangle$ in the near grid region of FIG. Distributions are given in 1 M_{eff} increment from 1 M_{eff} (a) to 17 M_{eff} (q).

It has been shown previously that the whole RST would be obtained if all velocity components are available. From 2-D PIV data $\langle uw \rangle = \langle wu \rangle$ is estimated as long as the assumption of symmetric flow is valid. However, distributions of Reynolds normal stress (RNS) $\langle u^2 \rangle$ and Reynolds shear stress (RSS) $\langle uv \rangle$ normalized by the free stream velocity U_0, are obtained and some examples are illustrated in Figure 3-44 to Figure 3-51. When averaging Reynolds shear stresses on $x = cte$ planes, due to symmetry the values near zero are expected. Average of Reynolds normal stress $\langle u^2 \rangle$ will show the same trend as in TKE. Normalized Reynolds shear stress (NRSS) $\frac{\langle uv \rangle}{U_u^2}$ obtained from PIV data is also compared to the magnitude of the static pressure drop $\left| C_{\Delta P_S} \right|$ in

83

Figure 3-52. It should be noted that the values are selected along the centerline of TGG's; therefore high shear in the case of FIG should not confuse the reader. This time, CSG dominates over fractal grids.
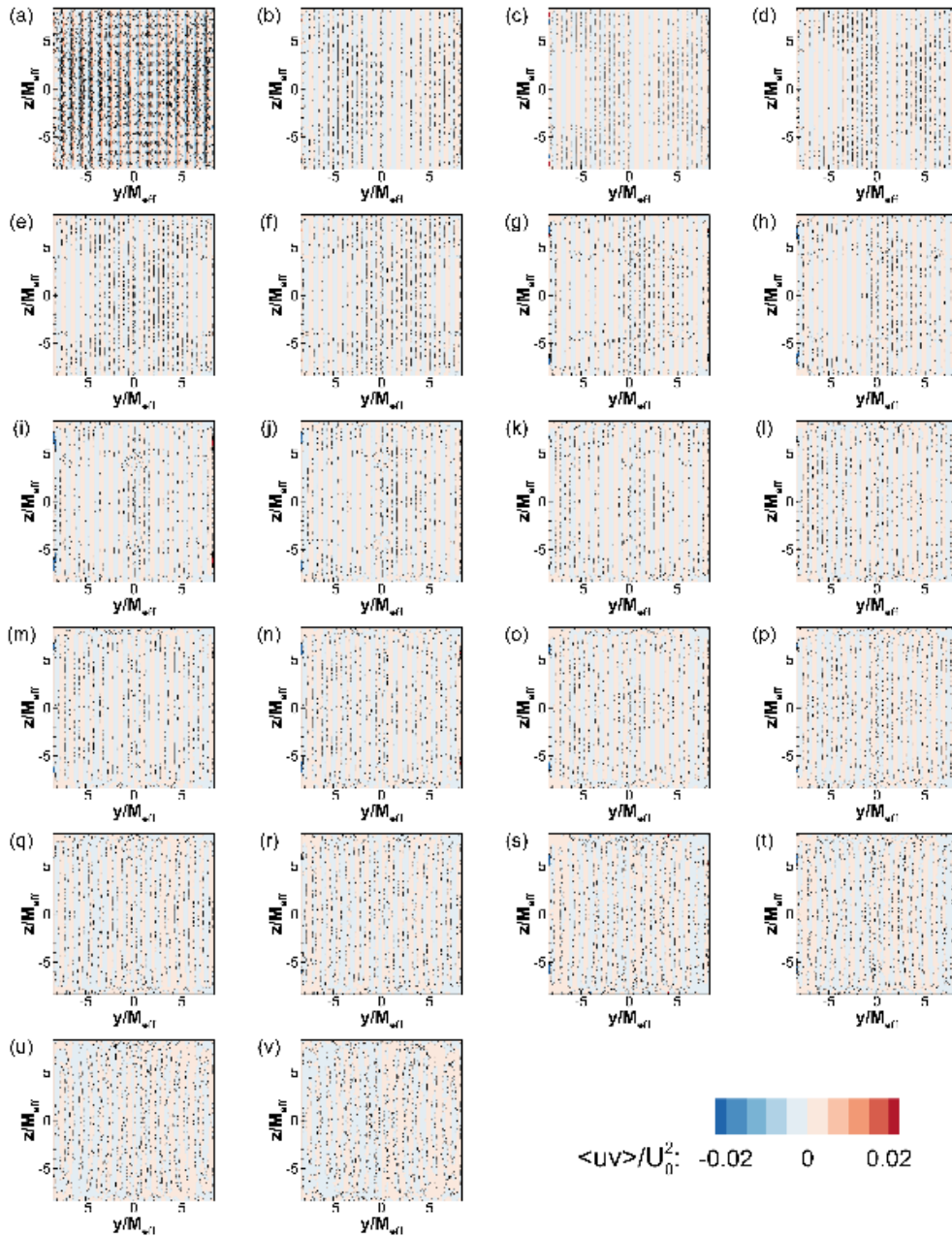
Figure 3-48 Development of the Reynolds shear stress $\langle uv \rangle$ in the near grid region of CSG. Distributions are given in 1 M_{eff} increment from 1 M_{eff} (a) to 22 M_{eff} (v).
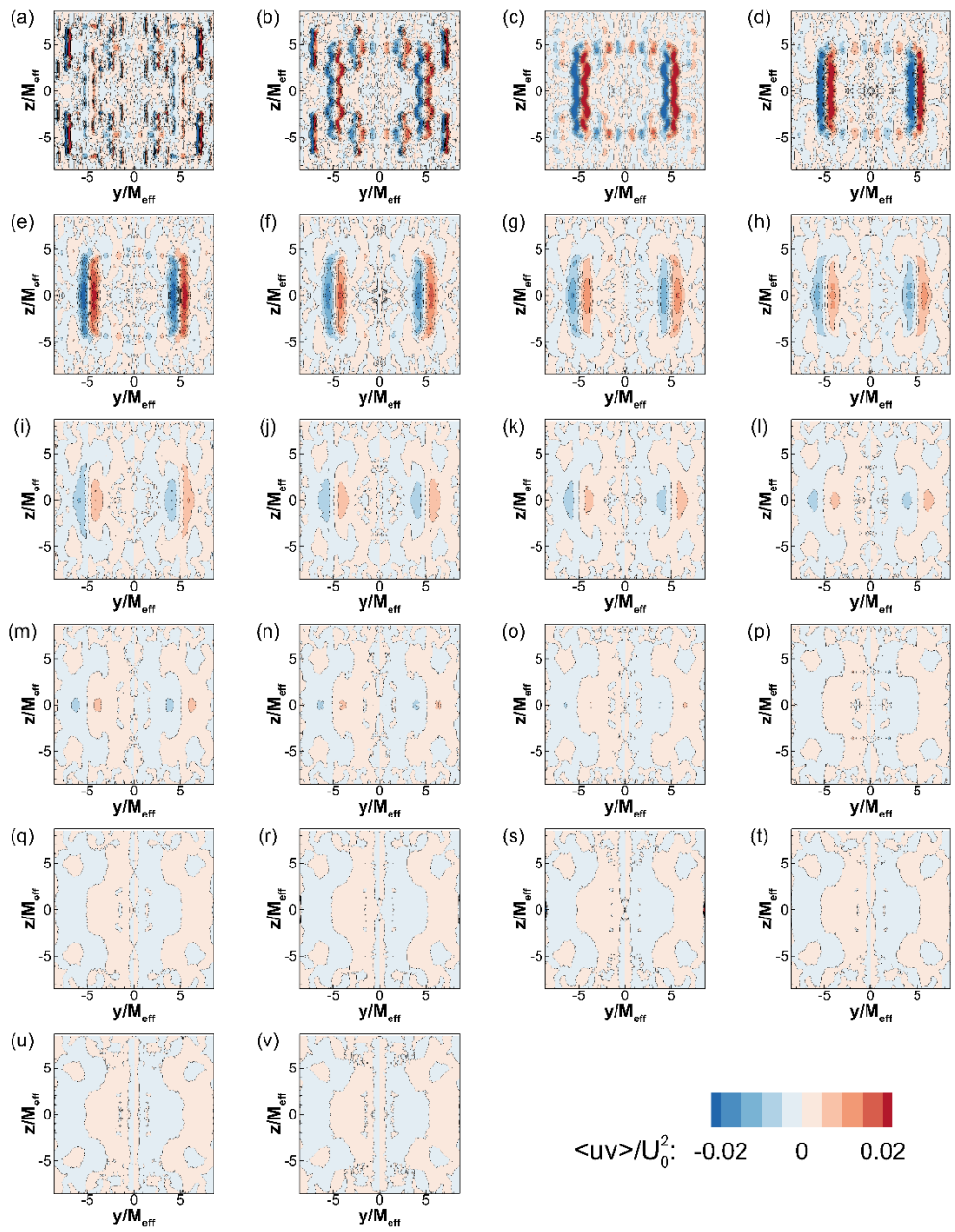
Figure 3-49 Development of the Reynolds shear stress $\langle uv \rangle$ in the near grid region of FSG. Distributions are given in 1 M_{eff} increment from 1 M_{eff} (a) to 22 M_{eff} (v).

85
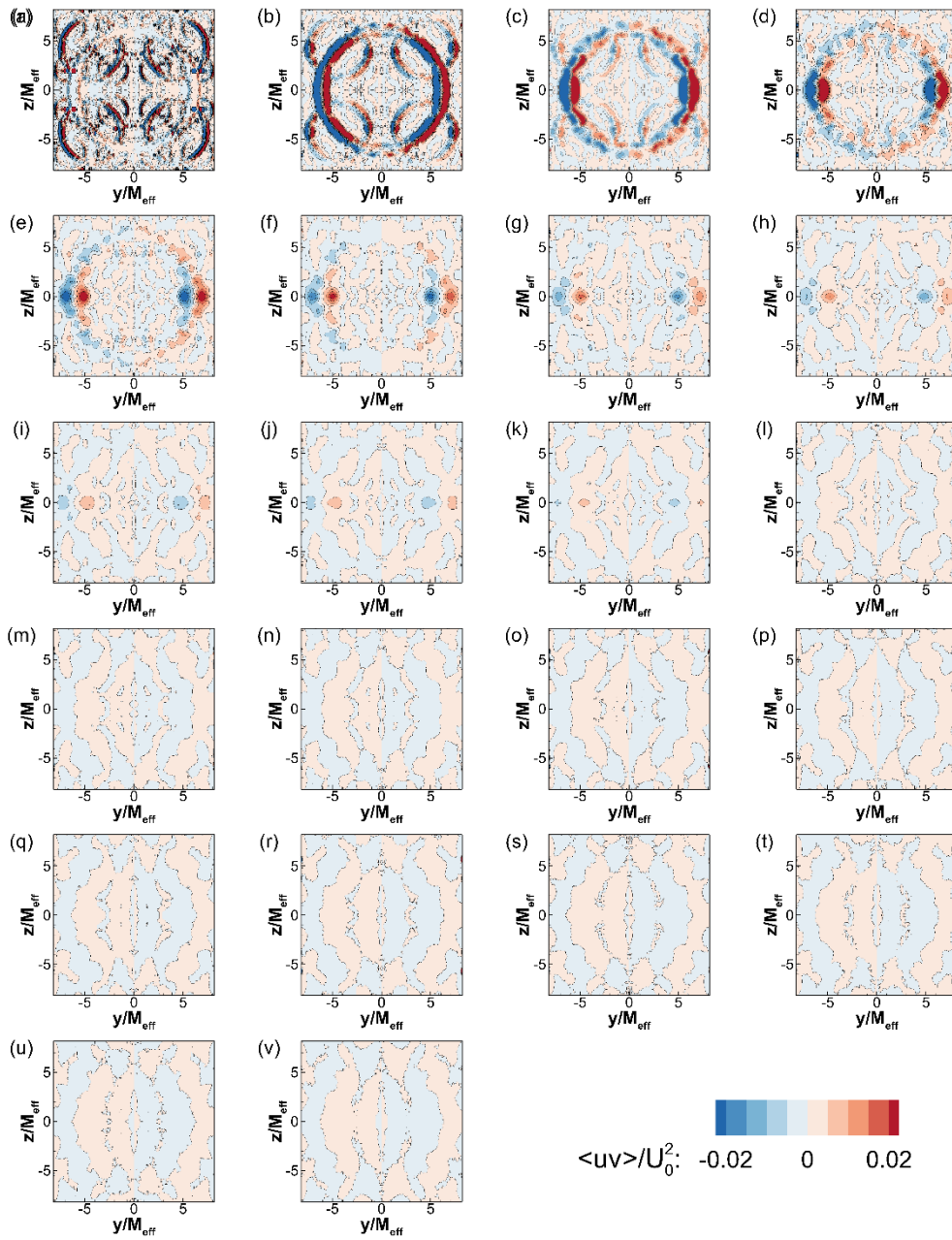
Figure 3-50 Development of the Reynolds shear stress $\langle uv \rangle$ in the near grid region of FCG. Distributions are given in 1 M_{eff} increment from 1 M_{eff} (a) to 22 M_{eff} (v).
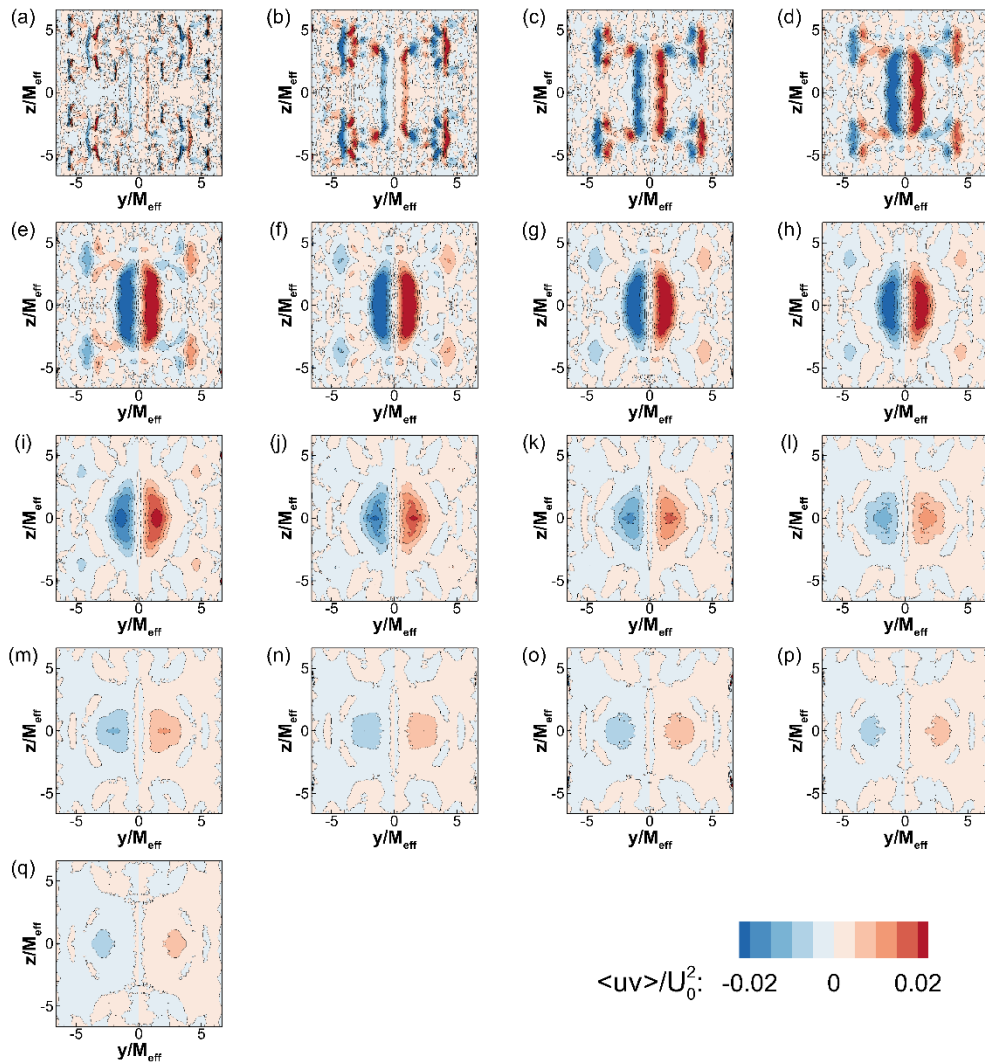
Figure 3-51 Development of the Reynolds shear stress $\langle uv \rangle$ in the near grid region of FIG. Distributions are given in 1 M_{eff} increment from 1 M_{eff} (a) to 17 M_{eff} (q).

Again, the "Reynolds shear stress performance" is normalized with respect to grid solidity to obtain better evaluation. This is depicted in Figure 3-53.
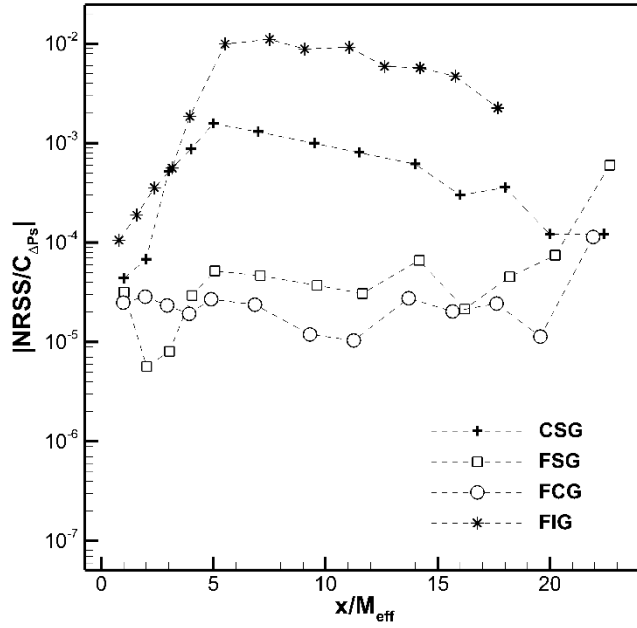
Figure 3-52 Normalized Reynolds shear stress as a function of static pressure drop coefficient along the centerline of TGG's. Downstream distance x is normalized by effective mesh size (M_{eff}).
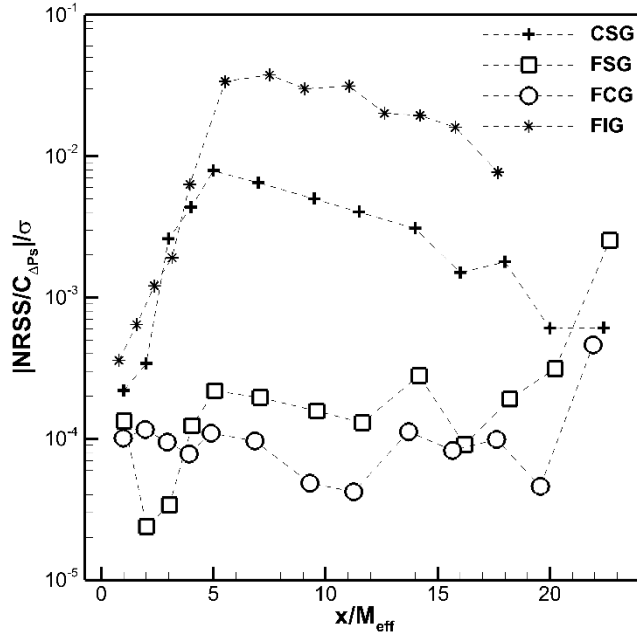
Figure 3-53 Performance of conventional and fractal grids normalized by grid solidity ($^{TI_u}/_{C_{\Delta P_S}}/\sigma$). Downstream distance x is normalized by effective mesh size (M_{eff}).

88

3.3   Turbulent kinetic energy $\langle k \rangle$

Turbulent kinetic energy (TKE) is important in two aspects. Physically, it is often used as an experimental benchmark to evaluate existing turbulence theories and models since it provides an empirical approximation of homogeneous isotropic turbulence (HIT) [43]. Second, if the place and the peak values of turbulent kinetic energy (turbulence intensity equivalently) can be modified or custom tailored, it can be used as a tool to control the turbulence in many engineering applications, such as combustors and burners. In this section, we will look at the distribution of turbulent kinetic energy in the near-wake region of the conventional and fractal grids.

Turbulent kinetic energy (TKE) is the energy of the velocity fluctuations. Mean TKE is then,

$$\langle k \rangle = \frac{1}{2} \left(\langle u^2 \rangle + \langle v^2 \rangle + \langle w^2 \rangle \right) \tag{3.13}$$

where $u, v,$ and w are fluctuating part of the velocity. Reconstruction of the 3-D mean flow field for CSG, FSG, and FCG, makes it possible to give a full approximation of TKE, while for FIG there exist only in-plane fluctuations, therefore TKE is computed based on the isotropic turbulence assumption, i.e.

$$\langle w^2 \rangle = \frac{1}{2} \left(\langle u^2 \rangle + \langle v^2 \rangle \right) \tag{3.14}$$

thus,

$$\langle k \rangle_{ISO} = \frac{3}{4} \left(\langle u^2 \rangle + \langle v^2 \rangle \right) \tag{3.15}$$

TKE development in the near-grid region is qualitatively shown in Figure 3-54 to Figure 3-57 for CSG, FSG, FCG, and FIG, respectively. These as well as rms streamwise velocity fluctuations (not shown here to save space) suggest that these grids can be used in applications in which a specific level of turbulence at desired locations and especially in the limit of short distances is required. As it is stated previously [61] in the case of FSG, fractal grids can be used as an efficient additional turbulence-generator in the near-field.

The assumption of grid generated turbulent flow to be symmetric is fair according to the literature [3,39,46]. Thus the variance of spanwise and vertical velocity fluctuations can be thought of as equal,

$$\langle w^2 \rangle \cong \langle v^2 \rangle \qquad (3.16)$$

Therefore in case of diagonally symmetric grids, one can estimate TKE as,

$$\langle k \rangle_{RS} = \frac{1}{2} (\langle u^2 \rangle + 2\langle v^2 \rangle) \qquad (3.17)$$

To check the validity of either isotropy or reflectional symmetry in the grids, we present the variation of the TKE along characteristic lines shown in the previous section for CSG, FSG, and FCG. These straight streamwise lines start from the grid and extend through the whole domain under investigation.

Variation of normalized mean TKE $\frac{\langle k \rangle}{U_0^2}$, normalized TKE based on isotropy assumption $\frac{\langle k \rangle_{ISO}}{U_0^2}$ and normalized TKE based on reflectional (diagonal) symmetry $\frac{\langle k \rangle_{RS}}{U_0^2}$ in CSG is shown in Figure 3-58 along four characteristic lines, C1 to C4. It is clear that the only deviation of estimated TKE ($\frac{\langle k \rangle_{ISO}}{U_0^2}$ and $\frac{\langle k \rangle_{RS}}{U_0^2}$) from that obtained by full velocity components ($\frac{\langle k \rangle}{U_0^2}$) belongs to the region in the vicinity of the grid which extends at most to $x = 5M_{eff}$.

Values of estimated and actual TKE in the jet region of CSG (Figure 3-58-a) are more or less the same while the largest deviations exist in the middle of horizontal/vertical bars (C4). Looking at Figure 3-33-e one can realize that the global isotropy factor (area-averaged value of u'/v') stays more or less constant after about $5M_{eff}$. This confirms the convergence of isotropic and actual TKE values in CSG. Criteria in (3.16) is validated by plotting the ratio of spanwise to vertical velocity fluctuations variance, $\frac{\langle v^2 \rangle}{\langle w^2 \rangle}$ and shown in Figure 3-58. The scale is on the right side vertical axis and values are depicted in blue color. These variations also suggest a good symmetry after a downstream distance of $x = 5M_{eff}$.
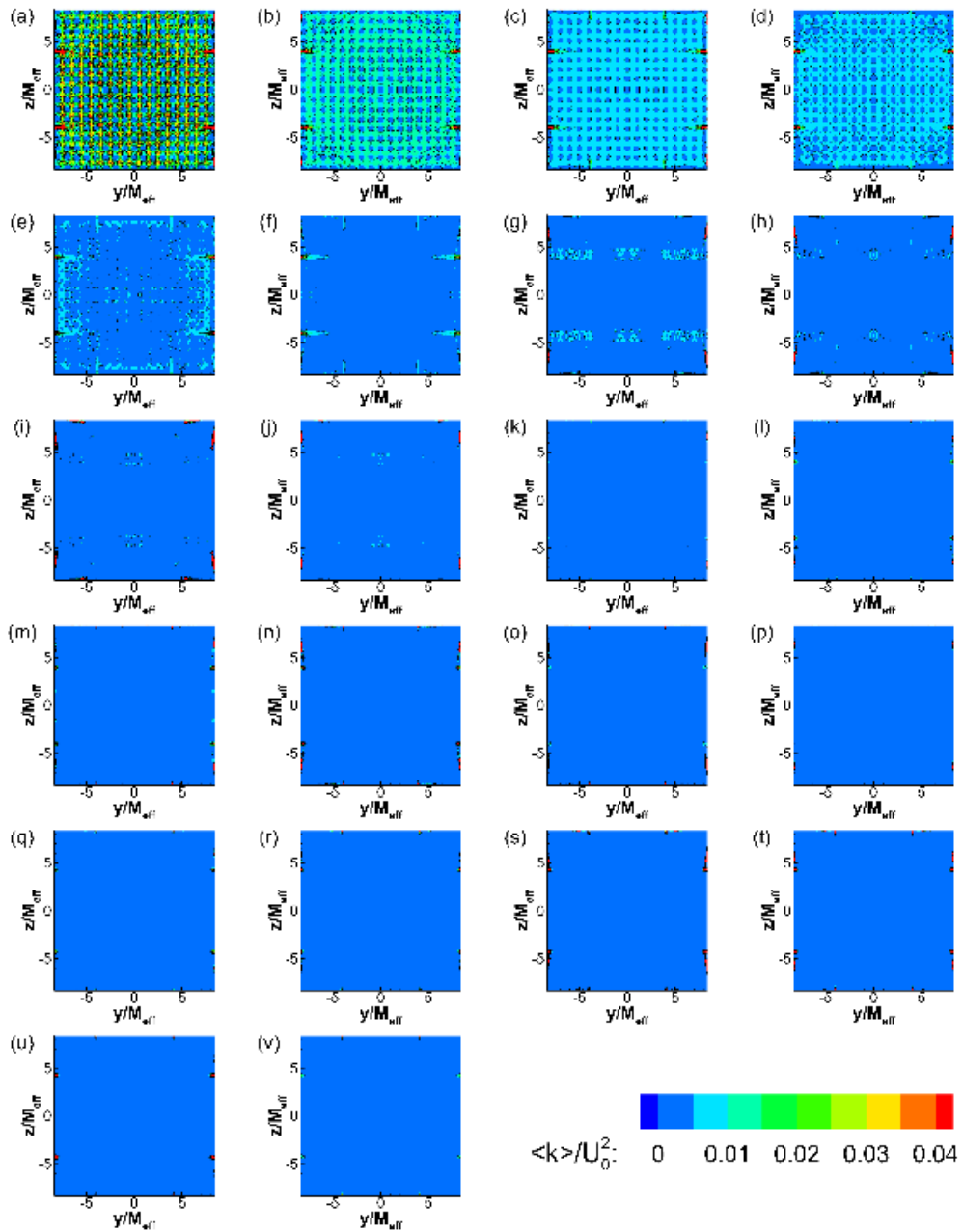
Figure 3-54 Development of the normalized TKE k/U_0^2 in the near grid region of CSG. Distributions are given in 1 M_{eff} increment from 1 M_{eff} (a) to 22 M_{eff} (v).

91
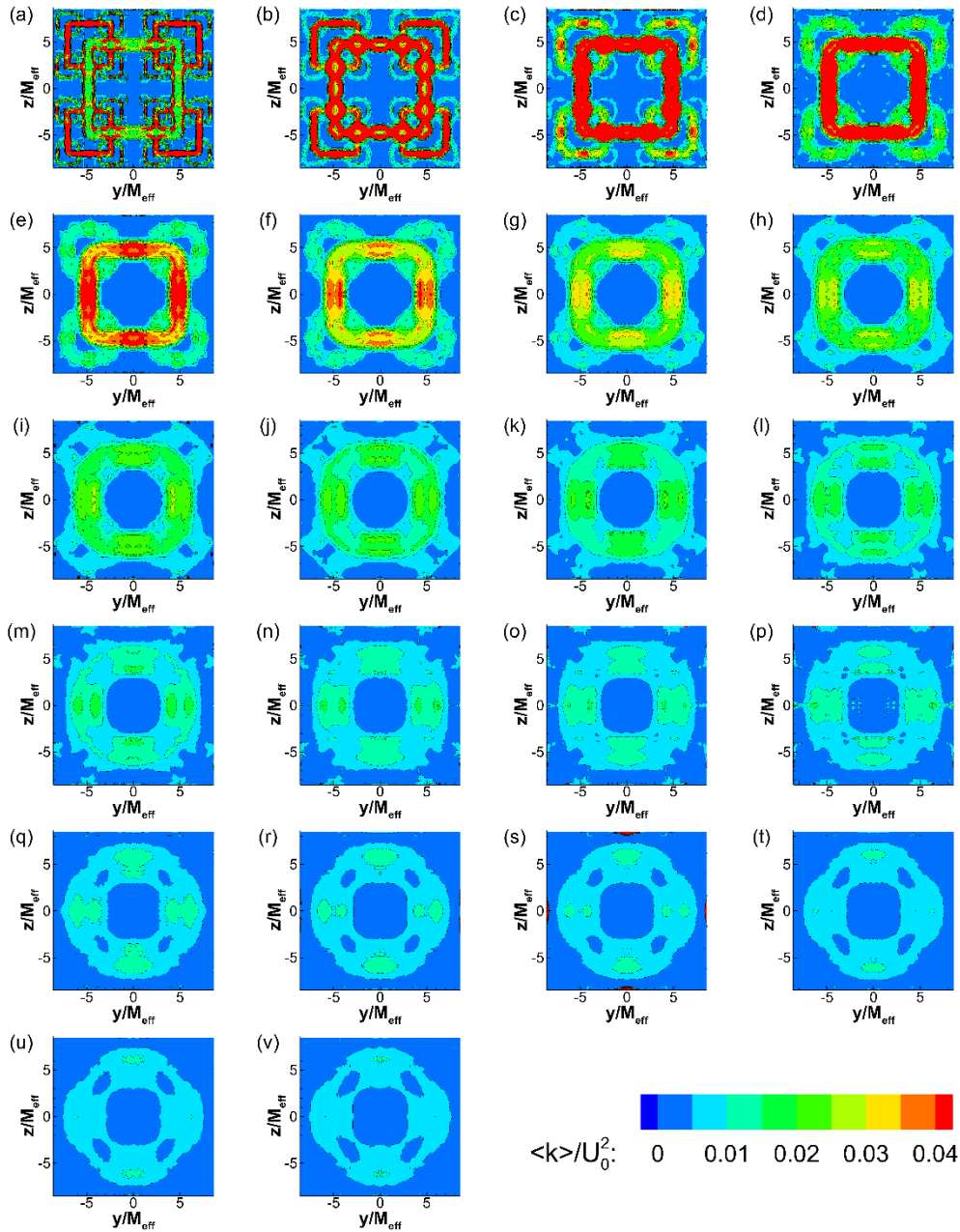
Figure 3-55 Development of the normalized TKE k/U_0^2 in the near grid region of FSG. Distributions are given in 1 M_{eff} increment from 1 M_{eff} (a) to 22 M_{eff} (v).
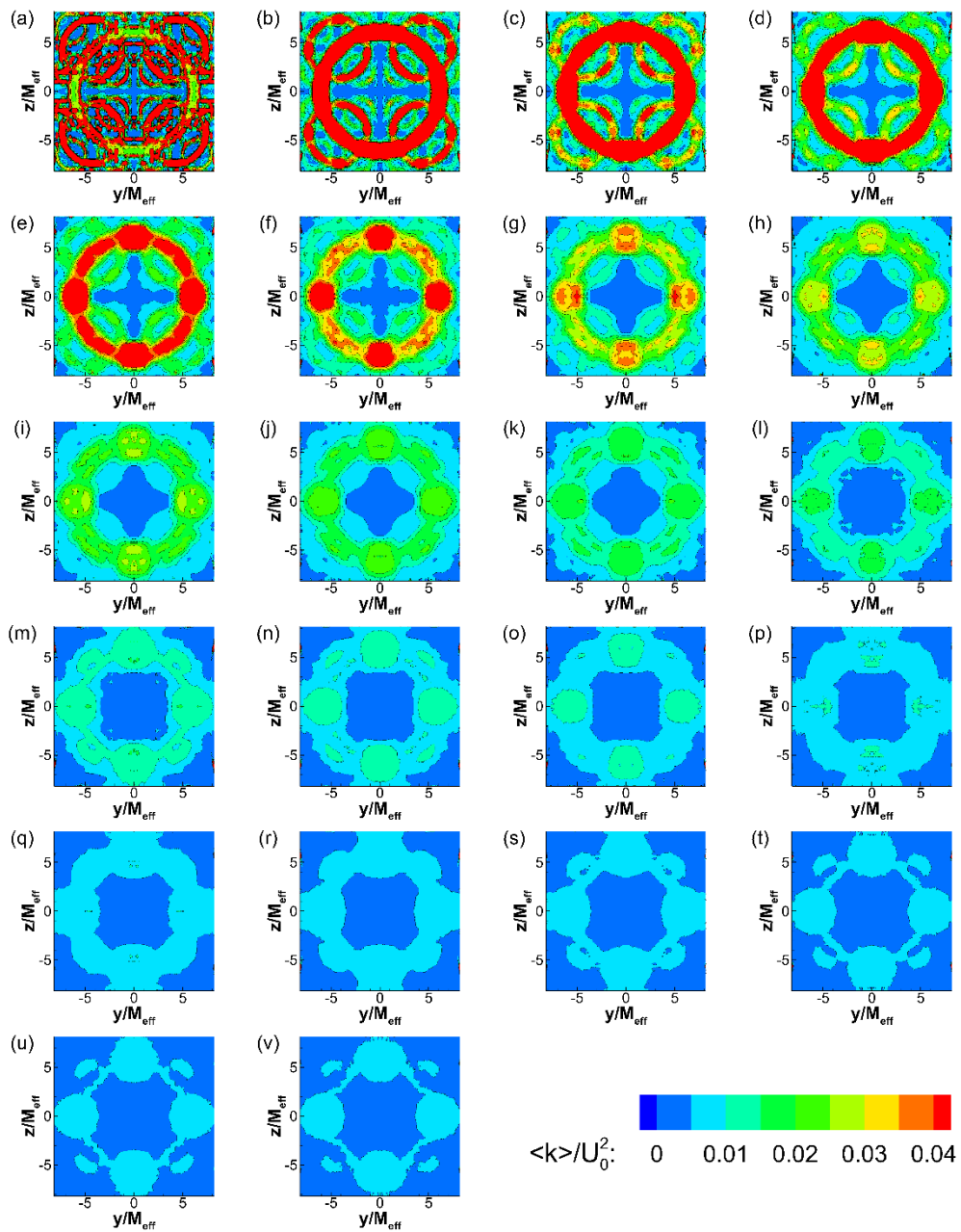
Figure 3-56 Development of the normalized TKE k/U_0^2 in the near grid region of FCG. Distributions are given in 1 M_{eff} increment from 1 M_{eff} (a) to 22 M_{eff} (v).

93
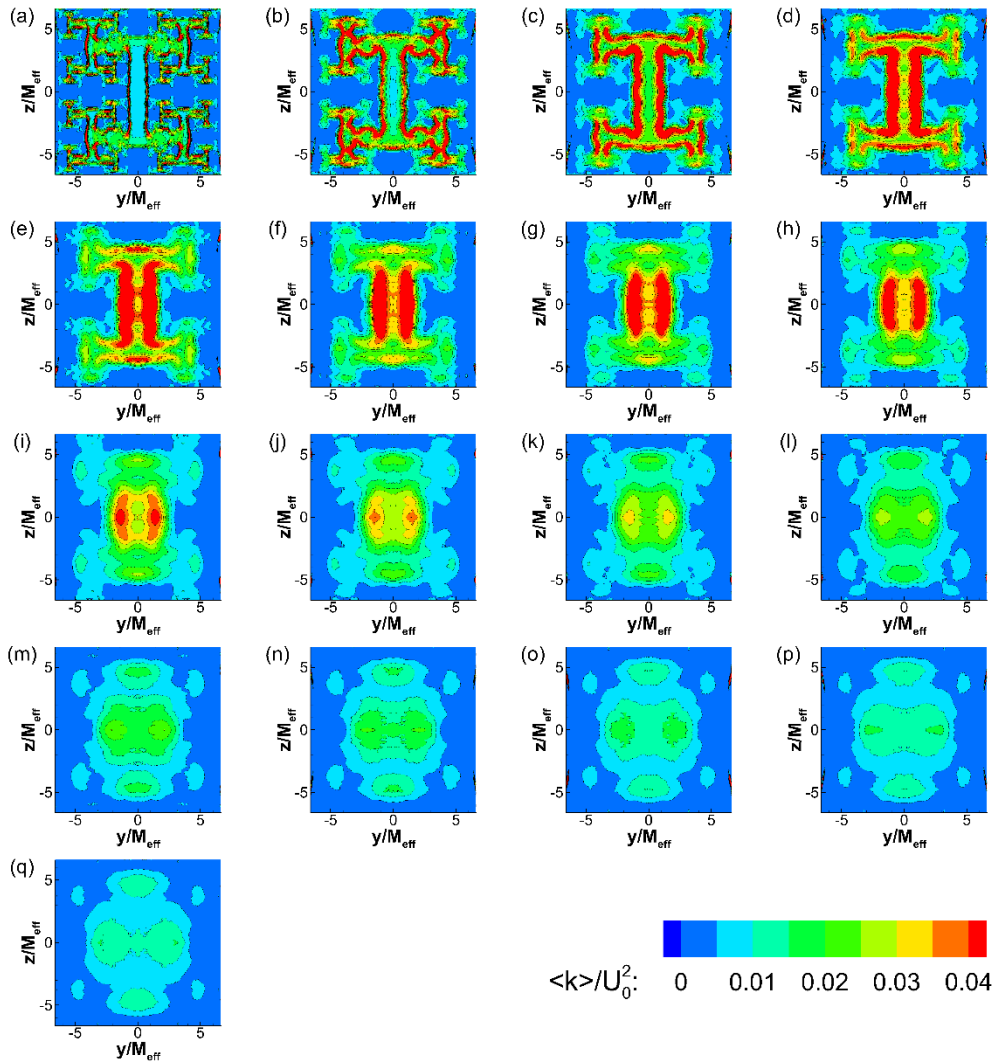
Figure 3-57 Development of the normalized TKE k/U_0^2 in the near grid region of FIG. Distributions are given in 1 M_{eff} increment from 1 M_{eff} (a) to 17 M_{eff} (q).

For FSG, different values of normalized TKE are compared along three characteristic lines FS1, FS2, and FS3 in Figure 3-59. Through the jet-like flow in the center of the grid and the corner of the largest iteration (Figure 3-59-a and c) all three TKE values match, while along the horizontal bar and up to location about $x = 16M_{eff}$ the assumption of isotropy and symmetry will result in underestimated TKE (Figure 3-59-b). This is also clear from the deviation of symmetry parameter ($\langle v^2 \rangle / \langle w^2 \rangle$).
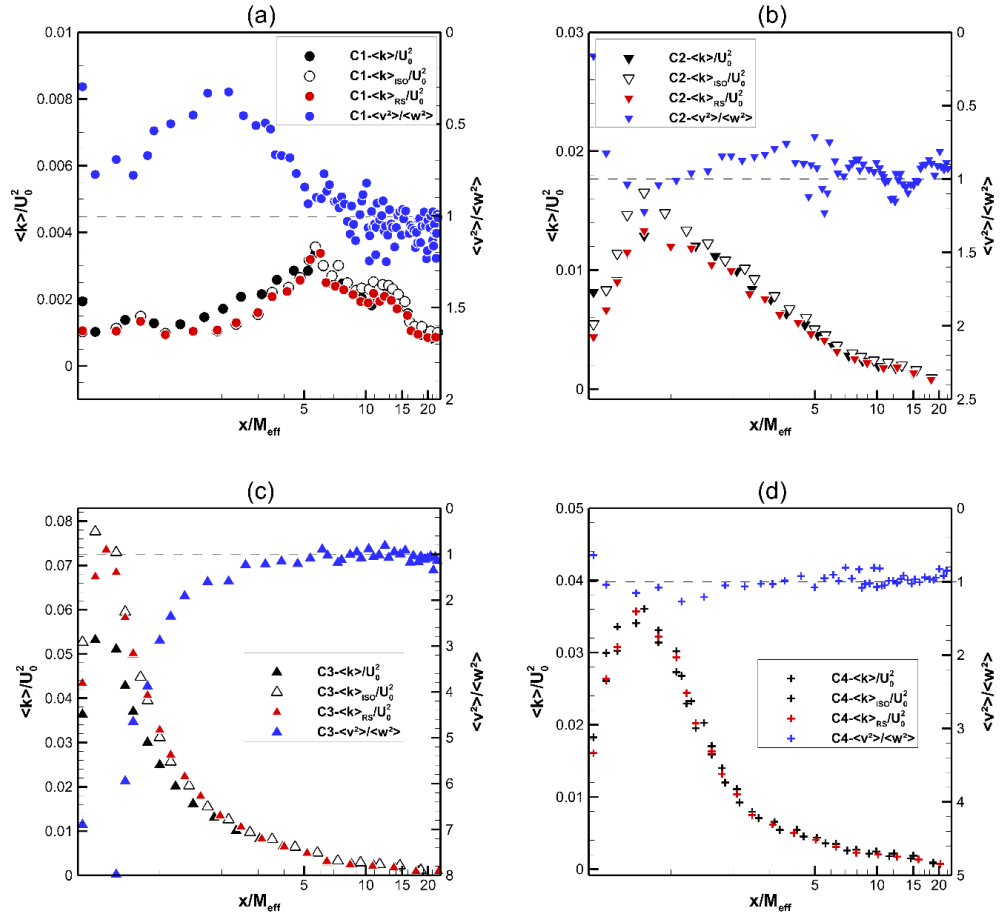
Figure 3-58 Comparison of TKE values obtained by three velocity components (k/U_0^2), isotropy assumption k_{ISO}/U_0^2, and reflectional symmetry assumption k_{RS}/U_0^2, for CSG; along the centerline (a), along a line starting from the middle of horizontal bars (b), along a line starting from the middle of a vertical bar (c), and along a line starting from the cross of horizontal and vertical bars (d). Horizontal axis (x/M_{eff}) is shown in logarithmic increment to emphasize on the near-grid region. Right side vertical axis scales $\langle v^2 \rangle/\langle w^2 \rangle$ which is the representative of reflectional symmetry when equals to 1.

In FCG, while there is conformity of all three TKE values along grid center-line (FC1) as well as line FC2, there exist underestimation along FC3. It is worth to note that the symmetry criteria is always less than unity in the FCG case.
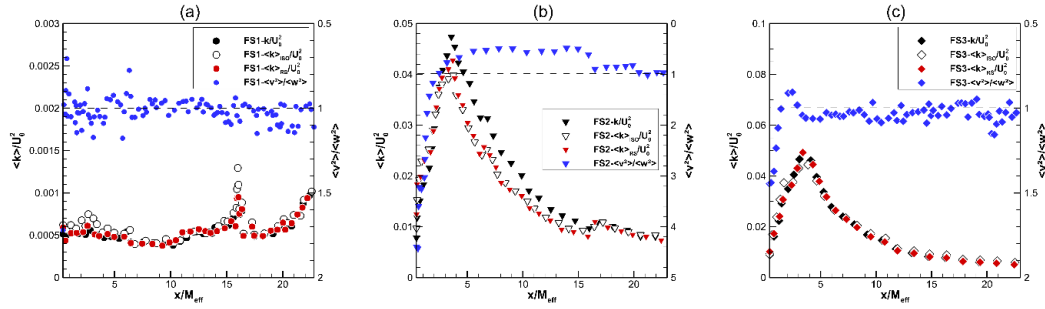
Figure 3-59 Comparison of TKE values obtained by three velocity components ($\frac{\langle k \rangle}{U_0^2}$), isotropy assumption $\frac{\langle k \rangle_{ISO}}{U_0^2}$, and reflectional symmetry assumption $\frac{\langle k \rangle_{RS}}{U_0^2}$, for FSG; along FS1 (a), FS2 (b), and FS3(c). Right side vertical axis scales $\langle v^2 \rangle / \langle w^2 \rangle$ which is the representative of reflectional symmetry when equals to 1.
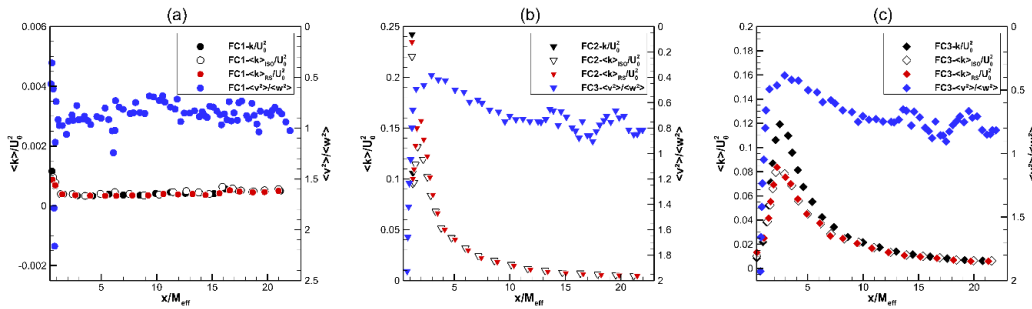
Figure 3-60 Comparison of TKE values obtained by three velocity components ($\frac{\langle k \rangle}{U_0^2}$), isotropy assumption $\frac{\langle k \rangle_{ISO}}{U_0^2}$, and reflectional symmetry assumption $\frac{\langle k \rangle_{RS}}{U_0^2}$, for FCG; along FC1 (a), FC2 (b), and FC3(c). Right side vertical axis scales $\langle v^2 \rangle / \langle w^2 \rangle$ which is the representative of reflectional symmetry when equals to 1.

3.3.1   The decay of turbulent kinetic energy in the near-grid region

The production and decay of TKE are qualitatively shown in contour plots above in Figure 3-54 through Figure 3-57. This increasing–decreasing trend is also visible along characteristic lines of grids in Figure 3-58, Figure 3-59, and Figure 3-60. While the near-field is intrinsically non-homogeneous and anisotropic, there is still a matter of question that the decay in TKE can still be fitted as power-law or not.

In homogeneous and isotropic turbulence (HIT), the kinetic energy of the fluctuating velocities decays following a power law, according to the von Kármán–Howarth equation ([115]),

$$\langle q^2 \rangle \sim (t - t_0)^n \tag{3.18}$$

where $\langle q^2 \rangle = \langle u^2 \rangle + \langle v^2 \rangle + \langle w^2 \rangle$ is twice the total turbulent kinetic energy of the flow. 't' is time, and 't_0' is a virtual origin [43]. The exponent value 'n' is reported to fall in the range of $[-1.4, -1]$ according to ([7,12,25,116,117]). The temporal decay could be converted to spatial one using Taylors frozen turbulence[1] relation, $t = \frac{x}{U}$, if the velocity (U) remains constant throughout the test section [43]. The power-law may then be expressed as

$$\langle q^2 \rangle \sim \left(\frac{x}{U} - \frac{x_0}{U} \right)^n \rightarrow \langle q^2 \rangle = A \left(\frac{x}{\mathcal{L}} - \frac{x_0}{\mathcal{L}} \right)^n \tag{3.19}$$

where A is the constant of proportionality. $\mathcal{L}$ is normalizing length scale which is chosen to be mesh size (M) for the case of classical grids. The virtual origin x_0, can be considered equal to zero according to [117].

Normalized TKE ($\frac{\langle k \rangle}{U_0^2}$) is averaged on $x = cte$ planes and the results are plotted along the normalized streamwise distance ($\frac{x}{M_{eff}}$) in Figure 3-61. Vertical dashed lines point to the peak location of TKE for each grid. A power function (i.e., $\frac{\langle k \rangle}{U_0^2} = A \left(\frac{x}{M_{eff}} \right)^{-n}$) is fitted to the curves (from the peak point to the last available data and erroneous data is blanked). The values for coefficient and slope of power fit as well as the goodness of the fits are listed in Table 3-6. A narrow production in the region between $0.4 \leq \frac{x}{M_{eff}} \leq 0.55$ is detected for CSG.

---

[1] Taylor's frozen flow hypothesis supposes that turbulence advects with the local mean velocity without any distortion [131].
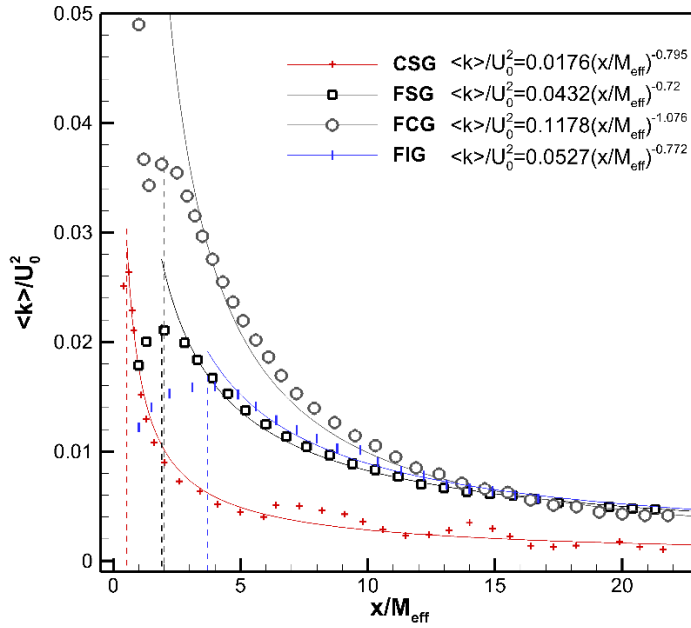
Figure 3-61 Power function fit to the decay region of area-averaged TKE of TGG's. Only every 10th point is plotted.

Table 3-6 Results of power function fit to area averaged TKE in the near grid region of TGG's.

Grid	Number of x-planes used	Peak of TKE ($\frac{x}{M_{eff}}$)	Power function coefficient (A)	Power function slope (n)	Goodness of fit (R^2)
CSG	203	~0.53	0.0176	0.795	0.9016
FSG	197	~1.9	0.0432	0.72	0.99
FCG	211	~2.0	0.1178	1.076	0.9819
FIG	161	~3.7	0.0527	0.772	0.9761

Production and decay of TKE is investigated in more detail by considering the changes of normalized TKE ($\frac{\langle k \rangle}{U_0^2}$) along characteristic lines in each grid. These lines were first introduced in section 3.1.4. The variation of $\frac{\langle k \rangle}{U_0^2}$ along each line is shown in Figure 3-62. A power-law curve $\left(\frac{\langle k \rangle}{U_0^2} = A \left(\frac{x}{M_{eff}} \right)^{-n} \right)$ as well as an exponential curve $\left(\frac{\langle k \rangle}{U_0^2} = A' e^{-n' \left(\frac{x}{M_{eff}} \right)} \right)$ are fitted on the decay region to compare the best fit in the near-field of the grids. Lines are extending between $0.4 \leq \frac{x}{M_{eff}} \leq 22.5$ for CSG and

FSG, $0.4 \leq \frac{x}{M_{eff}} \leq 22$ for FCG and $0.4 \leq \frac{x}{M_{eff}} \leq 17.75$ for FIG. FS1 and FC1 pertain to the center of the FSG and FCG. Since there is an opening in this region, the flow would behave like a jet flow and there is no/very small forcing from to grid bars to this region. From Figure 3-62-b,c it is also clear that the TKE is changing slightly along the centerline in the near grid region. Within the measurement region, the change of the TKE is 1.6% and 0.9% for FS1 and FC1, respectively. In CSG, C1 belongs to a similar jet region but since this region is surrounded by very close bars, the effect of the shear is clearly seen along that line and a production region is extended to $\frac{x}{M_{eff}} \sim 5.8$.

Table 3-7 Results of power and exponential fits on the decay region of TKE along characteristic lines in grids under investigation.

Grid	Line	Peak of TKE $(\frac{x}{M_{eff}})$	Power function coefficient (A)	Power function slope (n)	Goodness of fit (R^2)	Exp. function coefficient (A')	Exp. function slope (n')	Goodness of fit (R^2)
CSG	C1	~5.8	0.0196	1.031	0.98	0.0048	0.082	0.91
	C2	~0.78	0.0224	1.074	0.95	0.0093	0.13	0.95
	C3	~0.53	0.0283	1.119	0.98	0.0114	0.135	0.87
	C4	~0.66	0.0238	1.11	0.98	0.0093	0.131	0.88
FSG	FS1	N/A	-	-	-	-	-	-
	FS2	~3.61	0.2248	1.087	0.98	0.0536	0.095	0.94
	FS3	~3.48	0.3194	1.352	0.99	0.0544	0.119	0.94
FCG	FC1	N/A	-	-	-	-	-	-
	FC2	~2.53	0.6849	1.53	0.99	0.1131	0.149	0.95
	FC3	~1.84	0.4813	1.538	0.99	0.0911	0.159	0.93
FIG	FI1	~6.0	0.3524	1.158	0.89	0.0759	0.108	0.96
	FI2	~7.77	0.148	1.0	0.96	0.0331	0.08	0.92
	FI3	~4.1	0.13	-1.271	0.97	0.0276	0.128	0.94

In FIG, the peak location of TKE along FI2 is unclear since it preserves the peak in the range between 3.1 to 7.7 M_{eff}. This is visible in Figure 3-62-c. The power and

exponential curves are fitted to the data after the last peak at $x/M_{eff} = 7.77$. Variation of TKE along FI3 is also interesting. There are two distinct peaks at $x/M_{eff} \sim 1.0$ and $x/M_{eff} \sim 4.11$. Again, curves are fitted after the last peak point in TKE.

As it can be realized from the values in Table 3-7, power-law fit almost always gives better results on the decay of TKE in the near wake of the grids. The only exception is for the wake region in the center of FIG (FI1 point).
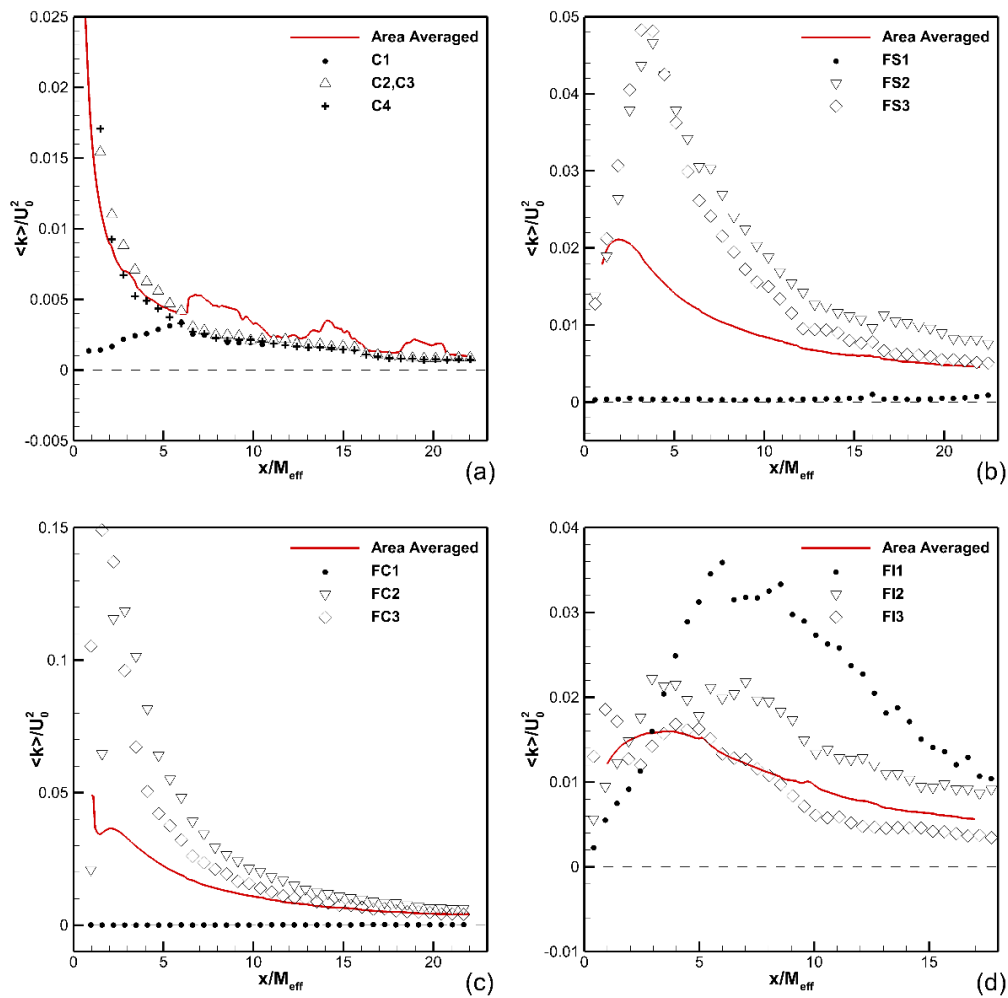
Figure 3-62 Production and decay of normalized TKE along characteristic lines for the grids under investigation. (a) CSG, (b) FSG, (c) FCG, and (d) FIG. Lines are specified in section 3.1.4.

3.3.2 Turbulent kinetic energy mean dissipation rate $\langle \varepsilon \rangle$

Turbulent kinetic energy dissipation rate (ε) is governed by the large (energy-containing) scales of turbulence [118]. In fact, one of the cornerstone assumptions in the theory of turbulence is the scaling between the rate of dissipation of energy at small scales and large ones, i.e., ε scales as,

$$\varepsilon \propto \frac{u'^3}{L} \tag{3.20}$$

in which $u' = \sqrt{\langle u^2 \rangle}$ is the rms velocity fluctuation of the large scales and L pertains to the integral length scale. Dissipation rate (ε) can be simply explained by the cascade of energy. In the cascade process, each eddy has energy of u^2. If we assume it takes some time equal to T_e – which is known as eddy turnover time – for the eddy to turn one complete round and transfer its energy to smaller scales, then the rate of loss of energy to smaller scales is $\frac{u^2}{T_e}$. The eddy turnover time is almost equal to $\frac{L}{u}$ where L is the diameter or length scale of that typical eddy. Therefore, the rate of loss of energy to the smallest scales $\sim \frac{u^3}{L} = \varepsilon$ (dissipation rate of turbulent kinetic energy). If the flow is in equilibrium (meaning that the rate of the production is equal to the rate of the dissipation, locally), this energy is transferred to smaller scales without any loss, where it is ultimately dissipated to heat by the action of viscosity. In this case, we can write

$$\varepsilon = C_\varepsilon \frac{u'^3}{L} \tag{3.21}$$

which is the classic estimate for the scaling of dissipation rate and known as Taylor's scaling. Here, C_ε is a universal and non-dimensional coefficient, i.e., it is independent of Reynolds number, time and space, at least for conventional turbulent flows (there were evidence of variable C_ε in the case of turbulence generated by fractal square grids).

If the turbulence produced by a grid is homogeneous and isotropic (HIT) –which we believe to occur only in the far-field– mean kinetic energy dissipation rate is obtained from the turbulent energy budget [43],

$$\langle\varepsilon\rangle_d = -\frac{\langle U\rangle}{2}\frac{d\langle q^2\rangle}{dx} \tag{3.22}$$

The subscript d denotes that the dissipation is determined from kinetic energy decay. The gradient of $\langle q^2\rangle$ in (3.22) is commonly estimated using a power function fit to $\langle q^2\rangle$. Since, there is non-negligible turbulence production and transverse transport of turbulent kinetic energy in the near-field [41][107], equation (3.22) is not a proper approximation of $\langle\varepsilon\rangle$.

Dissipation rate of turbulent kinetic energy per unit mass (i.e. $\frac{1}{2}\langle u_i u_i\rangle$) is given by,

$$\varepsilon = 2\nu\langle s_{ij}s_{ij}\rangle = \nu\left\langle\left[(\frac{\partial u_i}{\partial x_j}+\frac{\partial u_j}{\partial x_i})\frac{\partial u_i}{\partial x_j}\right]\right\rangle \tag{3.23}$$

where s_{ij} is the fluctuating rate of strain tensor. This means dissipation is due to viscosity and strain rate. If all nine components of the fluctuating velocity gradient tensor are available, the mean energy dissipation rate can be found as [67],

$$\begin{aligned}
\langle\varepsilon\rangle = \nu\Bigg\{ &2\left[\left\langle\left(\frac{\partial u}{\partial y}\frac{\partial v}{\partial x}\right)\right\rangle + \left\langle\left(\frac{\partial u}{\partial z}\frac{\partial w}{\partial x}\right)\right\rangle + \left\langle\left(\frac{\partial v}{\partial z}\frac{\partial w}{\partial y}\right)\right\rangle\right] \\
&+ \left\langle\left(\frac{\partial u}{\partial y}\right)\right\rangle + \left\langle\left(\frac{\partial v}{\partial x}\right)\right\rangle + \left\langle\left(\frac{\partial u}{\partial z}\right)\right\rangle + \left\langle\left(\frac{\partial w}{\partial x}\right)\right\rangle \\
&+ \left\langle\left(\frac{\partial v}{\partial z}\right)\right\rangle + \left\langle\left(\frac{\partial w}{\partial y}\right)\right\rangle \\
&+ 2\left[\left\langle\left(\frac{\partial u}{\partial x}\right)^2\right\rangle\left\langle\left(\frac{\partial v}{\partial y}\right)^2\right\rangle\left\langle\left(\frac{\partial w}{\partial z}\right)^2\right\rangle\right]\Bigg\}
\end{aligned} \tag{3.24}$$

In isotropic turbulence [119],

$$\begin{cases}
\left\langle\left(\frac{\partial u}{\partial x}\right)^2\right\rangle = \left\langle\left(\frac{\partial v}{\partial y}\right)^2\right\rangle = \left\langle\left(\frac{\partial w}{\partial z}\right)^2\right\rangle \\
\left\langle\left(\frac{\partial u}{\partial y}\right)^2\right\rangle = \left\langle\left(\frac{\partial u}{\partial z}\right)^2\right\rangle = \left\langle\left(\frac{\partial v}{\partial x}\right)^2\right\rangle = \left\langle\left(\frac{\partial v}{\partial z}\right)^2\right\rangle = \left\langle\left(\frac{\partial w}{\partial x}\right)^2\right\rangle = \left\langle\left(\frac{\partial w}{\partial y}\right)^2\right\rangle \\
\left\langle\left(\frac{\partial u}{\partial y}\frac{\partial v}{\partial x}\right)\right\rangle = \left\langle\left(\frac{\partial u}{\partial z}\frac{\partial w}{\partial x}\right)\right\rangle = \left\langle\left(\frac{\partial v}{\partial z}\frac{\partial w}{\partial y}\right)\right\rangle = \cdots
\end{cases} \tag{3.25}$$

Therefore, the relation for the dissipation becomes,

$$\langle \varepsilon \rangle_{ISO} = 6\nu \left[\left\langle \left(\frac{\partial u}{\partial x} \right)^2 \right\rangle + \left\langle \left(\frac{\partial u}{\partial y} \right)^2 \right\rangle + \left\langle \left(\frac{\partial u}{\partial y} \frac{\partial v}{\partial x} \right) \right\rangle \right] \tag{3.26}$$

On the other hand, assuming local isotropy (isotropy in small scales which is always true at large Reynolds numbers [106]), one can obtain the dissipation as [43,51,52,119],

$$\langle \varepsilon \rangle_{iso} = 15\nu \left\langle \left(\frac{\partial u}{\partial x} \right)^2 \right\rangle \tag{3.27}$$

Note that there is a distinction between the local isotropy and the whole flow field isotropy so we use two different notations "iso" and "ISO" for locally isotropic and isotropic flow, respectively. The value obtained with (3.27) is within 10% from the dissipation calculated by integrating the corresponding energy spectra [105],

$$\varepsilon = \nu \left[15 \int_0^\infty \kappa_1^2 E_{11}(\kappa_1) d\kappa_1 \right] \tag{3.28}$$

When there is a possibility of measuring two components of the velocity vector, using x-wire data [41,43], the less restrictive form of (3.27) is,

$$\langle \varepsilon \rangle_{iso} = 3\nu \left\langle \left(\frac{\partial u}{\partial x} \right)^2 + 2 \left(\frac{\partial v}{\partial x} \right)^2 \right\rangle \tag{3.29}$$

According to Tanaka and Eaton [120], assuming local isotropy and using 2-D PIV data the equivalent form of (3.27) is,

$$\langle \varepsilon \rangle_{2-C\ PIV} \approx 3\nu \left(\overline{\left(\frac{\partial u}{\partial x} \right)^2} + \overline{\left(\frac{\partial v}{\partial y} \right)^2} + \overline{\left(\frac{\partial u}{\partial y} + \frac{\partial v}{\partial x} \right)^2} \right) \tag{3.30}$$

In fact, as four (out of 9) components of the fluctuating velocity gradient tensor are available, and the fifth one can indirectly be obtained from incompressibility equation, Tanaka and Eaton [120] suggested an approximation of energy dissipation from 2-D PIV data as,

$$\varepsilon \approx 3\nu(\langle s_{11}^2 \rangle + \langle s_{22}^2 \rangle) + 12\nu\langle s_{12}^2 \rangle \qquad (3.31)$$

which is the same as (3.30) with the assumption of locally isotropic turbulence. In the case of diagonal (reflectional) symmetry of the flow field (for CSG, FSG, and FCG), the assumption $\langle s_{33}^2 \rangle = \frac{\langle s_{11}^2 \rangle + \langle s_{22}^2 \rangle}{2}$ would be better replaced by $\langle s_{33}^2 \rangle = \langle s_{22}^2 \rangle$ [40,43]. Then (3.31) will be,

$$\varepsilon \approx 2\nu[\langle s_{11}^2 \rangle + 2\langle s_{22}^2 \rangle + 6\langle s_{12}^2 \rangle] \qquad (3.32)$$

alternatively, regarding fluctuating velocity gradients,

$$\langle\varepsilon\rangle_{2-C\ PIV\ (RS)} \approx 2\nu\left(\overline{\left(\frac{\partial u}{\partial x}\right)^2} + 2\overline{\left(\frac{\partial v}{\partial y}\right)^2} + \frac{3}{2}\overline{\left(\frac{\partial u}{\partial y} + \frac{\partial v}{\partial x}\right)^2}\right) \qquad (3.33)$$

where $\langle\varepsilon\rangle_{2-C\ PIV\ (RS)}$ indicates the value of the mean dissipation rate obtained for 2-C PIV data in the case of reflectional symmetry.

An important issue in the estimation of the mean dissipation rate of TKE out of PIV data is the high dependency to resolution. When the resolution is bigger than the Kolmogorov length scale, since the small-scale fluctuations are filtered, the values for $\langle\varepsilon\rangle$ are underestimated. On the other hand, if the resolution is higher than the Kolmogorov scale, amplification of noise in the numerical differentiation procedure would tremendously increase the error [120]. The energy dissipation rate using 2-D PIV data is estimated with the help of (3.30) for all four grids and with the help of (3.33) for CSG, FSG, and FCG. The procedure starts with loading the instantaneous velocity fields into MATLAB®. The mean and fluctuating velocity fields are then obtained and the gradients of the fluctuating velocity components as in (3.30) are calculated. Then, estimated values for mean dissipation rate ($\langle\varepsilon\rangle_{2-C\ PIV}$, and $\langle\varepsilon\rangle_{2-C\ PIV\ (RS)}$) at each (x,y) coordinate system are obtained. The data is stored as '.dat' file for further interpretations.

Despite knowing the degrading spatial resolution of the available data set (1.28 mm), we combined the whole 4×35 windows for each grid to create a 3-D field for mean dissipation, to study on the distribution and evolution of ε in the near-grid region.

Figure 3-63 through Figure 3-66 show the evolution of $\langle\varepsilon\rangle_{2-C\ PIV}$ in the near-wake region of all 4 grid types.
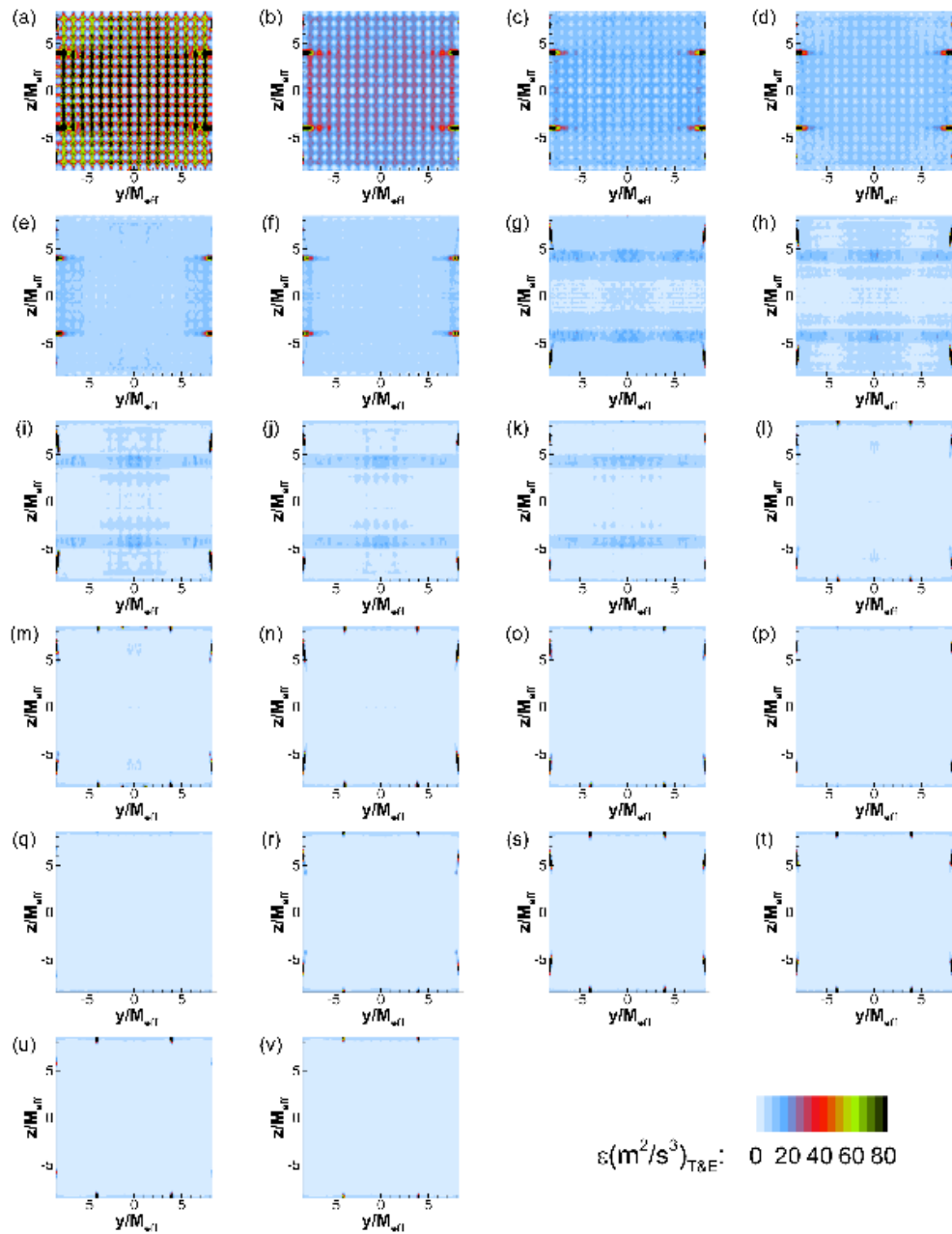
Figure 3-63 Development of 2-D estimated mean dissipation rate $\langle\varepsilon\rangle_{2D}$ in the near grid region of CSG. Distributions are given in $1\ M_{eff}$ increment from $1\ M_{eff}$ (a) to $22\ M_{eff}$ (v).
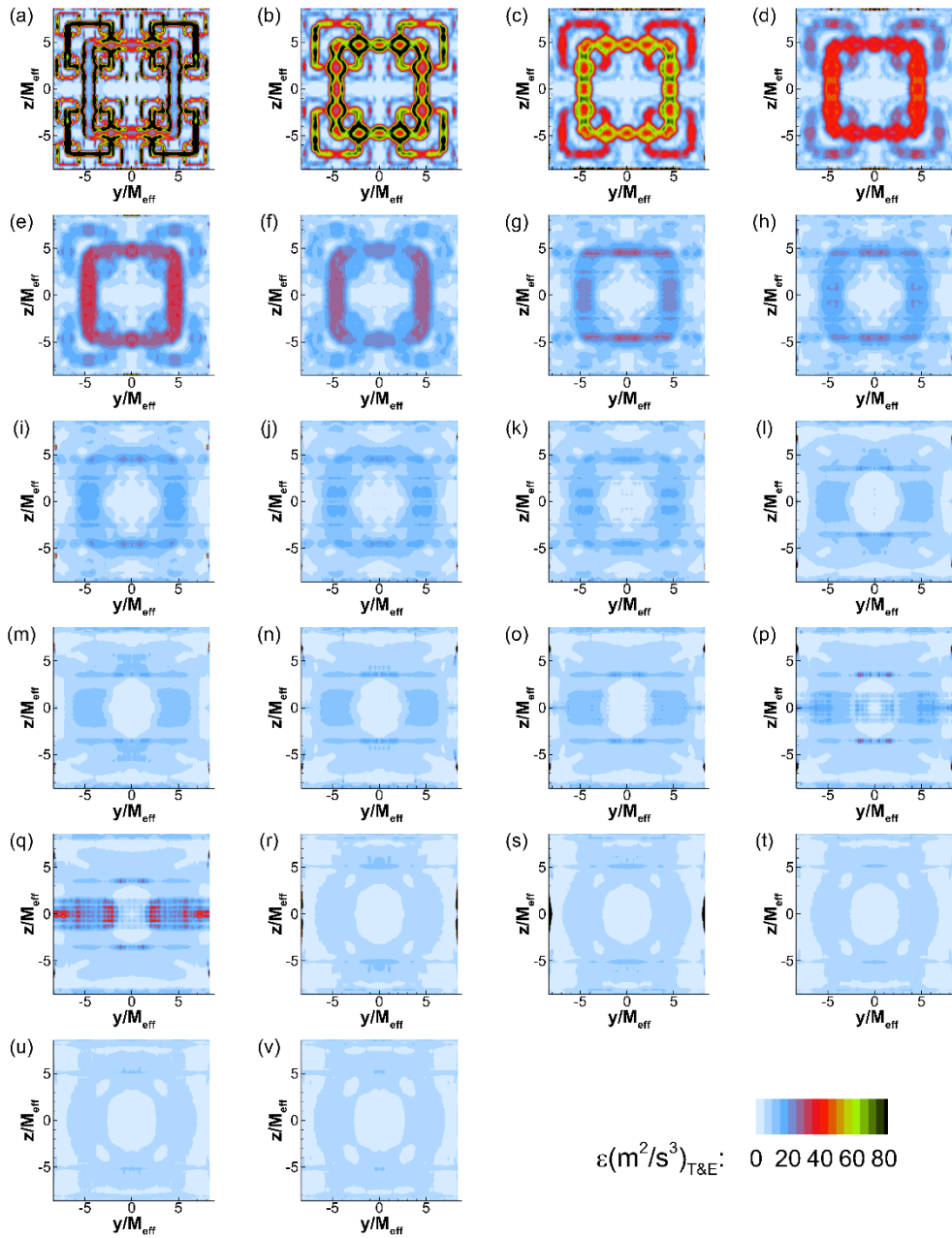
Figure 3-64 Development of 2-D estimated mean dissipation rate $\langle\varepsilon\rangle_{2D}$ in the near grid region of FSG. Distributions are given in 1 M_{eff} increment from 1 M_{eff} (a) to 22 M_{eff} (v).
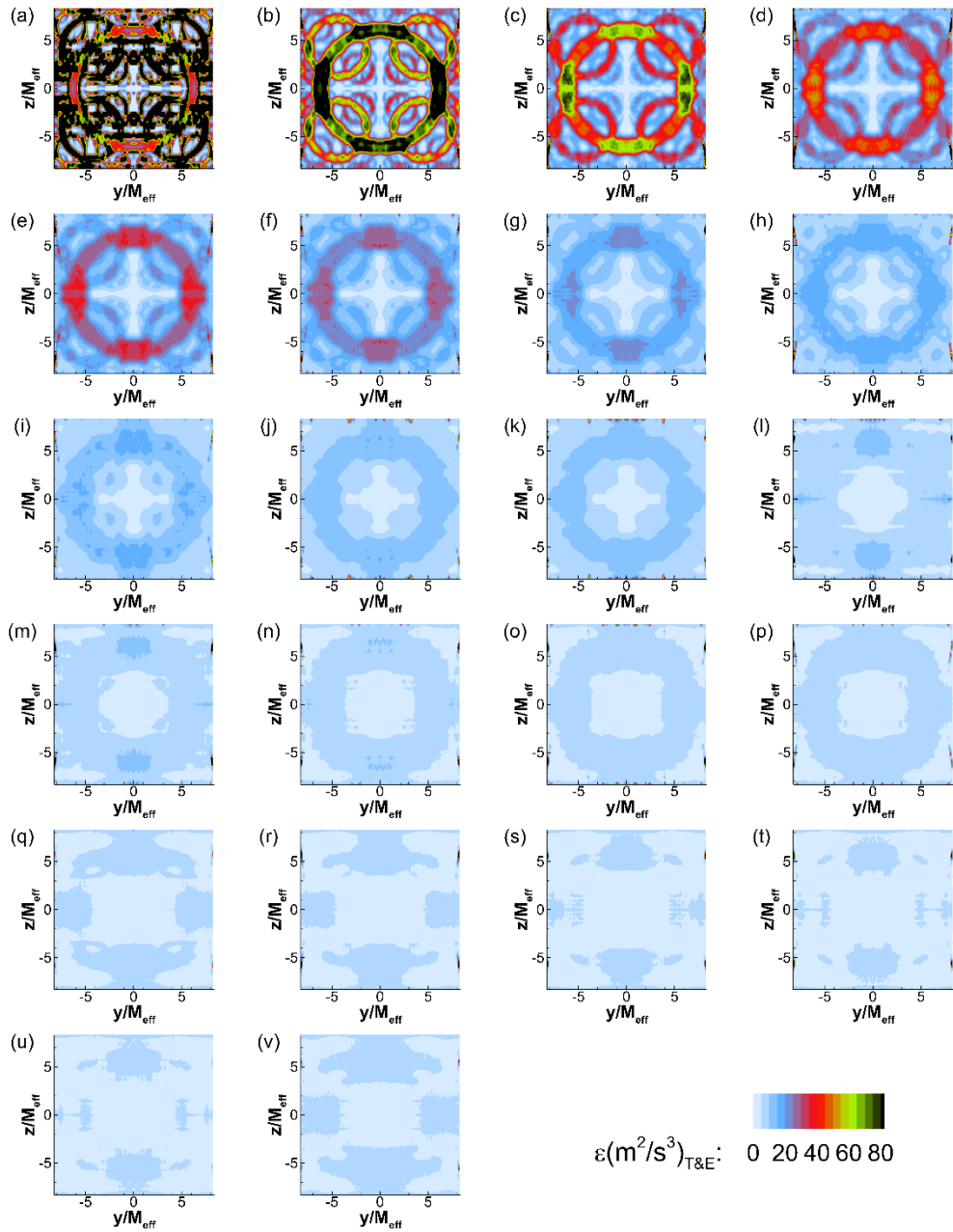
Figure 3-65 Development of 2-D estimated mean dissipation rate $\langle\varepsilon\rangle_{2D}$ in the near grid region of FCG. Distributions are given in $1\,M_{eff}$ increment from $1\,M_{eff}$ (a) to $22\,M_{eff}$ (v).
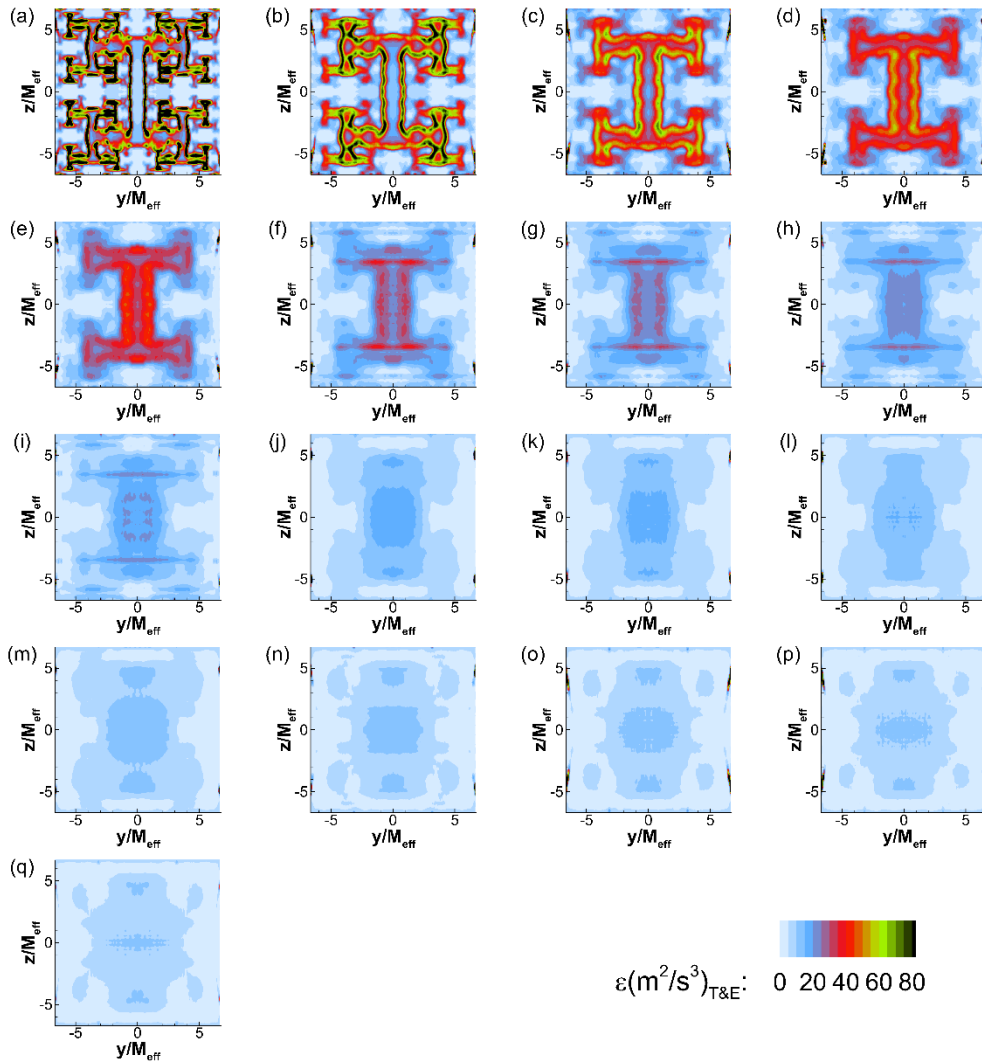
Figure 3-66 Development of 2-D estimated mean dissipation rate $\langle\varepsilon\rangle_{2D}$ in the near grid region of FIG. Distributions are given in 1 M_{eff} increment from 1 M_{eff} (a) to 17 M_{eff} (q).

Mean dissipation rate approximated by 2-D PIV data, is averaged over $x = cte$ planes to show the distribution of dissipation, qualitatively. Results are depicted in Figure 3-69 and Figure 3-70 and compared to the rate of dissipation along characteristic lines of TGG's in Figure 3-69.

Knowing the mean dissipation rate, the equation,

$$\eta = \frac{\nu^3}{\varepsilon} \tag{3.34}$$

is used in section 3.4.4 to estimate the Kolmogorov microscale.

108
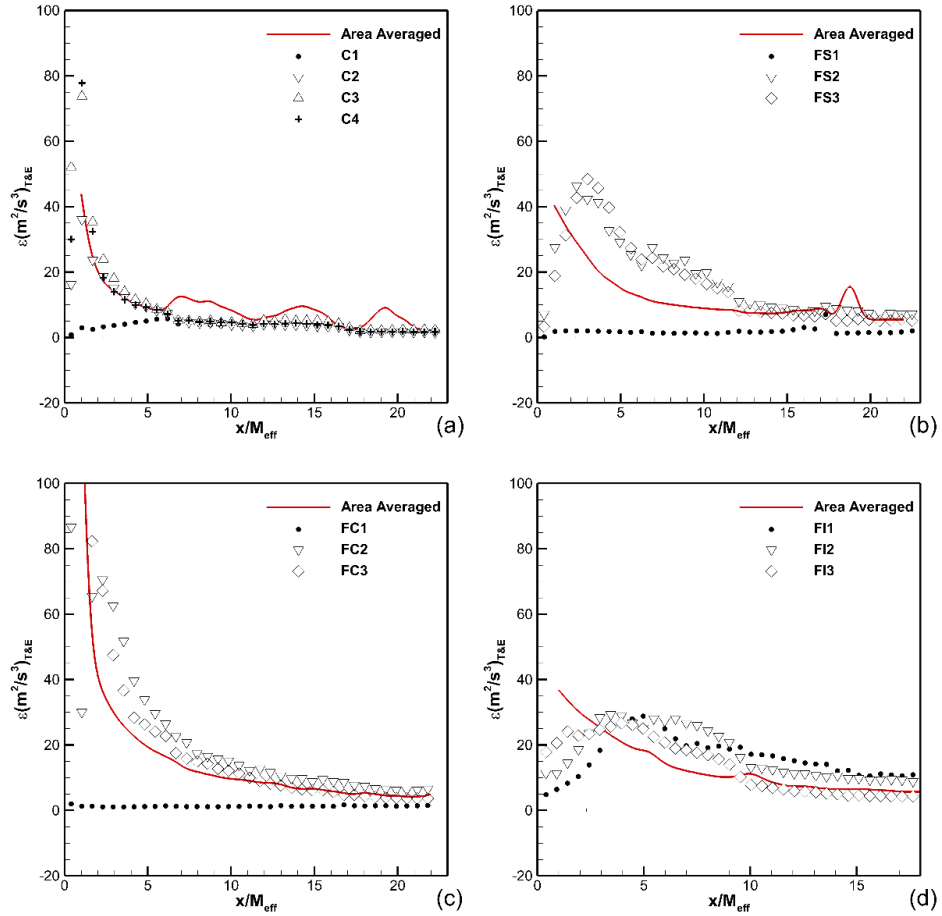
Figure 3-67 Mean dissipation rate of TKE, averaged on planes parallel to TGG's (red curve), and along characteristic lines of (a) CSG, (b) FSG, (c) FCG, and (d) FIG.
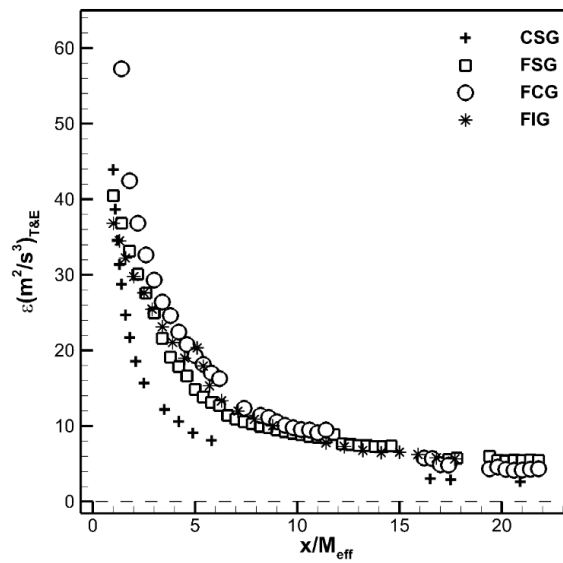
Figure 3-68 Streamwise evolution of area-averaged mean dissipation rate for all TGG's. Every 4th symbols are plotted to reduce the clutter.

3.3.3 The rate of production of turbulent kinetic energy

The production term shows itself as a source in the equation for the turbulent kinetic energy. It is generally positive and can be calculated from the multiplication of Reynolds stress and the mean velocity gradient at any point. The production rate is scalar, hence, invariant of the coordinate system.

$$\mathcal{P} \equiv -\overline{u_i u_j} \frac{\partial \overline{U_i}}{\partial x_j} \tag{3.35}$$

The terms inside (3.35) can be shown by a matrix in which elements are multiplications of the stress and the mean velocity gradient,

$$\mathcal{P}_{3D} = \begin{bmatrix} -\langle uu \rangle \dfrac{\partial \langle U \rangle}{\partial x} & -\langle uv \rangle \dfrac{\partial \langle U \rangle}{\partial y} & -\langle uw \rangle \dfrac{\partial \langle U \rangle}{\partial z} \\[2mm] -\langle vu \rangle \dfrac{\partial \langle V \rangle}{\partial x} & -\langle vv \rangle \dfrac{\partial \langle V \rangle}{\partial y} & -\langle vw \rangle \dfrac{\partial \langle V \rangle}{\partial z} \\[2mm] -\langle wu \rangle \dfrac{\partial \langle W \rangle}{\partial x} & -\langle wv \rangle \dfrac{\partial \langle W \rangle}{\partial y} & -\langle ww \rangle \dfrac{\partial \langle W \rangle}{\partial z} \end{bmatrix} \tag{3.36}$$

Then the production is the sum of all nine components of the above. Using data obtained with planar PIV, one can calculate the in-plane production rate which we call 2-D production ($\mathcal{P}_{2-D}$). Then (3.35) becomes,

$$\mathcal{P}_{2-D} = -\langle uu \rangle \frac{\partial \langle U \rangle}{\partial x} - \langle uv \rangle \frac{\partial \langle U \rangle}{\partial y} - \langle vu \rangle \frac{\partial \langle V \rangle}{\partial x} - \langle vv \rangle \frac{\partial \langle V \rangle}{\partial y} \tag{3.37}$$

Using diagonal symmetry condition in the case of CSG, FSG, and FCG, there might be three more terms added to the above, and since it includes more terms than 2-D version but still is far from the complete version, we call it 2.5-D production ($\mathcal{P}_{2.5D}$),

$$\mathcal{P}_{2.5D} = \mathcal{P}_{2-D} - \langle uw \rangle \frac{\partial \langle U \rangle}{\partial z} - \langle wu \rangle \frac{\partial \langle W \rangle}{\partial x} - \langle ww \rangle \frac{\partial \langle W \rangle}{\partial z} \tag{3.38}$$

One can realize that both $\mathcal{P}_{2-D}$ and $\mathcal{P}_{2.5D}$ are just estimations of the whole production rate. Therefore, some deviation may exist while interpreting production whether as 2.5-D or 2-D. For example, there are some minor regions where the production rate is

slightly negative. However, the in-plane rate of production (2-D production) is calculated for all grids.

Using MATLAB®, instantaneous velocity field on each window is loaded. This data field consists of 1003 velocity maps with coordinates x and y and velocity components U and V. Fluctuating data fields (u, v) are calculated by subtracting the mean values $(\langle U \rangle, \langle V \rangle)$. At each (x, y) position, the 2-D production rate is calculated using three Reynolds stress tensor components ($\langle uu \rangle$, $\langle uv \rangle = \langle vu \rangle$, and $\langle vv \rangle$) and four mean velocity gradients (mean strain rate tensor components), i.e. $\frac{\partial \langle U \rangle}{\partial x}, \frac{\partial \langle U \rangle}{\partial y}, \frac{\partial \langle V \rangle}{\partial x},$ and $\frac{\partial \langle V \rangle}{\partial y}$ as in (3.37). The results are stored in a '.dat' file to use in Tecplot afterwards. Two cases for CSG and FSG are shown in the following.

CSG is not a perfect case to validate the production in TKE budget since the spatial resolution is not enough to resolve the wake of the grid bars. The thickness of each bar is 2.1 mm, and the spatial resolution is 1.28 mm. However, some characteristics of wakes are in agreement with typical results in [107]. In-plane production data ($\mathcal{P}_{2-D}$) was generated for $^{z}/_{M_{eff}} = 0$ plane. Contour plot of 2-D production is shown in Figure 3-69. It is clear that the production region is extended only a few downstream distance from the grid ($\sim 1 M_{eff}$) and then it vanishes. In the figure, $^{y}/_{M_{eff}} = 0$ is the grid center in which region a jet is flowing. The profiles of the production rate across the jet-wake combination are illustrated at the right of Figure 3-69, each along specified transverse lines at $\frac{x}{M_{eff}} = 0.65, 1.0, 2.0,$ and 3.0. As the flow develops downstream of the grid, the production is continuously decreased where it reaches zero after $\frac{x}{M_{eff}} = 1.2$. The production distribution of the wakes are in agreement with the literature (see figure 5.29 in [107]).

As another example, a bigger – thus resolved – wake belonging to the largest bar in FSG grid is investigated. On $^{z}/_{M_{eff}} = 0$ plane, there are two large wake regions emanating from two vertical bars (look at Figure 3-8-b). A wake region downstream of the left side bar is shown in Figure 3-70 along with values of 2-D production rate.
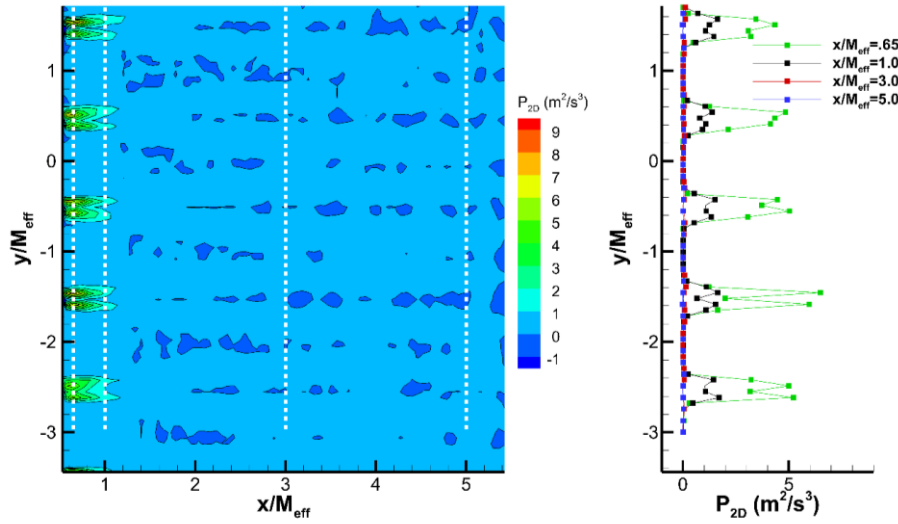
Figure 3-69 Map of in-plane production rate in the near-field of CSG at $\frac{Z}{M_{eff}}$=0 plane (left). Profiles of production rate along lines specified in the production map (right).
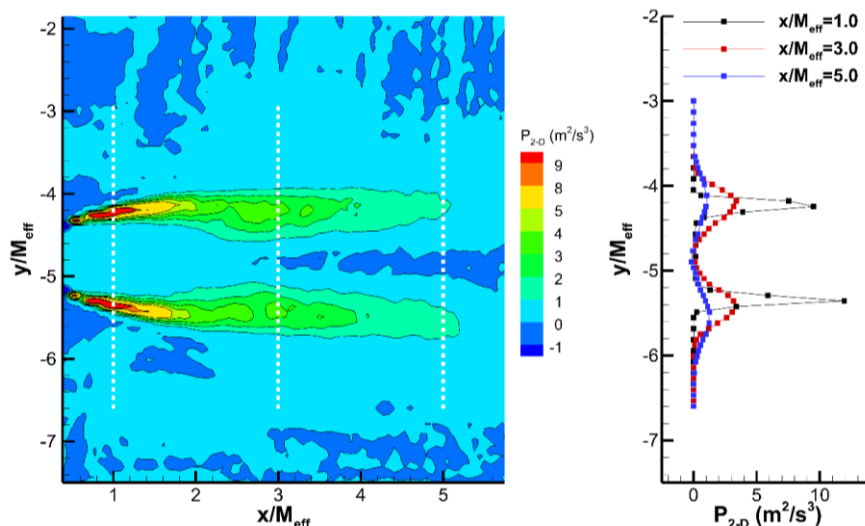
Figure 3-70 Map of in-plane production rate in the near-field of FSG at Z=0 plane. The area under investigation is the wake of the largest vertical bar in FSG (left). Profiles of production rate along lines specified in the production map (right).

Along the center of the bar $\left(\frac{y}{M_{eff}} \cong -4.8\right)$, there is a very low and almost zero production region. However, there are two side regions with higher production rates originated from the edges of the bar. The rate of production calculated using only in-plane variables (P_{2-D}) is non-negative in almost entire region under investigation.

112

Since the spatial resolution (1.28mm) is enough to resolve the wake behind this bar with the thickness of 10.2mm, the results clearly follow the production shape in the self-similar axisymmetric wake (see figure 5.29 in [107]).
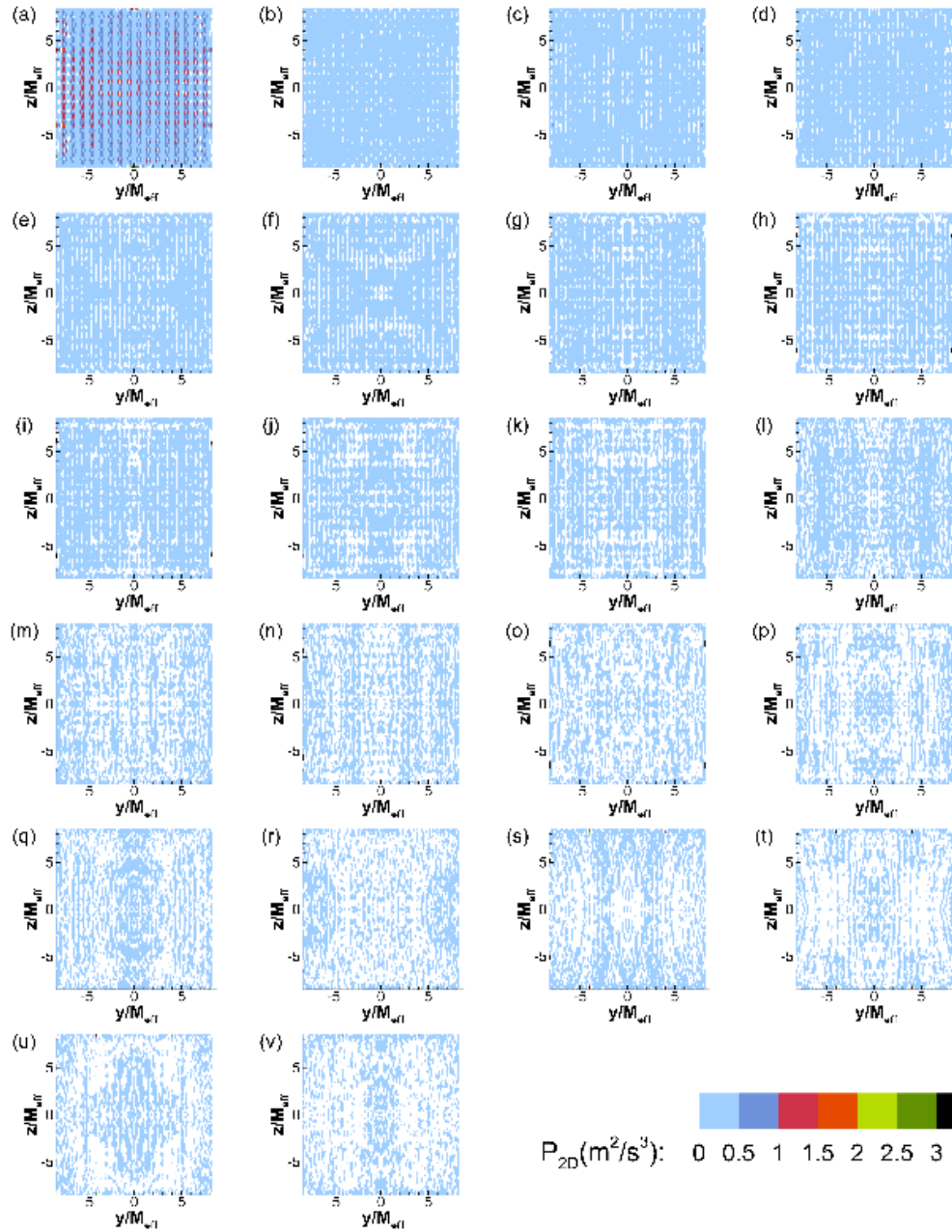
Figure 3-71 Evolution of the 2-D mean production rate P_{2D} in the near grid region of CSG. Distributions are given in 1 M_{eff} increment from 1 M_{eff} (a) to 22 M_{eff} (v).
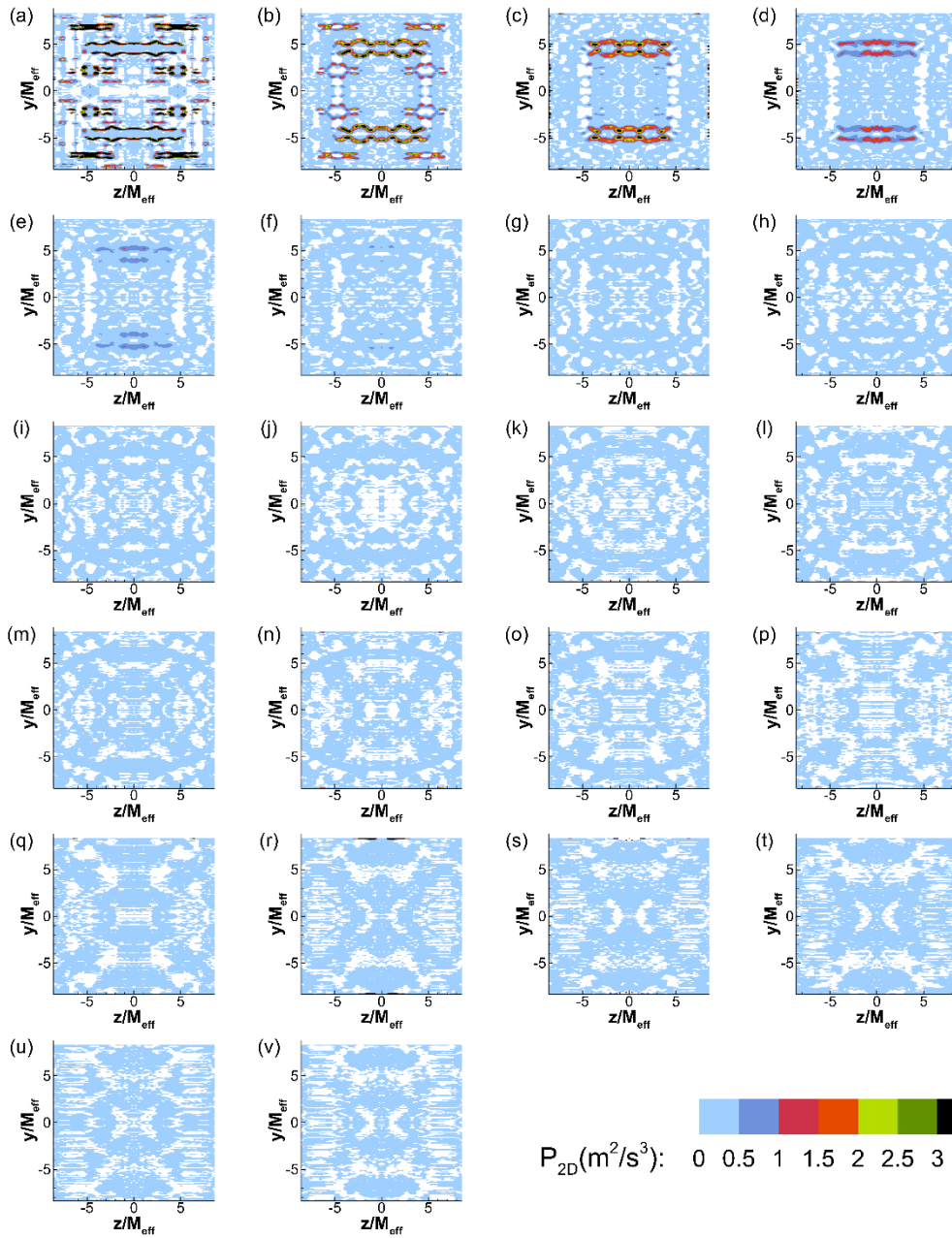
Figure 3-72 Evolution of the 2-D mean production rate P_{2D} in the near grid region of FSG. Distributions are given in 1 M_{eff} increment from 1 M_{eff} (a) to 22 M_{eff} (v).

114
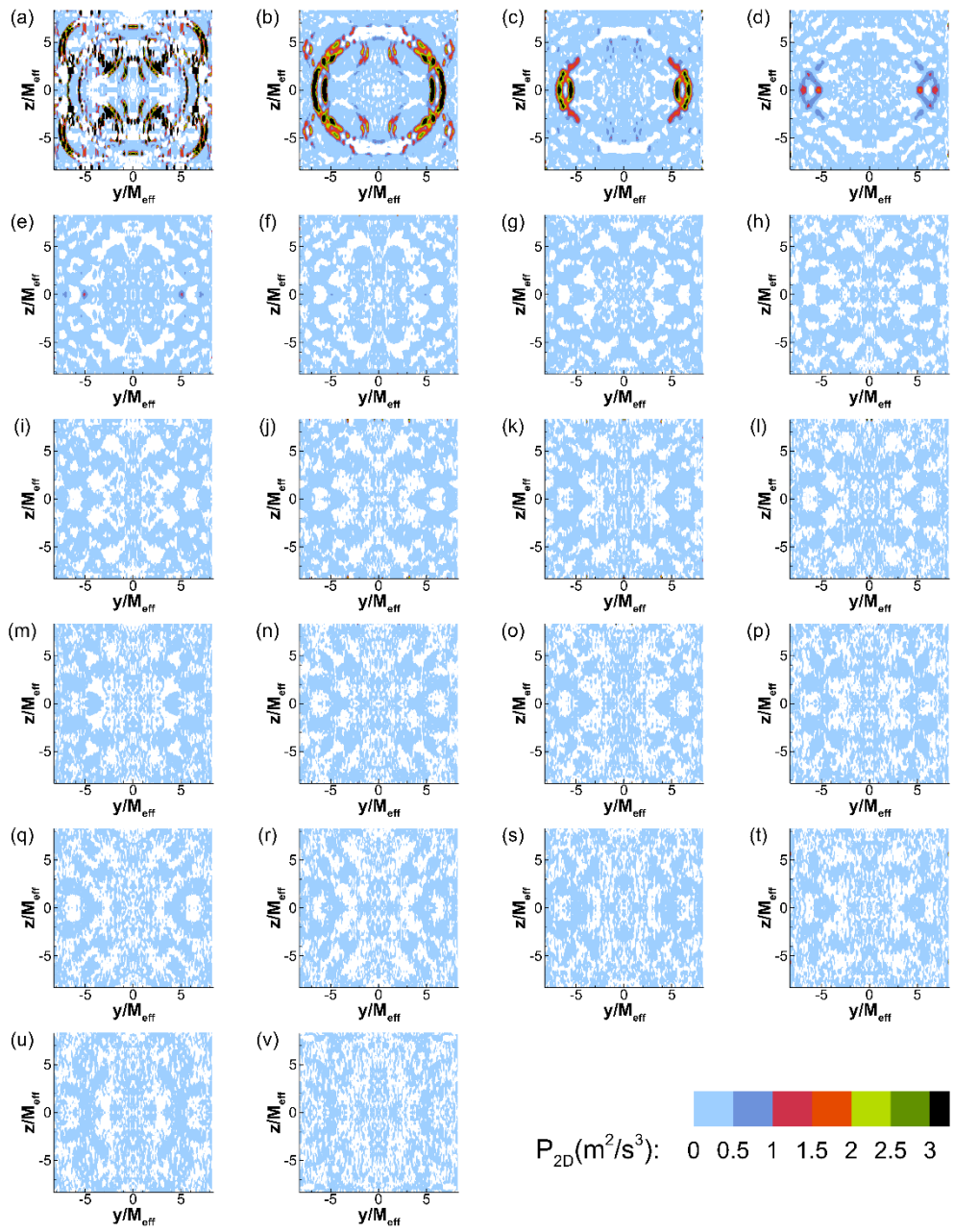
Figure 3-73 Evolution of the 2-D mean production rate P_{2D} in the near grid region of FCG. Distributions are given in 1 M_{eff} increment from 1 M_{eff} (a) to 22 M_{eff} (v).
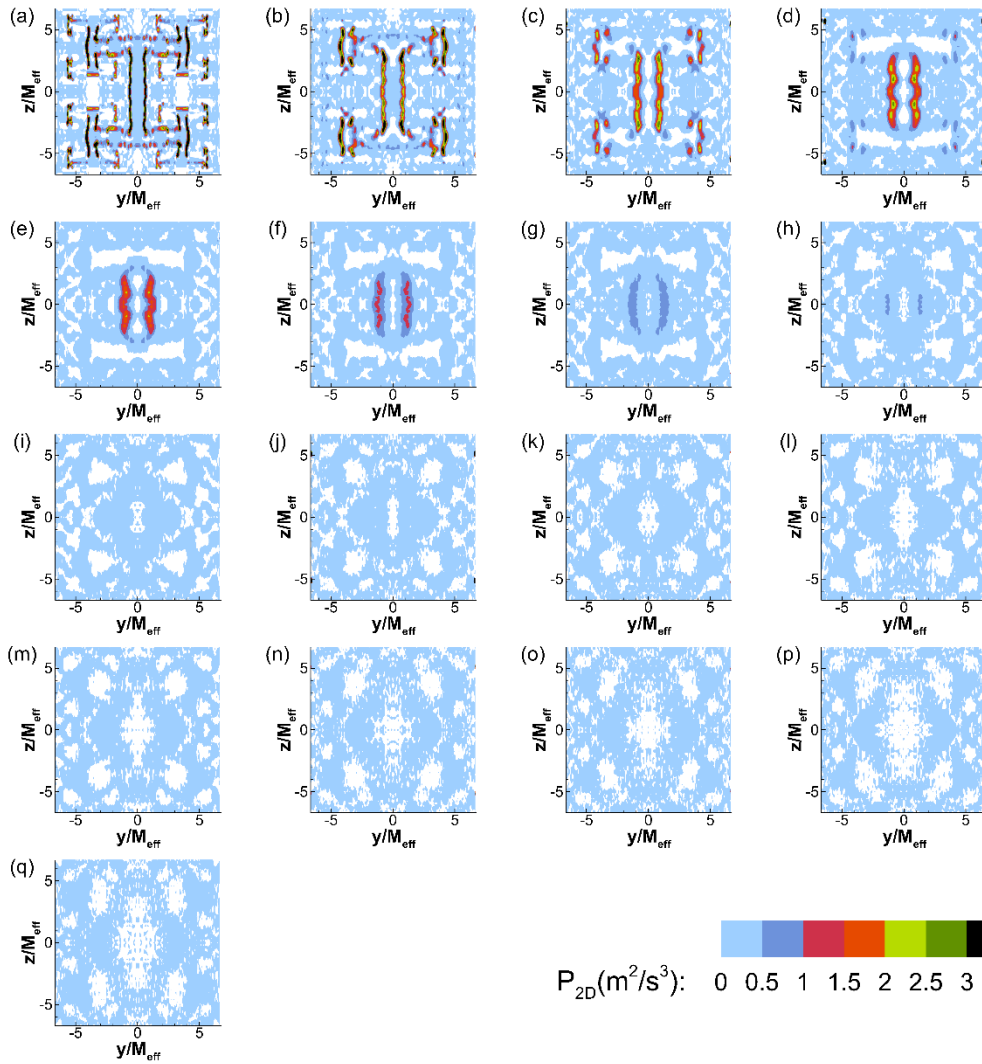
Figure 3-74 Evolution of the 2-D mean production rate P_{2D} in the near grid region of FIG. Distributions are given in 1 M_{eff} increment from 1 M_{eff} (a) to 17 M_{eff} (v).

One can obtain a 3-D map of the production rate to study on the distribution of production and its evolution in the near grid region. This can be done by patching all 4×35 windows. Parallel planes to the grid are extracted from the resultant volume data in every effective mesh size step. These $x = cte$ planes are shown in Figure 3-71 through Figure 3-74 to give idea about the distribution of 2-D production rate in the near-field of TGG's. Also, the 2-D production rate is averaged on these planes and depicted as red curves in Figure 3-75, together with its values along characteristic lines of each TGG.

116
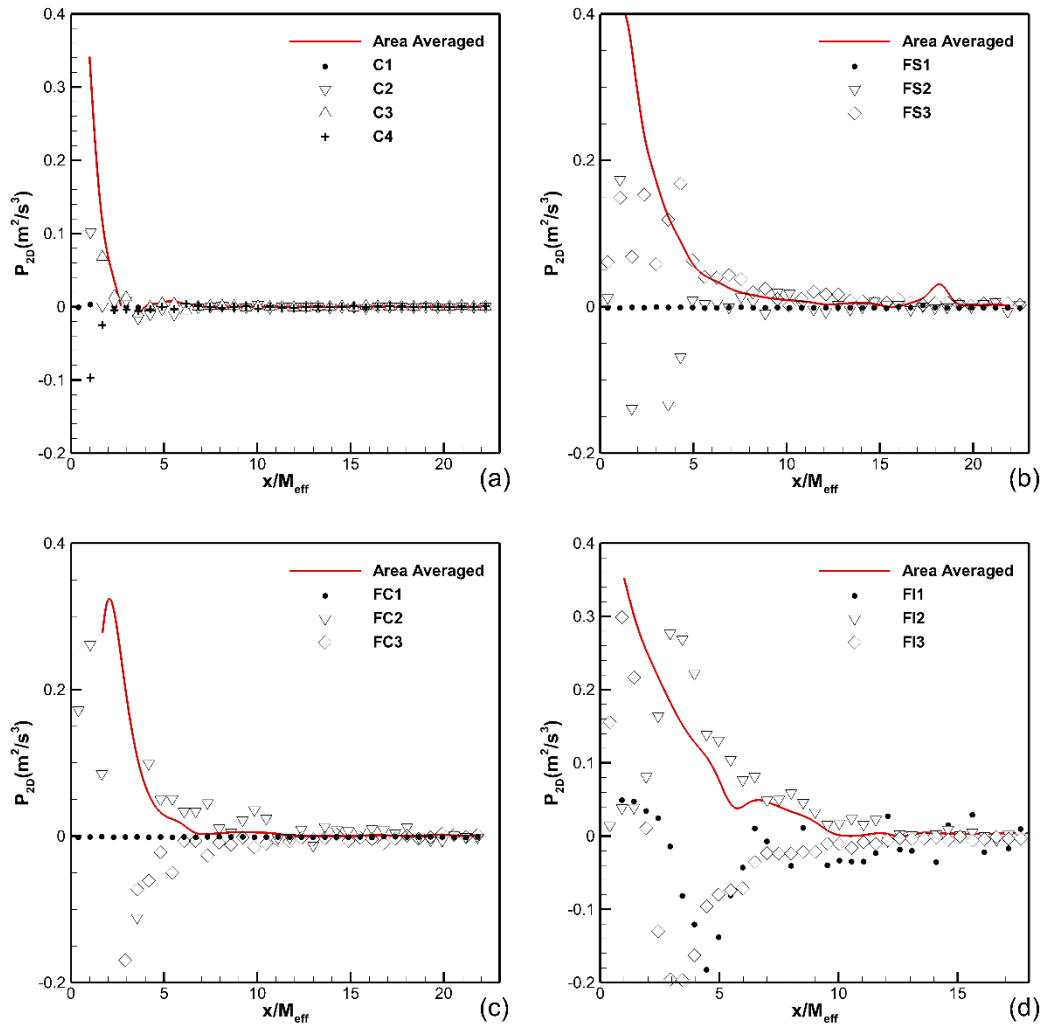
Figure 3-75 2-D production rate of TKE, averaged on planes parallel to TGG's (red curve), and along characteristic lines of (a) CSG, (b) FSG, (c) FCG, and (d) FIG.

One is able to compare the production rate and the estimated dissipation rate. In the near wake region, there exist regions with non-equilibrium condition (production is not equal to dissipation). This is depicted in Figure 3-76. In fact, production mainly occurs in the proximity of the grid ($\frac{x}{M_{eff}} \leq 5.0$) and with two orders of magnitude smaller than dissipation.
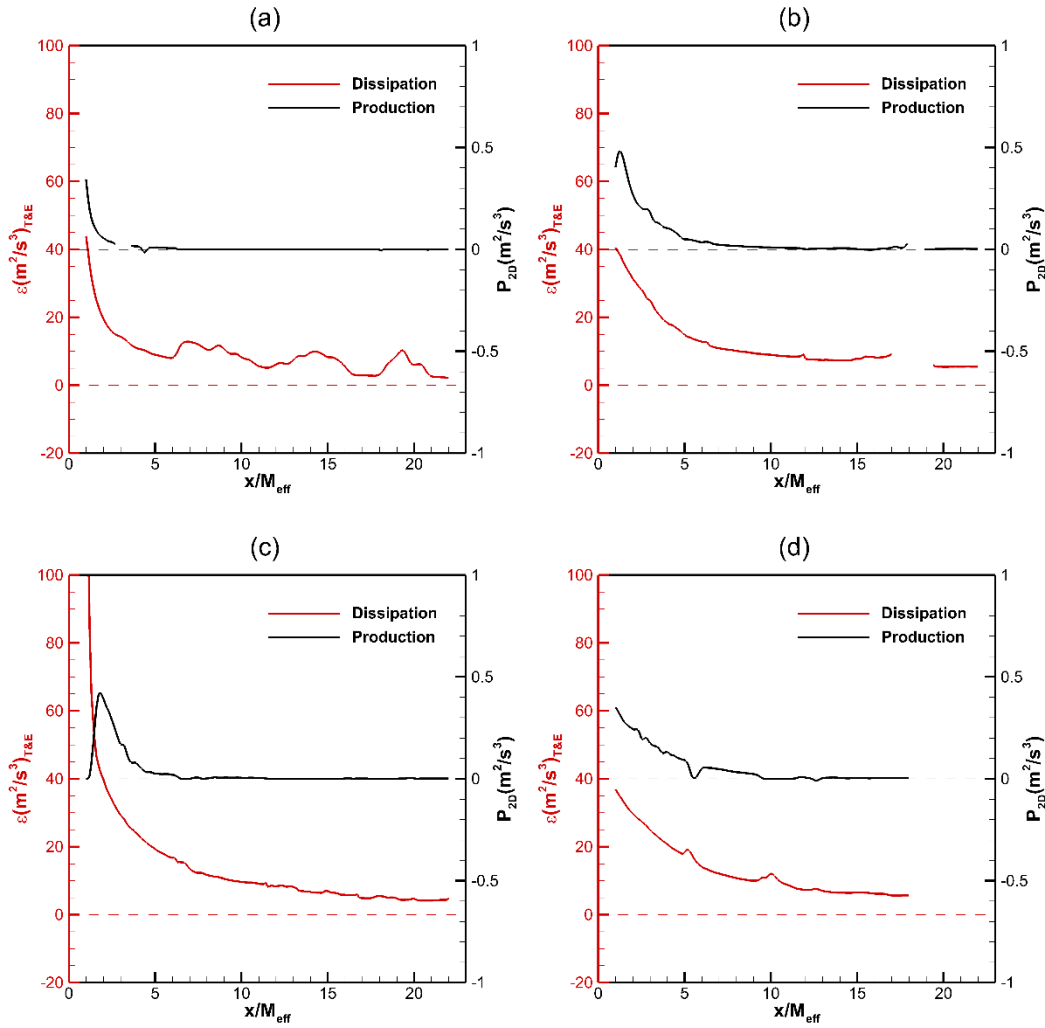
Figure 3-76 Comparison between rate of dissipation (red curve) and 2-D production rate (black curve) of TKE, averaged on parallel planes to TGG's for (a) CSG, (b) FSG, (c) FCG, and (d) FIG.

Area averaged 2-D production rate for all four types of TGG's is compared in Figure 3-77. The Highest rate of production belongs to FSG which happens at about 1.5 M_{eff} and just behind it, there is FCG which has its peak of production at about 1.8 M_{eff}. The rate at which the production decreases is the highest in CSG where P_{2-D} reaches literally zero at 3Mesh sizes downstream. After about 12 M_{eff} there exist very small 2-D production rate for all grids.
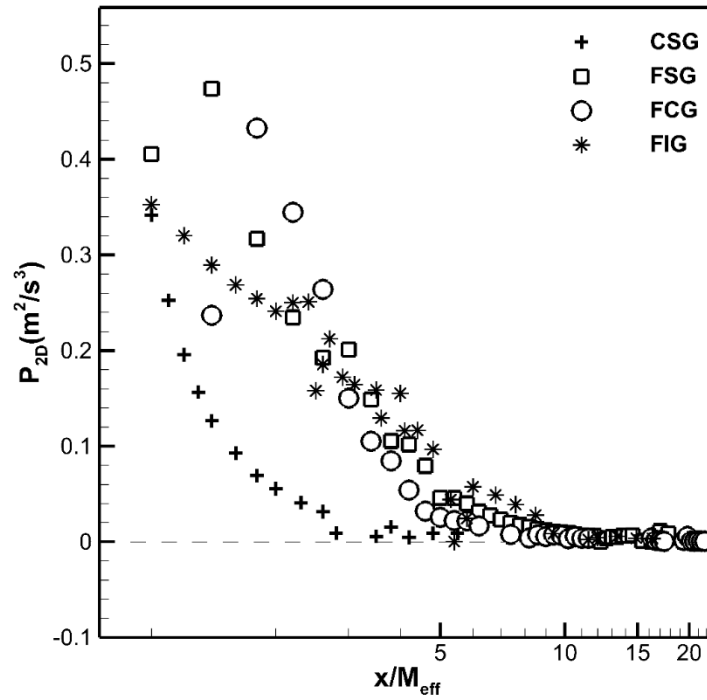
Figure 3-77 Streamwise evolution of area-averaged 2-D production rate for all TGG's. Every 4th symbols are plotted to reduce the clutter. Also, streamwise distance is plotted in logarithmic increment to emphasize on the very near grid region ($1 < \dfrac{x}{M_{eff}} < 10$).

3.4   Length scales in grid-generated-turbulence

There exist three standard length scales in a general turbulent flow. The one that is a measure of the largest separation distance over which the eddy's velocity components at two separate points are correlated, the one for which viscous dissipation begins to affect the eddies, and the one which characterizes the smallest dissipative eddies, Integral length scale, Taylor microscale, and Kolmogorov microscale, respectively [106,119,121]. Integral and Taylor scales can be obtained from the autocorrelation of the velocity fluctuations, i.e. $\langle u(t)u(t + \tau)\rangle$. The time separation ($\tau$) is exchangeable to space separation (r) by Taylor's frozen turbulence hypothesis,

$$\frac{\partial}{\partial r} \approx \frac{1}{\langle U \rangle}\frac{\partial}{\partial \tau} \tag{3.39}$$

Integral and Taylor scales are schematically shown in Figure 3-78. The vertical axis is the autocorrelation coefficient. By definition, the area underneath $f(r) - (r)$ is the

119

integral scale and the curvature of $f(r)$ at the origin is the Taylor microscale. In the following, we will obtain theses length scales as well as estimation of the Kolmogorov length scale in the near-field of the grids.
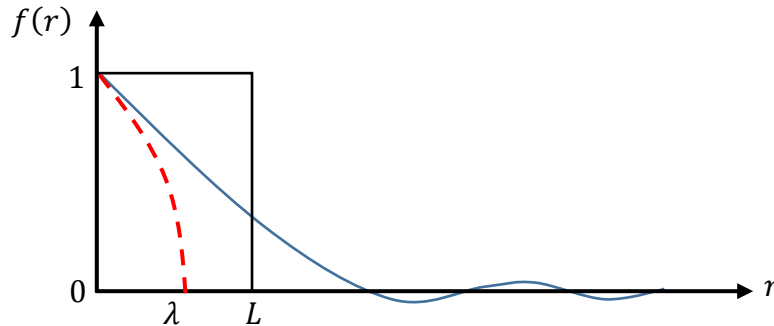
Figure 3-78 A sketch of an autocorrelation coefficient, Integral (L) and Taylor (λ) length scales.

3.4.1 Integral length scales

Integral length scale (ILS) is a rough measure of the interval over which the fluctuating velocity is correlated with itself [106,108]. Physically, ILS shows the size of energetic eddies [122,123], and in the case of GGT, it shows the geometry of the turbulence generator [124] and the scale at which turbulence is forced [125]. If the turbulence is homogeneous and isotropic, the integral length scale also shows the scale at which the kinetic energy of the flow (k) is injected into the turbulence [107]. Integral length scale L_{pq} is defined as [40],

$$L_{pq} = \frac{1}{\langle u_p^2 \rangle} \int_0^\infty R_{pp}(r_1, r_2) dr_q \qquad (3.40)$$

where 'p' and 'q' stand for the velocity component and the component over which the direction of separation is chosen, respectively. The autocorrelation function for the velocity fluctuations is R and dr is the separation distance. Data obtained from 2-D PIV, will give four different integral scales ($L_{uu}, L_{uv}, L_{vu,}$ and L_{vv}) among which L_{uu} and L_{vv} are more common than other two, called longitudinal and lateral integral length scales, respectively. We will use L_u instead of L_{uu} for the sake of simplicity.

It is rather hard for PIV measurements to result in integral length scale L_u and the Taylor microscale λ simultaneously. Former requires a field of view (FOV) at least 6-7 times of the integral length scale, while latter calls for high resolution to resolve the Taylor microscales. A lack of high dynamic spatial range in two-pulse digital PIV technique makes it difficult to easily reach such a high resolution [40]. In case of FOV sizes in the same order of L_u, it has been shown that fitting a function with exponential decay to the tails of the longitudinal two-point correlation function (R_{uu}), will result in a good estimation of longitudinal integral length scale (LILS) L_u [126]. The validity of the exponential fit was checked for the 2-D PIV data obtained at the centerline of a fractal square grid inside a water tunnel [14] and the data from a similar experiment in the wind tunnel [55]. It is expected to have integral length scale to be of the order of magnitude of the effective mesh size [40] while in [35] the integral scale of the order of 1/10 of the test section dimension is reported for the fractal grids.

Integral length scales can be estimated from the spatial two-point correlation of longitudinal and transverse velocity fluctuations, $u = U - \langle U \rangle$ and v= $V - \langle V \rangle$, for a separation "r" as defined by [107]. Integrating the two-point correlation coefficient of velocity fluctuation along any dimension results the integral length scale along that direction. Here we report the LILS by integrating the two-point correlation coefficient of velocity fluctuations along the 'x' axis. Two-point correlation of velocity fluctuation along 'x' direction is written as,

$$\tilde{f}(r) = \langle u(x,y)u(x+r,y) \rangle \qquad (3.41)$$

where $\langle \quad \rangle$ indicates the spatial average over 'x' and 'y' and ensemble average over all the fluctuating velocity fields $u(x,y)$ – For each PIV window there are 1003 realizations – and the correlation function of velocity fluctuations is defined as,

$$f(r) = \frac{\tilde{f}(r)}{f(0)} = \frac{\langle u(x,y)u(x+r,y) \rangle}{\langle u^2(x,y) \rangle} \qquad (3.42)$$

The LILS is defined as [52],

$$L_u = \int_0^{\infty} f(r)\, dr \qquad (3.43)$$

121

The upper bound of the integration is usually taken as the first zero-crossing of the correlation function (i.e., where $f(r) = 0$) [127]. Due to the limited field of view, $f(r)$ may not always cross zero, in which case, the value for L_u is blanked over the corresponding starting point.

To calculate for L_u, each PIV window is divided by sections of five neighboring rows, taking the middle one as the destination row. Note that all windows are horizontal windows with 'x' and 'y' coordinates in streamwise and spanwise directions respectively. Hence, five rows of data includes 5 successive 'y' values, i.e. $y_{j-2}, y_{j-1}, y_j, y_{j+1}$, and y_{j+2}. Longitudinal cross correlation function is then calculated for a starting point (i.e. x_i) to the endpoint (i.e. x_f) on the central row, i.e. $y_j{}^{th}$ one, averaged over 1003 vector maps and all the cells in the cropped section. If the correlation function crosses zero somewhere in the $(x_f - x_i)$ range, then the integration (3.43) yields a true value for L_u. In this situation, some index as a true value (i.e., 1) is assigned to the x_i point. Otherwise, the integration is calculated over the entire distance $(x_f - x_i)$ with false index (i.e., 0) assigned to the x_i point and the result is called as $L_{u_{inf}}$. As an example, the longitudinal correlation function $\langle u(x,y)u(x+r,y)\rangle$ of streamwise component of velocity fluctuations along the centerline in W1 of CSG is shown in Figure 3-79 .
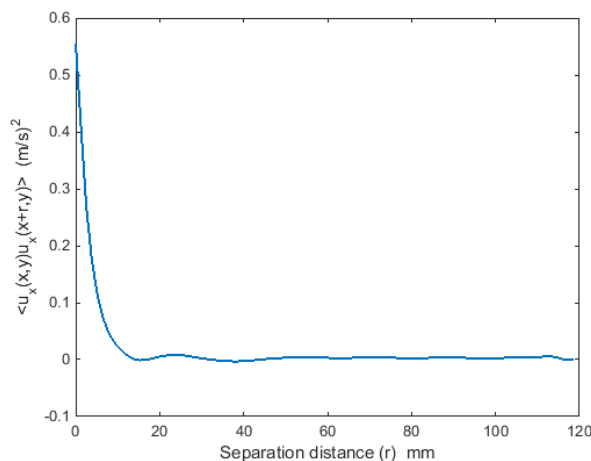
Figure 3-79 Longitudinal correlation function $\langle u(x,y)u(x+r,y)\rangle$ of streamwise component of velocity fluctuations calculated for W1 in CSG, MATLAB® output.

122

Corresponding values for LILS are $L_{u_{inf}} = 4.3859\ mm$ and $L_u = 4.3535\ mm$, where $L_{u_{inf}}$ indicates the integration upper bound to the maximum separation distance which is limited to the PIV window size along 'x' direction, and L_u is the length scale based on the first zero-crossing of the correlation function (i.e., where $f(r) = 0$).

There are also two other values calculated for the longitudinal length scale, $L_{u_{0.1}}$ and $L_{u_{0.2}}$ indicating two different criteria for integration limit. When the value of $f(r)$ reaches to $\frac{1}{10}f(0)$, i.e., when the correlation strength drops to 90% of its initial value, one can calculate $L_{u_{0.1}}$ by,

$$L_{u_{0.1}} = \int_0^{r|_{f(r)=0.1f(0)}} f(r)\ dr \tag{3.44}$$

the same applies to $L_{u_{0.2}}$ such that,

$$L_{u_{0.2}} = \int_0^{r|_{f(r)=0.2f(0)}} f(r)\ dr \tag{3.45}$$

The idea of calculating L_u by (3.44) and (3.45) is that due to small FOV, the longitudinal extent of each window (typically 128 mm) may not be enough for correlation to pass zero – especially at some locations starting from the endpoints of the FOV – hence resulting in a true value for L_u.

Using integration limit $r|_{f(r)=0.1f(0)}$ instead of $r|_{f(r)=0}$, has to be justified. In order to do that, a comparison is made between the results of all longitudinal and lateral length scales calculated based on both criteria. As an example, evolution of ILS L_{uu} and L_{vu} along characteristic lines of CSG, is shown in Figure 3-80. Values of L_0 and $L_{0.1}$ are shown by filled (solid) and hollow (dashed) symbols (lines), respectively.
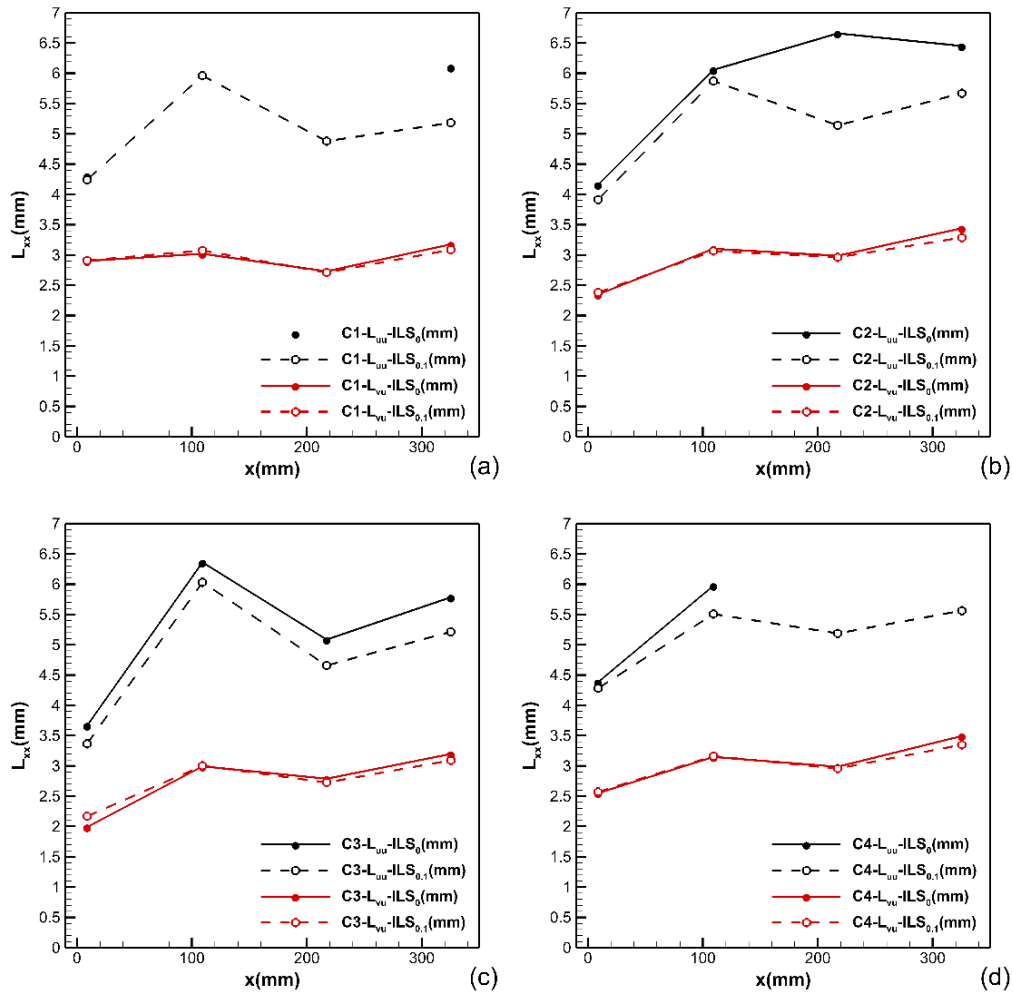
Figure 3-80 Comparison between values of ILS L_{uu} and L_{vu}, along characteristic lines (a) C1, (b) C2, (c) C3, and (d) C4, of CSG. Length scales are calculated based on integration limits $r|_{f(r)=0.1f(0)}$ and $r|_{f(r)=0}$, indicated by ILS_0 and $ILS_{0.1}$, respectively.

In Figure 3-81, L_{uu} and L_{vu} along characteristic lines of FSG are compared.
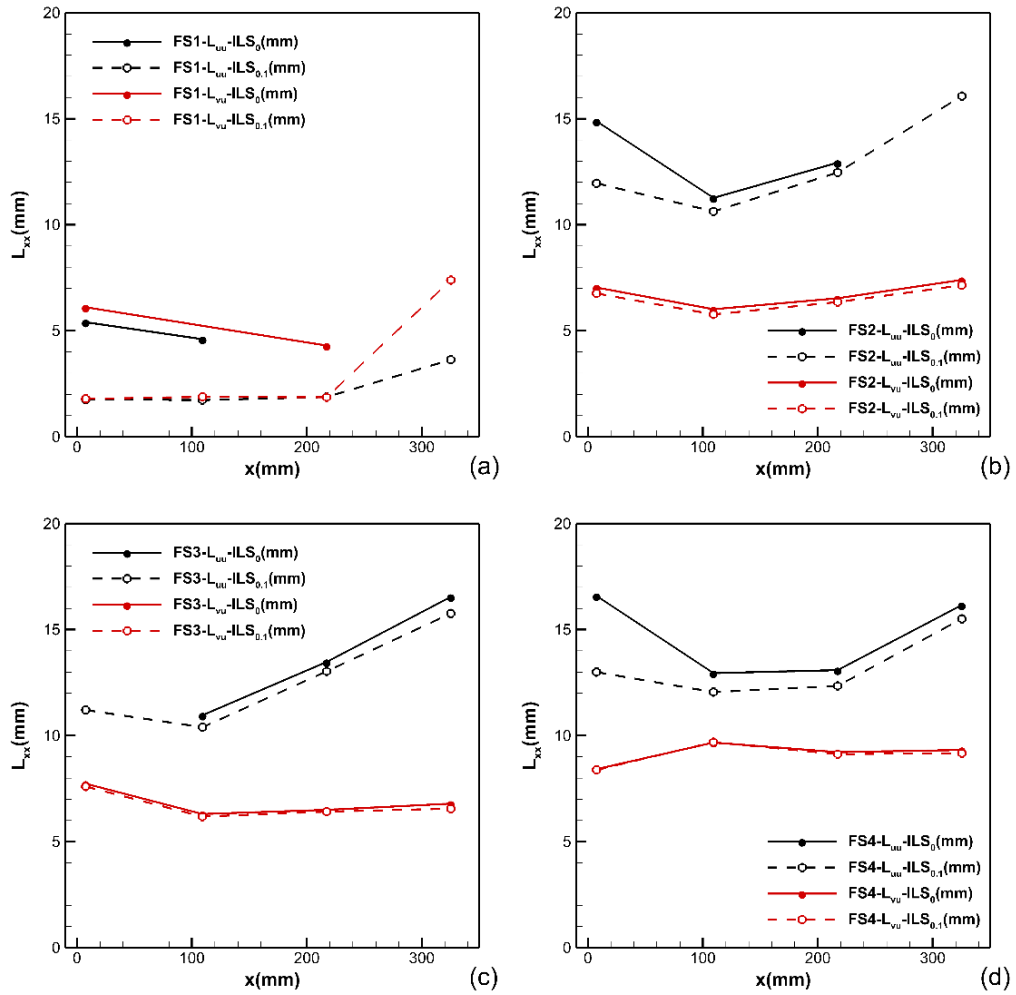
Figure 3-81 Comparison between values of ILS L_{uu} and L_{vu}, along characteristic lines (a) FS1, (b) FS2, (c) FS3, and (d) FS4, of FSG. FS4 is at the center of the largest vertical bar. Length scales are calculated based on integration limits $r|_{f(r)=0.1f(0)}$ and $r|_{f(r)=0}$, indicated by ILS_0 and $ILS_{0.1}$, respectively.

Another example is the variation of ILS L_{vv} and L_{uv} on the center-plane of TGG's which is shown in Figure 3-82. To conclude, values of $L_{0.1}$ always are underestimated which is normal due to lower integration limit. Nevertheless, its value is acceptable within 20% of L_0 value at most points. Of course center line data is excluded in this case.
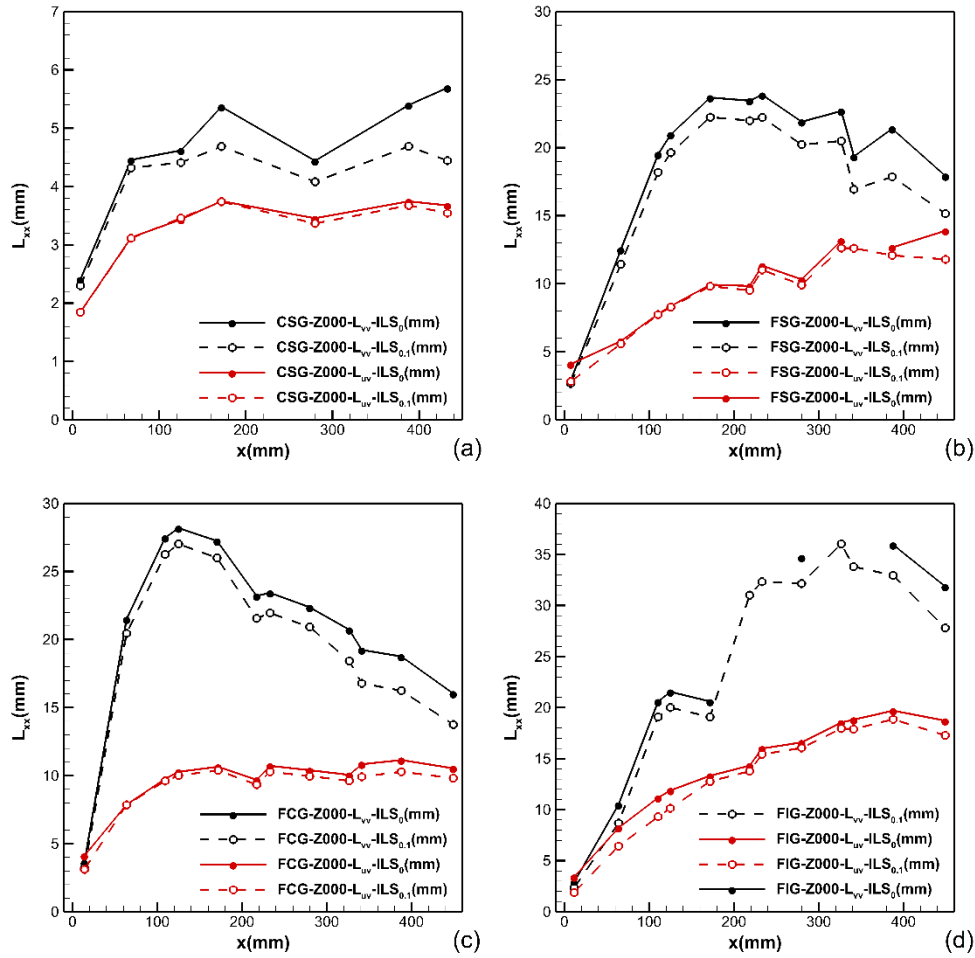
Figure 3-82 Comparison between values of ILS L_{vv} and L_{uv}, on the center-plane of (a) CSG, (b) FSG, (c) FCG, and (d) FIG. Length scales are calculated based on integration limits $r|_{f(r)=0.1f(0)}$ and $r|_{f(r)=0}$, indicated by ILS_0 and $ILS_{0.1}$, respectively.

Evolution of LILS (L_{uu} and L_{vv}) along characteristic lines and planes of interest, mentioned in section 3.1.4 and Table 3-5, respectively, is shown in Figure 3-83. In total, values of LILS downstream of CSG are smaller than fractal grids and stay more or less constant (or with a little increase). For FSG and FCG, the largest L_{vv} is found on the center plane wherein FCG it drops faster than FSG. Centerline of both grids shows the same variation of L_{uu} while it is very different in FIG due to its completely different geometry and flow field.

126
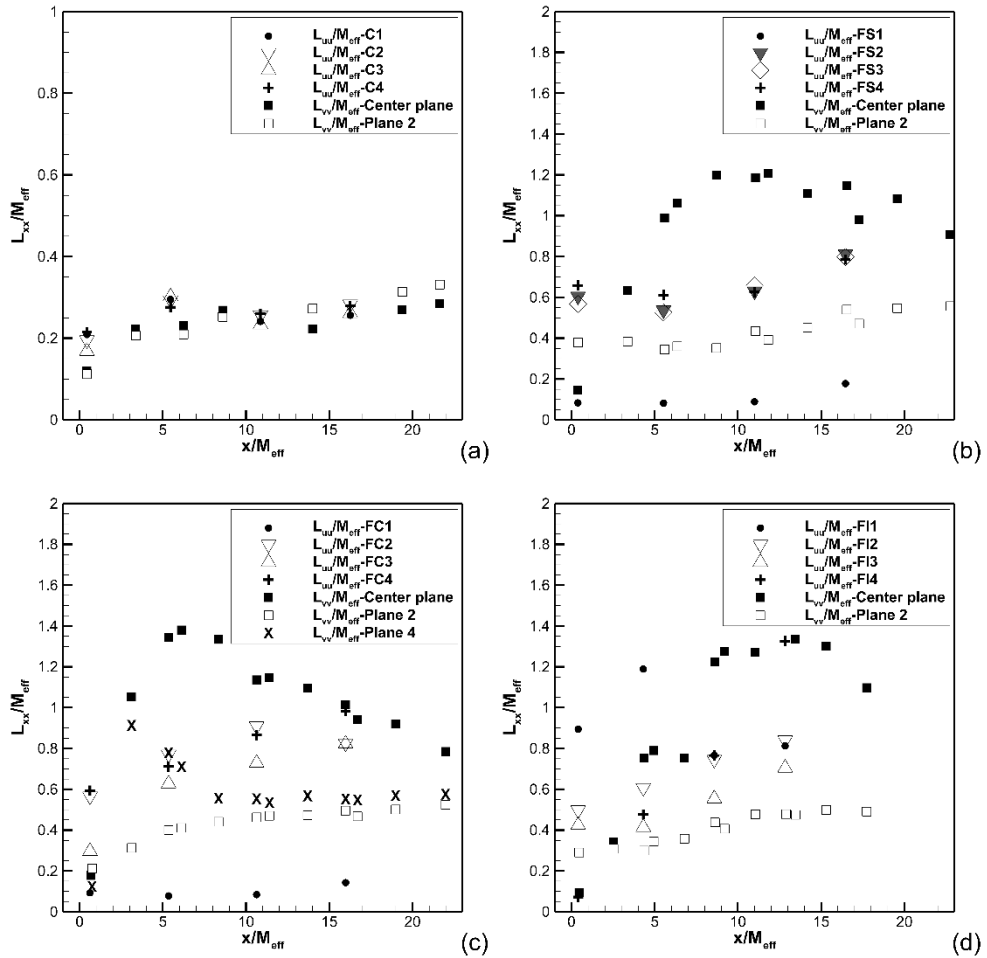
Figure 3-83 Comparison between values of LILS L_{uu} and L_{vv}, on characteristic lines and planes of interest in (a) CSG, (b) FSG, (c) FCG, and (d) FIG. L_{uu} is calculated along characteristic lines while L_{vv} is calculated along spanwise lines on the plane of interest. Plane 4 in case of FCG is a horizontal plane passing point FC3 on the corner of the largest circular element.

After calculating the LILS on each PIV window, all windows are patched together to form a volume. Mirroring this quarter volume about XY and XZ axes gives a complete volume of near grid data. Previous studies mainly focused on the centerline variation of integral scales since the majority of experiments were performed in the far-field region. In this study, we are so close to the grid that the local differences make it impossible to rely on the centerline. The evolution of $L_{u_{0.1}}$ on some planes parallel to the grids are shown in Figure 3-84 to Figure 3-87, where these local differences are clearly seen.

127
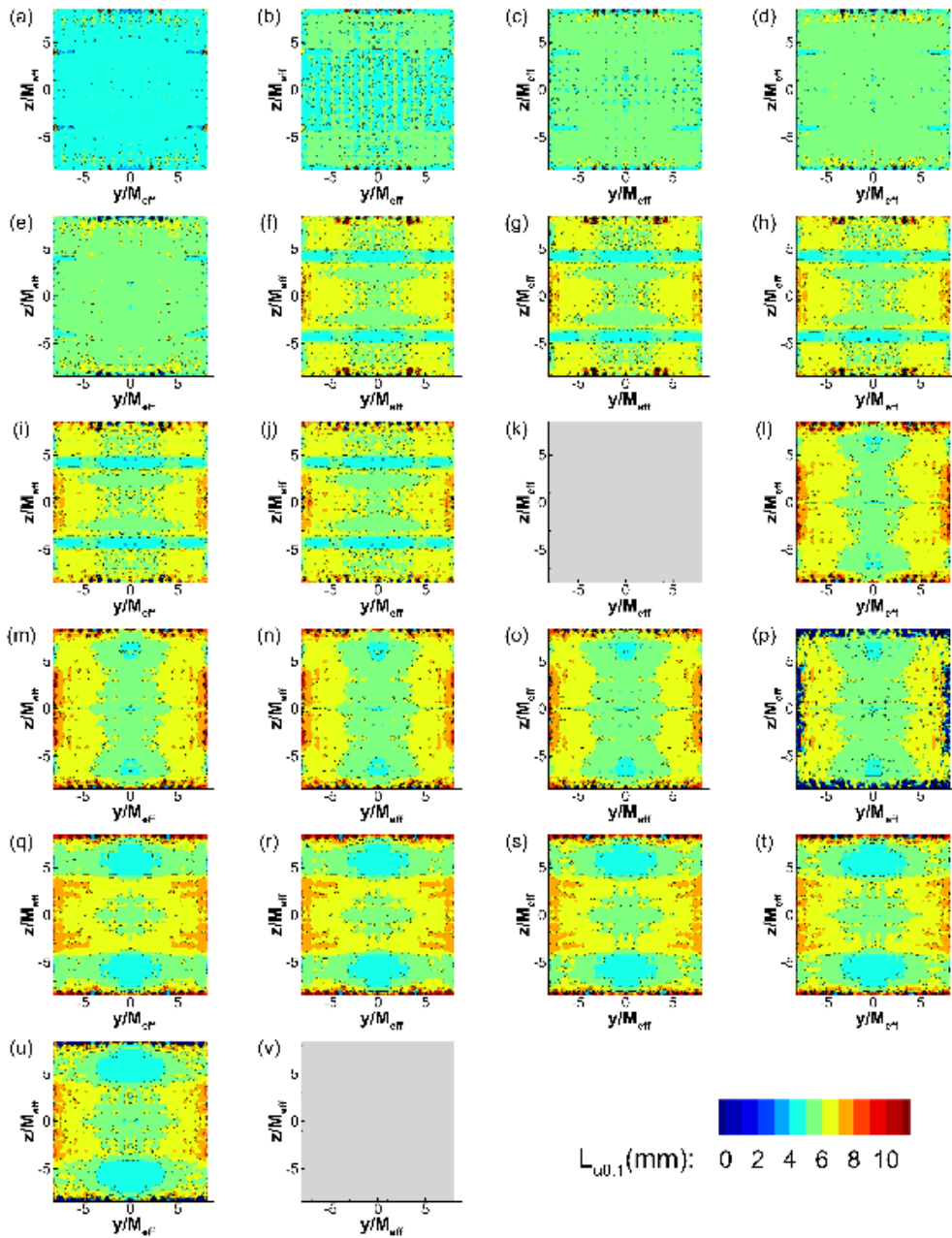
Figure 3-84 Evolution of longitudinal integral length scale ($L_{u_{0.1}}$) in the near-grid region of CSG. Distributions are given in $1\,M_{eff}$ increment from $1\,M_{eff}$ (a) to $22\,M_{eff}$ (v). Blanked regions are those at which the calculation of $L_{u_{0.1}}$ does not provide any result.
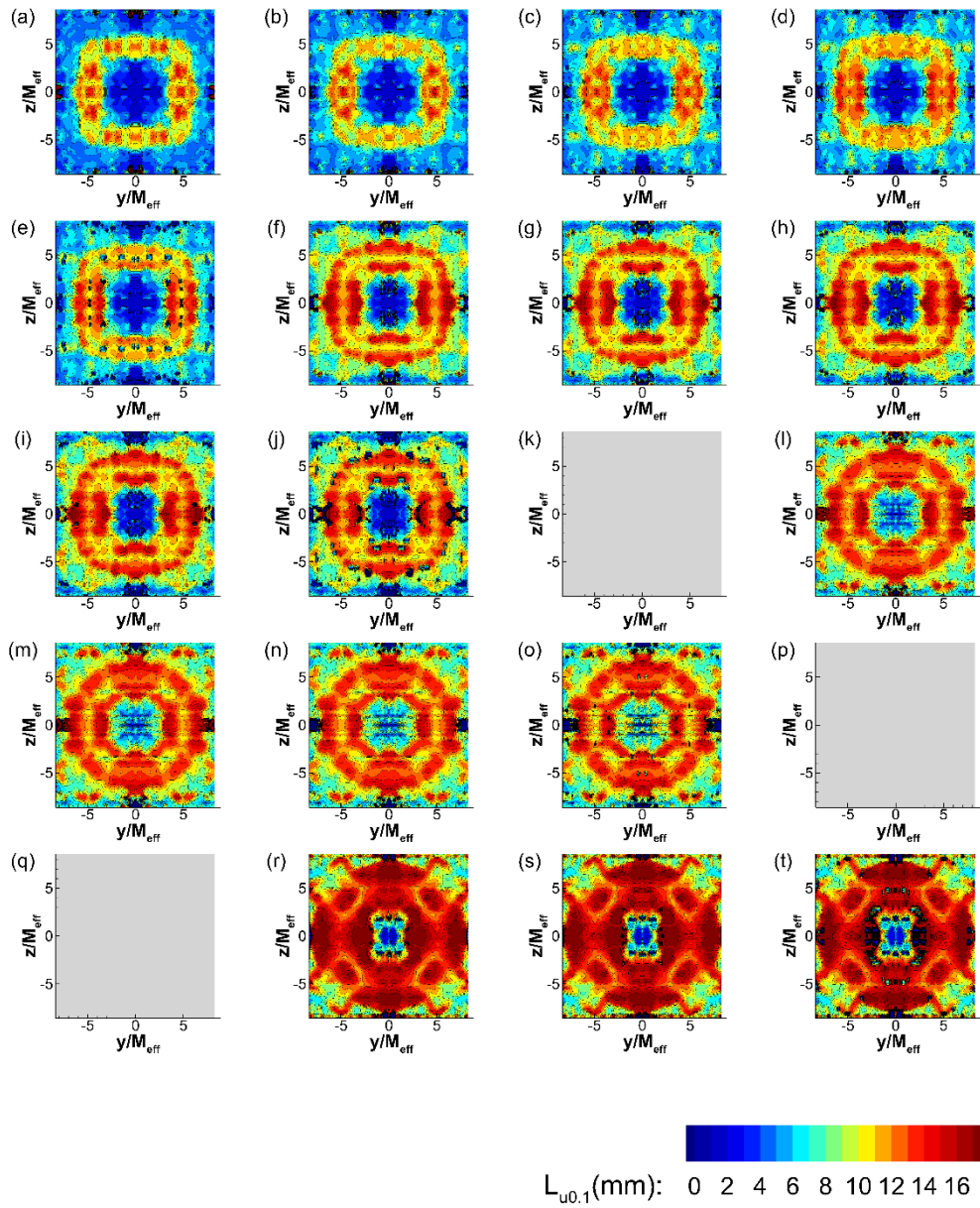
Figure 3-85 Evolution of longitudinal integral length scale ($L_{u_{0.1}}$) in the near-grid region of FSG. Distributions are given in 1 M_{eff} increment from 1 M_{eff} (a) to 20 M_{eff} (t). Blanked regions are those at which the calculation of $L_{u_{0.1}}$ does not provide any result.

129
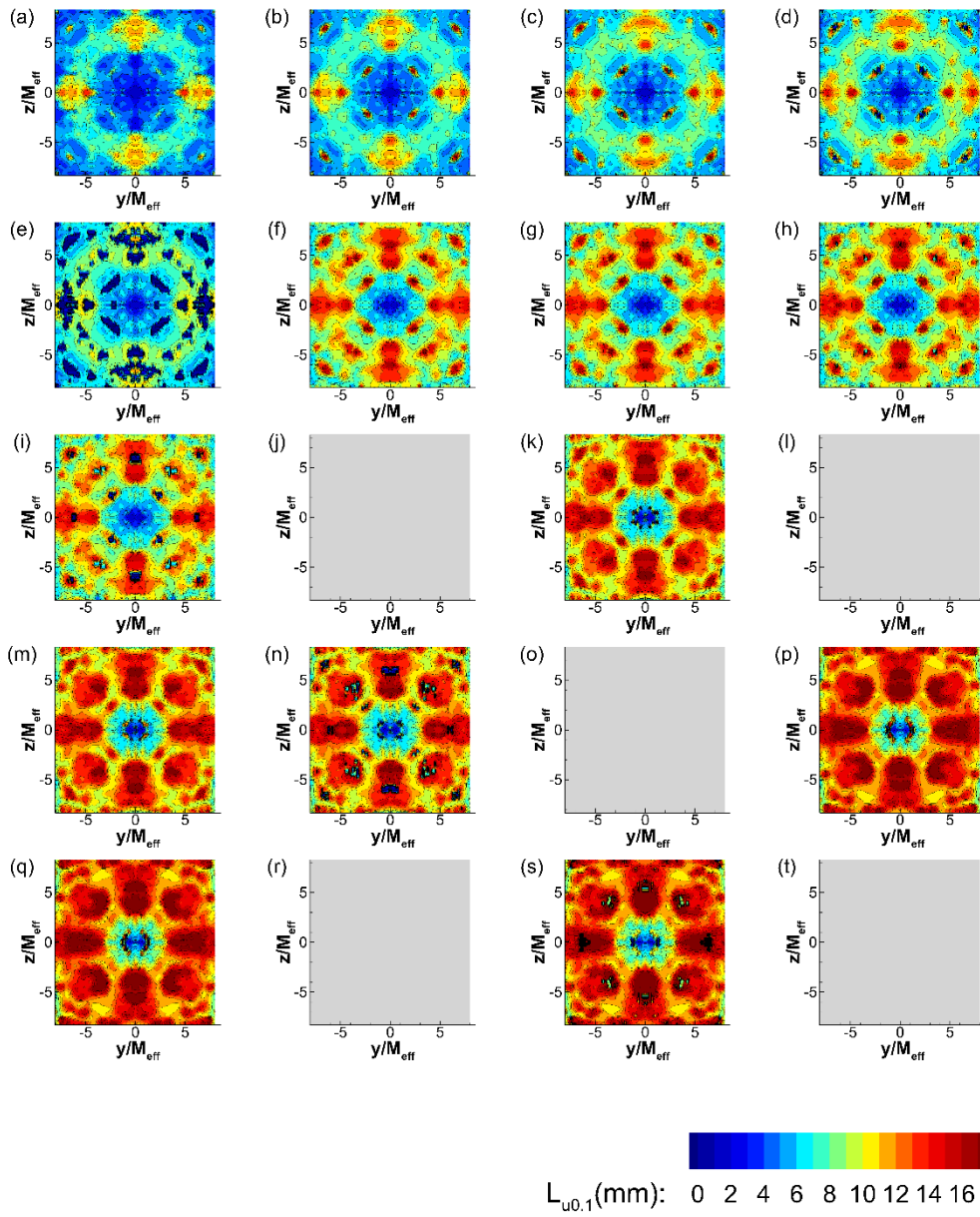
Figure 3-86 Evolution of longitudinal integral length scale ($L_{u_{0.1}}$) in the near-grid region of FCG. Distributions are given in $1\,M_{eff}$ increment from $1\,M_{eff}$ (a) to $20\,M_{eff}$ (t). Blanked regions are those at which the calculation of $L_{u_{0.1}}$ does not provide any result.
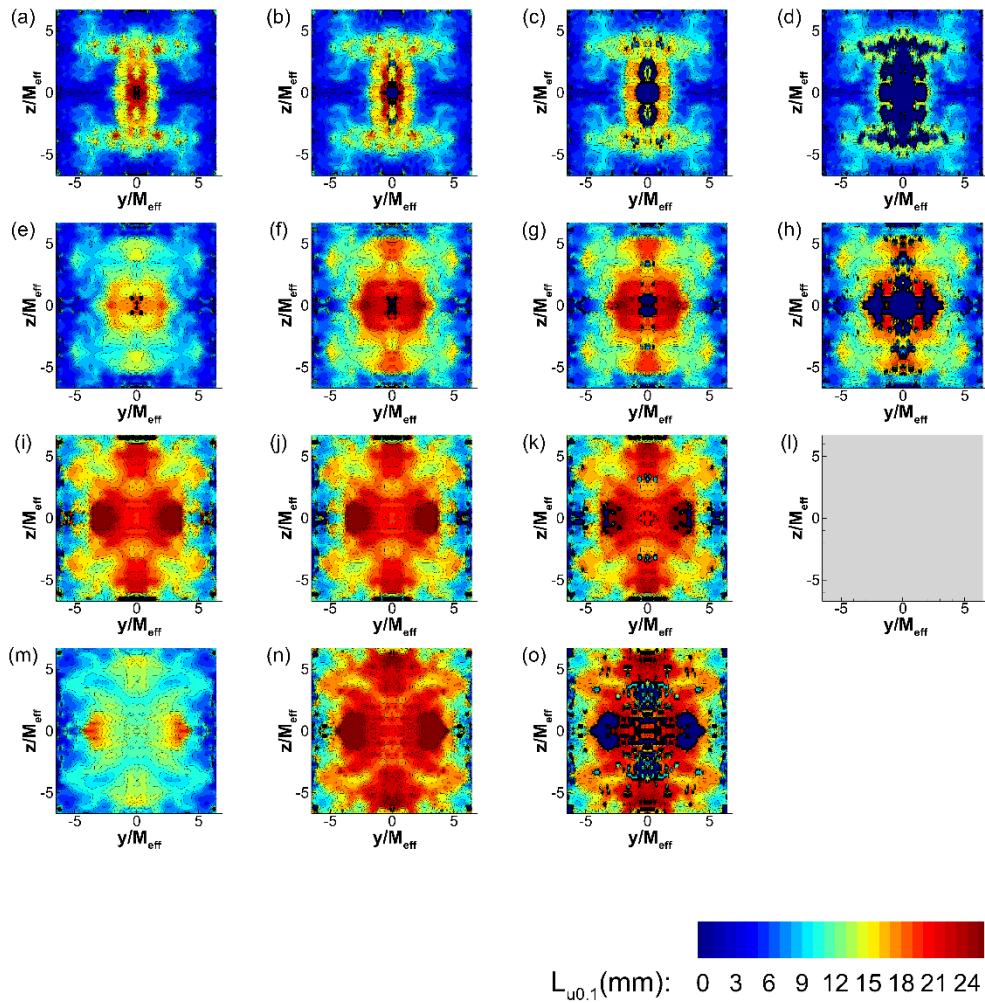
Figure 3-87 Evolution of longitudinal integral length scale ($L_{u_{0.1}}$) in the near-grid region of CSG. Distributions are given in 1 M_{eff} increment from 1 M_{eff} (a) to 15 M_{eff} (o). Blanked regions are those at which the calculation of $L_{u_{0.1}}$ does not provide any result.

It is interesting that contours of LILS stay more or less constant within a certain window. This can imply that the eddy size is either very small or very large comparing to the window streamwise extension. To show the variation of LILS in the near grid region, one can do averaging on the planes parallel to the grid (i.e., planes shown in Figure 3-84 to Figure 3-87). Two first contours of $L_{u_{0.2}}$ in Figure 3-84 suggests that the overall LILS is about 4mm for CSG grid. Note that the largest geometry size for CSG is in fact the thickness of the Plexiglas material the grid is made of which is 4mm.

131

For the rest of fractal grids, the imposed ILIS in the region $\frac{x}{M_{eff}} \leq 2$ obeys from the largest thickness of the corresponding grid, though when wakes of different size bars are interacting, then L_u is not a good approximation of largest eddy size. This is also explained in [18] for multiscale cross grids.

As one approaches to the endpoint of measurement region, there are still regions of very high and very low LILS (contour 't' in Figure 3-85 and Figure 3-86). While the distribution of LILS is different for FSG and FCG at this location ($x/M_{eff} \approx 20$), the area averaged LILS shown in Figure 3-88 suggest the same magnitude of about 13mm for LILS in both cases. Comparing the maximum values of estimated LILS and the extent of FOV ($128\ mm$) reveals that there would exist at least five ILS inside each PIV measurement region. This assures us a thorough capture of LILS within the measurement area [128].

It is beneficial to compare the trend of area-averaged values of LILS which are illustrated in Figure 3-88. According to this figure, LILS is always increasing for fractal grids. This is in agreement with the results of [35,40,52]. For CSG, until about $\frac{x}{M_{eff}} = 10$, it is increasing and then it remains almost constant until the end of the measurement region. The results from CSG are in agreement with those from [18] in the range $0 < \frac{x}{M_{eff}} < 10$ but there is no certain justification to explain why the trends are quite opposite after $\frac{x}{M_{eff}} = 10$. FSG and FCG result in more or less similar LILS magnitudes and on cross sections at the end of measurement region they both end up with averaged LILS of about 13mm. LILS for FIG also start at the same order of that in FSG and FCG but with a higher rate of growth. A linear function ($\frac{L_u}{M_{eff}} = a + b\left(\frac{x}{M_{eff}}\right)$) as well as a power function ($\frac{L_u}{M_{eff}} = A\left(\frac{x}{M_{eff}}\right)^B$) is fit onto these variations and the details are given in Table 3-8.
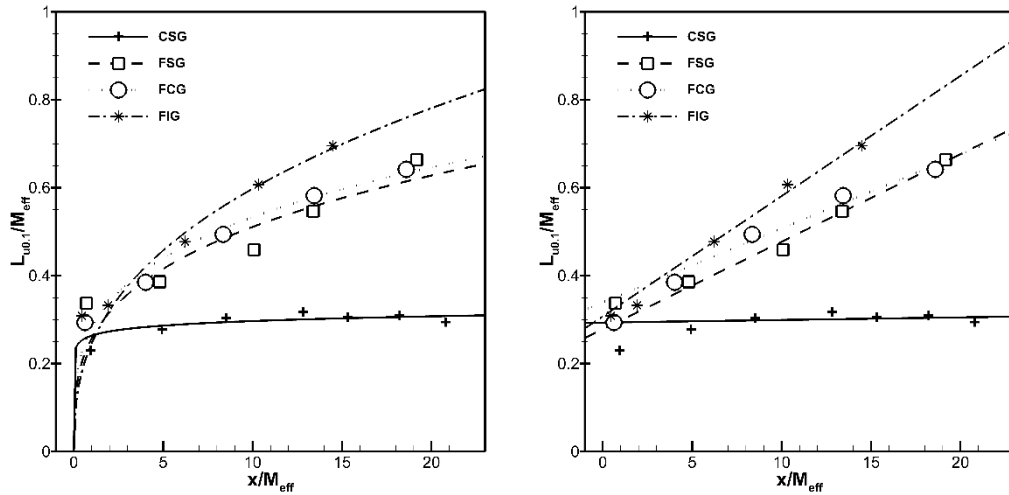
Figure 3-88 Streamwise development of $L_{u_{0.1}}$ in the near grid region, averaged on x=cte planes (symbols). Power function fit (left) and linear function fit (right) are shown by lines. For CSG, the power function is fit only in the region $0 < \frac{x}{M_{eff}} < 6$.

Table 3-8 coefficients and slopes of power function fit to the area averaged LILS in the near grid region of TGG's.

Grid	Linear Function			Power function		
	a	b	R^2	A	B	R^2
CSG-W1				0.2171	0.1201	0.993
CSG	0.2934	0.0006	0.05			
FSG	0.2783	0.01991	0.986	0.2589	0.2624	0.887
FCG	0.3395	0.01679	0.965	0.2722	0.2435	0.979
FIG	0.3077	0.02734	0.985	0.2331	0.3694	0.99

Except for the near grid region ($0 < \frac{x}{M_{eff}} < 2$) wherein a very sharp change in LILS were observed, anywhere inside the same window along characteristic lines (see section 3.1.4) LILS seem to be constant. Therefore, the value for LILS along characteristic lines are reported with a symbol at each window. These values are compared to the area averaged LILS in Figure 3-89.
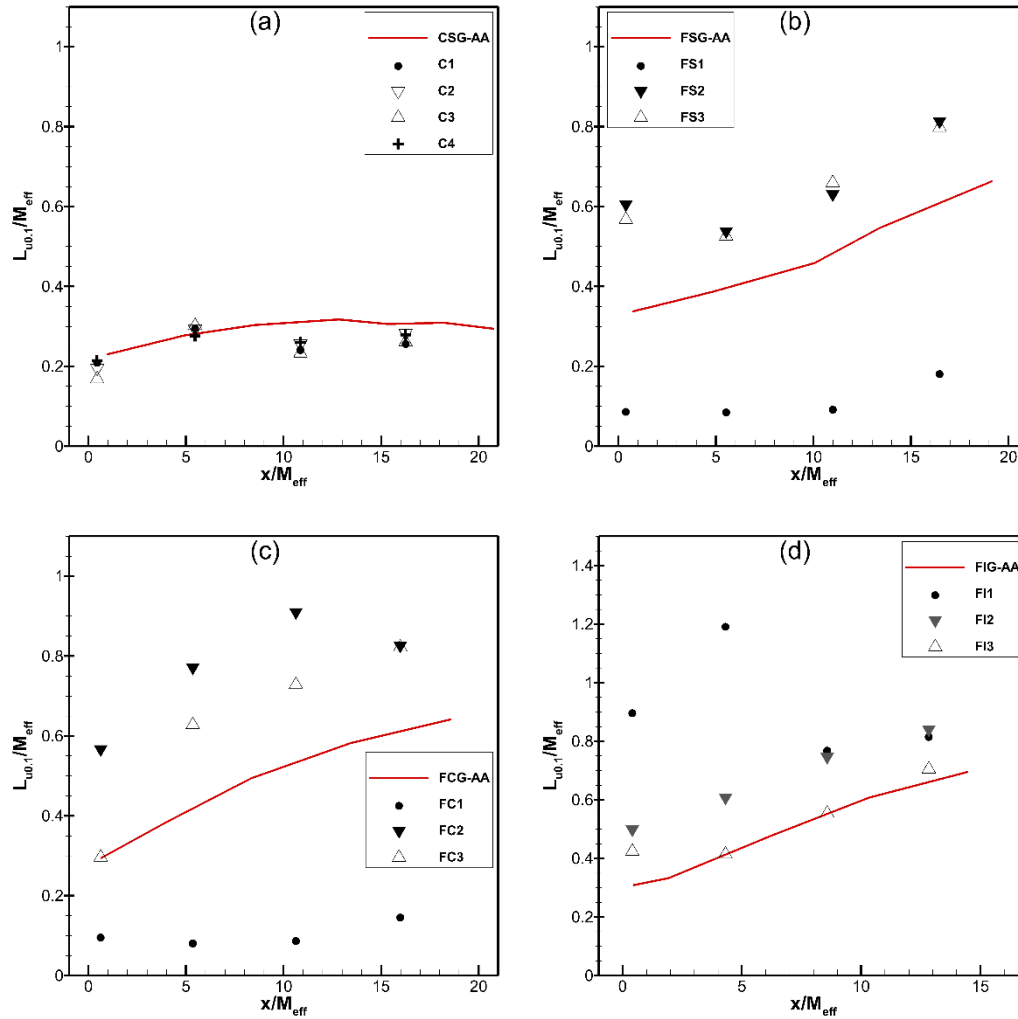
Figure 3-89 $L_{uu_{0.1}}$ as a function of downstream distance averaged on cross sectional planes (red live) and along characteristic lines (symbols) of (a) CSG, (b) FSG, (c) FCG, and (d) FIG.

Characteristic lines can be considered as representatives for local variations. From Figure 3-89 one can notice that the local variations are not so different from the averaged values in the case of CSG which is due to its uniform geometry. In the case of fractal square and circular grids, centerline always shows very low LILS, while along largest element LILS are higher than the cross-sectional averaged ones. It is interesting that at the last window ($\frac{x}{Meff} \approx 16.0$) L_{uu} along FS2 and FS3 and along FC2 and FC3, both converge to about $0.8 M_{eff}$. This is valid also for FIG, along centerline and FI2 lines.

A set of space-filling (Df=2.0) fractal square grids with different thickness ratios and a conventional grid were studied by Mazellier and Vassilicos [52] (denoted by MV(2010)), among which SFG8 grid is very similar to FSG in the current study. SRG grid in [52] is also comparable to our CSG grid. Details of these grids are given in Table 2-3 and the near grid data for CSG is compared to that of [52] and [18] in Figure 3-90. Although there exist limited data to compare with current results, Figure 3-90 clearly shows that effective mesh size is not an appropriate length scale to collapse values of LILS obtained from different experiments. There seems to be a sudden jump in LILS along centerline both in GK(2016) (around $2 - 3.5M_{eff}$) and in current results (around $10 - 12M_{eff}$) and using effective mesh size, they still do not collapse.
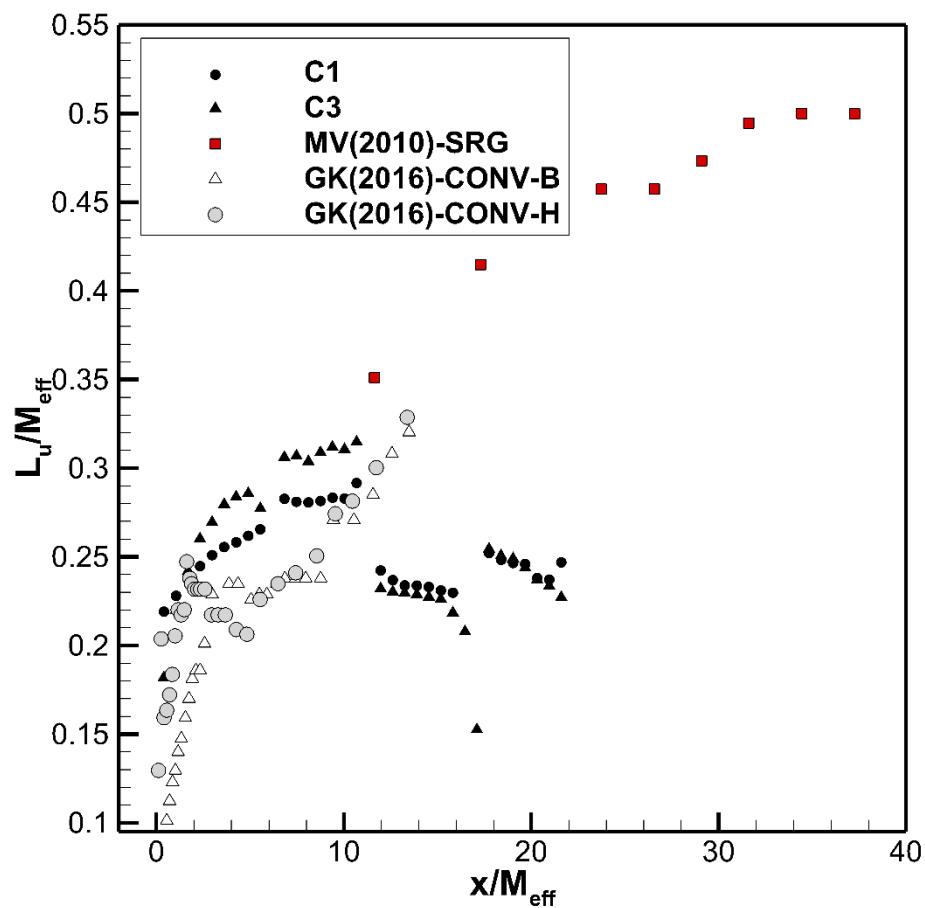
Figure 3-90 Comparison of ILIS for conventional grids from [52] (MV2010) and [18] (GK2016) to the results of the current study (C1 and C3).

135

3.4.2 Taylor microscale

Taylor microscale marks the transition from inertial subrange to the dissipation range [121]. It is called in honor of G. I. Taylor who first defined it [106]. Unfortunately, Taylor incorrectly claimed that it is the average size of the dissipative eddies since he came up with this length scale during the calculation of TKE dissipation rate. By definition, λ is the curvature of the autocorrelation coefficient at the origin (see Figure 3-78), i.e.

$$\left. \frac{d^2 f}{dr^2} \right|_{r=0} \equiv -\frac{2}{\lambda^2} \tag{3.46}$$

If the autocorrelation function (f) is expanded in Taylor series about the origin, for the stationary variable $U = \langle U \rangle + u$ [106],

$$\left\langle \left(\frac{\partial u}{\partial x} \right)^2 \right\rangle \equiv \frac{\langle u^2 \rangle}{\lambda^2} \tag{3.47}$$

Dimensional analysis would also result in the same expression for Taylor microscale, assuming isotropic turbulence. In fact, this length scale is defined in a way that it is associated with the energy dissipation, i.e., it could be a ratio of dissipative (what Taylor was thinking as dissipative eddies back in his time) eddy's velocity ($\langle u^2 \rangle$) to it's velocity gradient ($\left\langle \left(\frac{\partial u}{\partial x} \right)^2 \right\rangle$). Since there exist neglected terms in the Taylor expansion of the correlation coefficient, the value obtained for λ from equation (3.47), is estimated. From (3.46) it is possible to write Taylor microscale for any fluctuating velocity component along any direction [40],

$$\lambda_{ij} = \sqrt{\frac{\langle u_i^2 \rangle}{-\left. \frac{\partial^2}{\partial r_j^2} R_{ii}(r_1, r_2) \right|_{r_1, r_2 = 0}}} \tag{3.48}$$

The expression (3.47) is used to calculate Taylor microscale at each PIV window. The gradient is calculated using the central difference method [52]. By patching all horizontal planes, a volumetric zone in the near grid region is formed. Taylor

136

microscale averaged on cross-sectional planes is compared to that along the characteristic lines for each grid in Figure 3-91.
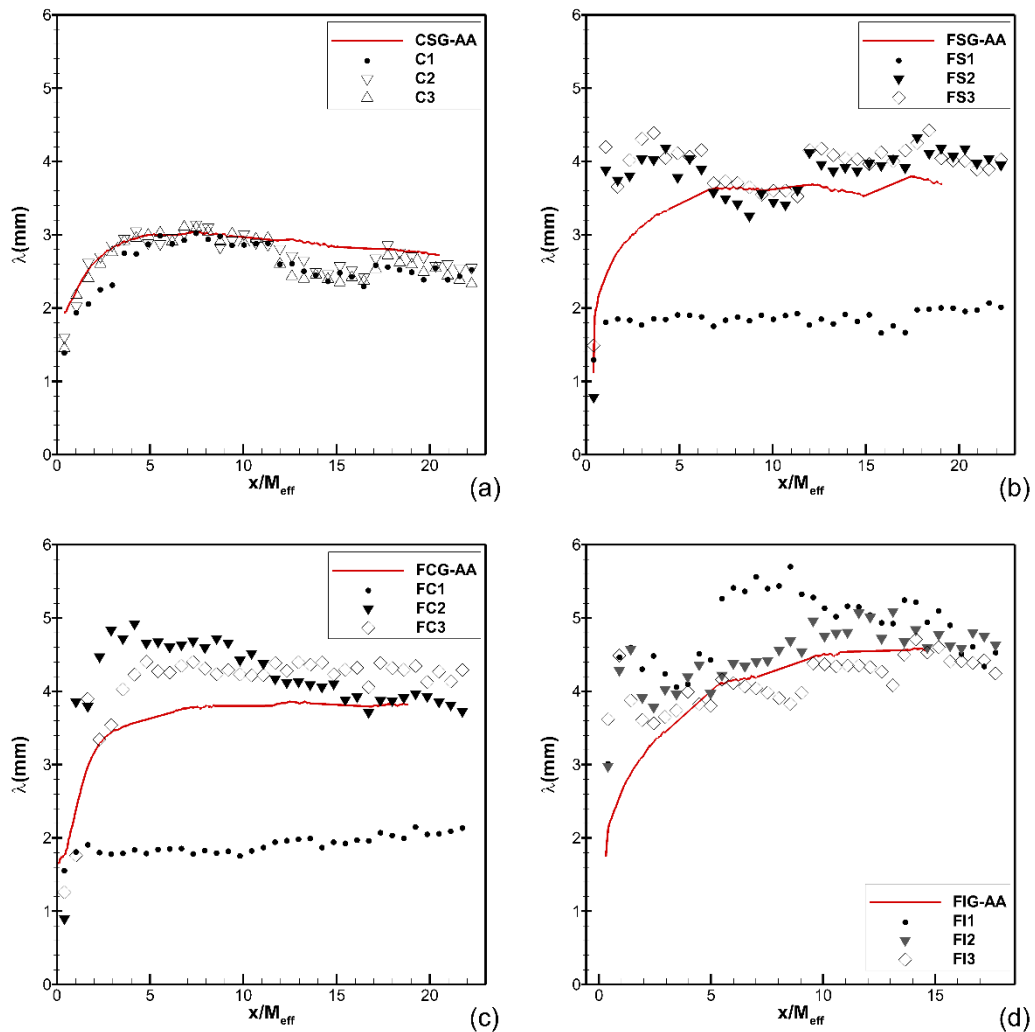
Figure 3-91 Evolution of Taylor microscale λ averaged on x=cte planes (red line) and along characteristic lines for grids (a) CSG, (b) FSG, (c) FCG, and (d) FIG. Only every 10th point is plotted to reduce clutter.

Taylor microscale was shown to increase slowly along the centerline [35,40]. According to Table 2-3, the measurement region and the FSG grid thickness ratio in [40] and [35] is not similar to those of FSG in this study. However, a small increase from 3.5mm to about 4mm in Taylor length scale can be seen from Figure 3-91-b for fractal square grid under investigation.

Hurst and Vassilicos [22] found that the longitudinal and lateral integral length scales (L_u, L_v) and the Taylor microscale are approximately constant during the decay of space-filling FSG. In our study, the decay region is not captured for any of fractal grids, but the shape of area averaged λ suggests that the Taylor microscale is moving towards some constant values much downstream. Increase in cross-sectionally averaged λ in the near-field is in agreement with previously reported DNS results [129]. Another method to calculate Taylor microscale is introduced in [40]. There a parabola is fit using the first 6 points on the correlation function, and a range of uncertainty of about 10-15% is reported in calculating λ.

3.4.3   Normalized dissipation rate (C_ε) in the near-field

It has been shown in (dissipation part) that dissipation rate of TKE is governed by the large scales of turbulence, assuming the forward cascade model proposed by Richardson in 1922 [130], i.e., the rate of turbulent energy dissipation is determined by the rate of transfer of energy from large-scale eddies to the small-scale ones,

$$\varepsilon \propto \frac{k^{\frac{3}{2}}}{L} \propto \frac{u'^3}{L} \tag{3.49}$$

Where k is TKE, L is ILS usually the longitudinal one based on u and u' is the characteristic velocity scale (rms fluctuating velocity $\langle u^2 \rangle^{\frac{1}{2}}$). When the turbulence is isotropic, the dissipation rate can be expressed as [2],

$$\langle \varepsilon \rangle_{iso} = \frac{15 \nu u'^2}{\lambda^2} \tag{3.50}$$

where $\langle \varepsilon \rangle$ is the mean dissipation rate of TKE. It should be noted that λ does not refer to a physical diameter for eddies; yet, because this length scale is associated with energy dissipation through (3.50), it is still broadly used by experimentalists. Equation (3.49) can be converted into an equation using a constant C_ε,

$$\langle \varepsilon \rangle_{iso} = C_\varepsilon \frac{u'^3}{L} \tag{3.51}$$

This constant is non-dimensional, independent of Reynolds number, time and space [119]. A significant result of '*forward energy cascade*' is the independence of 'non-dimensional mean energy dissipation rate' – or simply 'normalized dissipation rate' – (C_ε) also from viscosity [2,63]. Therefore, C_ε is defined as,

$$C_{\varepsilon_{iso}} = \langle \varepsilon \rangle_{iso} \frac{L}{u'^3} \tag{3.52}$$

This is the most common method to estimate the normalized dissipation rate because it is based on the isotropy assumption [21], that is why the subscript "iso' is used in (3.52). The order of magnitude of C_ε is found to be unity [131].

On the other hand, one can combine (3.50) and (3.51) to obtain,

$$C_\varepsilon \frac{u'^3}{L} = \frac{15\nu u'^2}{\lambda^2} = \frac{15u'^2}{\lambda} . \frac{\nu u'}{\lambda u'} \tag{3.53}$$

Defining local Reynolds number Re_λ (Reynolds number based on the Taylor microscale),

$$Re_\lambda \equiv \frac{u'\lambda}{\nu} \tag{3.54}$$

Equation (3.53) can be written as,

$$C_\varepsilon \frac{u'^3}{L} = \frac{15u'^2}{\lambda} . u' . \frac{1}{Re_\lambda} \rightarrow C_\varepsilon \frac{1}{L} = \frac{15}{\lambda} \frac{1}{Re_\lambda} \rightarrow \frac{15L}{\lambda} = C_\varepsilon Re_\lambda \tag{3.55}$$

Equation (3.55) was used to assess the constancy of normalized dissipation rate in the decay region of fractal-generated-grid turbulence [35,105,132]. It has been observed by Valente and Vassilicos [35,132] that far downstream of FSG, in the decay region where the turbulence is nearly isotropic, and the basic assumption of Kolmogorov theory seems to be valid, Re_λ decreases but $\frac{L}{\lambda}$ stays more or less constant. Looking at (3.55), this implies an increase in C_ε to maintain the equation balance. Non-constant C_ε is in contradiction with the Kolmogorov turbulence model and as stated in [40], it conflicts with Reynolds-averaged Navier-Stokes (RANS) modelling in which the semi-empirical quantity C_ε is assumed to be constant. To make it clear, in the two-

equation model ($k - \varepsilon$) in which the turbulent kinetic energy and dissipation rate are modeled using transport equations including some empirically constants, the turbulence dissipation rate follows as,

$$\varepsilon = \frac{C_\mu^{\frac{3}{4}} k^{\frac{3}{2}}}{L}$$

(3.56)

where C_μ is considered equal to 0.09 as a constant [133]. Thus the value of $C_\varepsilon = C_\mu^{\frac{3}{4}}$ is 0.164. On the other hand, there are plenty of studies on C_ε concentrating in the near-field of regular and fractal grids [19,43,44,105]. Since turbulence is not isotropic in the near-field of TGGs and C_ε is inherently not constant, these studies try to relate the growth of C_ε to some initial and local characteristics of the flow. Valente and Vassilicos [132] showed that in the near-field of grid turbulence,

$$C_\varepsilon \sim \frac{Re_M^{\frac{1}{2}}}{Re_\lambda}$$

(3.57)

where $Re_M = \frac{U_0 M_{eff}}{\nu}$ implies the initial condition. Isaza et. al. [105] showed that $\frac{L_u}{\lambda}$ is independent of Re_λ but it depends on Re_M. They found their results in agreement with the bi-planar regular grid (See Fig.5 in [132]). Hearst and Lavoie [43] used a fractal square grid attached to a background regular grid primarily to study on the decay of TKE in the near and far-fields. They obtained the same results as with [35] and [132] that $\frac{L_u}{\lambda}$ is approximately constant in the near-field of such grids (see Fig.10 in [43]). In a later study searching for a link between the evolution of $S\left(\frac{\partial u}{\partial x}\right)$ to that of C_ε, they [44] found that C_ε in the near-field changes (grows) by,

$$C_\varepsilon \sim \frac{Re_M^\alpha}{Re_L^\beta}$$

(3.58)

They found that and $\alpha = \beta = 1$ is satisfying for the estimation. In equation (3.58), $Re_L = \frac{u'L}{\nu}$ is the local Reynolds number based on the integral length scale and the velocity fluctuations. They stated that rapid energy decay and non-constant C_ε are the characteristics of "*non-equilibrium*" turbulence. "N*on-equilibrium*" turbulence is

140

summarized by Vassilicos [134] and is not just a property of fractal grids [41,43], but also has been seen in the near-field of regular grids wake [132]. Since the near-field of different TGGs are reconstructed in this study and many flow characteristics has been investigated so far, it is also beneficial to obtain the distribution of C_ε in the near-field. Prior to that, evolution of $\frac{L_u}{\lambda}$ in all four types of grids is shown in Figure 3-92. In all fractal grids, after a sudden reduction in the proximity of grids ($0.4 \leq \frac{x}{M_{eff}} \leq 2$), $\frac{L_u}{\lambda}$ slowly increases whereas in the conventional grid it stays more or less constant after $\frac{x}{M_{eff}} \cong 15$. This is in agreement with results in [105].
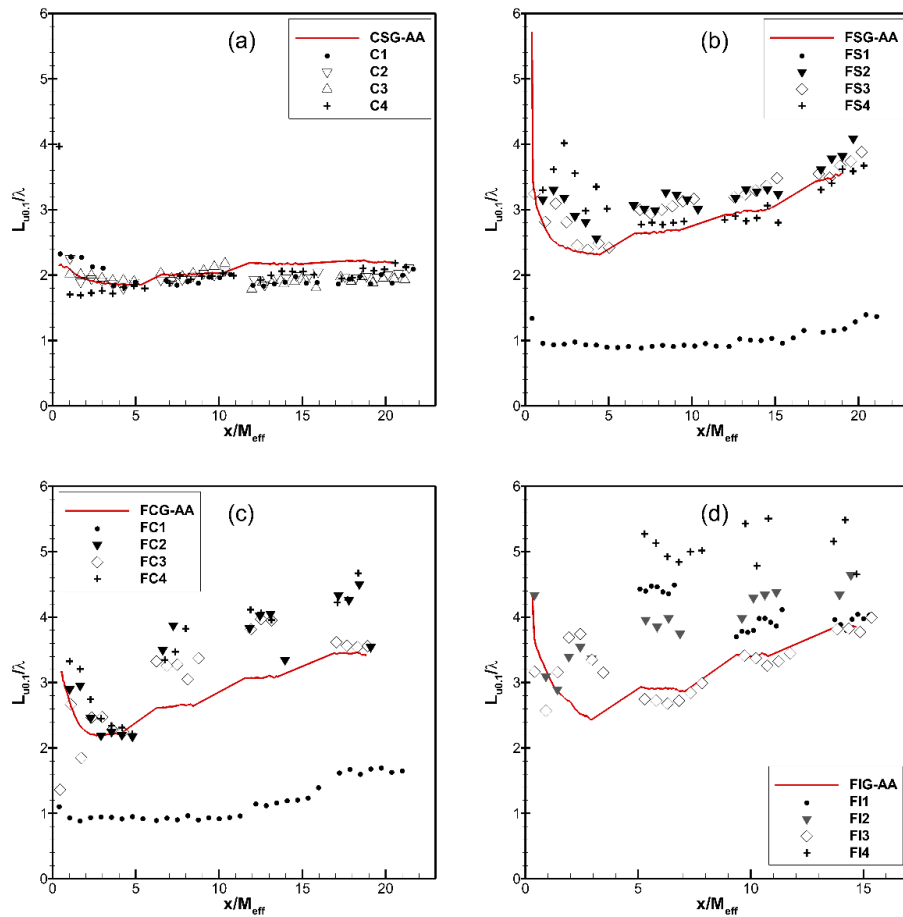
Figure 3-92 $\frac{L_{u_{0.1}}}{\lambda}$ as a function of normalized streamwise distance, averaged on x=cte planes (red curves) and along characteristic lines of (a) CSG, (b) FSG, (c) FCG, and (d) FIG.

141

Streamwise development of Re_λ averaged on planes parallel to grids is shown in Figure 3-93. While Re_λ is always decreasing in case of the regular grid, it shows a plateau – just the same as turbulence intensity variation – with different increment and decrement rates. Neglecting the rising part, Re_λ is always decreasing with streamwise distance. This has to be compensated by increment in $\frac{L_u}{\lambda}$ to balance Equation (3.55). In addition, one can calculate C_ε using (3.55).
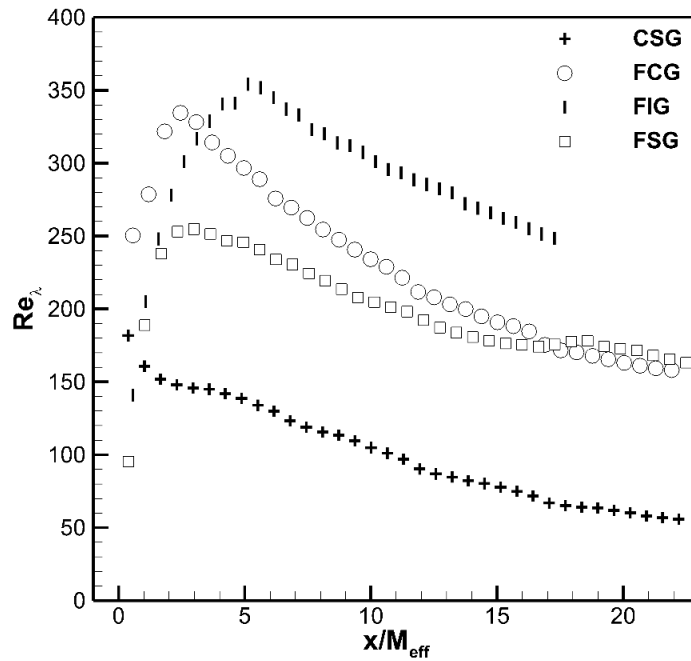
Figure 3-93 Re_λ as a function of normalized streamwise distance, averaged on x=cte planes for different grid types.

Distribution of dissipation rate coefficient (C_ε) in the near-field of regular and fractal grids is shown in Figure 3-94 to Figure 3-97. Blanked contours are those at which calculation of $L_{u_{0.1}}$ does not provide meaningful results due to a limited streamwise extension. Looking at the distribution, it seems that high C_ε can be found in the central jet region of FSG and FCG, while it is working just opposite in FIG case. C_ε seems to be distributed more homogeneously in the near-field of CSG.
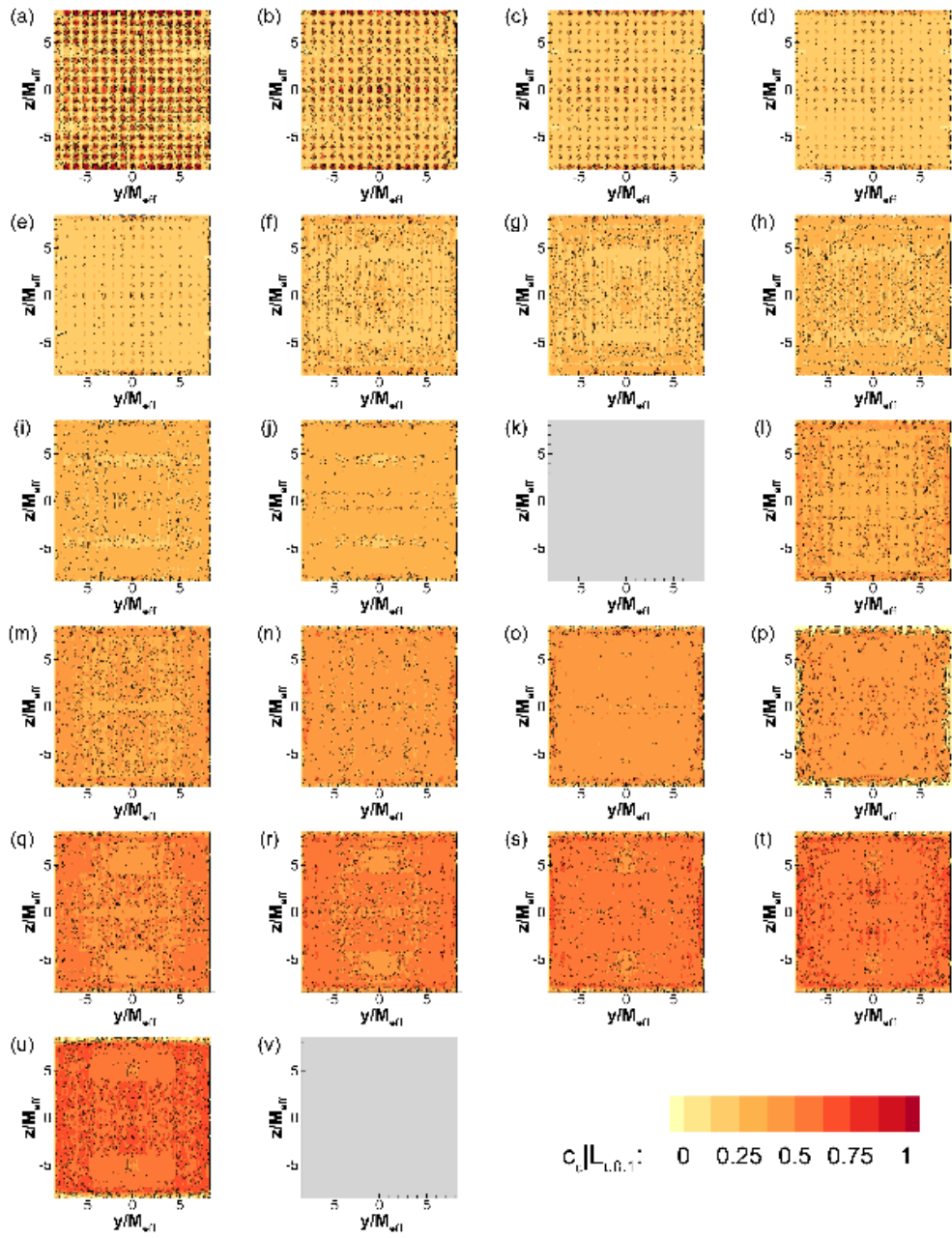
Figure 3-94 Distribution of dissipation rate coefficient (C_ε) in the near grid region of CSG. Distributions are given in 1 M_{eff} increment from 1 M_{eff} (a) to 22 M_{eff} (v).
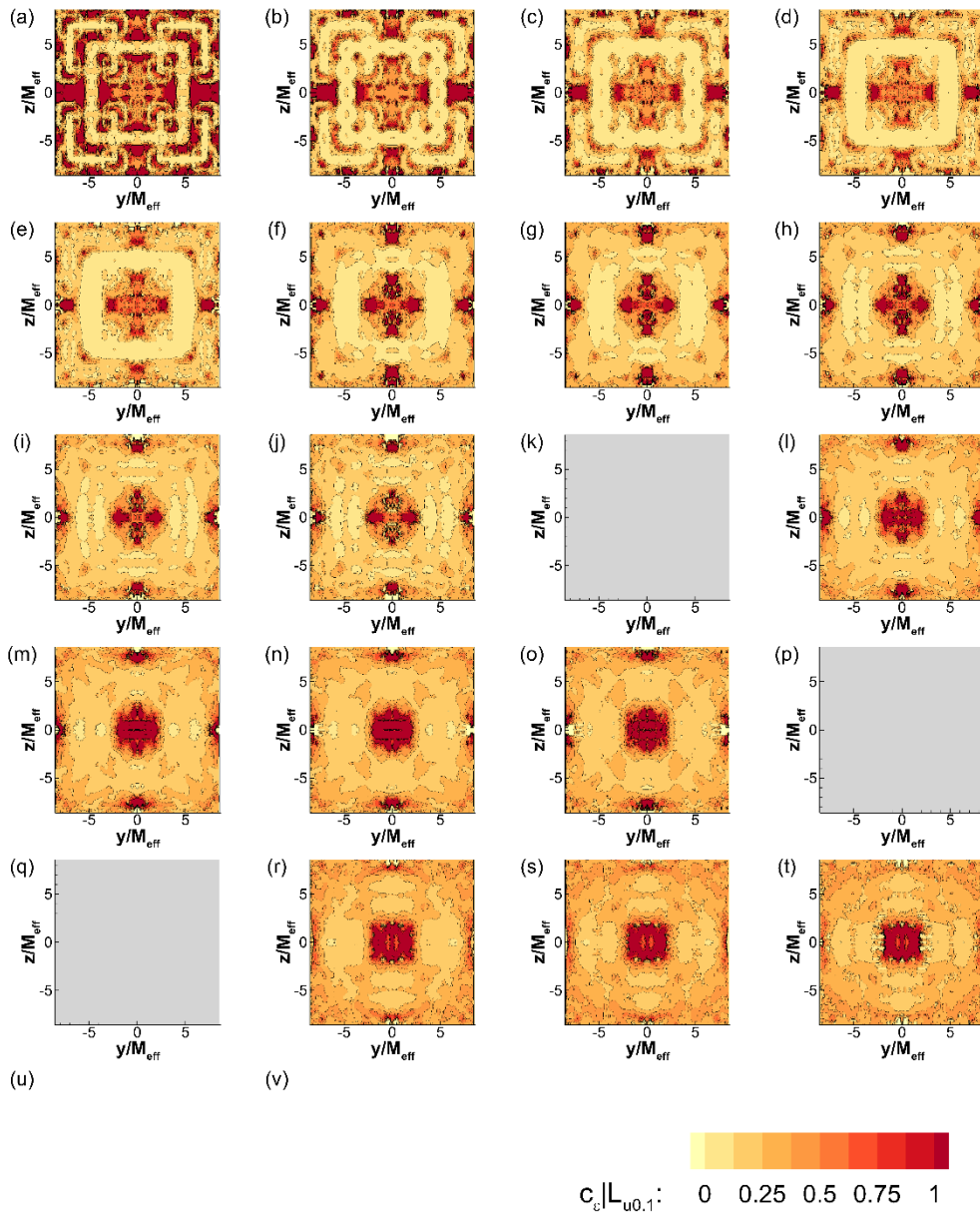
Figure 3-95 Distribution of dissipation rate coefficient (C_ε) in the near grid region of FSG. Distributions are given in 1 M_{eff} increment from 1 M_{eff} (a) to 20 M_{eff} (t).

144
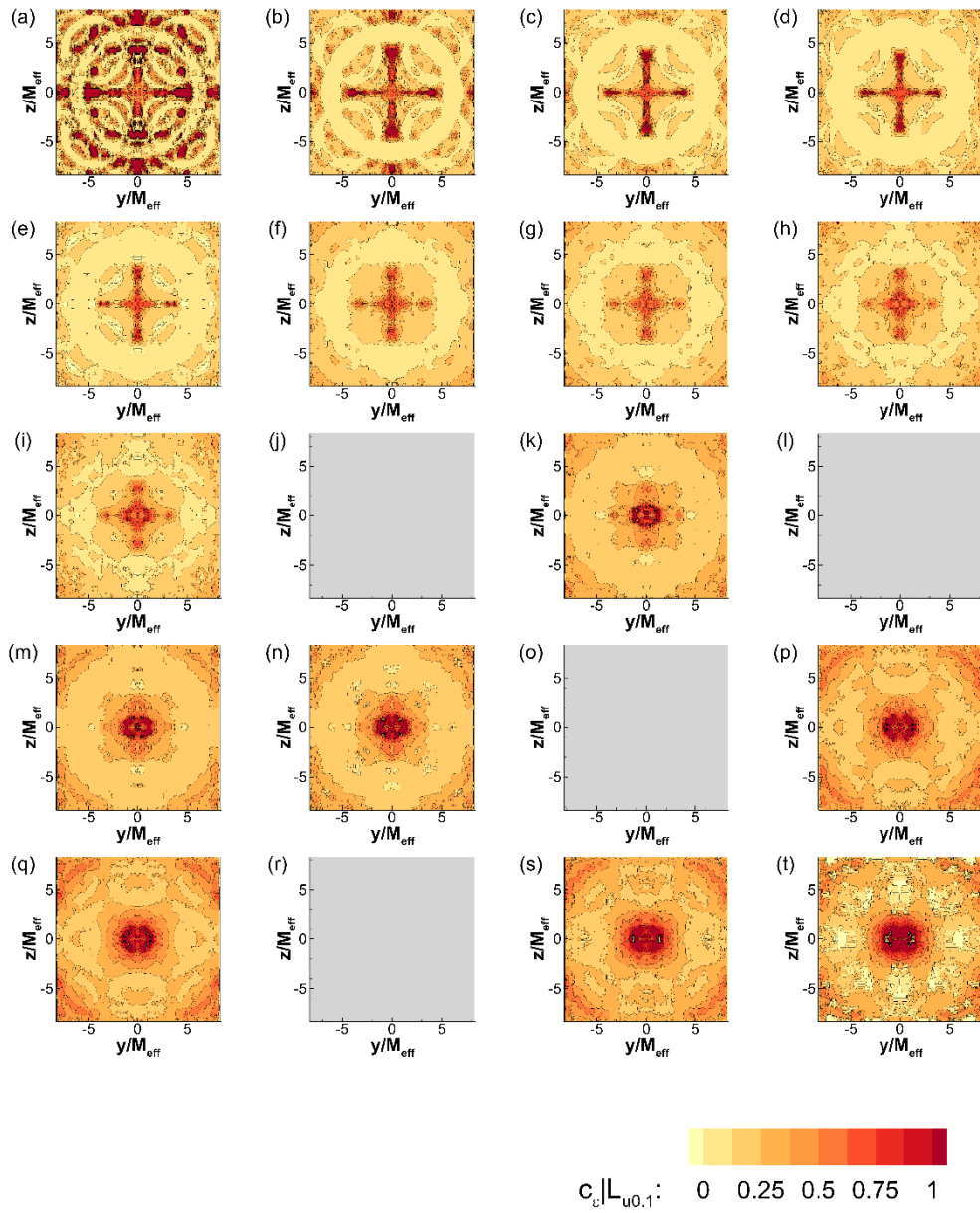
Figure 3-96 Distribution of dissipation rate coefficient (C_ε) in the near grid region of FCG. Distributions are given in 1 M_{eff} increment from 1 M_{eff} (a) to 20 M_{eff} (t).

145
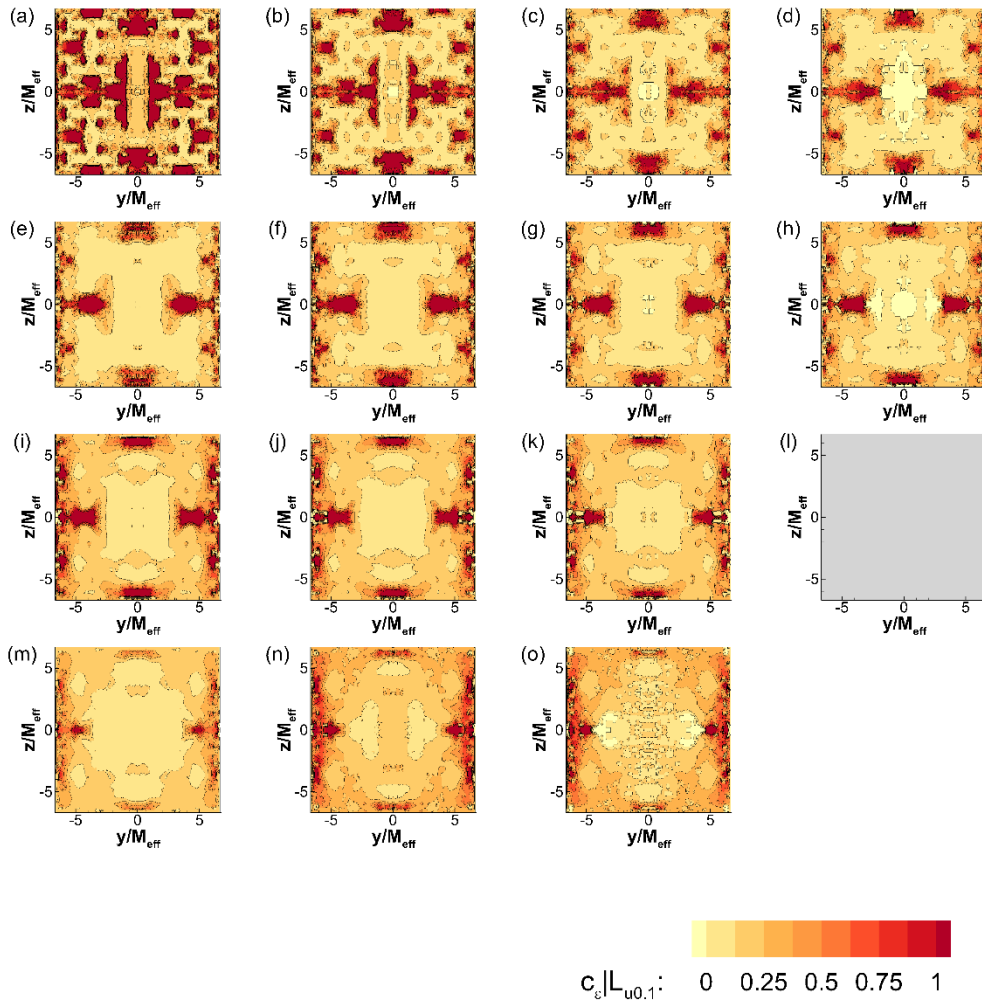
Figure 3-97 Distribution of dissipation rate coefficient (C_ε) in the near grid region of FIG. Distributions are given in 1 M_{eff} increment from 1 M_{eff} (a) to 15 M_{eff} (o).

While different values ($L_u, L_{u_{0.1}}, L_{u_{0.2}}$) for ILS are included to obtain C_ε using Equation (3.55), only $L_{u_{0.1}}$ is used to put into Equation (3.52). Notice that the value for isotropic dissipation is replaced by the value of the mean dissipation rate obtained using 2-D 2-C PIV estimation ($\langle \varepsilon \rangle_{2-C\ PIV}$). Comparison between C_ε values obtained by different magnitudes of ILS is made in Figure 3-98. Here, C_ε is averaged on planes parallel to the grid ($x = cte$ planes) and $C_\varepsilon | \varepsilon_{ISO}$ is the one calculated from Equation (3.52).

146
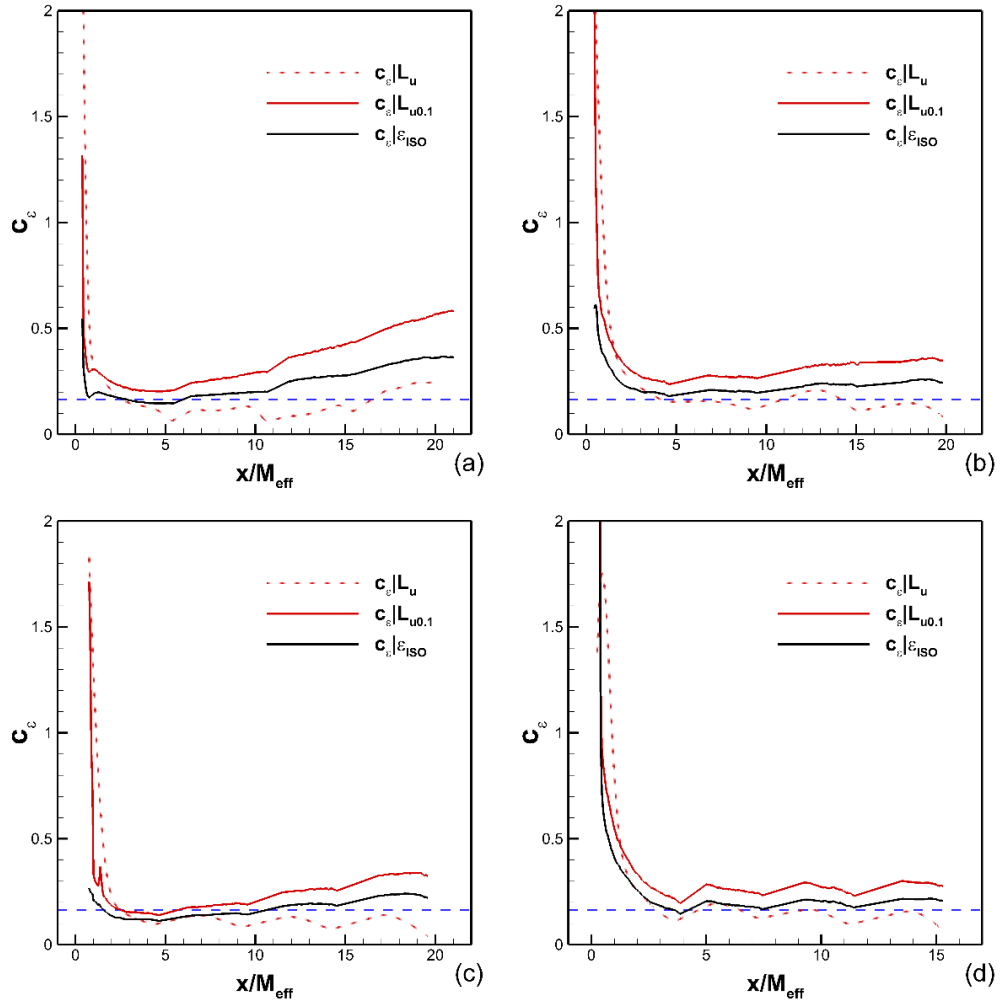
Figure 3-98 Comparison of C_ε obtained by different ILS values for (a) CSG, (b) FSG, (c) FCG, and (d) FIG. Area averaged values are used. Blue dashed line is $C_\varepsilon = 0.164$ as a constant value used in the $k - \varepsilon$ model.

Looking at Figure 3-98-a, one can notice the area averaged C_ε for the regular grid is consistently increasing after some initial distance ($\frac{x}{M_{eff}} \cong 5$) and the trend is the same whether C_ε is calculated from dissipation rate – equation (3.52) – or from length scales in Equation (3.55). This increase in C_ε also shows itself in fractal grids but with a smaller rise. Comparing to the constant C_ε value in the $k - \varepsilon$ model, deviations are clearly visible.
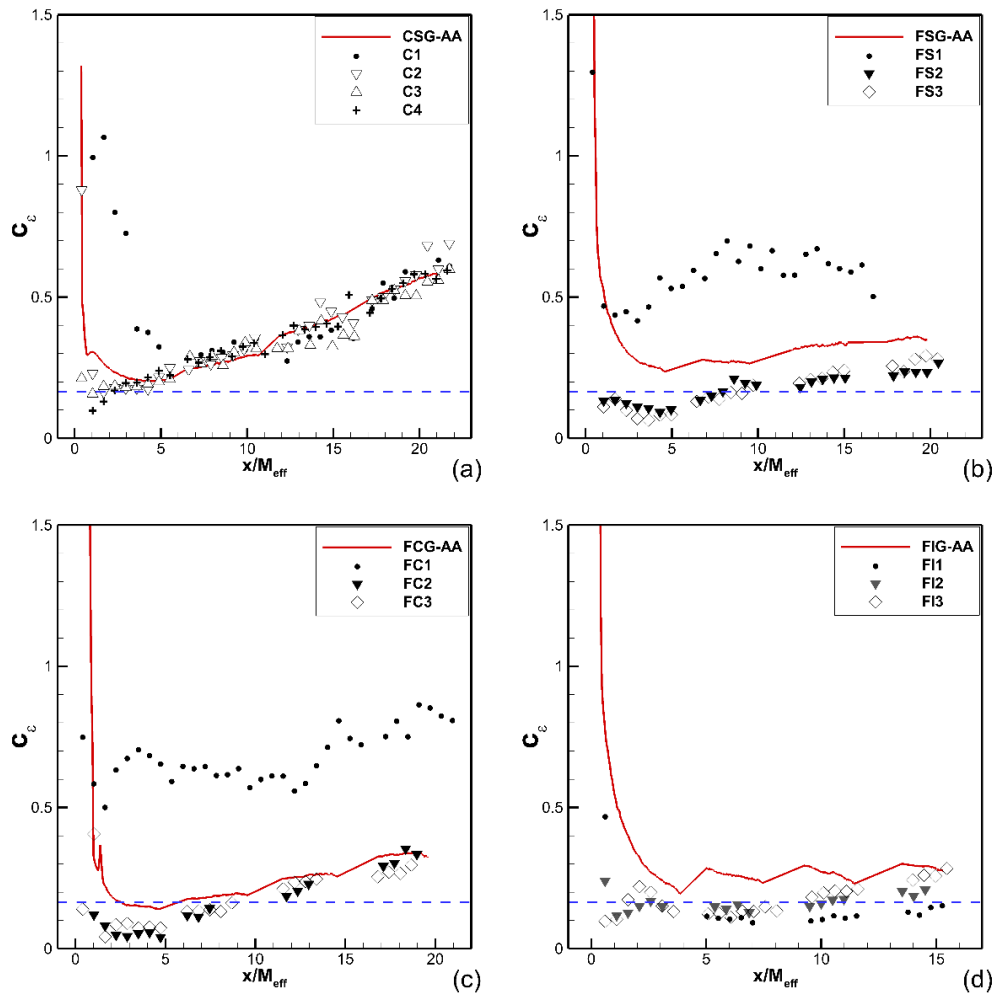
Figure 3-99 Evolution of C_ε on parallel planes to the grid (red curve) and along characteristic lines of (a) CSG, (b) FSG, (c) FCG, and (d) FIG. Blue dashed line is $C_\varepsilon = 0.164$ as a constant value used in $k - \varepsilon$ model.

Values of C_ε averaged on parallel planes are compared to above mentioned scaling models of Valente and Vassilicos [132] and Hearst and Lavoie [43] in Figure 3-100. Table 3-9Table 3-9 also provides information on the coefficients of equations (3.57) and (3.58) pertaining to those aforementioned scalings. Value of c_1 and c_2 coefficients are obtained in a region far from the "very-near-field", where there exist sudden variations according to Figure 3-100. Numbers inside parentheses are error estimation of the coefficient for each grid in the scaling model.
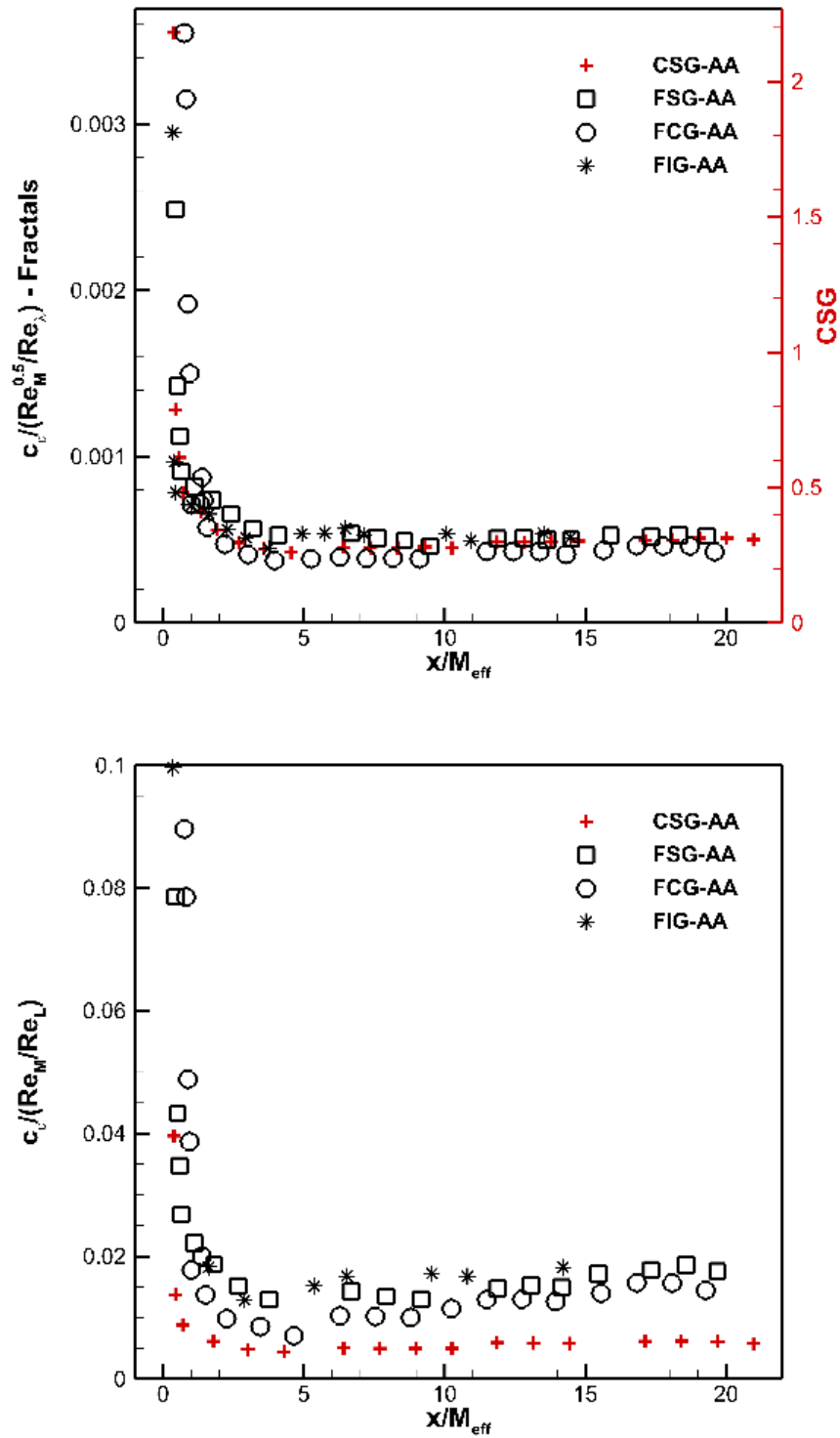
Figure 3-100 Ratio of area averaged values of C_ε to the scaling proposed by Valente and Vassilicos (top) and the scaling proposed by Hearst and Lavoie (bottom), developing in the near-field region of conventional and fractal grids.

Table 3-9 Coefficient of equality of normalized dissipation rate scaling models in Equations (3.57) and (3.58).

Grid	CSG	FSG	FCG	FIG
$c_1 = C_\varepsilon / \left(Re_M^{0.5} \big/ Re_\lambda \right)$	0.2944 ($\pm$4%)	0.0005 ($\pm$3%)	0.0004 ($\pm$7%)	0.0005 ($\pm$7%)
$c_2 = C_\varepsilon / \left(Re_M \big/ Re_L \right)$	0.005564 ($\pm$8%)	0.0157 ($\pm$12%)	0.0126 ($\pm$17%)	0.0178 ($\pm$10%)

The model proposed by Valente and Vassilicos gives better estimations that that of Hearst and Lavoie. Since there is an uptrend in coefficient c_2 in the latter scaling, the magnitude of error goes beyond 10% according to Table 3-9.

3.4.4   Kolmogorov microscale

Kolmogorov microscale is used to characterize the smallest dissipative eddies. At this scale, the rate at which the kinetic energy is supplied must be equal to the rate at which it is depleted by viscosity. The parameters available to calculate the Kolmogorov length scale are the TKE dissipation rate and the fluid kinematic viscosity.

$$\eta = \left(\frac{v^3}{\varepsilon} \right)^{\frac{1}{4}}$$

(3.59)

and the corresponding Reynolds number (Re_η) is equal to one[1]. If the turbulence is isotropic, one can calculate the Kolmogorov microscale as [52],

$$\eta = \left(\frac{v^2}{15 \langle \left(\frac{\partial u}{\partial x} \right)^2 \rangle} \right)^{\frac{1}{4}}$$

(3.60)

Variation of Kolmogorov microscale estimated in the near grid region is shown in Figure 3-101. η is calculated using the mean dissipation rate calculated from 2-D PIV data, i.e. $\langle \varepsilon \rangle_{2-C\ PIV}$. The red line expresses the area averaged quantity (on x=cte planes). Changes along centerline are shown by filled dots in all grids. As it is mentioned before, the limited spatial resolution could introduce some error in the

---

[1] By dimensional analysis one finds, $Re_\eta = \eta u_\eta / v = lRe^{-\frac{3}{4}} u' Re^{-\frac{1}{4}} / v = ReRe^{-1} = 1$

calculation of Kolmogorov microscale because of velocity gradients included in any formulation of η (see dissipation rate part). As long as this error is considered as a part of overall measurement uncertainty, it can be neglected [46].

Values of Kolmogorov microscale can be compared to that from [108], a DNS study of fractal generated turbulence (See Figure 2.2 there). The ranges of length scales in two different wind tunnels are presented in Table IV in [52]. The ranges of Taylor and Kolmogorov microscales, there, are in agreement with the ones calculated in this study. However, the range of L_u is far larger than that in our case.
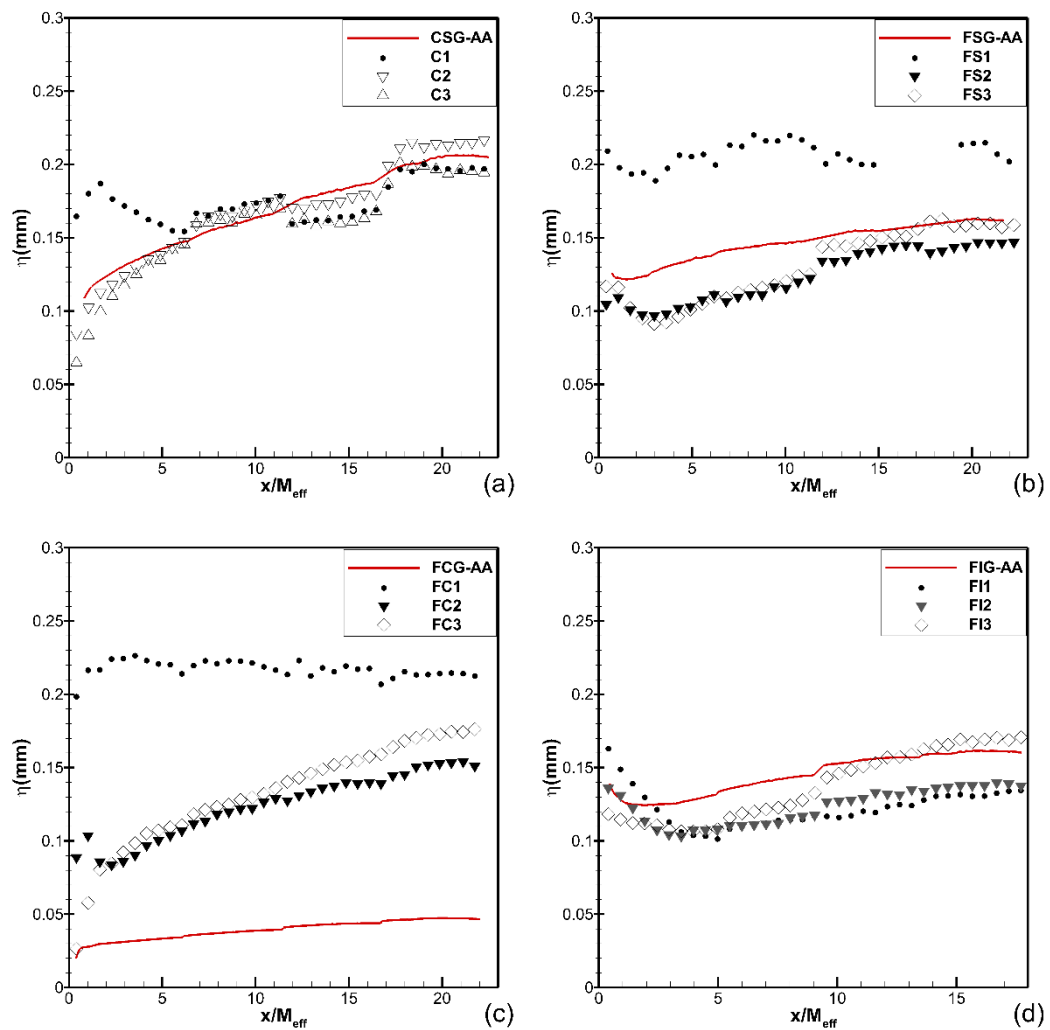
Figure 3-101 Estimated Kolmogorov microscale (η) averaged on x=cte planes (red line) and along characteristic lines for grids (a) CSG, (b) FSG, (c) FCG, and (d) FIG.

CHAPTER 4

CONCLUSIONS

The focus of this study is to experimentally investigate the near-field of turbulent flow generated by grids. For this purpose, one conventional as well as three different pattern fractal grids are designed and manufactured, and two-dimensional particle image velocimetry technique was used as the measurement method. Turbulence-generating grids are designed such a way that their effective mesh size and solidity are similar. This wat one can ensure the pressure drop induced by grids is more or less in the same order of magnitude. Thirty-five horizontal (X-Y) planes separated by five milimeter distance (different Z locations) are illuminated, and 1000 image pairs are taken. These planes are extended to more than a half of the grid in the spanwise (y) direction. This configuration is repeated for three more streamwise locations to reach almost 22 effective mesh sizes downstream of grids; hence, an array of 4×35 two-dimensional PIV images is formed for each grid and analyzed to obtain instantaneous velocity data. Mean flow quantities ($\langle U \rangle, \langle V \rangle, \langle u^2 \rangle, \langle v^2 \rangle, \langle uv \rangle$) are then calculated over each plane.

With the help of symmetry in the geometry of conventional, fractal square and fractal circular grids, additional mean variables ($\langle W \rangle, \langle w^2 \rangle, \langle uw \rangle$) are obtained on horizontal planes. Moreover, all components of mean vorticity $\langle \Omega_i \rangle$ and mean strain rate $\langle S_{ij} \rangle$, as well as turbulent kinetic energy (k) are obtained. In the case of the Reynolds stress tensor, five out of six components are obtained ($\langle vw \rangle$ is still unknown). By combining the improved two-dimensional mean (ensemble averaged) velocity fields, a three-dimensional mean flow pattern is reconstructed for each turbulence-generating-grid.

Mixing characteristics – those regarding to turbulence – in the near wake region of TGG's are obtained by investigating the homogeneity and isotropy of the mean flow, turbulence intensity, and Reynolds shear stress. The static pressure drop across grids are obtained using a Pitot-static probe, and the efficiency of each TGG is quantified as the ratio of turbulence intensity/shear stress to the pressure loss.

To investigate turbulence characteristics in the near-field region of TGG's, turbulent kinetic energy is obtained by assuming isotropic flow and diagonally symmetric flow. Nonconformities does exist mostly in the very near grid region ($x \leq 5M_{eff}$) after which both approaches converge. Although defining a power law decay is not appropriate for the very near grid region, this is evaluated by fitting a power function to cross sectional area averaged TKE, and also along some characteristic lines of TGG's. These generic lines are starting from the centerline, and the largest iterations of TGSS's where the resolution is enough to resolve the wakes. Power decay is also compared to exponential decay. In fractal square and circular grids, TKE averaged on cross sections peaks at a similar downstream distance ($\frac{x}{M_{eff}}$) but with a higher magnitude as well as steeper decay for FCG. For CSG a narrow production region is detected in the range $0.4 < \frac{x}{M_{eff}} < 0.55$. The production region for I grid is extended to about $x = 4M_{eff}$.

Mean dissipation rate of TKE is evaluated using 2-D PIV data. Although effective mesh size is not an appropriate length to scale the dissipation rate, CSG shows the fastest decay of dissipation rate among the grids. The rate of production of TKE in the near grid region is also calculated on 2-D PIV planes. CSG also shows the fastest decay in production rate among TGG's, and the production of TKE is limited to 2-3 mesh sizes. However, the magnitude of production reaches zero almost after 10-12 mesh sizes downstream of all fractal grids. Different distributions of mean velocity, turbulence intensity, and TKE suggest that these grids can be used in applications where a specific level of turbulence at desired locations is required. As it is stated previously in the case of FSG, and shown here, fractal grids can be used as an efficient additional turbulence-generator in the near-field which is essential in applications where there is a limit of downstream distance, e.g., combustors and etc. Significant differences between the evolution of turbulence parameters along the centerline of TGG's and averaged on the parallel planes to the grid, once again show the high geometry dependent flow in the very near grid region and the importance of the whole flow rather than the centerline.

Integral length scales are important to us since they are measures of the size of the energetic eddies, the geometry of the turbulence generator and the scale at which

turbulence is forced. In this study longitudinal and lateral ILS's are obtained by integrating velocity fluctuation correlation functions along streamwise and spanwise directions. For the specific case of LILS along x-axis (L_{uu}), a complete 3-D map is reconstructed to reveal the distribution and evolution of integral scales in the near-field region. Evolution of L_{uu} along characteristic lines of TGG's also shows this variances. Curve fits to the variations of area averaged L_{uu}, shows good conformity with power function ($L_{uu} = Ax^B$). Also, it turns out that the largest LILS belong to FIG, mainly due to its completely different geometry, while both FSG and FCG force the flow to generate scales with the same lengths. LILS for CSG case follow the power function only in some mesh sizes ($0 < \frac{x}{M_{eff}} < 5$) downstream and then it maintains a constant value of length scale.

Taylor microscale is calculated in the near-field to evaluate the constancy of the dissipation rate coefficient (C_ε) assumed by Richardson forward cascade model. This model is used in RANS calculations. Results show that the near grid region of fractal grids, the ratio $\frac{L_{uu}}{\lambda}$ first drops sharply and then increases by the order of about 50%. These results are obtained on the averaged cross section planes. However, a jet region along the centerline of FSG and FCG shows constant $\frac{L_{uu}}{\lambda}$ until 10-15 $\frac{x}{M_{eff}}$ and then it is increasing. Considering the region $\frac{x}{M_{eff}} > 10$, where local Reynolds number (Re_λ) is always decreasing, C_ε results not to be a constant but increasing value. Kolmogorov microscale which characterizes the smallest dissipative-eddies is also estimated with the assumption of isotropic turbulence.

For future works, some suggestions are listed below.

Effects of additional iterations of fractal elements are studied numerically before on fractal square grids [61]. To get more insight into the interactions of smaller iterations as well as to compare existing results to the higher Reynolds number results it is suggested to study on these effects experimentally by designing proper fractal grids with square and circular patterns with 0th, 1st, 2nd, and 3rd iterations.

In this study, dissipation rate is calculated with the assumption of local isotropy and based on 2-D PIV data. In fact, it is shown that in the near grid region, small scales

are still anisotropic to a large extent. Study on the level of influence of local anisotropy to the dissipation rate is suggested provided that the spatial resolution is enough to rely on the values of velocity gradient.

It is shown in this study that the dissipation rate coefficient (C_ε) has some distribution in the near wake region and is not always constant as it is assumed in RANS based turbulence modeling. In fact, this validates the non-equilibrium condition in the near wake region of the grids as it was shown before through non-common decay rates of TKE. In addition to that, the divergence of Reynolds stress components from mean velocity strain rates can be investigated to check the Boussinesqu assumption.

Upstream data is essential for testing of large eddy simulation (LES) codes. It is beneficial to obtain upstream data – typically with more samples and probably resolved in time – for good convergence of higher order statistics, to be used as input in LES simulations.

Structure functions and scaling, energy spectra, as well as probability density functions can be studied in the near wake region. This requires lower spatial and temporal resolutions and therefore, a time-resolved PIV equipped with high-resolution camera(s). In this sense, Stereo/Tomographic PIV could also be carried out to study on the wake-jet interactions.

A proper-orthogonal-decomposition (POD) analysis can be carried out on a time-resolved data, to extract the information on dominating structures of the flow. This is beneficial to get insight into the underlying dynamics of TGG flows. For example, instantaneous turbulence structures contribute significantly to the first and second POD modes, i.e., TKE. Forcing dominating structures leads to controlling the turbulence. POD analysis would result in a much reduced computational cost to CFD modeling since almost all the necessary information can be extracted within some first modes (POD bases) to reproduce a close match to the original flow.

REFERENCES

[1]   L.F.G. Simmons, C. Salter, Experimental Investigation and Analysis of the Velocity Variations in Turbulent Flow, Proc. R. Soc. London. 106 (1934) 463–477. doi:10.1103/RevModPhys.4.87.

[2]   G.I. Taylor, Statistical Theory of Turbulence, Proc. R. Soc. A Math. Phys. Eng. Sci. 151 (1935) 444–454. doi:10.1098/rspa.1935.0159.

[3]   G. Comte-Bellot, S. Corrsin, The use of a contraction to improve the isotropy of grid-generated turbulence, J. Fluid Mech. 25 (1966) 657. doi:10.1017/S0022112066000338.

[4]   H.S. Kang, S. Chester, C. Meneveau, Decaying turbulence in an active-grid-generated flow and comparisons with large-eddy simulation, J. Fluid Mech. 480 (2003) 129–160. doi:10.1017/S0022112002003579.

[5]   G.A. Voth, K. Satyanarayan, E. Bodenschatz, Lagrangian acceleration measurements at large Reynolds numbers, Phys. Fluids. 10 (1998) 2268. doi:10.1063/1.869748.

[6]   E.D. Siggia, Numerical study of small-scale intermittency in three-dimensional turbulence, J. Fluid Mech. 107 (1981) 375. doi:10.1017/S002211208100181X.

[7]   P. Lavoie, L. Djenidi, R. a. Antonia, Effects of initial conditions in decaying turbulence generated by passive grids, J. Fluid Mech. 585 (2007) 395. doi:10.1017/S0022112007006763.

[8]   A. Thormann, C. Meneveau, Decay of homogeneous, nearly isotropic turbulence behind active fractal grids, Phys. Fluids. 26 (2014). doi:10.1063/1.4865232.

[9]   I. Wygnanski, F. Champagne, B. Marasli, On the large-scale structures in two-dimensional, small-deficit, turbulent wakes, J. Fluid Mech. 168 (1986) 31–71. doi:10.1017/S0022112086000289.

[10]   W.K. George, The self-preservation of turbulent flows and its relation to initial conditions and coherent structures, Adv. Turbul. (1989) 39–73.

[11] Y. Zhou, R.A. Antonia, Memory effects in a turbulent plane wake, Exp. Fluids. 19 (1995) 112–120. doi:10.1007/BF00193857.

[12] P.-Å. Krogstad, P. Davidson, Freely-Decaying, Homogeneous Turbulence Generated by Multi-scale Grids, J. Fluid Mech. 032042 (2011) 417–434. doi:10.1088/1742-6596/318/3/032042.

[13] P.A. Krogstad, P.A. Davidson, Near-field investigation of turbulence produced by multi-scale grids, Phys. Fluids. 24 (2012). doi:10.1063/1.3693132.

[14] R. Gomes-Fernandes, B. Ganapathisubramani, J.C. Vassilicos, Particle image velocimetry study of fractal-generated turbulence, J. Fluid Mech. (2012) 1–31. doi:10.1017/jfm.2012.394.

[15] J.I. Cardesa, T.B. Nickels, J.R. Dawson, 2D PIV measurements in the near field of grid turbulence using stitched fields from multiple cameras, Exp. Fluids. 52 (2012) 1611–1627. doi:10.1007/s00348-012-1278-4.

[16] G. Cafiero, S. Discetti, T. Astarita, Flow field features of the near-wake of jets with fractal inserts, 115103 (2014) 7–10. doi:10.1063/1.4935185.

[17] R. Gomes-Fernandes, B. Ganapathisubramani, J.C.C. Vassilicos, The energy cascade in near-field non-homogeneous non-isotropic turbulence, J. Fluid Mech. 771 (2015) 676–705. doi:10.1017/jfm.2015.201.

[18] L. Gan, P.A. Krogstad, Evolution of turbulence and in-plane vortices in the near field flow behind multi-scale planar grids, Phys. Fluids. 28 (2016). doi:10.1063/1.4960025.

[19] K. Nagata, T. Saiki, Y. Sakai, Y. Ito, K. Iwano, Effects of grid geometry on non-equilibrium dissipation in grid turbulence, Phys. Fluids. 29 (2017). doi:10.1063/1.4973416.

[20] M. Hideharu, Realization of a large-scale turbulence field in a small wind tunnel, Fluid Dyn. Res. 8 (1991) 53–64. doi:10.1016/0169-5983(91)90030-M.

[21] R.J. Hearst, Fractal, Classical, and Active Grid Turbulence: From Production to Decay, University of Toronto, 2015.

[22] Hurst D. and Vassilicos J. C., Scalings and decay of fractal-generated turbulence, Phys. Fluids. 19 (2007). doi:10.1063/1.2676448.

[23] P. Saffman, The large-scale structure of homogeneous turbulence, J. Fluid Mech. 27 (1967) 581–593. http://authors.library.caltech.edu/10122/.

[24] J.C.C. Bennett, S. Corrsin, Small Reynolds number nearly isotropic turbulence

in a straight duct and a contraction, Phys. Fluids. 21 (1978) 2129. doi:10.1063/1.862168.

[25] P.A. Krogstad, P.A. Davidson, Is grid turbulence Saffman turbulence?, J. Fluid Mech. 642 (2010) 373. doi:10.1017/S0022112009991807.

[26] N.A. Buchmann, C. Atkinson, J. Soria, Tomographic and Stereoscopic PIV measurements of Grid generated Homogeneous Turbulence, Int. Symp. Appl. Laser Tech. to Fluid Mech. (2010) 5–8.

[27] F. Hausdorff, Dimension und äußeres Maß, Math. Ann. 79 (1919) 157–179.

[28] S. Laizet, J.C. Vassilicos, Multiscale Generation of Turbulence, J. Multiscale Model. 01 (2009) 177–196. doi:10.1142/S1756973709000098.

[29] Koch Snowflake, (n.d.). https://en.wikipedia.org/wiki/Koch_snowflake.

[30] J.C. Queiros-Conde, D. Vassilicos, Turbulent wakes of 3-D fractal grids, in: J.C. Vassilicos (Ed.), Intermittency Turbul. Flows, Cambridge University Press, 2001.

[31] A. Staicu, B. Mazzi, J.C. Vassilicos, W. van de Water, Turbulent wakes of fractal objects., Phys. Rev. E. Stat. Nonlin. Soft Matter Phys. 67 (2003) 066306. doi:10.1103/PhysRevE.67.066306.

[32] B. Mazzi, F. Okkels, J.C. Vassilicos, A shell-model approach to fractal-induced turbulence, Eur. Phys. J. B. 28 (2002) 243–251. doi:10.1140/epjb/e2002-00226-6.

[33] L. Biferale, M. Cencini, A.S. Lanotte, M. Sbragaglia, F. Toschi, Anomalous scaling and universality in hydrodynamic systems with power-law forcing, New J. Phys. 6 (2004) 37–37. doi:10.1088/1367-2630/6/1/037.

[34] B. Mazzi, J.C. Vassilicos, Fractal-generated turbulence, J. Fluid Mech. 502 (2004) 65–87. doi:10.1017/S0022112003007249.

[35] P. Valente, C. Vassilicos, The decay of turbulence generated by a class of multi-scale grids, J. Fluid Mech. 687 (2011) 300–340. doi:10.1017/jfm.2011.353.

[36] P.C. Valente, J.C. Vassilicos, Comment on "Dissipation and decay of fractal-generated turbulence" [Phys. Fluids 19, 105108 (2007)], Phys. Fluids. 23 (2011) 10–12. doi:10.1063/1.3657088.

[37] S. Laizet, J.C. Vassilicos, Fractal space-scale unfolding mechanism for energy-efficient turbulent mixing, Phys. Rev. E - Stat. Nonlinear, Soft Matter Phys. 86 (2012) 1–11. doi:10.1103/PhysRevE.86.046302.

[38] P.C. Valente, J.C. Vassilicos, Dependence of decaying homogeneous isotropic turbulence on inflow conditions, Phys. Lett. Sect. A Gen. At. Solid State Phys. 376 (2012) 510–514. doi:10.1016/j.physleta.2011.11.040.

[39] K. Nagata, Y. Sakai, T. Inaba, H.H. Suzuki, O. Terashima, H.H. Suzuki, Turbulence structure and turbulence kinetic energy transport in multiscale/fractal-generated turbulence, Phys. Fluids. 25 (2013). doi:10.1063/1.4811402.

[40] S. Discetti, I.B. Ziskin, T. Astarita, R.J. Adrian, K.P. Prestridge, PIV measurements of anisotropy and inhomogeneity in decaying fractal generated turbulence, Fluid Dyn. Res. 45 (2013) 061401. doi:10.1088/0169-5983/45/6/061401.

[41] R.J. Hearst, P. Lavoie, Scale-by-scale energy budget in fractal element grid-generated turbulence, J. Turbul. 15 (2014) 540–554. doi:10.1080/14685248.2014.916041.

[42] P.C. Valente, J.C. Vassilicos, The non-equilibrium region of grid-generated decaying turbulence, J. Fluid Mech. 744 (2014) 5–37. doi:10.1017/jfm.2014.41.

[43] R.J. Hearst, P. Lavoie, Decay of turbulence generated by a square-fractal-element grid, J. Fluid Mech. 741 (2014) 567–584. doi:10.1017/jfm.2013.684.

[44] R.J. Hearst, P. Lavoie, Velocity derivative skewness in fractal-generated, non-equilibrium grid turbulence, Phys. Fluids. 27 (2015). doi:10.1063/1.4926356.

[45] G. Melina, P.J.K. Bruce, J.C. Vassilicos, Vortex shedding effects in grid-generated turbulence, Phys. Rev. Fluids. 1 (2016) 044402. doi:10.1103/PhysRevFluids.1.044402.

[46] J. Nedić, S. Tavoularis, Measurements of passive scalar diffusion downstream of regular and fractal grids, J. Fluid Mech. 800 (2016) 358–386. doi:10.1017/jfm.2016.385.

[47] R.J. Hearst, P. Lavoie, Effects of multi-scale and regular grid geometries on decaying turbulence, J. Fluid Mech. 803 (2016) 528–555. doi:10.1017/jfm.2016.515.

[48] S. Weitemeyer, N. Reinke, J. Peinke, M. Hölling, Multi-scale generation of turbulence with fractal grids and an active grid, Fluid Dyn. Res. 45 (2013) 061407. doi:10.1088/0169-5983/45/6/061407.

[49] P. Baj, P.J.K. Bruce, O.R.H. Buxton, The triple decomposition of a fluctuating

velocity field in a multiscale flow, Phys. Fluids. 27 (2015) 1–43. doi:10.1063/1.4923744.

[50] R. Gomes-Fernandes, B. Ganapathisubramani, J.C. Vassilicos, Evolution of the velocity-gradient tensor in a spatially developing turbulent flow, J. Fluid Mech. 756 (2014) 252–292. doi:10.1017/jfm.2014.452.

[51] E.R. Seoud, C.J. Vassilicos, Dissipation and decay of fractal-generated turbulence, Phys. Fluids. 19 (2007). doi:10.1063/1.2795211.

[52] N. Mazellier, J.C. Vassilicos, Turbulence without Richardson-Kolmogorov cascade, Phys. Fluids. 22 (2010) 1–25. doi:10.1063/1.3453708.

[53] R. Stresing, J. Peinke, R.E. Seoud, J.C. Vassilicos, Defining a new class of turbulent flows, Phys. Rev. Lett. 104 (2010) 1–4. doi:10.1103/PhysRevLett.104.194501.

[54] H. Suzuki, K. Nagata, Y. Sakai, R. Ukai, High-Schmidt-number scalar transfer in regular and fractal grid turbulence, Phys. Scr. T142 (2010) 014069. doi:10.1088/0031-8949/2010/T142/014069.

[55] S. Discetti, I.B. Ziskin, R.J. Adrian, K. Prestridge, PIV study of fractal grid turbulence, 9Th Int. Symp. Part. Image Velocim. (2011) 15–18.

[56] S. Laizet, J. Nedić, J.C. Vassilicos, The spatial origin of −5/3 spectra in grid-generated turbulence, Phys. Fluids. 27 (2015) 065115. doi:10.1063/1.4923042.

[57] K. Nagata, H. Suzuki, Y. Sakai, T. Hayase, T. Kubo, Direct numerical simulation of turbulent mixing in regular and fractal grid turbulence, Phys. Scr. T142 (2010) 014065. doi:10.1088/0031-8949/2008/T132/014054.

[58] S. Laizet, E. Lamballais, J.C. Vassilicos, A numerical strategy to combine high-order schemes, complex geometry and parallel computing for high resolution DNS of fractal generated turbulence, Comput. Fluids. 39 (2010) 471–484. doi:10.1016/j.compfluid.2009.09.018.

[59] S. Laizet, J.C. Vassilicos, DNS of fractal-generated turbulence, Flow, Turbul. Combust. 87 (2011) 673–705. doi:10.1007/s10494-011-9351-2.

[60] S. Laizet, J.C. Vassilicos, C. Cambon, Interscale energy transfer in decaying turbulence and vorticity–strain-rate dynamics in grid- generated turbulence, Fluid Dyn. Res. 45 (2013) 61408. doi:10.1088/0169-5983/45/6/061408.

[61] Y. Zhou, K. Nagata, Y. Sakai, H. Suzuki, Y. Ito, O. Terashima, T. Hayase, Relevance of turbulence behind the single square grid to turbulence generated

by regular- and multiscale-grids, Phys. Fluids. 26 (2014). doi:10.1063/1.4890746.

[62] S. Laizet, J.C. Vassilicos, Stirring and scalar transfer by grid-generated turbulence in the presence of a mean scalar gradient, J. Fluid Mech. 764 (2015) 52–75. doi:10.1017/jfm.2014.695.

[63] G.K. Batchelor, The Theory of Homogeneous Turbulence (Cambridge Science Classics), Cambridge University Press, 1982. http://www.amazon.com/Homogeneous-Turbulence-Cambridge-Science-Classics/dp/0521041171 (accessed August 10, 2017).

[64] S. Corrsin, Turbulence: Experimental Methods, in: Strömungsmechanik II / Fluid Dyn. II. Ser. Handb. Der Phys. / Encycl. Physics, ISBN 978-3-662-10110-0. Springer Berlin Heidelb. (Berlin, Heidelberg), Ed. by C. Truesdell, Vol. 3 / 8 / 2, Pp. 524-590, 1963: pp. 524–590. doi:10.1007/978-3-662-10109-4_4.

[65] K. Bai, C. Meneveau, J. Katz, Near-Wake Turbulent Flow Structure and Mixing Length Downstream of a Fractal Tree, Boundary-Layer Meteorol. 143 (2012) 285–308. doi:10.1007/s10546-012-9700-2.

[66] J.I. Cardesa-Dueñas, T.B. Nickels, J.R. Dawson, Experimental study of homogenisation in grid turbulence, J. Phys. Conf. Ser. 318 (2011) 032041. doi:10.1088/1742-6596/318/3/032041.

[67] T. Earl, L. Thomas, S. Cochard, R. Ben-Salah, B. Tremblais, L. David, Volumetric Measurements by Tomographic PIV of Grid Generated Turbulence in an Open Channel Flow, in: Eighth Int. Symp. Turbul. Shear Flow Phenom., France, 2013: pp. 1–6.

[68] W.S.J. Uijttewaal, G.H. Jirka, Grid turbulence in shallow flows, J. Fluid Mech. 489 (2003) 325–344. doi:10.1017/S0022112003005020.

[69] G. Cafiero, S. Discetti, T. Astarita, Heat transfer enhancement of impinging jets with fractal-generated turbulence, Int. J. Heat Mass Transf. 75 (2014) 173–183. doi:10.1016/j.ijheatmasstransfer.2014.03.049.

[70] P. Geipel, K.H.H. Goh, R.P. Lindstedt, Fractal-generated turbulence in opposed jet flows, Flow, Turbul. Combust. 85 (2010) 397–419. doi:10.1007/s10494-010-9288-x.

[71] L. Djenidi, Lattice-Boltzmann simulation of grid-generated turbulence, J. Fluid Mech. 552 (2006) 13. doi:10.1017/S002211200600869X.

[72] Ö. Ertunç, N. Özyilmaz, H. Lienhart, F. Durst, K. Beronov, Homogeneity of turbulence generated by static-grid structures, J. Fluid Mech. 654 (2010) 473–500. doi:10.1017/S0022112010000479.

[73] G.R. Coffey, C. J.; Hunt, Mixing effectiveness of fractal grids for inline static mixers, Proof Concept …. (2007). http://workspace.imperial.ac.uk/tmfc/public/proof_FG.PDF.

[74] Amalgamated Research LLC (ARi), (n.d.). http://www.arifractal.com/ (accessed March 22, 2017).

[75] Fractal Blade Fluid Mixers, (n.d.). https://www.imperialinnovations.co.uk/industry/available-technologies/fractal-blade-fluid-mixers/ (accessed January 22, 2018).

[76] F.C.G.A. Nicolleau, S.M.M. Salim, A.F. Nowakowski, Experimental study of a turbulent pipe flow through a fractal plate, J. Turbul. 12 (2011) N44. doi:10.1080/14685248.2011.637046.

[77] B. Manshoor, F.C.G.A.C.G.A. Nicolleau, S.B.M.B.M. Beck, The fractal flow conditioner for orifice plate flow meters, Flow Meas. Instrum. 22 (2011) 208–214. doi:10.1016/j.flowmeasinst.2011.02.003.

[78] J. Nedic, B. Ganapathisubramani, J.C. Vassilicos, J. Borée, L.E. Brizzi, A. Spohn, J. Nedić, B. Ganapathisubramani, J.C. Vassilicos, J. Borée, L.E. Brizzi, A. Spohn, Aeroacoustic Performance of Fractal Spoilers, AIAA J. 50 (2012) 2695–2710. doi:10.2514/1.J051387.

[79] J. Nedić, B. Ganapathisubramani, J.C. Vassilicos, Drag and near wake characteristics of flat plates normal to the flow with fractal edge geometries, Fluid Dyn. Res. 45 (2013) 061406. doi:10.1088/0169-5983/45/6/061406.

[80] A.A. Verbeek, T.W.F.M. Bouten, G.G.M. Stoffels, B.J. Geurts, T.H. van der Meer, Fractal turbulence enhancing low-swirl combustion, Combust. Flame. 162 (2015) 129–143. doi:10.1016/j.combustflame.2014.07.003.

[81] T. Sponfeldner, N. Soulopoulos, F. Beyrau, Y. Hardalupas, A.M.K.P. Taylor, J.C. Vassilicos, The structure of turbulent flames in fractal- and regular-grid-generated turbulence, Combust. Flame. 162 (2015) 3379–3393. doi:10.1016/j.combustflame.2015.06.004.

[82] K.H.H. Goh, P. Geipel, R.P. Lindstedt, Lean premixed opposed jet flames in fractal grid generated multiscale turbulence, Combust. Flame. 161 (2014)

2419–2434. doi:10.1016/j.combustflame.2014.03.010.

[83] S.M. Mcclure, Experimental investgation of turbulent flow induced by new-generation wind fences with multi-scale fractal structure, (2016) 88.

[84] Ş. Çoşkun, H.A. Hazaveh, O. Uzol, Ö. Kurç, Experimental investigation of wake flow field and wind comfort characteristics of fractal wind fences, J. Wind Eng. Ind. Aerodyn. 168 (2017) 32–47. doi:10.1016/j.jweia.2017.05.001.

[85] D.M. Calamas, D.G. Dannelley, G.H. Keten, Experimental Effectiveness of Sierpinski Carpet Fractal Fins in a Natural Convection Environment, J. Heat Transfer. 139 (2017) 092501. doi:10.1115/1.4036595.

[86] A.Y. Alharbi, A Study of Micro-Scale, Fractal-Like Branching Flow Networks for Reduced Pumping Power and Improved Temperature Uniformity, Oregon State University, 2001.

[87] D.B. Heymann, On the Optimization of Performance in Fractal-like Branching Microchannel Heat Transfer Devices, Oregon State University, 2010.

[88] Fractal Antenna Systems: The World's Smallest Wideband and Multiband Antennas, (n.d.). http://www.fractenna.com/ (accessed March 22, 2017).

[89] Fractus Antennas - miniature antennas for smartphones, wireless and IoT Newserver, (n.d.). http://www.fractusantennas.com/ (accessed March 22, 2017).

[90] S. Laizet, J.C. Vassilicos, C. Cambon, Interscale energy transfer in decaying turbulence and vorticity–strain-rate dynamics in grid- generated turbulence Interscale energy transfer in decaying turbulence and vorticity–strain-rate dynamics in grid-generated turbulence, Fluid Dyn. Res. 45 (2013) 61408. doi:10.1088/0169-5983/45/6/061408.

[91] S. Chester, C. Meneveau, M.B. Parlange, Modeling turbulent flow over fractal trees with renormalized numerical simulation, J. Comput. Phys. 225 (2007) 427–448. doi:10.1016/j.jcp.2006.12.009.

[92] S. Chester, C. Meneveau, Renormalized numerical simulation of flow over planar and non-planar fractal trees, Environ. Fluid Mech. 7 (2007) 289–301. doi:10.1007/s10652-007-9026-7.

[93] N. Mazellier, J.C. Vassilicos, The turbulence dissipation constant is not universal because of its universal dependence on large-scale flow topology, Phys. Fluids. 20 (2008). doi:10.1063/1.2832778.

[94] P.E. Roach, The generation of nearly isotropic turbulence by means of grids, Int. J. Heat Fluid Flow. 8 (1987) 82–92. doi:10.1016/0142-727X(87)90001-4.

[95] A. Sciacchitano, Uncertainty quantification in particle image velocimetry, Delft University of Technology, 2014.

[96] A. Sciacchitano, B. Wieneke, PIV uncertainty propagation, Meas. Sci. Technol. 27 (2016). doi:10.1088/0957-0233/27/8/084006.

[97] C. Brossard, J.-C. Monnier, P. Barricau, F.-X. Vandernoot, Y. Le Sant, F. Champagnat, G. Le Besnerais, Principles and applications of particle image velocimetry, Onera AerospaceLab J. AL01-03 (2009) 1–11.

[98] A. Sciacchitano, B. Wieneke, F. Scarano, PIV uncertainty quantification by image matching, Meas. Sci. Technol. 24 (2013) 045302. doi:10.1088/0957-0233/24/4/045302.

[99] J.J. Charonko, P.P. Vlachos, Estimation of uncertainty bounds for individual particle image velocimetry measurements from cross-correlation peak ratio, Meas. Sci. Technol. 24 (2013) 065301. doi:10.1088/0957-0233/24/6/065301.

[100] M. Raffel, C. Willert, J. Kompenhans, Particle Image Velocimetry: A Practical Guide, Springer Berlin, 2002. http://www.amazon.com/dp/3540636838 (accessed April 20, 2018).

[101] G. Northem, G. Anderson, Survey of supersonic combustion ramjet research at Langley, in: 24th Aerosp. Sci. Meet., 1986. doi:10.2514/6.1986-159.

[102] J.A. Schetz, F.S. Billing, Studies of scramjet flowfields, in: 43rd AIAA Aerosp. Sci. Conf., 1987.

[103] H. Suzuki, K. Nagata, Y. Sakai, Y. Hasegawa, Fractal analysis of turbulent mixing in fractal-generated turbulence by planar laser-induced fluorescence, Phys. Scr. 88 (2013). doi:10.1088/0031-8949/2013/T155/014062.

[104] C.C. LIN, W.H. REID, Turbulent Flow, Theoretical Aspects., in: Sel. Pap. C. C. Lin with Comment., WORLD SCIENTIFIC, 1987: pp. 175–260. doi:10.1142/9789814415651_0014.

[105] J.C.C.C. Isaza, R. Salazar, Z. Warhaft, On grid-generated turbulence in the near- and far field regions, J. Fluid Mech. 753 (2014) 402–426. doi:10.1017/jfm.2014.375.

[106] H. (Hendrik) Tennekes, J.L. (John L. Lumley, A first course in turbulence, MIT Press, 1972. https://mitpress.mit.edu/books/first-course-turbulence (accessed

March 9, 2018).

[107] S.B. Pope, Turbulent Flows, 1st ed., cambridge university press, Cambridge, 2000. doi:10.1088/1468-5248/1/1/702.

[108] Y. Zhou, Direct Numerical Simulations on Grid-Generated Turbulence, Nagoya University, 2015.

[109] R.A. Antonia, T. Zhou, Y. Zhu, Three-component vorticity measurements in a turbulent grid flow, J. Fluid Mech. 374 (1998) 29–57. doi:10.1017/S0022112098002547.

[110] H.L. Grant, I.C.T. Nisbet, The inhomogeneity of grid turbulence, J. Fluid Mech. 2 (1957) 263–272. doi:10.1017/S0022112057000117.

[111] A.L. Kistler, T. Vrebalovich, Grid turbulence at large Reynolds numbers, J. Fluid Mech. 26 (1966) 37. doi:10.1017/S0022112066001071.

[112] E.M. Laws, J.L. Livesey, Flow Through Screens, Annu. Rev. Fluid Mech. 10 (1978) 247–266. doi:10.1146/annurev.fl.10.010178.001335.

[113] R.A. Pinker, M. V. Herbert, Pressure loss Associated with Compressible flow through Square-Mesh wire Gauzes, J. Mech. Eng. Sci. 9 (1967) 11–23. doi:10.1243/JMES_JOUR_1967_009_004_02.

[114] A. Omilion, J. Turk, W. Zhang, Turbulence Enhancement by Fractal Square Grids : Effects of Multiple Fractal Scales, (2018) 1–16. doi:10.3390/fluids3020037.

[115] T. van Karman, L. Howarth, On the statistical theory of isotropic turbulence, Proc. R. Soc. Lond. A. Math. Phys. Sci. 164 (1938) 192–215. http://rspa.royalsocietypublishing.org/content/164/917/192 (accessed September 2, 2017).

[116] M. Gad-El-Hak, S. Corrsin, Measurements of the nearly isotropic turbulence behind a uniform jet grid, J. Fluid Mech. 62 (1974) 115. doi:10.1017/S0022112074000607.

[117] M.S. Mohamed, J.C. Larue, The decay power law in grid-generated turbulence, J. Fluid Mech. 219 (1990) 195. doi:10.1017/S0022112090002919.

[118] P. Holmes, J.L. Lumley, G. Berkooz, C.W. Rowley, Turbulence, Coherent Structures, Dynamical Systems and Symmetry, Cambridge University Press, Cambridge, 2012. doi:10.1017/CBO9780511919701.

[119] J.O. Hinze, Turbulence, McGraw-Hill, 1975.

166

[120] T. Tanaka, J.K. Eaton, A correction method for measuring turbulence kinetic energy dissipation rate by PIV, Exp. Fluids. 42 (2007) 893–902. doi:10.1007/s00348-007-0298-y.

[121] A.A. (Albert A. Townsend, The structure of turbulent shear flow, Cambridge University Press, 1976. https://catalogue.nla.gov.au/Record/1822067 (accessed March 9, 2018).

[122] S. Corrsin, S. Corrsin, Estimates of the Relations between Eulerian and Lagrangian Scales in Large Reynolds Number Turbulence, J. Atmos. Sci. 20 (1963) 115–119. doi:10.1175/1520-0469(1963)020<0115:EOTRBE>2.0.CO;2.

[123] K.R. Sreenivasan, On the scaling of the turbulence energy dissipation rate, Phys. Fluids. 27 (1984) 1048. doi:10.1063/1.864731.

[124] C.M. White, A.N. Karpetis, K.R. Sreenivasan, High-Reynolds-number turbulence in small apparatus: Grid turbulence in cryogenic liquids, J. Fluid Mech. 452 (2002) 189–197. doi:10.1017/S0022112001007194.

[125] P.K. Yeung, S.B. Pope, Lagrangian statistics from direct numerical simulations of isotropic turbulence, J. Fluid Mech. 207 (1989) 531. doi:10.1017/S0022112089002697.

[126] J. De Jong, L. Cao, S.H. Woodward, J.P.L.C. Salazar, L.R. Collins, H. Meng, Dissipation rate estimation from PIV in zero-mean isotropic turbulence, Exp. Fluids. 46 (2009) 499–515. doi:10.1007/s00348-008-0576-3.

[127] F.H. Champagne, V.G. Harris, S. Corrsin, Experiments on nearly homogeneous turbulent shear flow, J. Fluid Mech. 41 (1970) 81. doi:10.1017/S0022112070000538.

[128] P. Lavoie, G. Avallone, F. De Gregorio, G.P. Romano, R.A. Antonia, Spatial resolution of PIV for the measurement of turbulence, Exp. Fluids. 43 (2007) 39–51. doi:10.1007/s00348-007-0319-x.

[129] et al. Nagata, K., Direct numerical simulation of turbulence characteristics generated by fractal grids, Int. Rev. Phys. 2 (2008) 400–409.

[130] L.F. Richardson, Weather Prediction by Numerical Process, Cambridge University Press, Cambridge, 1922.

[131] K. Sreenivasan, The energy dissipation rate in turbulent shear flows, in: S.M. Deshpande and A. Prabhu and K.R. Sreenivasan (Ed.), Dev. Fluid Mech.

Aerosp. Eng., Interline Publishers, Viswanath, Bangalore, 1995: pp. 159–190. https://nyuscholars.nyu.edu/en/publications/the-energy-dissipation-rate-in-turbulent-shear-flows (accessed September 6, 2017).

[132] P.C. Valente, J.C. Vassilicos, Universal dissipation scaling for nonequilibrium turbulence, Phys. Rev. Lett. 108 (2012) 1–5. doi:10.1103/PhysRevLett.108.214503.

[133] H. Versteeg, Malalasekera W., An introduction to computational fluid dynamics. The finite volume method itle, 1995.

[134] J.C. Vassilicos, Dissipation in Turbulent Flows, Annu. Rev. Fluid Mech. 47 (2015) 95–114. doi:10.1146/annurev-fluid-010814-014637.

APPENDICES

(A) Budget for turbulent kinetic energy

Budget for turbulent kinetic energy is the equation for kinetic energy of the velocity fluctuations. What will come next, is the tedious exercise of obtaining this equation. We will start with the famous Navier-Stokes equation; Continuity and momentum equations in tensorial form read,

$$\frac{\partial u_i}{\partial x_i} = 0 \tag{App.1}$$

and

$$\frac{\partial u_j}{\partial t} + \frac{\partial}{\partial x_j}(u_i u_j) = -\frac{1}{\rho}\frac{\partial P}{\partial x_j} - g\delta_{i3} + \nu\nabla^2 u_j \tag{App.2}$$

then, apply Reynolds decomposition, i.e.

$$u_i = \overline{u_i} + u'_i$$
$$P = \overline{P} + P' \tag{App.3}$$

Continuity equation (App.1) will then become,

$$\frac{\partial}{\partial x_i}(\overline{u_i} + u'_i) = 0 \rightarrow \frac{\partial \overline{u_i}}{\partial x_i} + \frac{\partial u'_i}{\partial x_i} = 0 \xrightarrow{averageing} \frac{\partial \overline{u_i}}{\partial x_i} + 0$$
$$= 0 \rightarrow \frac{\partial \overline{u_i}}{\partial x_i} = \frac{\partial u'_i}{\partial x_i} = 0 \tag{App.4}$$

Momentum equation (App.2) also becomes,

$$\frac{\partial}{\partial t}\left(\overline{u_j} + u'_j\right) + \frac{\partial}{\partial x_i}\left(\overline{u_i}\,\overline{u_j} + \overline{u_i}u'_j + u'_i\overline{u_j} + u'_iu'_j\right)$$

$$= -\frac{1}{\rho}\frac{\partial}{\partial x_j}\left(\overline{P} + P'\right) + \nu\nabla^2\left(\overline{u_i} + u'_i\right) + 0$$

(App.5)

Where body forces due to gravity are ignored. Averaging (App.5) gives:

$$\frac{\partial}{\partial t}\left(\overline{u_j}\right) + \frac{\partial}{\partial x_i}\left(\overline{u_i}\,\overline{u_j} + \overline{u'_iu'_j}\right) = -\frac{1}{\rho}\frac{\partial}{\partial x_j}\left(\overline{P}\right) + \nu\nabla^2\left(\overline{u_i}\right)$$

(App.6)

Remainder terms – i.e., subtracting (App.6) from (App.5) – would be,

$$\frac{\partial}{\partial t}\left(u'_j\right) + \frac{\partial}{\partial x_i}\left(\overline{u_i}u'_j + u'_i\overline{u_j} + u'_iu'_j - \overline{u'_iu'_j}\right)$$

$$= -\frac{1}{\rho}\frac{\partial}{\partial x_j}\left(P'\right) + \nu\nabla^2\left(u'_j\right)$$

(App.7)

In which, $-\overline{u'_iu'_j}$ is the Reynolds stress.

Turbulent kinetic energy is defined as,

$$k = \frac{1}{2}\left(\overline{u'_ju'_j}\right)$$

(App.8)

To obtain the equation for turbulent kinetic energy we need to search for the velocity fluctuation term (u'_j) then. Such a term can be found in (App.7). Multiplying (App.7) by u'_j gives,

$$u'_j\frac{\partial}{\partial t}\left(u'_j\right) + u'_j\frac{\partial}{\partial x_i}\left(\overline{u_i}u'_j + u'_i\overline{u_j} + u'_iu'_j - \overline{u'_iu'_j}\right)$$

$$= -\frac{1}{\rho}u'_j\frac{\partial}{\partial x_j}\left(P'\right) + \nu u'_j\nabla^2\left(u'_j\right)$$

(App.9)

Rearranging (App.9):

$$\frac{\partial}{\partial t}\left(\frac{1}{2}u'_j u'_j\right) + \overbrace{u'_j \frac{\partial}{\partial x_i}\left(\overline{u_i}u'_j + u'_i\overline{u_j} + u'_i u'_j - \overline{u'_i u'_j}\right)}^{A}$$

$$= -\frac{1}{\rho}\frac{\partial}{\partial x_j}\left(u'_j P'\right) + \nu\frac{\partial}{\partial x_i}\left(u'_j \frac{\partial u'_j}{\partial x_i}\right) \qquad \text{(App.10)}$$

$$- \nu\left(\frac{\partial u'_j}{\partial x_i}\right)^2$$

keeping in mind that,

$$-\frac{1}{\rho}u'_j\frac{\partial}{\partial x_j}(P') = -\frac{1}{\rho}\left[\frac{\partial}{\partial x_j}\left(u'_j P'\right) - P'\overbrace{\frac{\partial u'_j}{\partial x_j}}^{=0}\right]$$

$$= -\frac{1}{\rho}\frac{\partial}{\partial x_j}\left(u'_j P'\right) \qquad \text{(App.11)}$$

and

$$\nu u'_j\nabla^2(u'_j) = \nu u'_j\frac{\partial}{\partial x_i}\left(\frac{\partial u'_j}{\partial x_i}\right)$$

$$= \nu\left[\frac{\partial}{\partial x_i}\left(u'_j\frac{\partial u'_j}{\partial x_i}\right) - \left(\frac{\partial u'_j}{\partial x_i}\right)\left(\frac{\partial u'_j}{\partial x_i}\right)\right] \qquad \text{(App.12)}$$

Arranging of triple terms (A) using continuity equation ($\frac{\partial \overline{u_i}}{\partial x_i} = \frac{\partial u'_i}{\partial x_i} = 0$) repeatedly,

$$(A): u'_j\frac{\partial}{\partial x_i}\left(\overleftarrow{\overline{u_i}}u'_j + \overleftarrow{u'_i}\overline{u_j} + \overleftarrow{u'_i}u'_j - \overline{u'_i u'_j}\right)$$

$$= \overrightarrow{u'_j}\overline{u_i}\frac{\partial u'_j}{\partial x_i} + u'_j u'_i\frac{\partial \overline{u_j}}{\partial x_i} + \overrightarrow{u'_j}u'_i\frac{\partial u'_j}{\partial x_i} \qquad \text{(App.13)}$$

$$- u'_j\frac{\partial}{\partial x_i}\left(\overline{u'_i u'_j}\right)$$

where $\overleftarrow{}$ and $\overrightarrow{}$ denote taking the corresponding value outside/inside the differentiation, respectively. Further arrangements on (App.13) yields,

$$(A): \overline{u_i} \frac{\partial}{\partial x_i}\left(\frac{1}{2}u'_j u'_j\right) + u'_j u'_i \frac{\partial \overline{u_j}}{\partial x_i} + \overrightarrow{u'_i} \frac{\partial}{\partial x_i}\left(\frac{1}{2}u'_j u'_j\right)$$

$$- u'_j \frac{\partial}{\partial x_i}\left(\overline{u'_i u'_j}\right)$$

$$= \overline{u_i} \frac{\partial}{\partial x_i}\left(\frac{1}{2}u'_j u'_j\right) + u'_j u'_i \frac{\partial \overline{u_j}}{\partial x_i}$$

$$+ \frac{\partial}{\partial x_i}\left(\frac{1}{2}u'_i u'_j u'_j\right) - u'_j \frac{\partial}{\partial x_i}\left(\overline{u'_i u'_j}\right)$$

(App.14)

Taking average on (App.14) gives,

$$\overline{A}: \overline{u_i} \frac{\partial}{\partial x_i}\left(\frac{1}{2}\overline{u'_j u'_j}\right) + \overline{u'_j u'_i} \frac{\partial \overline{u_j}}{\partial x_i} + \frac{\partial}{\partial x_i}\left(\frac{1}{2}\overline{u'_i u'_j u'_j}\right) - 0 \qquad \text{(App.15)}$$

Taking the average of (App.10) yields,

$$\frac{\partial}{\partial t}\left(\frac{1}{2}\overline{u'_j u'_j}\right)$$

$$+ \overbrace{\overline{u_i} \frac{\partial}{\partial x_i}\left(\frac{1}{2}\overline{u'_j u'_j}\right) + \overline{u'_j u'_i} \frac{\partial \overline{u_j}}{\partial x_i} + \frac{\partial}{\partial x_i}\left(\frac{1}{2}\overline{u'_i u'_j u'_j}\right)}^{\overline{A}}$$

(App.16)

$$= \underbrace{-\frac{1}{\rho}\frac{\partial}{\partial x_j}\left(\overline{u'_j P'}\right)}_{=-\frac{1}{\rho}\frac{\partial}{\partial x_i}\left(\overline{u'_i P'}\right)} + \nu \frac{\partial}{\partial x_i}\left(\overline{u'_j \frac{\partial u'_j}{\partial x_i}}\right) - \nu \overline{\left(\frac{\partial u'_j}{\partial x_i}\right)^2}$$

In a more compact form, taking $\frac{1}{2}\left(\overline{u'_j u'_j}\right) = k$ and grouping full derivatives,

$$\overbrace{\frac{\partial k}{\partial t} + \overline{u_i}\frac{\partial k}{\partial x_i}}^{\substack{\text{advection of } k \\ \text{by the average flow}}} + \overbrace{\overline{u'_j u'_i} \frac{\partial \overline{u_j}}{\partial x_i}}^{\text{shear production}}$$

$$= \underbrace{\frac{\partial}{\partial x_i}\left[\nu\left(\overline{u'_j \frac{\partial u'_j}{\partial x_i}}\right) - \left(\frac{1}{2}\overline{u'_i u'_j u'_j}\right) - \frac{1}{\rho}\left(\overline{u'_i P'}\right)\right]}_{\text{spatial redistribution}}$$

(App.17)

$$\underbrace{- \nu \overline{\left(\frac{\partial u'_j}{\partial x_i}\right)^2}}_{\substack{\text{viscous} \\ \text{dissipation}}}$$

172

keeping in mind that,

$$\frac{\partial k}{\partial t} + \overline{u_i}\frac{\partial k}{\partial x_i} = \frac{Dk}{Dt} \qquad \text{(App.18)}$$

is the total derivative of the turbulent kinetic energy.

Equation (App.17) is the budget for the turbulent kinetic energy. It simply says that the rate of change in 'k' is equal to the rate of production of 'k' + rate of redistribution of 'k' + rate of dissipation of 'k'. Hence, it reveals the interaction between the turbulence and the mean flow. Spatial redistribution consists of pressure-gradient work, transport by turbulent velocity fluctuations, and transport by viscous stresses. Shear production and viscous dissipation are kinds of deformation works [106]. Note that the viscous dissipation term is always negative.

We can rewrite equation (App.17) such that,

$$\frac{Dk}{Dt} = -\frac{\partial}{\partial x_j}\left(\frac{1}{\rho}\overline{u_j p} + \frac{1}{2}\overline{u_i u_i u_j} - 2\nu\overline{u_i s_{ij}}\right) - \overline{u_i u_j}S_{ij}$$
$$- 2\nu\overline{s_{ij}s_{ij}} \qquad \text{(App.19)}$$

where

$$s_{ij} \equiv \frac{1}{2}\left(\frac{\partial u_i}{\partial x_j} + \frac{\partial u_j}{\partial x_i}\right)$$
$$S_{ij} \equiv \frac{1}{2}\left(\frac{\partial \overline{u_i}}{\partial x_j} + \frac{\partial \overline{u_j}}{\partial x_i}\right) \qquad \text{(App.20)}$$

are the fluctuating and mean rate of strains, respectively. If the flow is steady and homogeneous, Equation (App.19) reduces to

$$-\overline{u_i u_j}S_{ij} = 2\nu\overline{s_{ij}s_{ij}} \qquad \text{(App.21)}$$

In other words, the rate of production of turbulent energy by Reynolds stresses equals the rate of viscous dissipation. This is not the case in many turbulent flows.

(B) Details on turbulence-generating-grids geometry and flow properties

Grid	CSG	FSG	FCG	FIG
T^2 (mm^2)	340×340			
L_{TS} (mm)	1000			
U_0 (ms^{-1})	10.2376			
S	2	4	N/A	3
N	1	4	4	4
D_f	2	2	2	2
σ (%)	20	23.7	24.6	29.4
R_L	1.0	0.5	0.5	0.5
R_t	1.0	0.49	0.49	0.49
t_r	1.0	8.5	8.5	8.5
M_{eff} (mm)	20.0	19.76	20.43	25.34
x_* (mm)	$\cong 189$	$\cong 3201$	$\cong 6078$	$\cong 1910$
$L_0 (mm)$	20.0	180.69	249.0	180.26
$L_1 (mm)$	-	90.34	124.54	90.13
$L_2 (mm)$	-	45.17	62.273	45.06
$L_3 = L_{min} (mm)$	-	22.58	31.136	22.53
$t_0 (mm)$	2.11	10.2	10.2	17
$t_1 (mm)$	-	4.99	4.99	8.33
$t_2 (mm)$	-	2.45	2.45	4.08
$t_3 = t_{min} (mm)$	-	1.2	1.2	2
$\dfrac{L_0}{T}$	0.06	0.531	0.732	0.53
Re_{Meff}	12060	11880	12320	15240
$Re_{L_0} = \dfrac{UL_0}{\nu}$	12060	108600	150200	108420
Re_{t_0}	1270	6150	6150	10225
$\Delta x / x_*$	[0.04-2.38]	[0.0025-0.139]	[0.0013-0.074]	[0.005-0.235]
$\Delta x / M_{eff}$	[0.4-22.5]	[0.4-22.5]	[0.4-22.0]	[0.4-17.7]

CURRICULUM VITAE

PERSONAL INFORMATION

Surname, Name: Amiri Hazaveh, Hooman
Nationality: Iranian
Date and Place of Birth: 15 September 1985, Tehran, Iran
Marital Status: Married
Phone: +90 538 030 5856
Email: hooman.hazaveh@metu.edu.tr

EDUCATION

Degree	Institution	Year of Graduation
M.Sc.	Azad University, Tehran, Iran	2012
B.Sc.	Azad University, Tehran, Iran	2009
High School	SAMA High School, Tehran, Iran	2003

WORK EXPERIENCE

Year	Place	Enrollment
2016-Present	METU Center for Wind Energy (RÜZGEM)	Scientific Project Expert
2012-2016	METU Center for Wind Energy (RÜZGEM)	Researcher
2010-2012	Azad University – Science and Research branch, Tehran, Iran	Laboratory Assistant

PUBLICATIONS

Journals

- Şemsi Çoşkun, Hooman Amiri Hazaveh, Oğuz Uzol, Özgür Kurç, "*Experimental investigation of wake flow field and wind comfort characteristics of fractal wind fences*", Journal of wind engineering and industrial aerodynamics, 168, 32-47, 2017. DOI: https://doi.org/10.1016/j.jweia.2017.05.001

- S.M. Nima Shojaee, Hooman Amiri Hazaveh, *"Investigation of Total Pressure Distribution at Aerodynamic Interface Plane of an "S-shaped" Air Intake at Sideslip Condition"*, International Journal of Natural and Engineering Sciences ISSN: 1307-1149, E-ISSN: 2146-0086, Vol. 6(3), 2012, pp 87-94.

Conferences and Proceedings

- Uluocak S., Amiri Hazaveh H., Perçin M., Akpolat M.T., Uzol O., *"Experimental Investigation of the Effect of Helicopter Blade Tip Shapes on Aerodynamic Performance and Tip Vortex characteristics"*, (*In Turkish*) 7th National Aerospace Conference (VII. UHUK 2018). September 12-14, 2018. Samsun, Turkey.

- Amiri Hazaveh H., Uzol O., *"Experimental Study on the Near Wake Flow Characteristics of Fractal Turbulence Grids"*, Wind Energy Science Conference (WESC), Technical University of Denmark, Lyngby Campus, 26 June - 29 June 2017.

- Alican O., Amiri Hazaveh H., and Uzol O., *"Experimental Investigation of the effects of squealer tips on the blade tip leakage characteristics in a linear cascade facility of a gas turbine"*, (*In Turkish*) 6th National Aerospace Conference (VI. UHUK 2016). September 28-30, 2016. Kocaeli, Turkey.

- Amiri Hazaveh H., Uzol O., *"Investigation of the Near Wake Steady Flow development of a Fractal Square Grid using Particle Image Velocimetry"*, 2nd International Conference on New Research Achievements in Mechanics, Industrial and Aerospace Engineering, September 29, 2016. Tehran, Iran.

- Amiri Hazaveh H., Uzol O., *"PIV study of wall bounded Fractal-grid-generated Turbulence"*, 11th EAWE PhD Seminar on Wind Energy in Europe, September 22-25, 2015, Stuttgart, Germany.

- Ostovan Y., Amiri H., Uzol O., *"Aerodynamic Characterization of NREL S826 Airfoil at Low Reynolds Numbers"*, RUZGEM 2013 Conference on Wind Energy Science and Technology, October 3-4, 2013, METU Ankara Campus.

RESEARCH INTERESTS

Turbulence, Flow control, Experimental Aerodynamics, Wind tunnel experiments and design